UNIVERSITY
OF TRENTO - Italy
Department of Materials Engineering
and Industrial Technologies

Doctorate School in Materials Engineering – XXI cycle

Viscoelastic and fracture behaviour of polyolefin based nanocomposites

Andrea Dorigato

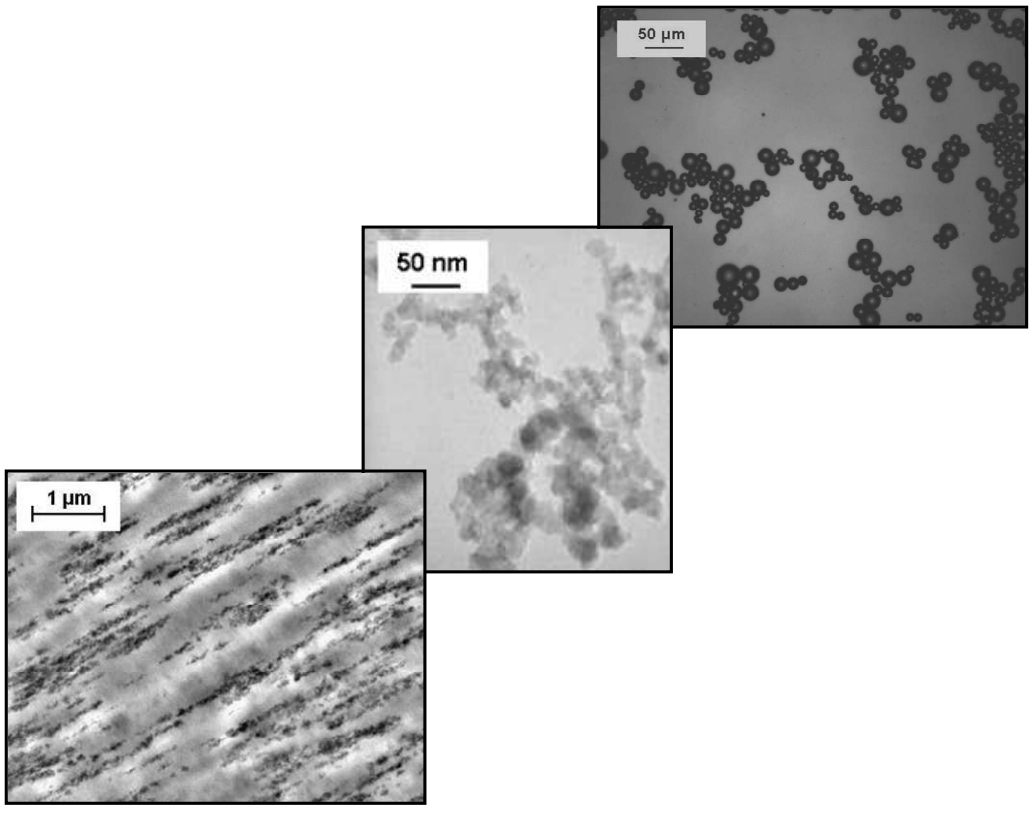

April 2009

UNIVERSITY
OF TRENTO - Italy
Department of Materials Engineering
and Industrial Technologies

Doctorate School in Materials Engineering – XXI cycle

Viscoelastic and fracture behaviour of polyolefin based nanocomposites

Andrea Dorigato

Tutors:

prof. Alessandro Pegoretti

prof. Amabile Penati

April 2009

“Per aspera ad astra”

Attraverso gli ostacoli si arriva alle stelle

Seneca

Table of Contents

List of Figures

List of Tables

Acronyms

BET	Brunauer-Emett-Teller
BHJ	Barrett-Joiner-Holenda
BN	Boron Nanotubes
CB	Carbon Black
CNT	Carbon Nanotubes
CVD	Chemical Vapor Deposition
DBP	DiButylPhtalate
DENT	Double Edge Notched Tension
DMTA	Dynamical Mechanical Thermal Analysis
DSC	Differential Scanning Calorimetry
EBM	Equivalent Box Model
ESCA	Electron Spectroscopy for Chemical Analysis
ESEM	Enviromental Scanning Electron Microscopy
EWF	Essential Work of Fracture
HDPE	High Density Polyethylene
IR	Infrared Spectroscopy
LDPE	Low Density Polyethylene
LLDPE	Linear Low Density Polyethylene

MMT	Montmorillonite
MWCNT	Multi-Walled Carbon Nanotubes
NT	Nanotechnology
OAN	Oil Absorption Number
OMMT	Organomodified Montmorillonite
PE	Polyethylene
PET	Polyethyleneterephtalate
PMMA	Polymethylmethacrylate
POSS	Polyhedral Oligomeric Silsesquioxanes
SEBS-gMA	Maleated Styrene-Ethylene-Buthylene-Styrene rubber
SEM	Scanning Electron Microscopy
SSA	Specific Surface Area
SWCNT	Single Walled Carbon Nanotubes
TEB	Tensile Energy to Break
TEM	Transmission Electron Microscopy
TEOS	Tetraethoxysilane
WLF	William-Landel-Ferry
WPPM	Whole Powder Pattern Model
XPS	X-Ray Photoelectron Spectroscopy
XRD	X-Ray Diffraction analysis

Abstract

In the last years it has been widely proven that the introduction of very small amounts of inorganic nanoparticles in polymeric matrices can lead to noticeable improvements of their mechanical properties, in terms of elastic modulus and tensile properties at yield and at break. Linear low density polyethylene (LLDPE) is widely applied in several industrial applications, especially for the production of transparent high performance film for the packaging industry. The objective of this work is to study the role played by different kinds of amorphous silica (SiO_2) micro and nanoparticles on the viscoelastic and fracture behaviour of LLDPE based composites, prepared through a melt compounding process.

Different typologies of silica filler have been considered : hydrophilic and hydrophobic fumed silica nanoparticles with different surface area, precipitated silica microparticles, and silica glass microbeads. In this way it has been possible to study the influence of the filler dimensions and morphology on the viscoelastic behaviour of the prepared composites, both in the molten and in the solid states, and on their fracture properties.

In the first part of the work, a detailed microstructural characterization was performed to assess the different morphologies and surface properties of the utilized powders. Furthermore a detailed analysis of the dispersion state of the fillers in the matrix and of the thermal behaviour of the prepared composites was also conducted through optical and electron microscopy.

In the second part of the work, viscoelastic behaviour of the composites in the molten state was studied through dynamic rheological tests. It was evidenced how the introduction of fumed silica nanoparticles and precipitated silica microparticles could lead very strong enhancement both of the storage (G') and shear moduli (G''), and of the viscosity (η), at low frequencies, especially by using high surface area fumed silicas at an high filler loading, while glass filled microcomposites showed the traditional rheological behaviour of microparticles filled polymeric systems, with marginal enhancements of rheological properties. Elaboration of new rheological models allowed us to find important correlations between fitting parameters and microstructural situation of the samples.

Viscoelastic behaviour in the solid state was analyzed through quasi-static tensile tests, creep tests and dynamic tensile tests. Elastic moduli of the prepared composites resulted to be strictly related to the surface area of the filler rather than by its dimensions. Even in this case a new model, taking into account the physical interfacial interaction between the matrix and particles, proposed to explain experimental results. The same conclusions could be drawn for the creep behaviour, with important improvements of the creep stability of the material due to the introduction of fumed silica nanoparticles, especially at high filler amounts. Moreover, the limit of the linear viscoelastic region was extended by adding fumed silica nanoperticles. Furthermore, a non linear tensile creep approach was succesfully applied to study the dependence of the creep behaviour from the free volume of the samples. The application of the classic time-temperature superposition principle was successfully adopted to the nanocomposite samples, evidencing that the reinforcing effect provided by the nanoparticles was more effective at high temperatures or longer times. Burgers model was adopted to model temperature dependent creep data, revealing interesting correlations between fitting parameters and nanofiller surface area.

For as concern tensile dynamic mechanical properties, the introduction of the nanofiller lead to an increase of dynamic moduli (E’ and E’’) and to a lowering of tanδ values, especially when high surface area nanoparticles and elevated filler amounts were used. Even in this case dynamic properties of the material were mainly ruled by the surface area of the filler.

The last part of the work was centered on the analysis of the fracture behaviour. Tensile properties at yield and at break increased with the surface area of the nanofiller and were positively affected by the presence of the organosilane on the surface of the nanoparticles. Tensile impact tests confirmed the enhancement of the fracture toughness provided by the nanoparticles. The application of the Essential Work of Fracture (EWF) approach led to the conclusion that the introduction of fumed silica nanoparticles produced a considerable improvement of the essential work of fracture (w_e) with the nanofiller surface area.

1 Introduction

Nanotechnology (NT) deals with materials and devices 1 to 100 nm in length [1]. NT is one of the most promising areas for current research and development in several technical disciplines. Polymer Science and Technology is also included, with investigations covering a broad range of topics. Microelectronics (which could now be referred to as nanoelectronics) are involved, as the critical dimension scale for modern devices is now below 100 nm. Other areas include polymer-based biomaterials, nanoparticle drug delivery, miniemulsion particles, fuel cell electrode polymer bound catalysts, layer-by-layer self-assembled polymer films, electrospun nanofibers, imprint lithography, polymer blends and nanocomposites. Even in the field of nanocomposites, several topics exist including composite reinforcement, barrier properties, flame resistance, electro-optical properties, cosmetic applications, bactericidal properties. While the reinforcement aspects of nanocomposites are the primary area of interest, a number of other properties and potential applications are important including barrier properties, flammability resistance, electrical/electronic properties, membrane properties, polymer blend compatibilization.

In the last 20 years, polymer matrix based nanocomposites have attracted the attention of many researchers, starting from the consideration that the addition of nanostructured materials to polymeric matrices can improve the physical, mechanical, thermal and electrical properties of polymeric matrices in relation to the application [2, 3]. Their potential use covers several fields such as automotive, medical, aerospace, sports and recreation, renewable energies, and so on. In recent years new processing routes have been developed to produce filler particles with dimensions from micrometric to nanometric range and for this reasons the term nanocomposites has been introduced [4-8]. The main thrust of this route is related to the possibility of improving the properties of the polymer matrix with reduced filler content (up to 5 wt%) and to the possibility of obtaining materials with new properties not obtainable with traditional micrometric fillers (as for example transparency and smoothness).

Both industrial and academic worlds look with great expectations toward the development of new nanocomposite materials: according to the ISI Web of Science database, about 10000 papers published in scientific journal in the period 1990-2008 contain the keywords “nanocomposite” and “polymer” [9].

Starting from these considerations, the aim of this work was mainly to investigate viscoelastic and fracture properties of fumed silica nanocomposites based on polyethylene matrix, that still represents one of the most used and versatile polymers [10]. In order to evaluate the effect of the filler surface area and dimensions, prepared nanocomposites were then compared with traditional microcomposites. Linear Low Density Polyethylene (LLDPE) based composites at different filler content (from 1 vol% to 4 vol%) were produced by melt compounding by using an internal mixer, followed by an hot pressing process (see Chapter 3.2). Different kinds of composites were considered:

- Nanocomposites with fumed silica nanoparticles. In order to evaluate the effect of the filler dimensions on the mechanical behaviour of the samples, nanofillers with different surface area, ranging from 90 m^2/g (primary particles diameter 20 nm) to 380 m^2/g (primary particles diameter 7 nm) were employed. The effect of the surface functonalization was also evaluated, by using organosilane treated nanoparticles with the same surface area of the untreated ones.

- Microcomposites with precipitated silica microparticles. This microfiller presents an average diameter of 7-8 μm, but surface area values comparable with that of fumed silica nanoparticles (165 m^2/g), because of the high surface porosity obtained during the synthesis process.

- Traditional microcomposites with silica glass beads microbeads. These microparticles have a mean dimension of about 20 μm and very low surface area values, due to their surface smoothness.

The viscoelastic behaviour of the prepared samples was studied with several techniques. Rheological tests allowed us to characterize the mechanical response of the samples at the molten state, in order to evaluate the effect of particle-particle and polymer-particle interactions on the deformational state of the material under shearing conditions. Viscoelastic properties in the solid

state were assessed through quasi-static tensile tests for the evaluation of the elastic modulus, tensile creep tests and dynamic mechanical tensile tests. Particular attention was devoted to the effect of the temperature and of the applied stress on the deformational behaviour of the samples under constant load conditions.

The fracture behaviour was evaluated through quasi-static tensile tests, in order to evaluate the effect of the various fillers on the tensile properties at yield and at break. Moreover a more detailed analysis on the fracture behaviour of nanocomposites based on fumed silica was conducted by the Essential Work of Fracture (EWF) approach.

Several tools were used in order to correlate the mechanical behaviour to the microstructure of the produced samples. The various typologies of fillers were characterized through the evaluation of their surface area and densities. Optical and electron microscopy techniques were employed to evaluate the filler dispersion in the matrix, while calorimetric analyses were conducted to evaluate the crystallization behaviour of the composites.

An attempt has been also made to interprete the obtained results through the application of classical predictive schemes developed for traditional microcomposites. These models resulted to be inadeguate to describe the mechanical response of nanocomposites, and new models have been proposed to interprete their viscoelastic and fracture behaviour.

2 Background

2.1 Micro and nano-composites

In the recent years, scientific and technological developments led to the development of two different types of particulate polymer composites, distinguished by the characteristic size of the inorganic filler particles:

- traditional composites or micro-composites that contain micrometer-scale fillers (carbon black, calcium carbide, metal oxides microparticles, etc.) [11, 12]
- nanocomposites that contain nanometer-scale fillers, i.e. fillers that have at least a characteristic size under 100 nm [4-6, 13-15]

The nanofillers are generally divided in three main categories according to the shape (Figure 2.1) :

- one nanodimensional fillers (1-D), i.e. plate-like materials such as all the types of layered silicates and graphite nanoplates [16-20]
- two nanodimensional fillers (2-D), i.e. nanotubes or nanofibers such as carbon nanotubes, carbon nanofibers, boron/nitrogen nanotubes, nanotubes made of dichalcogenides (MoS_2, WS_2, etc.), nanotubes of several oxides (V_2O_5, MoO_3, etc.) and organic nanotubes [8, 15]
- three nanodimensional fillers (3-D), i.e. particulate like-spherical materials such as metal oxides (ZnO, Al_2O_3, $CaCO_3$, TiO_2, etc.), fumed metal oxides (SiO_2, TiO_2, etc.), silicon carbide (SiC), polyhedral oligomeric silsesquioxanes (POSS) and carbon black (CB) [21-23]

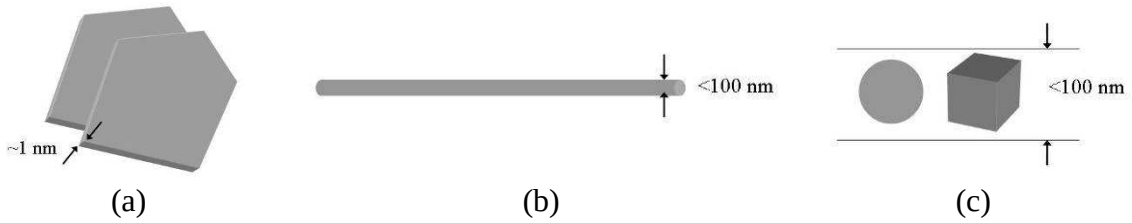

Figure 2.1 Examples of nanofillers: plate-like materials (a), nanotubes (b) and equi-axed nanofillers (c)

Research and development of nanocomposites greatly increased in recent years for several reasons. Most of all, unprecedented combinations of properties have been observed in some polymer nanocomposites. The unique properties of the nanocomposites are mainly related to the small size of the filler particles and to the particular properties of the particles themselves, as schematically represented in Figure 2.2 [24]. Moreover controlling the degree of interaction between the filler and the polymer it is possible to change the final properties of the composite, because the polymeric chains around nanofillers show a different behaviour than in the bulk matrix (e.g. degree of mobility, cross-linking or crystallinity). In the case of the nanocomposites the extent of the interphase (which typically has a thickness between 2 and 50 nm) is more important than in traditional microcomposites because the small size of the particles results in exceptionally large filler-polymer interfacial area. This means that original matrix properties can be altered significantly, even at low filler contents.

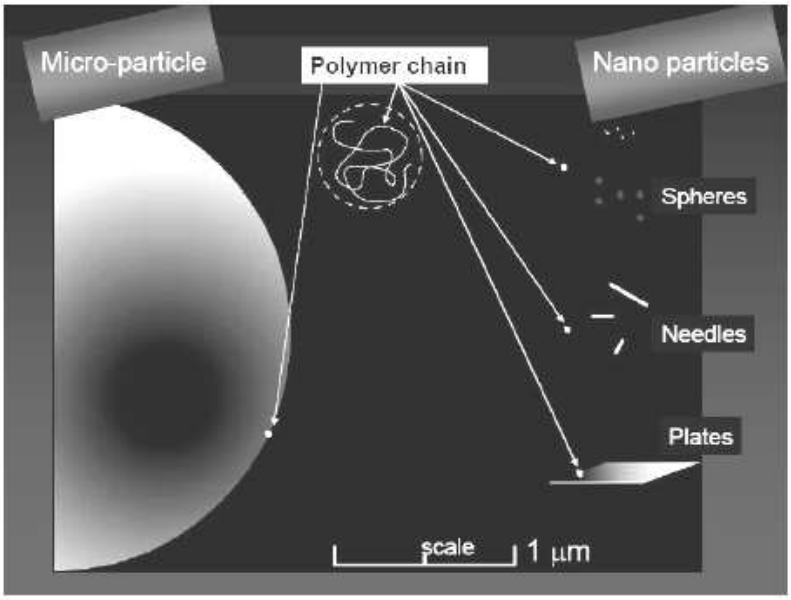

Figure 2.2 Dimensional comparison between microparticles and nanoparticles

The key factor in order to obtain all these advantages is controlling the nanoparticles dispersion degree, in the sense that nanofillers must be homogeneously distributed and dispersed in the polymer matrix. Figure 2.3 shows examples of the different dispersion and distribution conditions that can be eventually reached [4].

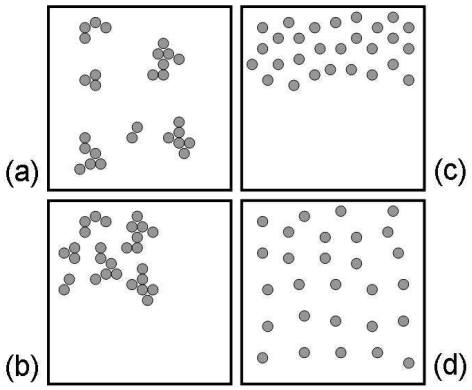

Figure 2.3 A schematic illustration of (a) good distribution but poor dispersion, (b) poor distribution and poor dispersion, (c) poor distribution but good dispersion and (d) good distribution and good dispersion

In order to obtain a high dispersion degree and a good interaction, several techniques can be used to prepared polymer matrix nanocomposites. The various processes can be grouped in three main categories [25]:

- Solution process : the nanofiller is previously dispersed in a solvent and then a soluble polymer is added. In this way an homogeneous solution, in which the nanoparticles are well dispersed, can be obtained. The solvent is then removed through evaporation .

- In situ polymerization : this method is mainly used when thermosetting resin, such as epoxies and polyurethanes, are chosen as matrices. In some cases thermoplastic matrices. The nanofiller is previously dispersed in the monomer or in an organic precursor, then the complete polymerization of the matrix is conducted by adding the crosslinking agent or the catalyst, or by simply heating the reactive system.

- Melt compounding process : this technique is mainly utilized for the preparation of thermoplastic based nanocomposites, and the nanofiller is simply added in the molten polymer as any other kind of additive. Traditional techniques, such as melt mixing with twin screw extruder or injection moulding, can be employed in this case.

In any case, the dispersion degree of the nanoparticles can be improved with surface treatment of the filler, in order to hinder agglomeration phenomena. Moreover, these treatment can be employed to improve the filler-polymer interaction.

It is difficult to construct a general scheme for the interpretation of the results available in the scientific literature on polymer based nanocomposites, because of the complex interaction possibilities between the inorganic nanofiller and the polymeric matrix. In general the advantages due to the use of nanocomposites are generally related to an improvement of the mechanical properties, to an increase of the dimensional stability, to a better thermal degradation resistance [20]. In many cases this improvements can be obtained without any loss of the original optical clarity of the unfilled matrix [26, 27].

For as concern the mechanical properties improvement, it is well known that the addition of high modulus fillers increases the modulus and the strength of a polymer, but in traditional composites this comes at the cost of an heavy reduction in ductility and in impact strength, because of stress concentrations caused by the fillers. Well dispersed nanoparticles can improve the stiffness and the strength of the pristine material, maintaining or even improving ductility, because their small size does not provoke large stress concentrations [28]. Moreover, the large interfacial area of nanocomposites provides an opportunity for significantly altering the original matrix properties. It is also clear that a proper dispersion is critical for improving the fracture toughness of the material. As an example, Hasegawa prepared polypropylene-clay nanocomposites, finding that the strain at break of the material is unaffected by the presence of clay when a complete exfoliation of the nanoplatelets occurred. For higher filler loading (>3 wt%), nanoclay aggregation leads to a strong decrease of the ductility of the material, typical of microcomposite systems. In the scientific literature there are several examples supporting these considerations, and many authors reported an optimum volume percent of filler, claiming that the decrease in ductility above the optimum is due to agglomeration [29, 30].

The extremely large interfacial region in nanocomposites gives a significant opportunity for changing the polymer mobility and relaxation dynamics. Although the specific mechanisms of chain dynamics are not completely understood, it is clear that the rheology/glass transition temperature of a polymer can be altered by changing the polymer mobility by nanofillers addition.

For example, in some cases it was demonstrated that the T_g can be suppressed for clay nanocomposites with intercalated polymer chains. This indicates a limited ability for cooperative motion when the polymers are confined between the layers [31]. On the contrary, if the clays are exfoliated, the polymer is not confined, and the T_g does not change significantly. Without the effect

of the confinement, the glass transition temperature can be increased if the polymer is tightly bound to the nanofller [29, 32, 33]. Many studies are now in course to understand the role of nanofillers in controlling damping and melt rheology [31, 34, 35]. The incorporation of nanoscale fillers may cause unexpected results on abrasion resistance. In traditional composites, as the filler size decreases to a size similar to that of the abrading particles, filler particles are removed and the abrasion resistance is compromised. This does not happen on nanocomposites. As an example, the addition of $CaCO_3$ nanoparticles to PMMA leads to a significant enhancement of the abrasion resistance of the material, with a filler content of only 3 wt% [36]. Moreover, nanoparticles can simultaneously improve wear resistance and decrease the coefficient of friction

Nanocomposites can also be an optimal solution for improving both thermal and environmental stability. This is due to the reduction in the coefficient of thermal expansion (CTE) due to the presence of the nanofiller [37, 38]. If for traditional low filled microcomposites the lowering of the CTE is almost linear, for nanofilled material this dependency is nonlinear anymore, because of the presence of a wide interfacial region. The formation of a thin film of polymer with very low CTE around the nanofiller can be hypothesized. For the same reason, the strong interaction between polymer and nanofiller leads to a strong increase of the swelling resistance, especially for nanofilled rubbers [39].

The presence of a tortuous diffusion path due to the complete dispersion of nanofillers in polymeric membranes can be exploited for a very important reduction of gas and liquid permeability of nanofilled polymers, making them attractive for industrial applications [40, 41]. Several simple models have been elaborated in order to predict the decrease of the relative permeability with the nanofiller content of polymeric materials [42, 43], taking into account the effect provided by the nanofiller dispersion state on the diffusion path and the matrix-filler interfacial interaction [44-46]. For the same reasons it is easy to understand that the dispersion of nanofillers (especially clays) can be very important to increase the degradation temperature of the material, and exfoliated nanocomposites have in general significantly higher degradation temperatures than intercalated nanocomposites or traditional microcomposites [47, 48]. In fact, if the oxygen cannot penetrate, then the oxidation of the resin is impossible. As an example, the degradation temperature increased of 50 °C for a polyethylene matrix intercalated with 10 wt% clay [49].

Moreover, the flammability properties of many nanofilled systems can be strongly improved [50, 51]. From the analysis of the resulting char for clay filled nanocomposites it is evident that the layered silicate collapses during combustion and forms a uniform layered structure, that acts to reinforce the char and reduce the permeability of the char itself, reducing the rate of volatile product

release [52, 53]. As an indication, clay nanocomposites commonly show a 60% reduction in peak HRR (heat release rate) relative to the unfilled polymer.

Electrical and optical properties of nanofilled polymers are promising areas of applications for these new systems. For example, it is possible to obtain composites that combine a good electrical conductivity with good wear properties and optical transparency. This is possible because in many cases the nanoparticles have diameters well below the Rayleigh scattering limit, still displaying a solid state behaviour when embedded in transparent matrices. If the permittivity of polymers can be increased also with traditional metallic microparticles, the use of microfiller results in a significant decrease in breakdown strength due to the field concentration created by the particles. By using nanoparticles the reduction in breakdown strength is not so dramatic, because of the good dispersion of the nanostructured domains. Relatively good optical clarity has been obtained in many nanocomposites, particularly at low volume fractions. For example, studies on modified PMMA were shown to maintain optical clarity up to 10 wt% bentonite. Moreover, with the use of nanoparticles it is also possible to significantly alter the original refractive index of the material, preparing nanocomposites with refractive indices over the entire range between 1 and 3.9 [54, 55]. As an example, the addition of nanoscale iron sulphide to polyethylene increased the index of refraction between up to 2.8 [56].

Obviously, many other applications and interesting properties can be obtained by incorporating nanostructured materials in polymers, but the complete description of these system is out of the main purposes of these introductive section, that was intended to provide a general overview on the most important technological possibilities related to the formulation of nanocomposites.

2.1.1 Layered crystals nanomaterials

Layered crystals are a particular kind of nanomaterials, characterized by only one dimension in the nanometer range. In this case the filler is present in the form of sheets of one to a few nanometer thick to hundreds to thousands nanometers long. For this reason layered crystals nanocomposites can be exclusively obtained by the intercalation of the polymer (or a monomer subsequently polymerized) inside the galleries of layered host crystals. There is a wide variety of crystalline fillers that are able, under specific conditions, to host a polymer in the interlayer galleries, as reported in Table 2.1.

Chemical nature	Examples
Element	Graphite
Carbon oxides	Graphite oxides
Metal phosphates	$Zr(HPO_4)$
Clays and layered silicates	Montmorillonite, hectorite, saponite, fluoromica, fluorohectorite, vermiculite, kaolinite, magadiite, …
Layered double hydroxides	$M_6Al_2(OH)_{16}CO_3 \cdot nH_2O$ (M = Mg, Zn)

Table 2.1 A summary of the main typologies of layered crystalline nanostructured materials [57]

Among all the layered crystals, those based on clay and layered silicates have been more widely investigated probably because the starting clay materials are easily available and because their intercalation chemistry has been studied for a long time. The layered silicates commonly used in nanocomposites belong to the structural family known as the 2:1 phyllosilicates [57]. Their crystal lattice consists of two-dimensional layers where a central octahedral sheet of alumina or magnesia is fused to two external silica tetrahedron by the tip so that the oxygen ions of the octahedral sheet do also belong to the tetrahedral sheets, as reported in Figure 2.4.

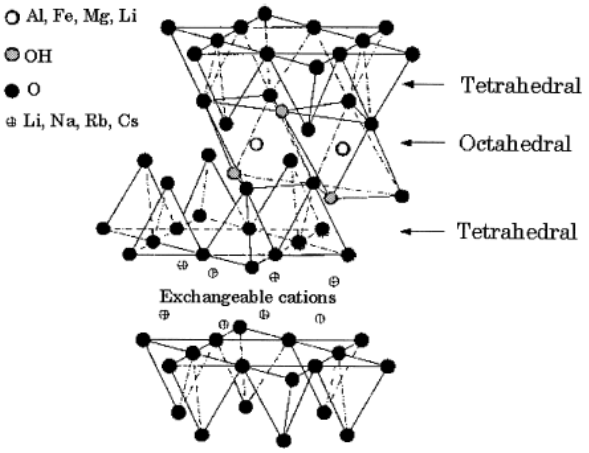

Figure 2.4 Typical chemical structure of a 2:1 phyllosilicate [58]

The layer thickness is around 1 nm and the lateral dimensions of these layers may vary from 300 Å to several microns and even larger depending on the particular silicate. These layers organize themselves to form stacks with a regular van der Walls gap in between them called the interlayer or the gallery. Isomorphic substitution within the layers (for example, Al^{3+} replaced by Mg^{2+} or by Fe^{2+}, or Mg^{2+} replaced by Li^{+}) generates negative charges that are counterbalanced by alkali or alkaline earth cations situated in the interlayer.

As the forces that hold the stacks together are relatively weak, the intercalation of small molecules between the layers is relatively easy [59]. In order to render these hydrophilic phyllosilicates more organophilic, the hydrated cations of the interlayer can be exchanged with cationic surfactants such as alkylammonium or alkylphosphonium (onium). The modified clay (or organoclay) being organophilic, its surface energy is lowered and is more compatible with organic polymers [60-62]. Montmorillonite, hectorite and saponite are the most commonly used layered silicates, and their chemical formula is reported in Table 2.2.

This type of clay is characterized by a moderate negative surface charge (known as the cation exchange capacity, CEC and expressed in meq/100 g). Even if a small part of the charge balancing cations is located on the external crystallite surface, the majority of these exchangeable cations is located inside the galleries. When the hydrated cations are ion-exchanged with organic cations such as more bulky alkyammoniums, it usually results in a larger interlayer spacing .

2:1 phyllosilicate type	**general formula**
Montmorillonite	$M_x(Al_{4-x}Mg_x)Si_80_{20}(OH)_4$
Hectorite	$M_x(Mg_{6-x}Li_x)Si_80_{20}(OH)_4$
Saponite	$M_xMg_6(Si_{8-x}Al_x)0_{20}(OH)_4$
M = monovalent cation; x = isomorphous substitution degree (0.5 -1.3)	

Table 2.2 General formulas of montmorillonite, hectorite and saponite [58]

Depending on the nature of the components used (layered silicate, organic cation and polymer matrix) and the method of preparation, three main types of composites may be obtained when a layered clay is associated with a polymer, as summarized in Figure 2.5. When the polymer is unable to intercalate between the silicate sheets, a phase separated microcomposite is obtained, whose

properties stays in the same range as traditional microcomposites. Beyond this classical family of composites, two types of nanocomposites can be recovered. Intercalated structure in which a single (and sometimes more than one) extended polymer chain is intercalated between the silicate layers resulting in a well ordered multilayer morphology built up with alternating polymeric and inorganic layers. When the silicate layers are completely and uniformly dispersed in a continuous polymer matrix, an exfoliated or delaminated structure is obtained [63].

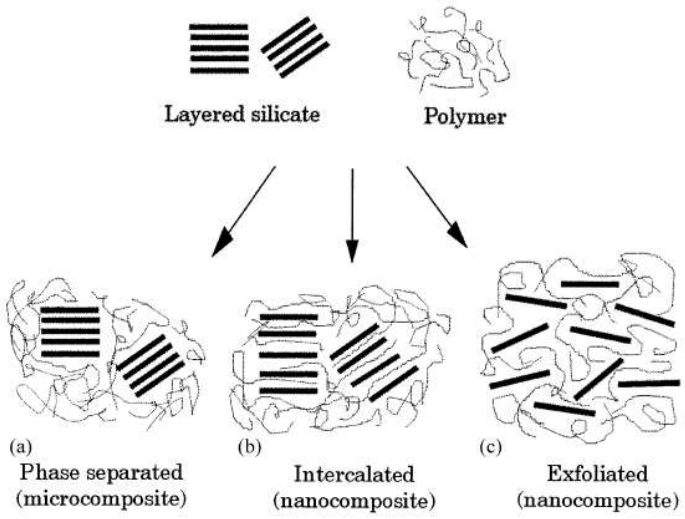

Figure 2.5 Three different microstrctural configuration of polymer clay nanocompsites

Two complementary techniques are used in order to characterize those structures. XRD is used to identify intercalated structures. In such nanocomposites, the repetitive multilayer structure is well preserved, allowing the interlayer spacing to be determined. The intercalation of the polymer chains usually increases the interlayer spacing, in comparison with the spacing of the organoclay used, leading to a shift of the diffraction peak towards lower angle values, according to the Bragg's law. Figure 2.6 reports an example of X-Ray diffractogram in the three different microstructural situations.

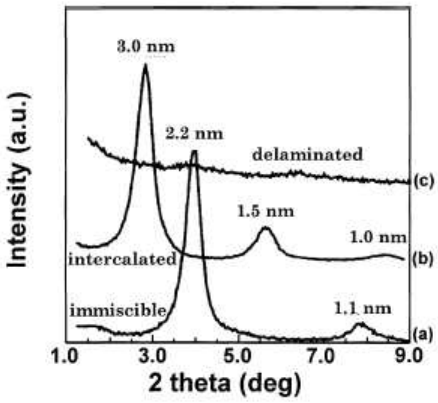

Figure 2.6 XRD patterns of: (a) phase separated microcomposite (organo-modified fluorohectorite in a HDPE matrix); (b) intercalated nanocomposite (same organomodified fluorohectorite in a PS matrix) and (c) exfoliated nanocomposite (the same organo-modified fluoro fluorohectorite in a silicone rubber matrix) [58]

As far as exfoliated structure is concerned, no more diffraction peaks are visible in the XRD diffractograms either because of a much too large spacing between the layers (i.e. exceeding 8 nm in the case of ordered exfoliated structure) or because the nanocomposite does not present ordering anymore. In the latter case, transmission electronic spectroscopy (TEM) is used to characterize the nanocomposite morphology [64, 65], as represented in Figure 2.7.

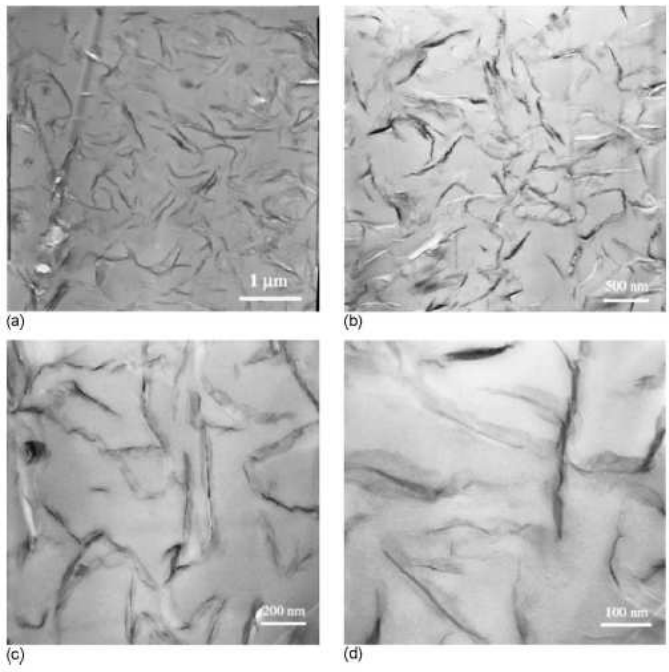

Figure 2.7 TEM micrographs of epoxy-clay (5 wt%) nanocomposite at various magnifications [14]

The thermodynamics that drives the intercalation is determined by an interplay of entropic and enthalpic factors [66]. In fact, although the confinement of the polymer chains inside the silicate

galleries results in a decrease in the overall entropy of the macromolecular chains (partially compensated by the increase in conformational freedom of the tethered alkyl surfactant chains as the inorganic layers separate), intercalation will rather be driven by the decrease of the total enthalpy, due to two components : apolar interactions generally unfavorable and arising from interaction between polymer and surfactant aliphatic (apolar) chains, and polar interactions which originate from the Lewis acid/Lewis base character of the layered polar silicates interacting with the polymer chains. The free energy curves may be grouped into three types, as reported in Figure 2.8. First, curves that are positive at all gallery heights (type I). In this case, polymer intercalation is unfavorable, and the polymer and the organo-modified layered silicates are immiscible. The second type regroups the curves displaying one minimum (type IIa and IIb), corresponding to well defined intercalated structures before complete layer exfoliation. Finally, the third type of curves displays a continuous decrease in the free energy values with gallery height expansion, indicating that polymer intercalation and complete layer separation is favorable. This last type corresponds to complete polymer-silicate layer miscibility, characteristic of exfoliation.

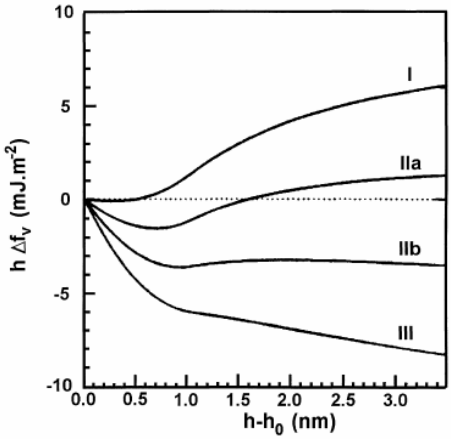

Figure 2.8 Variation of the free energy per unit area ($h\Delta f_V$) in function of the change in gallery height ($h-h_0$) calculated for an arbitrary polymer interacting with a silicate layer functionalized with octadecylammonium groups [66].

2.1.2 Nanofiber or nanotubes fillers

The most important class of 2-D nanomaterial is for sure that of carbon nanotubes. Since the discovery of carbon nanotubes (CNTs) in 1991 by Iijima [67], CNTs have been looked at with great

interest in the field of the polymer composites because their unique physical, mechanical, electrical, thermal and optical properties [68-70] .

The production of composites requires preliminary treatments to prepare the CNTs for the processing. In fact, most production processes generate a range of carbonaceous particles such as amorphous carbon, fullerenes, and nanocrystalline graphite. Moreover, metal catalysts remain as a residue. The most common methods to remove unwanted by-products include thermal treatment in air or oxygen for selective etching of amorphous carbons, and acid treatment for eliminating catalyst residues. Mechanical techniques like centrifugal separation, size exclusion chromatography and microfiltration may be applied as well. Obviously all these techniques reduce the effective yield of the production process. In addition a chemical functionalization, i.e. the addition of new functional groups, can be conducted on the CNTs to improve the nanotube-polymer interactions for processability and property enhancement. Several approaches have been employed to obtain surface modifications, but the most relevant treatments are the acid treatments. In fact, acid treatments with HNO_3, H_2SO_4, H_2O_2 or mixture oxidize the surface of CNT and introduce carboxylic acid, hydroxyl groups, etc. Then the new functional groups can be used as linking for subsequent chemical reactions to attach new chemical groups on the CNT surface. Examples of this procedure are the reactions with thionyl chloride, amines, silane coupling agents and thiols.

From a structural point of view a carbon nanotube is a hexagonal network of carbon atoms rolled up into a seamless, hollow cylinder, with each end capped with half of a fullerene molecule (Figure 2.9). There are two main kinds of nanotube. Single-walled nanotubes (SWCNTs) are individual cylinders of 1-2 nm in diameter, which are actually a single molecule, and multi-walled nanotubes (MWCNTs) are a collection of several concentric graphene cylinders. The diameter, the chirality, and the form of the nanotube determine its properties.

The mechanical properties of various types of nanotubes have been extensively studied both by experimental and computational tools. From a general point of view their modulus can be higher than 1 TPa and their tensile strength can reach 600 GPa with strain at break up to 40% (Figure 2.10). Moreover they can have the same electrical and thermal conductivity of the graphite (in-plane), i.e. 3000 $W \cdot m^{-1} \cdot K^{-1}$ and $5 \cdot 10^{-5}$ $\Omega \cdot cm$, and very low density, i.e. 1.3 g/cm^3. Nevertheless, these properties are achieved only in the case of individual SWCNT: the modulus of a ropes containing bundled SWCNT considerably decreases as the rope diameter increases because of the slippage occurring between the individual nanotubes within the rope. Moreover the MWCNTs have a lower modulus because only the outermost layers carry the load, and it can go down to 100 GPa.

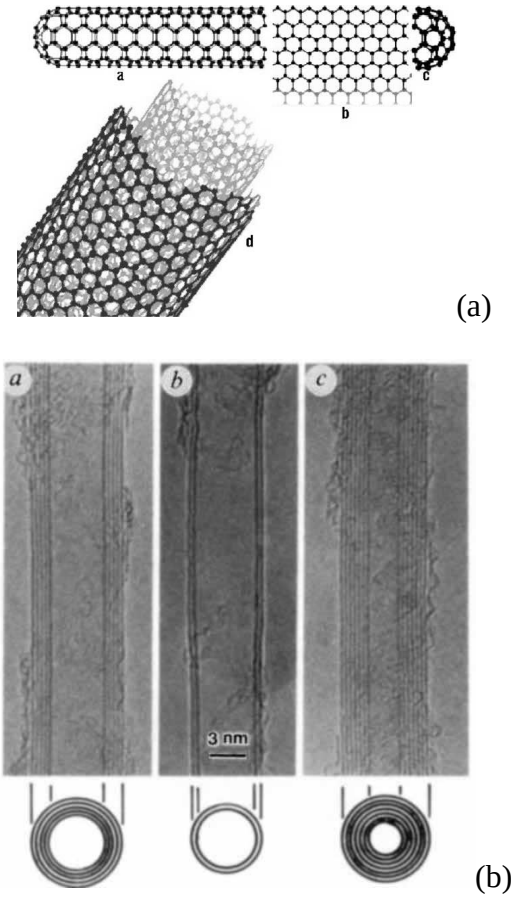

Figure 2.9. (a) Schematics of a single-walled carbon nanotube and a multiwalled carbon nanotube [5] and (b) TEM micrographs [67]

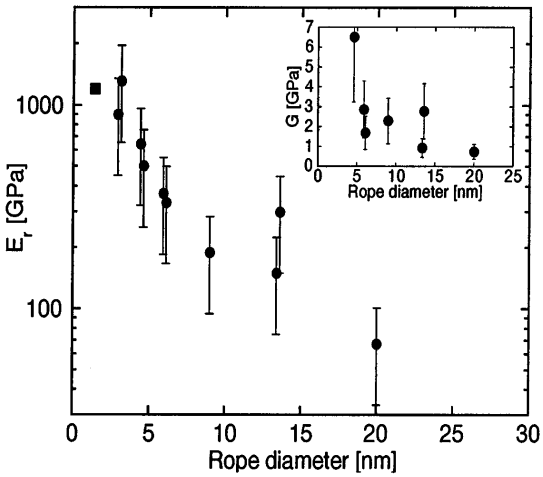

Figure 2.10. Tensile modulus and shear modulus (onset) of SWCNT as a function of rope diameter [71]

There are other types of carbon nanotubes with some role in the fabrication of nanocomposite materials. The closest in the structure and mechanical properties to carbon nanotubes are hexagonal boron/nitrogen (BN) nanotubes. Several techniques can be used to produce single walled and

multiwalled nanotubes : arc-discharge, laser ablation and CVD processes. The modulus and strength of BN nanotubes are very similar to those of their carbon counterparts, but they possess better oxidation resistance and electrical insulation [72]. It is also possible to dope the lattice of carbon nanotubes with boron and nitrogen, providing a broad range of BCN structures [73].
Furthermore most layered materials can be fabricated into nanotubes, for example starting from dichalcogenides (MoS_2, WS_2, etc.) [74], several oxides (V_2O_5, MoO_3, etc.) [75] and organic materials. These materials are not currently available in bulk quantities, and hence very little data are available on the mechanical and electrical properties of composites containing these nanostructures.

2.1.3 Equiaxic nanoparticles

The production of nanoparticles with controlled size and degree of aggregation is the goal of many research efforts. On of the main advantages of using nanoparticles in a composite structure is that the particle size and distribution can be stabilized. Moreover the particles can lend properties of the final composites that cannot be achieved with traditional fillers. Nanoparticles have been available for more than a century [76], but in the last decades important developments have been made in this field. Attrition of purified minerals is the most common method. In this technique, macro or micro scale particles are ground in a ball mill, a planetary ball mill, or other size reducing mechanism. The resulting particles are than air classified to recover nanoparticles.

2.1.3.1 Fumed metal oxides nanoparticles

Aerosol methods usually result in the formation of nanoparticles by condensation from a gas phase [77]. One example of a highly successful commercial aerosol process is flame hydrolysis, the principal technique to produce fumed oxides nanoparticles. Here, a vapour precursor (such as silicon tetrachloride to make silica) is burned an a hydrogen / oxygen fuel mixture to produce the metal oxide, as represented in Figure 2.11.

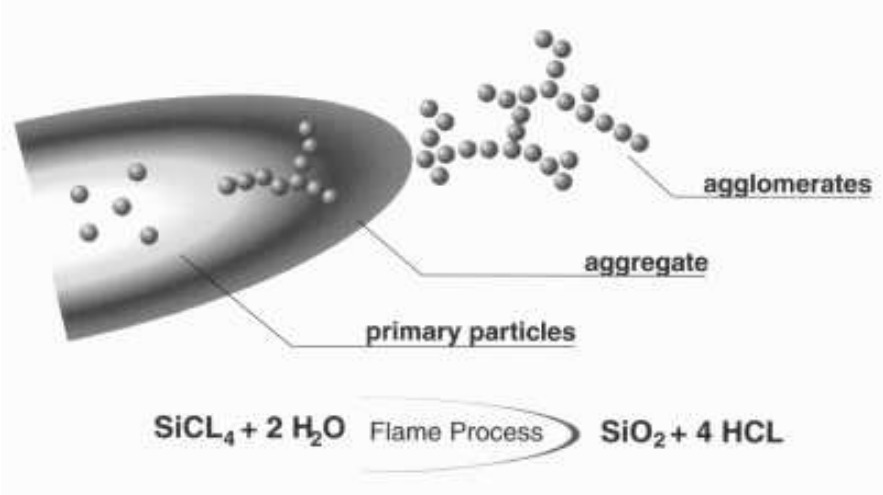

Figure 2.11 Production process of fumed silica nanoparticles

Titania, alumina, and zirconium oxide can all be produced this way. For silica, particle sizes from 7 to 27 nm of diameter and surface area ranging form 100 to 380 m^2/g can be produced. An example of silica fumed nanoparticles with a surface area of about 160 m^2/g is represented in Figure 2.12.

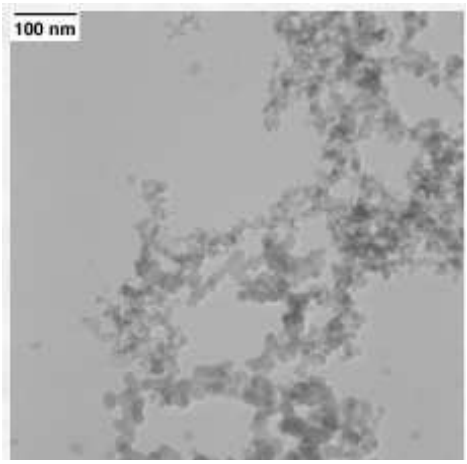

Figure 2.12 TEM images of the structure of fumed silica nanoparticles (160 m^2/g)

The structure can be controlled by adjusting the temperature and time of reaction. For example at higher temperatures particles coalescence is faster and low surface area materials are produced. At lower temperatures, coalescence is slow relative to the collision rate, and fractal agglomerates are generated [78]. The surface of these nanoparticles can then chemically treated in order to attach different functionalities and impart specific properties to the nanofiller. This process can be done by

using organosilanes, that can be chemically linked to the silanol groups present on the surface of the nanoparticles. The most important use of fumed mixed oxides nanoparticles is for improving the rheological properties of paints, for reinforcing elastomers and as surface modifiers. One of the most important properties of fumed metal oxides is their ability to increase viscosity and provide thixotropic effects. At rest, when fumed silica (or another fumed metal oxide) is incorporated into a liquid, interactions, i.e. forces of attraction, can arise between the particles. These surface forces cause aggregates that coalesce to form into large agglomerates, until a three dimensional network is formed. As this network forms, the viscosity of the liquid increases greatly. The special bulky structure of this nanofiller means that a high viscosity can be built up by only small amounts of nanoparticles. As reported in Figure 2.13, in the case of hydrophilic (not surface treated) nanoparticles, these interactions are typically caused by hydrogen bonds between silanol groups on the surfaces of adjacent particles. With hydrophobic (surface treated nanoparticles), additional hydrophobic interactions and forces of attraction occur between the silylated surfaces [22].

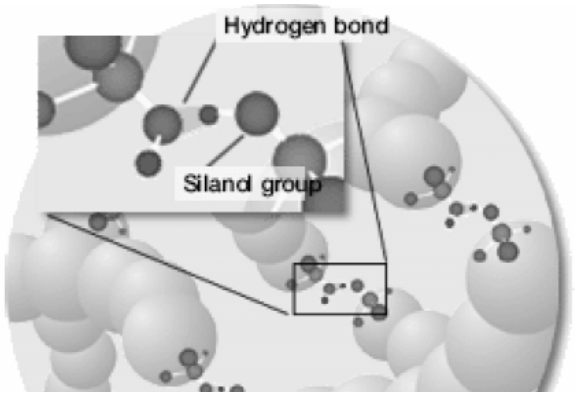

(a)

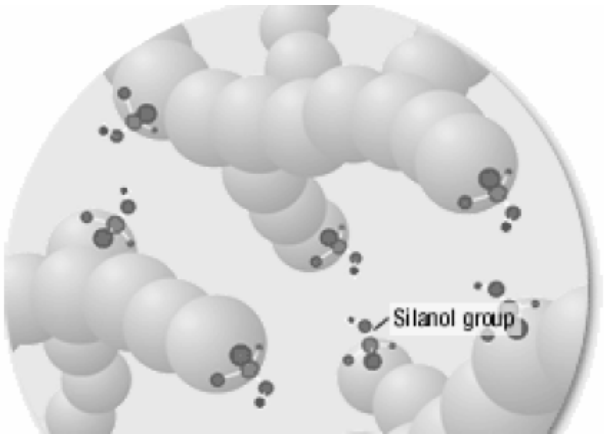

(b)

Figure 2.13 Filler-filler interactions of fumed silica aggregates (a) in the steady state, (b) after shearing

Under shearing, breakdown of hydrogen bonds occurs. The particle-particle interactions are broken down and the nanoparticles can move with respect to one another. This breaks down the particle network, and the agglomerates become smaller. The viscosity of the liquid decreases. The greater the applied shear force, the more fluid the substance becomes (Figure 2.14).

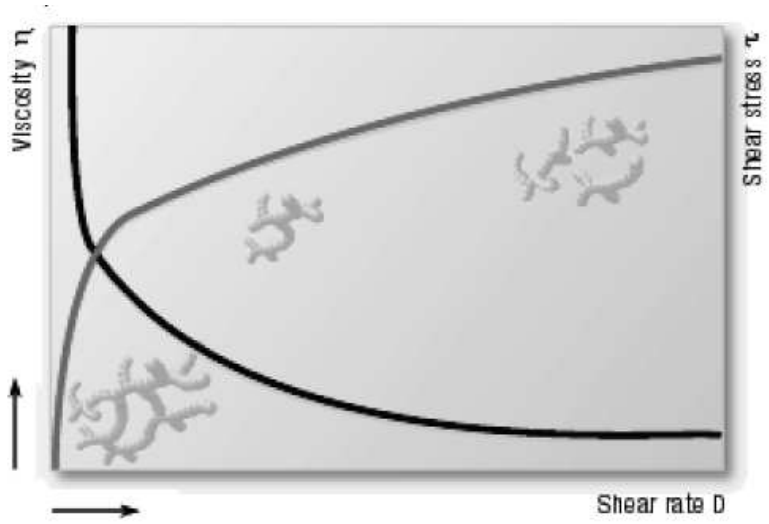

Figure 2.14 Viscosity and shear stress vs shear rate in fumed silica filled viscous liquid

For as concern the use of fumed metal oxides nanoparticles as reinforcement for elastomers, the addition of active fillers provides the required high level of elasticity to several kinds of elastomers. Moreover the addition of these fillers can improve the elastomer's mechanical properties, such as modulus, tensile strength or elongation at break [23].

The excellent reinforcing effect of fumed oxides nanoparticles can be directly attributed to their large specific surface area. This exists as an external surface, and is therefore readily available for a large number of interactions with polymer chains of the elastomer network. The characteristic particle structure allows mechanical stresses and forces to be distributed throughout the elastomer network, thus increasing strength and ensuring high elongation and loading capacity. In many applications, these nanofillers are used as reinforcing filler and rheological additive. In highly filled silicone elastomers, the high thickening effect of hydrophilic silicas can limit processability. High filler contents and good processability with low viscosity can be obtained by rendering the surface of these nanoparticles hydrophobic by reaction of the silanol groups with silylating agents to form dimethylsiloxy or trimethylsiloxy groups.

2.1.3.2 Carbon black nanoparticles

Pyrolysis is another aerosol method and is commonly used to make carbon black [79, 80]. The carbon black (CB) is a amorphous form of carbon produced by incomplete combustion or thermal decomposition of gaseous or liquid hydrocarbons under controlled conditions. The carbon atoms are arranged in blocks of graphene layers with reduced dimensions and then these basic units are organized with a turbostratic structure to form spherical particles with diameter from 10 to 100 nm. The graphene layers are very similar to the graphitic structure: most of the carbon atoms in carbon black are sp^2-hybridized to form benzene rings as for graphite, but the ordered structure is maintained only over short lengths (3-4 layers).

During the production process the primary particles fuses into aggregates. Moreover agglomerates can grow because the small distances between the aggregates and the strong van der Waals forces present (Figure 2.15). While an aggregate is indivisible, the agglomerates can be destroyed during the typical processing of the polymer. A CB characterized by primary aggregates composed of many prime particles, with considerable branching and chaining, is referred to as a high-structure black. If the primary aggregates consist of relatively few prime particles, the CB is referred to as a low-structure black. Moreover from a general point of view the primary particle diameter and the structure complexity are not directly related [81].

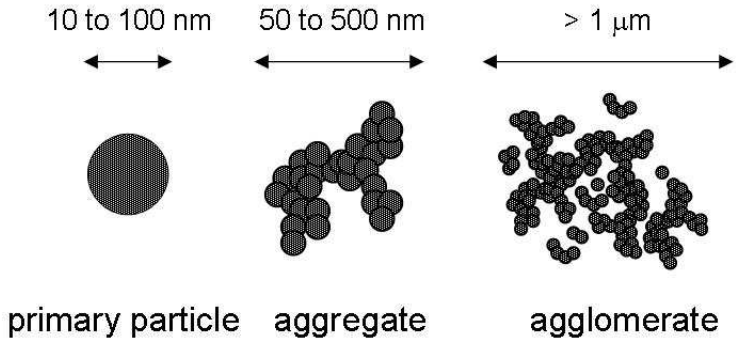

Figure 2.15. CB primary particles fused together to form aggregates and then agglomerates.

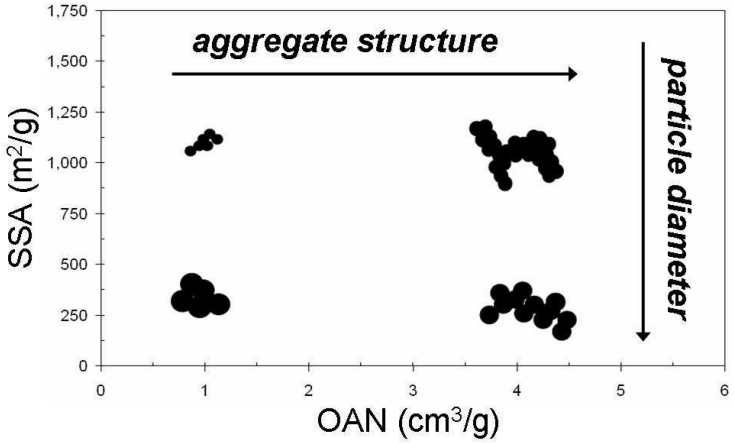

Figure 2.16. Scheme of the different CB conformations in relation to particle size and structure

The particle size is typically determined by transmission electron microscope (TEM) measurements (see ASTM D-3849). Alternatively the specific surface area (SSA) can be measured by nitrogen adsorption measurements using the Brunauer-Emmet-Teller procedure (ASTM D 6556) or by the iodine number test (ASTM D 1510): small particles will confer a large surface area per unit weight. SSA measured with the BET method typically varies between 25 and 1500 m^2/g (Figure 2.16). Furthermore Equation 2.1 holds in the case of spherical particles with low porosity:

Equation 2.1

$$d_{BET} = \frac{6000}{S_{BET}\rho}$$

where d_{BET} is the average primary particle diameter in nm, S_{BET} the specific surface area determined by BET method in m^2/g and ρ the density in g/cm^3.

On the other side CB structure is evaluated by oil adsorption number (OAN), which represents the amount of oil (normally dibutyl phthalate, DBP) that can be absorbed by CB to reach a critical viscosity (ASTM D 2414). A higher value of OAN indicates a higher structure. OAN measured with DBP typically varies between 0.05 and 5 cm^3/g. Moreover, CBs have to be evaluated by taking to account other factors such as the porosity, that in certain case can reach 30%, and the chemical groups on the surface introduced by the manufacturing process such as phenolic, quinolic and carboxyl chemisorbed complexes.

2.1.3.3 Other typologies of equiaxic nanoparticles

Gas condensation method is another important technique to produce equiaxic nanoparticles [82, 83]. In this case a metal vapour is formed in either an oxygen atmosphere or an inert gas. In an oxygen atmosphere, the metal reacts with the oxygen to form metal oxides, which are collected by cooling the gas and condensing the nanoparticles. In an inert atmosphere, metal nanoparticles result. Advantages of this technique are that the particle size distribution is narrow, the particles are crystalline and the surface are clean.

Laser ablation is another form of gas condensation [84-86]. Here, targets (metal, metal oxides, or semiconductors) are ablated with a laser. An inert or reactive is supplied to cool, condense, and sometimes react with the target material. Significant amount of nanoparticles can be produced with this technique.

Other methods for creating a vapour that condenses into nanoparticles include plasma and chemical vapour condensation, spray pyrolysis, electrospray, and plasma spray. These processes can form a wide range of nanoparticles.

One very interesting variation of the aerosol process recently developed combines sol-gel processing with the aerosol process [87]. Hydrolysis and condensation of tethraetoxysilane (TEOS) is carried out in a laminar flow chamber at temperatures ranging from room temperature to 100 °C. Through this technique large surface area (400 m^2/g) linearly agglomerated nanoparticles can be obtained.

There are several wet-chemistry methods, in which one or two precursor are placed in an appropriate solution and nanoparticles form [88, 89]. These can be stabilized with an emulsion, surfactant, or a macromolecule that surrounds and protects the nanoparticles from agglomerations.

There are also minor techniques, used in some particular applications. For example metal nanoparticles can be also made by sonication chemistry [90], while metal oxides can also be formed by taking advantage of hydrodynamic cavitation [91], produced by using a high pressure fluid system in the presence of a sol-gel solution.

Because the objective of this introductive part is giving a general panorama of the main technological aspects and of the properties of isodimensional nanoparticles, many significant aspects about the nanoparticle processing were left out, leaving a more detailed description to specific texts.

2.1.4 Polyhedral oligomeric silsesquioxanes (POSS)

Hybrid organic-inorganic materials are a very wide class of materials, that attracted the interest of many researchers in the last years. These materials can combine an inorganic structure with organic functionalities, or viceversa. From this definition it is immediately evident that a huge number of different chemical structures can be obtained. Leaving the complete description of these system to specific books, our attention is now focused on polyhedral oligomeric silsesquioxanes (POSS) , that are one of the most important kind of nanohybrids.

They were discovered and isolated for the first time in 1946 [92], starting from the hydrolytic condensation of trifunctional organosilicon monomers (for example $RSiCl_3$, $RSi(OMe)_3$). As represented in Figure 2.17, POSS are constituted by a Si-O cage, and by different organic functionalizations that can be chemically attached on silicon atoms of the cage. In this way a wide chemical versatility can be obtained, developing POSS nanoparticles that can be chemically or physically linked to the polymeric matrix.

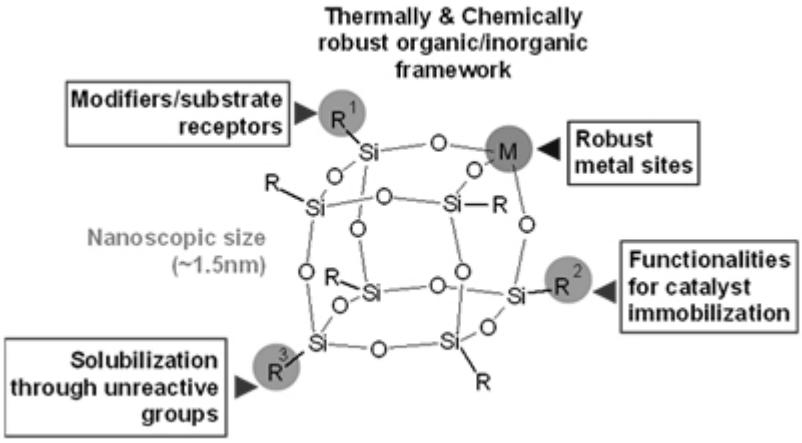

Figure 2.17 Structure of a polyhedral oligomeric silsesquioxane (POSS)

As represented in Figure 2.18, POSS molecules are physically large with respect to the lateral dimensions of polymeric chains, and nearly equivalent in size to most polymer segments and coils.

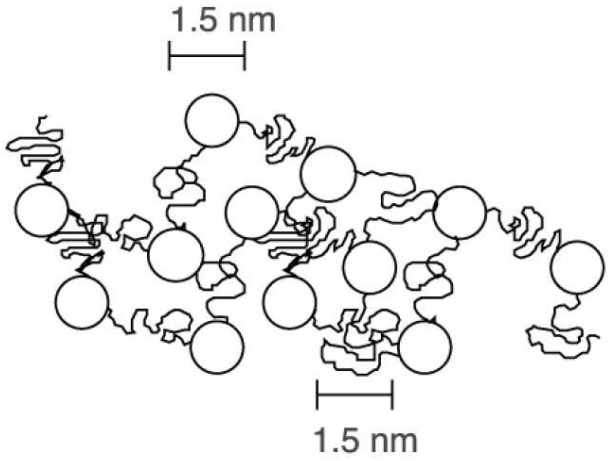

Figure 2.18 Comparison between POSS inorganic domains and polymer segments and coils

POSS molecules can be thought of as the smallest particles of silica possible [93, 94]. However unlike silica or modified clays, each POSS molecule contains covalently bonded reactive functionalities suitable for polymerization or grafting POSS monomers to polymer chains. Each POSS molecule contains non reactive organic functionalities for solubility and compatibility of the POSS segments with the various polymer systems. The chemical diversity of POSS technology is very broad and a large number of POSS monomers and polymers are currently available.

POSS chemical technology is easy to use with monomers available in both liquid and solid form and they are soluble in most common solvents. Hence, POSS technology can be used in the same manner as common organics, in either monomer or polymeric (resin) form. POSS chemical feedstocks can be added to nearly all polymer types (glassy, elastomeric, rubbery, semicrystalline and crystalline) and compositions.

Enhancements in the physical properties of polymers incorporating POSS segments result from POSS's ability to control the motions of the chains while still maintaining the processability and mechanical properties of the base resin. This is a direct result of POSS's nanoscopic size and its relationship to polymer dimensions.

It is widely demonstrated that the use of POSS segments in plastics results in enhancement of the physical properties of the compositions [95]. Compared to common fire retarded plastics, polymers containing POSS show delayed combustion and major reductions in heat evolution [96]. POSS's ability to control chain motion results in usage temperature enhancement of nearly all types of thermoplastics and thermoset polymers [97]. In many cases the glass transition can be increased by 100-200°C or even up to the decomposition temperature of the polymer. Moreover use of POSS

additives often eliminates the need to use common (dense) fillers such as silica. Depending on loading level, bulk density reductions of up to 10% have been observed with viscosity reductions of up to 24% relative to silica. In many cases POSS incorporation increases modulus and hardness while maintaining the stress and strain characteristics of the base resin [98]. Additionally since POSS is a chemical nanotechnology, processing and moldability is maintained. Because of its chemical nature POSS technology can be tailored to meet resin and consumer compatibility needs. Furthermore, since POSS is a new chemical feedstock technology it can be used to upgrade the properties of existing patented compositions while enabling the patentability of the new material composition.

2.2 Viscoelastic behaviour in the molten state : rheological properties

2.2.1 General definitions

The rheology is a science that studies how materials flow, in order to predict their deformational behaviour under different loading conditions. It is easy to understand that the field of application of rheological studies is very wide, because every material will, under different stresses, behave in a different way [99]. Theoretically, all the material present a viscoelastic response at an imposed load. In polymeric materials above the glass transition temperature (T_g), this behaviour is predominant, while in the glassy state the linear elastic response is prevalent. The viscoelasticity theory can be understood referring to two ideal models : the elastic solid and the viscous liquid. A perfect solid under a stress deforms itself elastically : all the deformational energy is stored as elastic potential energy, that will be released when loads are removed. On the contrary, ideal fluids deform irreversibly : all the deformational energy is dissipated and not recoverable. Hooke law (Equation 2.2) and Newton law (Equation 2.3) describe the behaviour of elastic bodies and viscous fluids, respectively [100]:

Equation 2.2

$$\tau = G\gamma$$

Equation 2.3

$$\tau = \eta\dot{\gamma}$$

Where τ is the applied shear stress, γ is the shear strain, G is the shear modulus and η is the viscosity. In elastic materials the stress is directly proportional to the deformation and completely independent from the deformation rate. Hooke law is valid both for normal and shear stresses. For pure viscous fluids the stress is proportional to the deformation rate and completely independent from the deformation itself. The viscosity defines the resistance of a fluid to the irreversible deformation. There are two important deviations from the purely Hookean or Newtonian behaviour.

1) The deformation in a solid or the deformation rate in a liquid can be not directly proportional to the applied stress, following more complex dependences, as reported in Equation 2.4 and in Equation 2.5 :

Equation 2.4

$$\tau = K(\dot{\gamma})^n$$

Equation 2.5

$$\eta = K(\dot{\gamma})^{n-1}$$

where n is an exponent that determines the rheological nature of the material [101]. If n > 1 the material is called dilatant, if n < 1 the fluid is pseudoplastic, while for n = 1 we have again a Newtonian fluid, as reported in Figure 2.19 and in Figure 2.20.

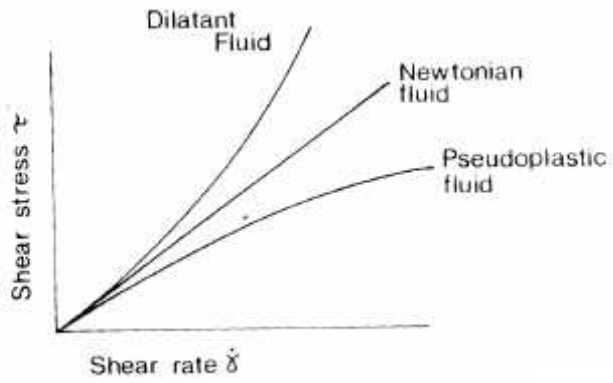

Figure 2.19 Deviation from the Newtonian behaviour: dilatant and pseudoplastic fluids

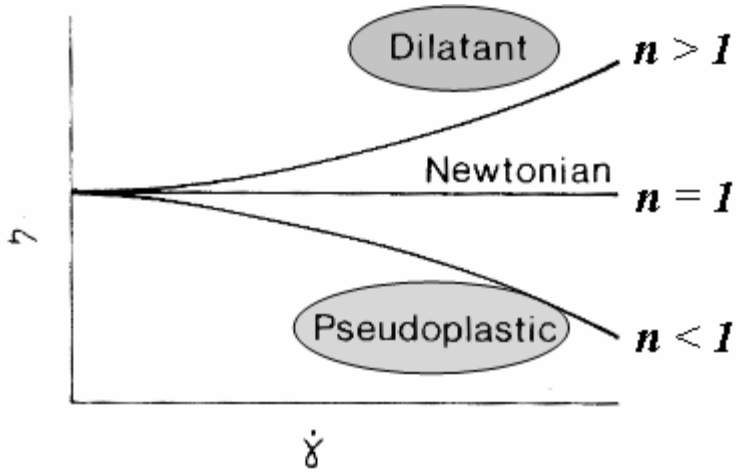

Figure 2.20 Rheological curves for Newtonian, Dilatant and Pseudoplastic fluids

Polymeric materials at the molten state behave typically as pseudoplastic materials, and Figure 2.21 reports a typical rheological curve, in which the shear rate intervals for the different technological processes, are reported. It is possible to see that at low shear rates, Newtonian behaviour is observed, and apparent viscosity corresponding to this region of a flow curve is called zero-shear or initial or maximum Newtonian Viscosity (η_0). Then the decrease of apparent viscosity (declining from the straight line) is observed, typical of non-Newtonian behaviour.

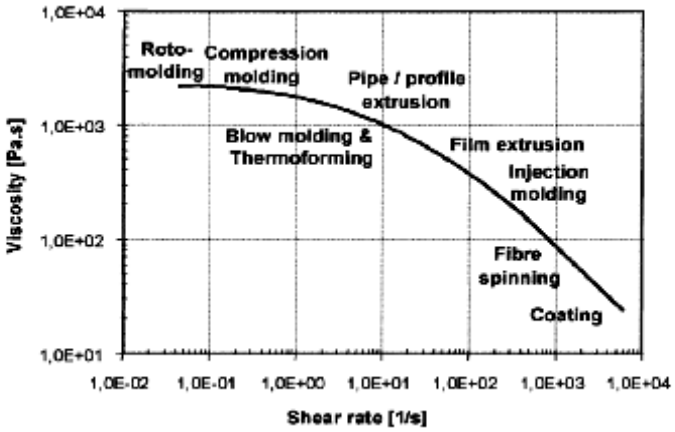

Figure 2.21 Typical rheological curve for a thermoplastic material

Many attempts were made to describe flow curves of various materials by analytical functions of different type, both on theoretical and empirical levels. The most frequently applied equations for the flow curves with distinctly expressed range of initial Newtonian viscosity are reported in Table 2.3 [102].

Cross equation	$\eta = \frac{\eta_0}{1+(\lambda\dot{\gamma})^m}$
Carreau equation	$\eta = \frac{\eta_0}{\left[1+(\lambda\dot{\gamma})^2\right]^p}$
Yasuda equation	$\eta = \frac{\eta_0}{\left[1+(\lambda\dot{\gamma})^a\right]^{\frac{n-1}{a}}}$
Vinogradov-Malkin equation	$\eta = \frac{\eta_0}{1+A(\dot{\gamma})^a + B(\dot{\gamma})^{2a}}$

Table 2.3 The most important equations used to analitically describe the rheological behaviour of polymeric materials

2) The stress can depend both on the deformation and on the strain rate, in this case the material presents simultaneously elastic and viscous properties and it is called viscoelastic. In this situation the basic relation that describes stress-strain relation is a linear expression, reported in Equation 2.6 :

Equation 2.6

$$\tau = \tau_e + \tau_v = G\gamma + \eta\dot{\gamma}$$

This relation puts in evidence a linear viscoelastic behaviour, in which the stresses associated to the strain and to the strain rate are additive. In many cases linear viscoelasticity is present when infinitesimal deformations are applied. For higher strain level stress-strain relations are more complex and the viscoelastic behaviour of the material is not linear anymore. In order to study the viscoelastic behaviour of a material it is possible to conduct creep (constant stress) or relaxation (constant strain) experiments, or referring to dynamic mechanical analyses.

2.2.2 Dynamic rheological tests

Creep or relaxation tests are very useful techniques in order to study the viscoelastic behaviour of the material at relatively high loading times. With dynamic methods it is possible to extend the

characterization curve of a material on a wide frequency range (10^{-9}-10^{9} Hz) in relatively short testing times [101]. The experimental procedure is based on the application of a sinusoidal shear strain with a certain frequency (ω) and the evaluation of the shear stress, or viceversa. The test are conducted with a rotational rheometer. Supposing that a sinusoidal shear strain is applied to the material (Equation 2.7) :

Equation 2.7

$$\gamma(t) = \gamma_0 \sin(\omega t)$$

the strain rate is defined as reported in Equation 2.8 :

Equation 2.8

$$\dot{\gamma}(t) = \frac{d\gamma}{dt} = \omega\gamma_0 \cos(\omega t)$$

If the material has a linear viscoelastic behaviour, it will answer with a sinusoidal shear stress, with a phase shifted by an angle δ on the shear stress, as reported in equations below :

Equation 2.9

$$\tau(t) = \tau_0 \sin(\omega t + \delta)$$

Equation 2.10

$$\tau(t) = \tau_0 \cos(\delta)\sin(\omega t) + \tau_0 \sin(\delta)\cos(\omega t)$$

Equation 2.11

$$\tau(t) = \tau_0 G' \cdot \sin(\omega t) + \tau_0 G'' \cos(\omega t)$$

$$\text{where :} \quad G' = \frac{\tau_0}{\gamma_0}\cos(\delta) \qquad G'' = \frac{\tau_0}{\gamma_0}\sin(\delta)$$

The quantities G’ and G’’ are defined storage and loss modulus, respectively. The equations reported above put in evidence that the shear stress can be expressed as a term in phase with the strain and a term in opposition (in phase with the strain rate). We can also refer to the complex notation :

Equation 2.12

$$\gamma^*(\omega) = \gamma_0 e^{i\omega t}$$

Equation 2.13

$$\tau^*(\omega) = \tau_0 e^{(i\omega t+\delta)}$$

Equation 2.14

$$\frac{\tau^*}{\gamma^*} = \frac{\tau_0}{\gamma_0} e^{i\delta} = G^* = G' + iG''$$

Dynamic measurements provide also the value of the complex modulus $G^*(\omega)$, defined as the ratio between the stress and the strain at a certain frequency.

Equation 2.15

$$\frac{\tau^*(\omega)}{\gamma^*(\omega)} = G^*(\omega) = G'(\omega) + iG''(\omega)$$

G'(ω) describes the capacity of the sample to store the input energy, while G''(ω) represents the ability of the material to dissipate the input energy. The frequency at which G'(ω) is equal to G''(ω) is called crossover frequency [102]. This point represents the frequency at which the material passes from an elastic to a dissipative behaviour, or viceversa, as reported in Figure 2.22.

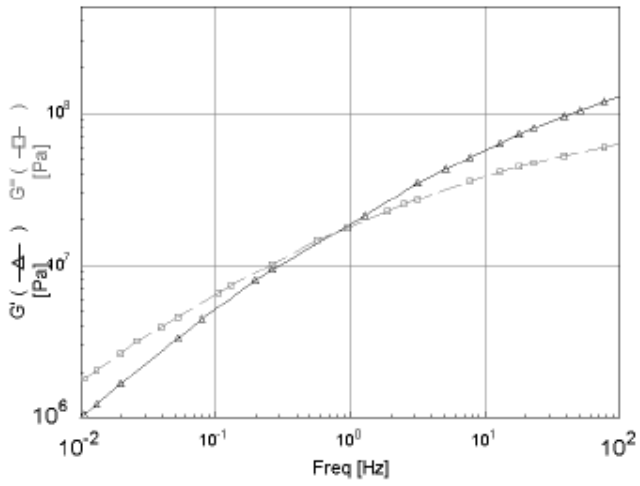

Figure 2.22 G' and G'' rheological curves with the crossover frequency

The ratio between the loss modulus and the storage modulus is defined as loss tangent, reported in Equation 2.16 :

Equation 2.16

$$tg(\delta) = \frac{G''(\omega)}{G'(\omega)}$$

Another important parameter to describe the behaviour of the material is the complex viscosity (η^*), defined as the ratio between the shear stress and the strain rate. Referring to the complex notation :

Equation 2.17

$$\eta^*(\omega) = \frac{\tau(\omega)}{\dot{\gamma}(\omega)} = \frac{G^*(\omega)}{i\omega} = \eta'(\omega) + i\eta''(\omega)$$

where : $\eta' = \frac{G''(\omega)}{\omega}$ $\eta'' = \frac{G'(\omega)}{\omega}$

The real part η', defined as dynamic viscosity, is the term describing the dissipative phaenomena, and it is the ratio between the stress in phase with the strain rate and the strain rate itself. For $\omega \rightarrow 0$ the dynamic viscosity tends to the steady flow viscosity (η_0), described in the previous paragraph.

2.2.3 Time-temperature superposition principle

Viscoelastic properties, especially at temperatures higher than the glass transition of the material, are greatly influenced by the temperature. For some materials, called thermorheologically simple, a time-temperature superposition principle can be introduced. According to this principle, a viscoelastic property (G', G'', tanδ,…) can be translated along the time (or frequency) scale by changing the test temperature [100].

Consequently it is possible to visualize on a single curve (called master curve) the viscoelastic behaviour of the material over a very wide range of frequencies, simplifying the analysis of the influence of the temperature on the mechanical properties. According to this method, every viscoelastic property (for example G') evaluated at a certain temperature can be shifted along the frequency axis to another curves taken at a reference temperature, as expressed in Equation 2.18 :

Equation 2.18

$$\overline{\omega}(T_0) = a_T \omega(T)$$

where ϖ is called reduced frequency.

In practice it is possible to shift all the experimental curves obtained at different temperatures over the same curve (master curve), determined at a reference temperature T_0. The quantity a_T (shift factor) is obtained from the evaluation of the horizontal translation necessary to superimpose curves obtained at a temperature T over the data obtained at a reference temperature T_0. The validity of this principle implies that shift factors are the same for all the viscoelastic properties. It is possible to visualize the construction of the master curve in Figure 2.23.

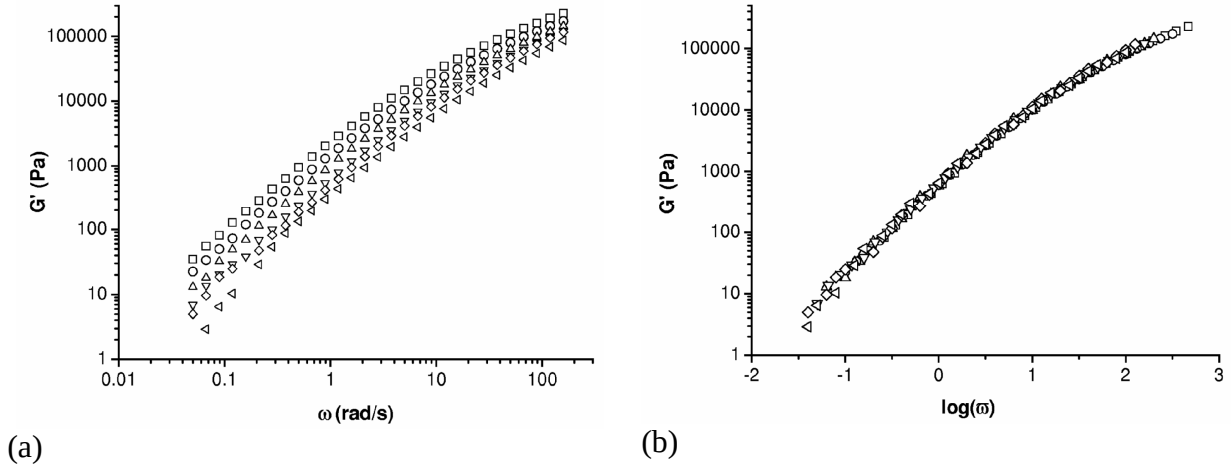

(a) (b)

Figure 2.23 Construction of the storage shear modulus (G') master curve of an LLDPE sample, (a) G' curves at temperatures ranging from 125 °C to 210 °C, (b) superimposed curves (T_0=170 °C)

The dependency of the shift factors from the temperature can be generally expressed by using two relations, the Williams-Landel-Ferry (WLF) and the Arrhenius equation. In the case of polymeric materials, WLF equation provides a good fitting of the shift factors in a temperature interval between T_g and T_g + 100 K :

Equation 2.19

$$\log\left(\frac{a(T)}{a(T_0)}\right) = \frac{-C_1(T-T_0)}{C_2+(T-T_0)}$$

Arrhenius equation can be applied below the glass transition temperature :

Equation 2.20

$$\log a(T) = \frac{E_a}{R}\left(\frac{1}{T}-\frac{1}{T_0}\right)$$

where E_a is the activation energy, R is the universal constant of the universal gases.

Among different techniques suitable to evaluate viscoelastic properties, parallel plate rheometers are widely used in order to conduct dynamic measurements. The configuration of the experimental apparatus for these tests is represented in Figure 2.24.

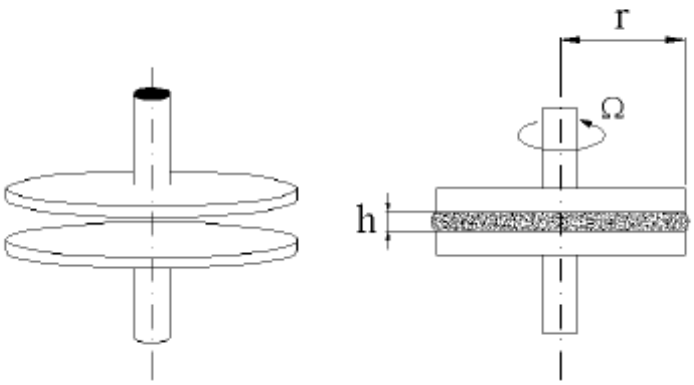

Figure 2.24 Parallel plate geometry for rheological tests

According to this geometry it is not possible to obtain a direct measurement for non Newtonian fluids, because the shear rate is not the same over the flow surface. The equation of the shear rate at a certain distance between the plates (h) is :

Equation 2.21

$$\dot{\gamma} = \dot{\gamma}(r) = \frac{v}{h} = \frac{\omega r}{h}$$

Consequently for a non-Newtonian fluid the viscosity varies from the centre to the external surface of the sample. In any case it is possible to estimate the viscosity trough some analytical approximations [101].

2.3 Viscoelastic behaviour in the solid state

2.3.1 Creep behaviour

2.3.1.1 Creep loading conditions

The distinction between solid (or elastic) and liquid (or viscous) is not an absolute distinction between different classes of materials: the ability to detect elastic or viscous responses depends in many cases on the time scale of the experiment. In this way, from a strict point of view, all the materials have a viscoelastic behaviour, i.e. the strain does not depend on the applied stress only, but also on the previous loading history of the material [10, 103-106]. Polymers are the most important viscoelastic systems. The viscoelastic behaviour is investigated with several method: in this work creep experiments and dynamical experiments were adopted.

In a creep experiment a constant stress σ_0 is applied to a sample and the strain ε is monitored as a function of time t. Normally the strain increases with time and creep curves (i.e. strain as function of time) may exhibit three regions (Figure 2.25): primary creep in which the curve is concave down, secondary creep in which deformation is proportional to time, and tertiary creep in which deformation accelerates until creep rupture occurs. The strain rate $\dot{\varepsilon}$, i.e. the derivative of the strain, also exhibits three regions. The material has a linearly viscoelastic behaviour if the stress is proportional to the strain at a given time: in this case it is also possible to apply the linear superposition principle. However, linearity does not hold at high strains: creep isochrones diagrams, i.e. curves of stress as a function of strain at a given time, may evidence the transition from linear to nonlinear behaviour in creep experiments (Figure 2.26). The creep compliance D(t) is the ratio of the strain to the stress and is generally a function of time, as reported in Equation 2.22. In linearly viscoelastic materials, the creep compliance is independent from the stress level.

Equation 2.22

$$D(t) = \frac{\varepsilon(t)}{\sigma_0}$$

Moreover, a compliance rate $\dot{D}$ can be defined as the derivative of the compliance over the time.

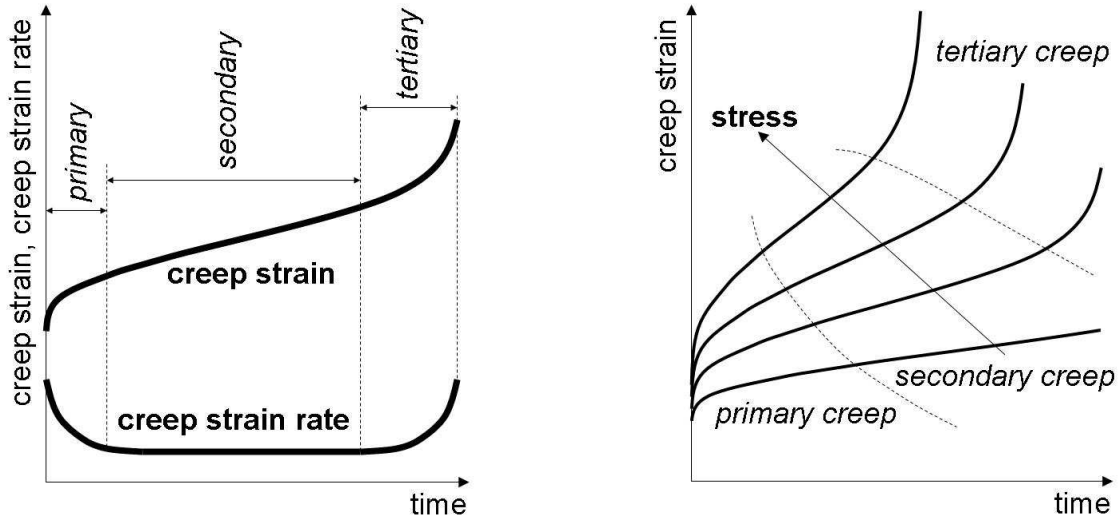

Figure 2.25 Creep strain and strain rate as a function of time at different applied stresses

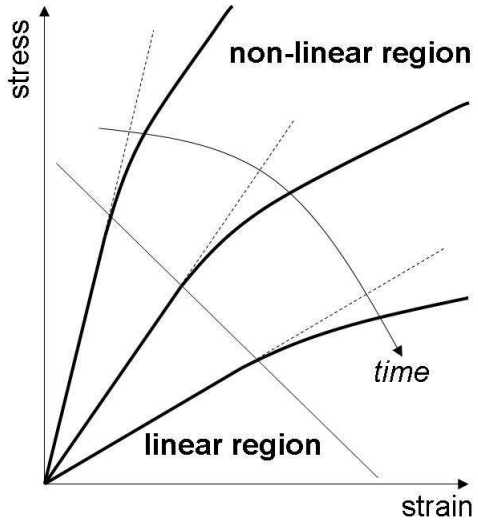

Figure 2.26 Isochronous stress-strain curves in creep experiments

Total strain at any instant of time ε(t) in a creep test of a linear material may be represented as the sum of the instantaneous elastic strain ε_E (i.e. the initial strain when the constant stress is applied) and the viscoelastic strain ε_V. Similarly the compliance can be divided into elastic and viscous components.

2.3.1.2 Linear superposition principle

As seen in the previous paragraph, linear viscoelasticity implies a linear superposition principle. These systems may be modelled as arrangements of springs (i.e. an elastic solid) and dashpots (i.e. a viscous liquid). The spring represents Hookean deformation (i.e. an element in which the force is proportional to the extension) and the dashpot Newtonian flow (i.e. an element in which the force is proportional to the strain rate). The behaviour of more complicated materials is described by connecting the basic elements in series or in parallel. In other words, stress, strain and time can be related with the characteristic constant of the mechanical elements [10, 104]. The overall system (mechanical model) behaves analogously to a real material, although the elements themselves may have no direct analogues in the actual material .

The basic configurations are the Kelvin (or Voigt) model and the Maxwell model (Figure 2.27). The first one results from a parallel combination of a spring and a dashpot, while the second one is represented by a spring connected in series with a dashpot. In both system a characteristic time τ, that is the ratio of the viscosity η (dashpot) to the elastic modulus E (spring), describes the viscoelastic behaviour of the material. This parameter is called retardation time for the Kelvin model, while relaxation time for the Maxwell model.

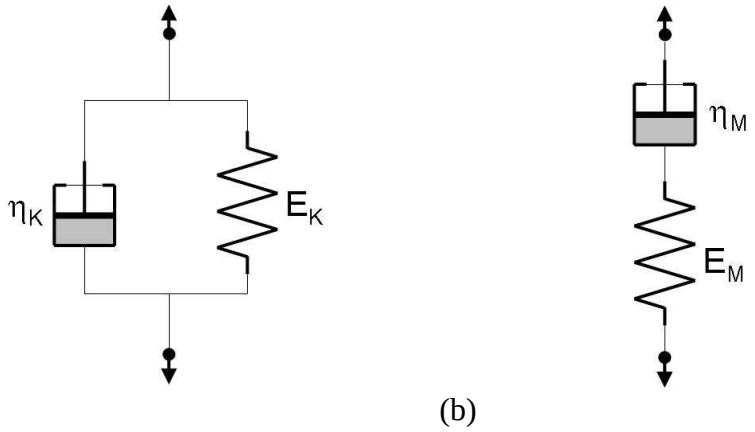

Figure 2.27 Simplest linear viscoelastic models: (a) the Kelvin model and (b) the Maxwell model

More complicated and complex models could be introduced, but all the models can be reduced to two canonical forms. The creep behaviour of polymeric materials can be successfully interpreted by applying Burgers model, derived from a series combination of a Maxwell and a Kelvin model, as represented in Figure 2.28.

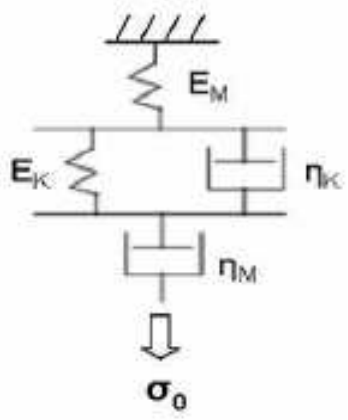

Figure 2.28 Schematic representation of the Burgers model

The equation of the creep compliance according to this model is reported in Equation 2.23 :

Equation 2.23

$$D(t) = \frac{1}{E_M} + \frac{t}{\eta_M} + \frac{1}{E_K}\left(1 - e^{-\frac{E_K t}{\eta_K}}\right)$$

Alternatively it is possible to consider the generalized Voigt-Kelvin model and the generalized Maxwell-Wiechert model. The generalized Maxwell-Wiechert model may have a finite number or an enumerable infinity of Maxwell elements, each with a different relaxation time, and similarly the generalized Voigt-Kelvin model may have a finite number or an enumerable infinity of Kelvin elements. Thus, by a suitable choice of the model parameters, the canonical forms themselves can be shown to be mechanically equivalent and it is also possible to compute the parameters of one canonical form from those of the other. In this way, by taking into account the generalized models, an enumerable infinity or a continuous distribution of retardation or relaxation times is obtained [106]. In particular the strain as a function of time with the generalized Kelvin model for a system with n pairs of elements has the following expression:

Equation 2.24

$$\varepsilon(t) = \sum_{i=1}^{n} \frac{1}{E_i \tau_i} \int_{-\infty}^{t} \{1 - \exp[-(t - t')/\tau_i]\} \sigma(t') dt'$$

where η_i and τ_i are the viscosity and the retardation times of the i-th Kelvin element. The extension to a continuous distribution of relaxation times is employed by introducing the distribution function of retardation times (or retardation spectrum) N'(1/τ): in detail N'(1/τ)dτ represents the contributions to the total modulus of all the Kelvin elements with relaxation times lying between τ and τ +dτ. The strain equation becomes:

Equation 2.25

$$\varepsilon(t) = \int_{-\infty}^{t} \left\{ \int_{0}^{+\infty} \frac{N'(1/\tau)}{\tau} \{1 - \exp[-(t-t')/\tau]\} d\tau \right\} \sigma(t') dt'$$

Alternatively the retardation spectrum function L(τ) = N'(1/τ)/τ can be used. An approximate value of L(τ) can be derived from the creep compliance function D(t) by means of the relationship:

Equation 2.26

$$L(\tau) \cong D(t) \left. \frac{d \log D(t)}{d \log t} \right|_{t=\tau}$$

Figure 2.29 reports a typical example of retardation spectrum of a polystyrene sample.

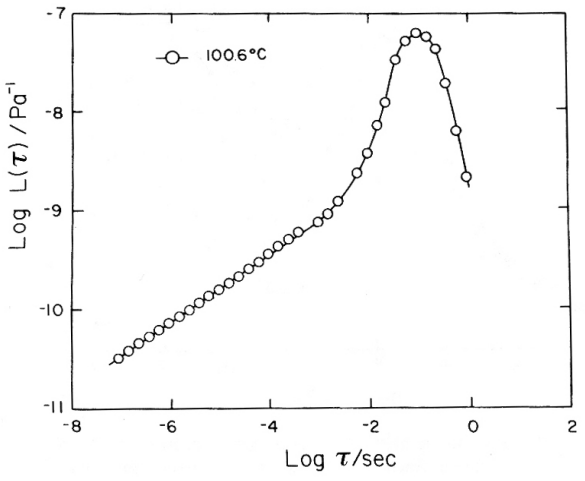

Figure 2.29 Example of retardation spectrum for polystyrene with a narrow molecular weight distribution. The weight average molecular weight is 3.4 kDa [107].

2.3.1.3 Time-temperature superposition principle

Viscoelastic functions, such as the creep compliance as a function of the time, depend on the temperature too. Theoretical and experimental results indicate that for many materials the effect due to time and temperature in the linearly viscoelastic region can be combined into a single curve trough the concept of the time-temperature superposition principle which implies that the following relations exist [104]:

Equation 2.27

$$D(T,t) = D(T_0, t^*)$$

Equation 2.28

$$t^* = t / a_{T_0}(T)$$

where T is the temperature and t* the reduced time. The reduced time is related to the real time t by the temperature shift factor $a_{T0}(T)$, and T_0 is the reference temperature. In this way the effect of temperature on time-dependent mechanical behaviour is equivalent to a stretching (or shrinking) of real time for temperatures above (or below) the reference temperature; or alternatively, since viscoelastic properties are usually plotted as a function of the logarithm of time or frequency, a temperature change corresponds to a rigid horizontal shift of the material property curves on the abscissa. In other words, high-temperature response is analogous to low-strain-rate behaviour, and low-temperature response corresponds to high-strain-rate behaviour. Thus, the determination of the temperature shift factor $a_{T0}(T)$ as a function of temperature provides the required information for determining the reduced time. Figure 2.30 reports the typical superposition procedure applied on creep curves of a polyethylene sample.

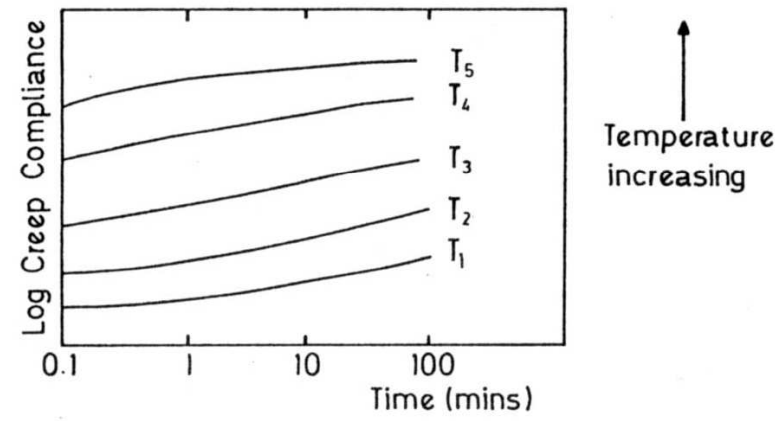

(a)

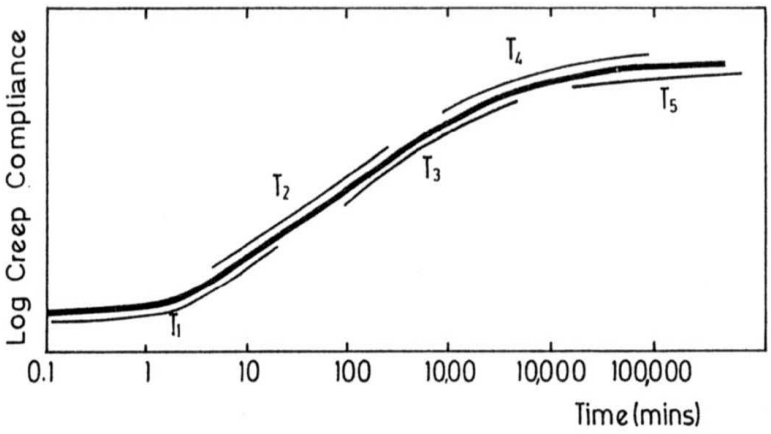

(b)

Figure 2.30. Example of master curve (b) from short term creep tests at different temperature (a). The data refer to an HDPE sample.

Many materials exhibit temperature-creep behaviour that follows the Arrhenius relation for temperature lower than the glass temperature and the relation proposed by Williams, Landel and Ferry (WLF equation) for higher temperatures [104, 106]

Equation 2.29

$$\ln a_{T_0}(T) = \frac{\Delta H}{R}\left(\frac{1}{T} - \frac{1}{T_0}\right) \qquad \text{(Arrhenius equation)}$$

Equation 2.30

$$\log a_{T_0}(T) = -\frac{C_1(T - T_0)}{C_2 + (T - T_0)} \quad \text{(WLF equation)}$$

In these expressions ΔH is an activation energy, R the ideal gas constant, and C_1 and C_2 are empirical constants that depend on the material. Experimentally, for many linear amorphous polymers, if the reference temperature is the glass transition temperature, the values of the constants in the WLF equation are independent of chemical structure (C_1=17.44 and C_2=51.6 K). Moreover the product of C_1 and C_2 (for any reference temperature) is almost always 900 K. The curves constructed on the basis of a time-temperature superposition principle are generally denoted as master curves. As an example, Figure 2.31 reports shift factor as a function of temperature of a polyethylene sample.

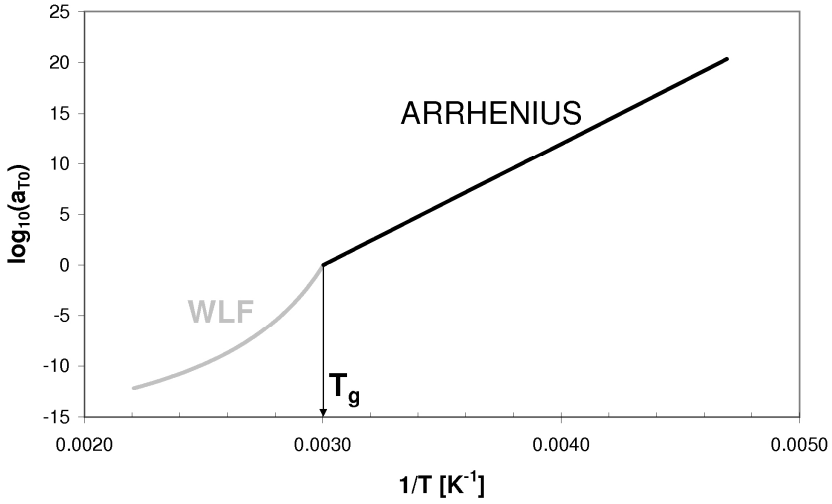

Figure 2.31. Example of shift factor as a function of temperature.

2.3.1.4 Non linear tensile creep behaviour

In most practical applications, isothermal compliance of polymeric materials depends on both time and stress, so that their non-linear viscoelastic behaviour is of primary importance. A very useful approach, reported in the works of Kolarik et al. [108, 109], starts from the consideration that the non-linearity of tensile creep is mainly brought about by the strain induced increment of the free volume. Consequently, the traditional stress-strain linearity limit can be viewed only as an artificial limit related to limited accuracy of the measurements at low stresses and strains. The internal time-tensile compliance superposition of non-linear creep data is applied to construct a generalized compliance curve, which corresponds to a pseudo iso-free volume state. The superposition of compliance curves obtained at different stresses requires shift factors along the time axis calculated a priori for individual data points. The outlined format is that the generalized dependence can be

employed for predicting the real time-dependent compliance for any stress in the range of reversible strains.

First of all, the strain in tensile creep, $\varepsilon(t,\sigma,T)$, depending on time t, stress σ and temperature T, is usually viewed as consisting of three components [12, 104, 106, 110-113] : (i) elastic (instantaneous, reversible) $\varepsilon_e(\sigma,T)$; (ii) viscoelastic (time-dependent, reversible) $\varepsilon_v(t,\sigma,T)$; (iii) plastic (irreversible) $\varepsilon_p(t,\sigma,T)$:

Equation 2.31

$$\varepsilon(t,\sigma,T) = \varepsilon_e(\sigma,T) + \varepsilon_v(t,\sigma,T) + \varepsilon_p(t,\sigma,T)$$

If no plastic deformation is produced in the course of creeping, the tensile compliance $D(t,\sigma) = \varepsilon(t,\sigma)/\sigma$ for the isothermal non-linear creep reads :

Equation 2.32

$$D(t,\sigma) = D_e(\sigma) + D_v(t,\sigma)$$

It would be practical to express the compliance as a product of independent functions of time, stress and temperature, i.e. $D(t,\sigma,T)=g_1(t)\bullet g_2(\sigma)\bullet g_3(T)$ [12]. However, experimental results often indicate interrelations between these presumably independent functions. A relatively simple equation was found suitable for describing isothermal creep of polypropylene and its blends [114] :

Equation 2.33

$$\log D(t,\sigma) = \log W(\sigma) + n\log\left(\frac{t}{\tau_{rm}}\right)$$

where $W(\sigma)$ is a function of stress (usually can be approximated by the power law or hyperbolic sine), τ_{rm} is the mean retardation time and $0 \le n \le 1$ is the shape parameter reflecting the distribution of retardation times. Indicated parameters are generally determined a posteriori by fitting experimental data. The free volume concept provides a simple unifying basis for explaining the effects of temperature, hydrostatic pressure, tensile deformation, chain ends, diluents (plasticizers), the state of physical aging, etc. on the viscoelastic behaviour of polymers. The dimensionless fractional free volume is routinely defined as [104, 106, 112, 115]:

Equation 2.34

$$f = \frac{(V - V_h)}{V} = \frac{V_f}{V}$$

where V is the specific volume, V_h is the specific volume occupied by molecules (extrapolated from the melt without change of phase) and V_f is the free volume. If solely the effects of temperature T and of time dependent tensile strain ε(t) in the region of reversible deformations are considered, the fractional free volume can be expressed as :

Equation 2.35

$$f[T, \varepsilon(t)] = f_g + \alpha_{fv}(T - T_g) + (1 - 2\nu)\varepsilon(t)$$

Equation 2.36

$$f[T, \varepsilon(t)] = f_g + \Delta f_T + \Delta f_\varepsilon$$

where f_g is the free volume at the glassy state (0.025 according to the Flory's theory), α_{fv} is the expansion coefficient of the free volume at $T > T_g$ (which can be approximated as the difference between the expansion coefficients of the material above and below T_g), ν is Poisson's ratio and $(1-2\nu)\bullet\varepsilon(t)$ is the strain-induced dilatation. The free volume f is assumed to control retardation times τ_r according to Equation 2.37 [105, 106, 115] :

Equation 2.37

$$\ln \tau_r = \ln \Omega + \frac{B}{f}$$

where Ω is the frequency of thermal motion inside a potential well and B is a numerical factor related to the ratio of the volume of a jumping segment to the volume of critical vacancy necessary for the implementation of a segment jump (B is generally expected to be close to 1). The effect of f on τ_r is routinely expressed by means of the shift factor (loga) along the time scale [105, 106, 115] :

Equation 2.38

$$\log a = \log \tau_r(f_2) - \log \tau_r(f_1)$$

The time-strain shift factor, $\log a_\varepsilon(t)$, is then obtained by combining Equation 2.38 and Equation 2.35 :

Equation 2.39

$$\log a_\varepsilon(t) = -\left(\frac{B}{2.303}\right)\frac{\left[(1-2\nu)M\varepsilon(t)/\left(f_g + \Delta f_{T\,c}\right)\right]}{\left[(1-2\nu)M\varepsilon(t) + \left(f_g + \Delta f_{Tc}\right)\right]}$$

where M is the ratio of the average strain of the creeping phase (or component) in the multiphase test specimen and of measured strain. The values of $\log a_\varepsilon(t)$ needed for the time-strain superposition are to be calculated a priori as a function of $\varepsilon(t)$. In this strain-based formulation, $\log a_\varepsilon(t)$ is not a constant for an iso-stress creep curve, but grows from point to point with the creep strain due to increasing free volume in the creeping specimen. If τ_{rm} obeys to Equation 2.37, then isothermal $D(t,\sigma)$ can be expressed as :

Equation 2.40

$$\log D(t,\sigma) = \left[\log W(\sigma) - n\log\tau_{rmi} - n\log a_\varepsilon(t)\right] + n\log(t)$$

Equation 2.41

$$\log D(t,\sigma) = \log C(t,\sigma) + n\log(t)$$

To separate the effects of stress and time, Equation 2.40 can be rewritten in the following form:

Equation 2.42

$$\log D(t,\sigma) = \left[\log W(\sigma) - n\log\tau_{rmi}\right] + n\left[\log(t) - \log a_\varepsilon(t)\right]$$

Equation 2.43

$$\log D(t,\sigma) = \log C^*(\sigma) + n^*\log\left(t^*\right)$$

where parameters C* and n* are related to internal time t* which reads:

Equation 2.44

$$\log t^* = \log t + \log a_\varepsilon(t) = \log t + \left(\frac{B}{2.303}\right)\frac{\left[(1-2\nu)M\varepsilon(t)/\left(f_g + \Delta f_{T\,c}\right)\right]}{\left[(1-2\nu)M\varepsilon(t) + \left(f_g + \Delta f_{Tc}\right)\right]}$$

To account for differing strains of amorphous and crystalline phases in the Equivalent Box Model (EBM), the strain magnifying factor M can be introduced as the mean ratio of the actual (microscopic) strain of the amorphous phase and the measured (macroscopic) strain of the specimen. If a crystalline polymer is deformed, the strain of the amorphous and crystalline fractions coupled in parallel, i.e. v_{1p} and v_{2p}, are identical with the measured strain. On the other hand, if the crystalline phase has the compliance by 2–3 orders of magnitude lower than the amorphous phase above its T_g, it is evident that the crystalline fraction v_{2s} coupled in series is not perceptibly deformed in the course of the creep (Figure 2.32).

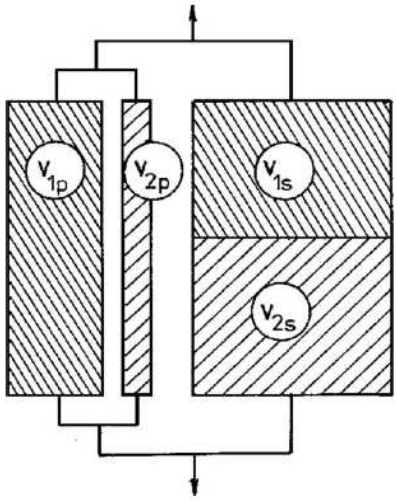

Figure 2.32 Equivalent Box Model (EBM) for a two-component system (schematically)

As the displacement in the fraction v_{1s} is equal to the macroscopic displacement, the resulting strain of the amorphous phase coupled in series is higher than the measured strain; consequently, the generation of the strain-induced free volume in the fraction v_{1s} will be higher than in the fraction v_{1p}. The mean value of M for the amorphous phase is :

Equation 2.45

$$M = 1 + \left(\frac{v_{2s}}{v_1} \right)$$

Utilizing a universal formula for the elastic modulus (or compliance) proposed by the percolation theory for heterogeneous binary systems [116], it is possible to derive the following equations for the volume fractions of the EBM :

Equation 2.46

$$v_{1p} = \left[\frac{v_1 - v_{1cr}}{1 - v_{1cr}} \right]^q$$

Equation 2.47

$$v_{2p} = \left[\frac{v_2 - v_{2cr}}{1 - v_{2cr}} \right]^q$$

where v_{1cr} and v_{2cr} are the critical volume fractions and q is the critical universal exponent. The fractions v_{1s} and v_{2s} can be calculated by using the following relations:

Equation 2.48

$$v_{1s} = v_1 - v_{1p}$$

Equation 2.49

$$v_{2s} = v_2 - v_{2p}$$

Values of q were mostly reported in an interval of 1.6–2.0, so that q = 1.8 may be used as a typical value. In this work, $v_{1cr} = v_{2cr} = 0.156$ and q = 1.8 for approximate calculations of the parameter M were used [116, 117].

2.3.2 Dymamic mechanical tensile behaviour

2.3.2.1 Dynamic loading conditions

In dynamical experiment a sinusoidal strain ε(t), with an amplitude ε_0 and a frequency ω, is imposed on a sample: the output stress σ(t), that follows a sinusoidal function with an amplitude σ_0 and a phase shift δ, is monitored [105, 106]. These data can be analyzed in following terms:

- the storage modulus $E'(\omega)=(\sigma_0/\varepsilon_0)\cos(\delta)$, that is related to output stress components in phase with the applied strain
- the loss modulus $E''(\omega)=(\sigma_0/\varepsilon_0)\sin(\delta)$, that is related to output stress components out of phase with the applied strain
- the loss factor $\tan(\delta)=E''(\omega)/E'(\omega)$.

In a dynamical experiments E', E'' and tanδ can be measured as a function of the temperature or of the frequency, as depicted in the following figures.

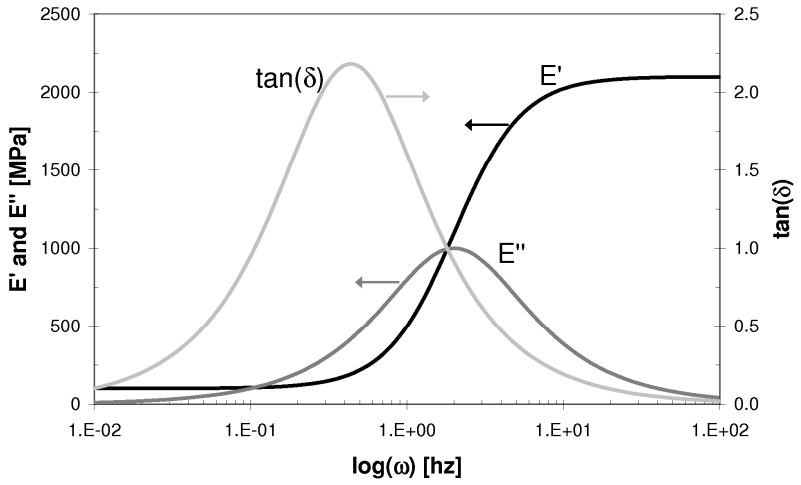

Figure 2.33. Examples of E', E'' and tanδ as a function of frequency

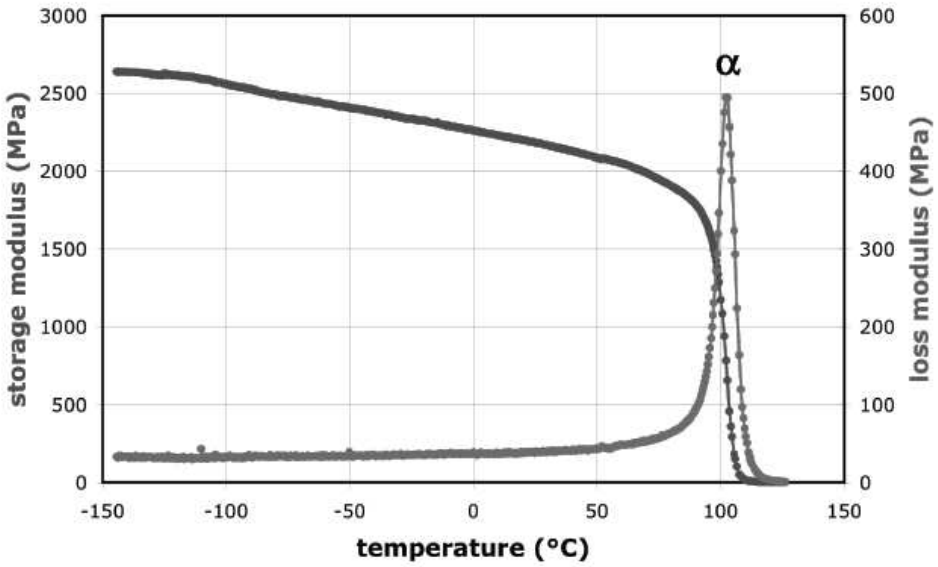

Figure 2.34 Typical E' and E'' tensile moduli for a polystyrene sample

2.3.2.2 Linear superposition principle

If the linear viscoelasticity holds, it is possible to apply the linear superposition principle as for the creep behaviour. Similarly a distribution function of relaxation times (or relaxation spectrum) H(τ) is defined in relation to viscoelastic function [104]:

Equation 2.50

$$E'(\omega) = \int_0^{+\infty} H(\tau) \frac{\omega^2 \tau}{1+\omega^2 \tau^2} d\tau$$

Equation 2.51

$$E''(\omega) = \int_{-\infty}^{+\infty} H(\tau) \frac{\omega}{1+\omega^2 \tau^2} d\tau$$

The approximate value of H(τ) can be derived from the storage modulus function E'(ω) by means of the following relationship:

Equation 2.52

$$H(\tau) \cong E'(\omega) \frac{d \log E'(\omega)}{d \log \omega}\Bigg|_{\tau=1/\omega}$$

2.3.2.3 Time-temperature superposition principle

As for the creep experiments, it is also possible to apply the time-temperature superposition principle for the dynamical experiments. In this case the frequency is used instead of the time and the master curve is a function of the reduced frequency ω*.

In practice the experiments are carried out at a limited number of frequencies (4 to 6) by scanning temperature. These data are used to build up a spectrum, i.e. the modulus as a function of the frequency at different temperatures, and then the time-temperature superposition principle is applied to obtain the master curve and the shift factor as a function of the temperature [106]. As an

example, Figure 2.35 reports the typical construction process of the storage modulus (E') master curve of a polyethylene sample.

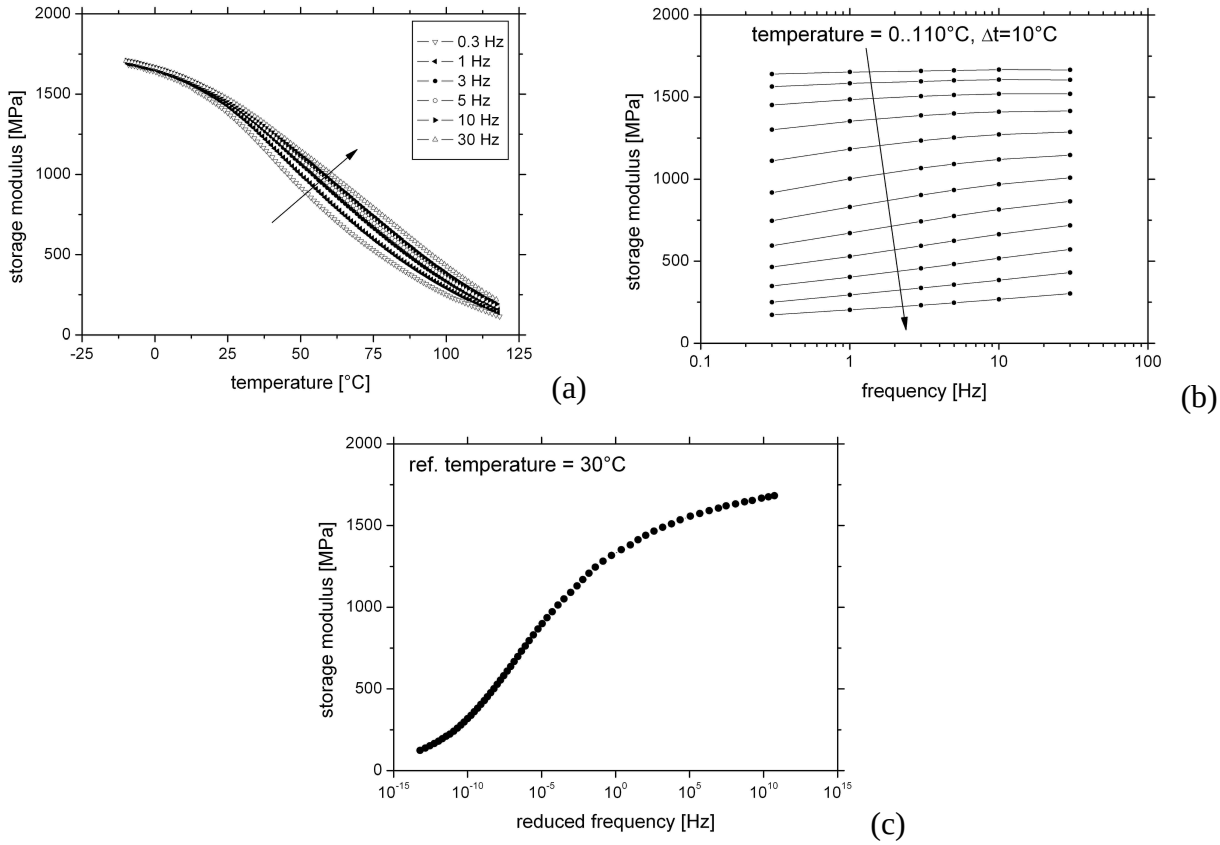

Figure 2.35. Example of the construction of the master curve of E' : E' as a function of temperature at different frequency (a), the spectrum of E' (b) and finally the master curve (c). The data refers to an HDPE

2.4 Fracture behaviour

2.4.1 Quasi-static tensile tests

The evaluation of the mechanical properties of a material (elastic modulus, strain and stress at yield, stress and strain at break) can be done through the elaboration of the stress (σ)-strain (ε) curve. This curve can be obtained through different loading conditions (tension, compression, flexure, torsion, shear). In any case these properties can be measured by using universal mechanical testing machines [118, 119]. There are two main categories of these machines : electromechanic and servo-hydraulic machines.

Electromechanic machines have a loading capacity between 0.5 and 600 kN, and the tests are conducted in displacement controlled conditions, with cross-head speeds between 0.001 and 1000 mm/min. Figure 2.36 reports a typical configuration of these machines

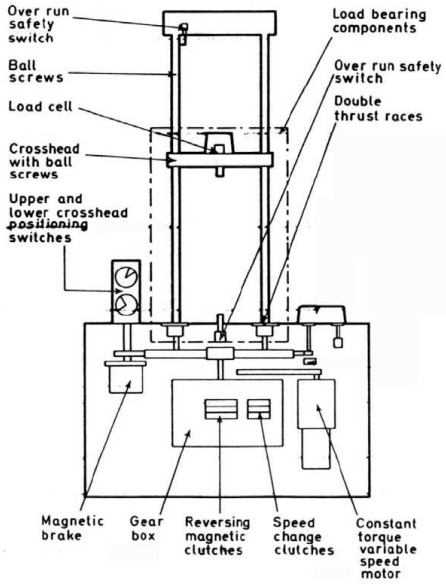

Figure 2.36 A typical configuration for an electromechanic tensile testing machine

In servo-hydraulic machines the strain is applied through an hydraulic actuator, able to work both under displacement or load controlled conditions. In this configuration it is possible to rapidly change the load and an higher loading capacity can be achieved (between 1 and 10000 kN). The typical configuration of an uniaxial tensile test is reported in Figure 2.37. On the cubic element an uniaxial tensile stress (σ_x) is applied, and a corresponding deformation (ε_x) is generated, as reported in Equation 2.53 and in Equation 2.54.

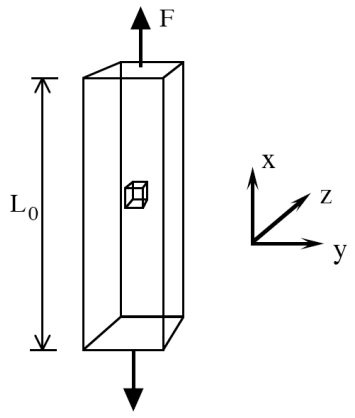

Figure 2.37 Typical configuration of an uniaxial tensile test

Equation 2.53

$$\sigma_x = \frac{F}{A}$$

Equation 2.54

$$\varepsilon_x = \frac{\Delta L}{L_0}$$

If the material as a linear elastic behaviour, Hooke's law can be applied :

Equation 2.55

$$\sigma_x = E\varepsilon_x$$

Where E is called elastic (Young) modulus of the material. Materials have in general a linear elastic behaviour only at small deformations. In the case of polymeric materials this limit is ε < 1%, while ceramic materials has a linear elastic behaviour until break. According to S.Venant's analysis, the hypothesis of uniaxial stress condition is valid only if the distance between the grips is sufficiently high with respect to the thickness of the sample. Moreover the section of the sample in the grips must be higher, in order to prevent the failure near the grips. For these reason "dumb-bell" specimens are generally used during tensile tests [119]. For example Figure 2.38 reports the dimensions of specimens used for uniaxial tensile tests of polymeric materials.

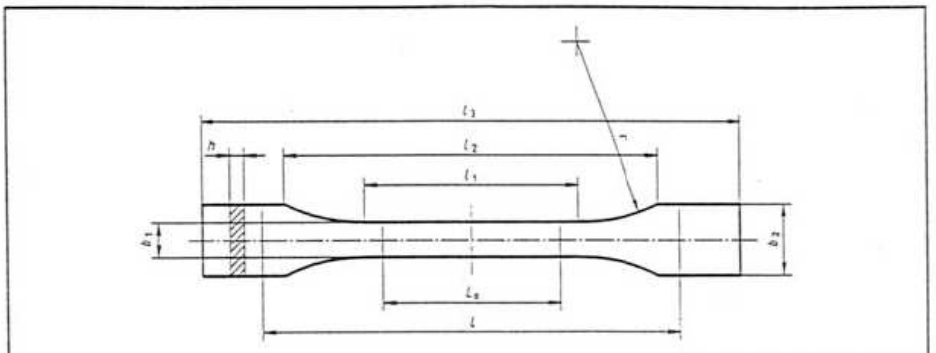

Dimensions in millimetres

	Specimen type	1A	1B
l_3	Overall length	⩾ 150 [1]	
l_1	Length of narrow parallel-sided portion	80 ± 2	60,0 ± 0,5
r	Radius	20 to 25	⩾ 60 [2]
l_2	Distance between broad parallel-sided portions	104 to 113 [3]	106 to 120 [3]
b_2	Width at ends	20,0 ± 0,2	
b_1	Width of narrow portion	10,0 ± 0,2	
h	Preferred thickness	4,0 ± 0,2	
L_0	Gauge length	50,0 ± 0,5	
L	Initial distance between grips	115 ± 1	$l_2{}_0^{+5}$

Figure 2.38 Dimension of dumbell specimen for the unaxial tensile tests (ISO 527)

The yielding is a phenomenon that occurs at relatively high deformations, and is characterized by a non-elastic, non-homogeneous and irreversibile deformation of the material. The yielding point is localized in a specific point of the sample. As reported in Figure 2.39, two possible configurations are possible for polymeric materials when the yielding occurs. In the first case the yielding is followed by a strain softening mechanism, due to a local increase of the temperature. In the second case a strain hardening mechanism, associated to the polymeric chain orientation, is represented.

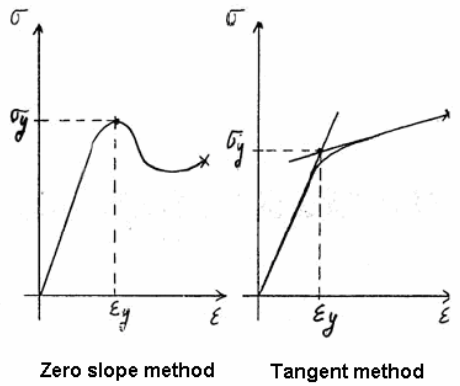

Figure 2.39 Possible configurations for the yielding of a polymeric material

In polymers two different yielding mechanisms can be active : shear yielding or crazing (Figure 2.40). In the case of shear yielding, the relative flow of polymeric chains occurs, with no loss of molecular cohesion or volumetric changes. The yielded zone can propagate at about 45° with respect to the stress direction. In the case of crazing, microcavitation associated to orientation of polymeric chains occurs. Even in this case there is no loss of molecular cohesion, but a strong decrease of density can be easily detected.

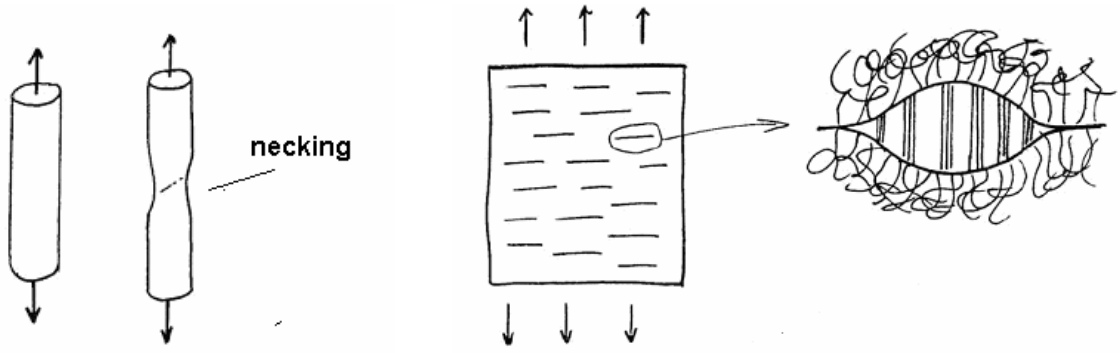

Figure 2.40 Yielding mechanisms of a polymeric material. (a) shear yielding, (b) crazing

The yielding process can be influenced by many variables, such as temperature, strain rate, and many structural (additives, molecular weight, cristallinity) and environmental factors (solvent and aggressive chemical agents).

2.4.2 Tensile impact test

It is often necessary the evaluation of the fracture behaviour of the material at high strain rate levels, not achievable with traditional tensile testing machines, by which a maximum strain rate of 1 m/min can be imposed. In this case tensile impact tests can be successfully employed. These tests are all characterized by the falling of a striker. There are different configurations (Figure 2.41): Charpy impact tests, Izod impact tests, falling weight normal impact and tensile impact tests.

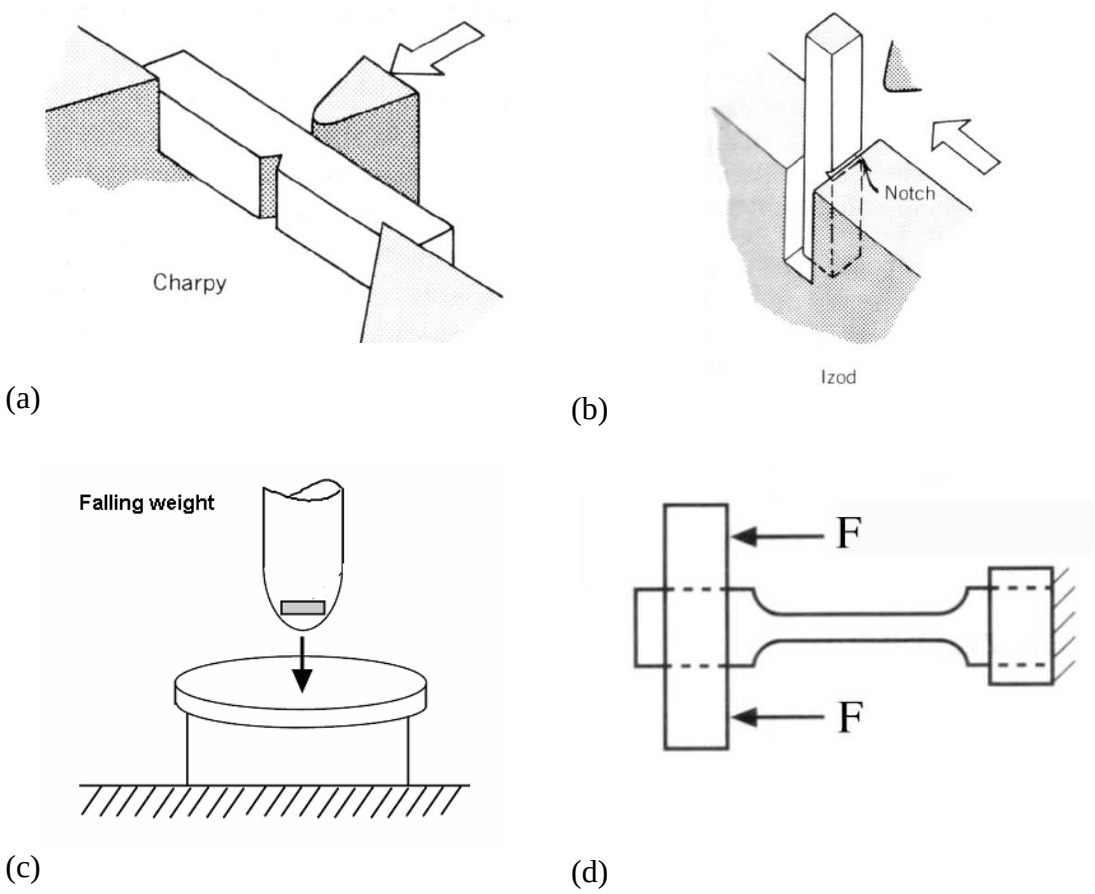

Figure 2.41 Configuration of impact tests. (a) Charpy, (b) Izod, (c) Falling Weight, (d) Tensile Impact tests

In tensile impact tests the impact energy due to a pendulum falling mass can be used to conduct an high speed uniaxial tensile test. These tests can be generally adopted only with plastic materials, following ISO 8256 (1990) standard. While for non-instrumented tensile impact tests it is possible only to measure the total energy adsorbed a break (ΔU) by the sample, with instrumented tests also stress and strain values during all the test can be measured. The force measurement is possible through piezoelectric load cells connected to the sample grips. In this way force-displacement curves can be easily elaborated.

2.4.3 Essential Work of Fracture (EWF) analysis

The essential work of fracture (EWF) method is an appropriate approach to experimentally characterize the ductile fracture of polymers and composites [7, 120-128]. According to Broberg [123] and Cotterel [124], the total work of fracture W_f can be divided into two parts: the essential work of fracture W_e, that is the work dissipated in the process zone close to the crack tip, and the non-essential work of fracture W_p, that is the work responsible for the plastic deformation outside the fracture-process zone. The total work of fracture may therefore be written as:

Equation 2.56

$$W_f = W_e + W_p$$

The principle of the technique is to measure the load-displacement trace and hence the energy to fracture for a series of notched specimens, reported in Figure 2.42, ensuring that plasticity in the ligament (L) (fracture region) is fully developed. Under plane stress conditions, the total work of fracture can be divided into a part required to create the new fracture surfaces and another part dissipated in plastic phenomena in a volume of material surrounding the crack. The former element is proportional to the fracture area and hence the ligament length, while the latter element is proportional to the volume of the outer region.

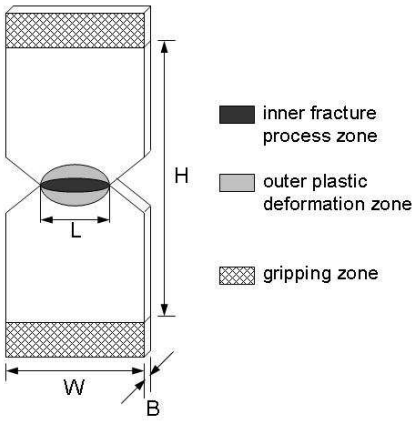

Figure 2.42. DENT specimen geometry: in evidence the crack tip deformation zones

For both metals and plastics, it has been observed that the volume of the outer region is proportional to the square of the ligament length. Thus the specific total work of fracture w_f may be written as:

Equation 2.57

$$w_f = \frac{W_f}{LB} = w_e + \beta w_p L$$

where B is the specimen thickness, β is a shape factor taking into account the shape of the outer plastic zone, which depends upon the geometry of the specimen and the crack, and w_e and w_p are the specific essential and non-essential work of fracture, respectively. The parameter w_e is regarded as a material property quantifying the fracture toughness. The parameters w_e and w_p can be evaluated by testing a series of specimens differing in ligament length, and by linearly interpolating a number of experimental data of w_f plotted against the ligament length L.

Notched specimens such as the double edge notched tension (DENT) is commonly used for this purpose. A rectangular specimen of width W and length H is cut from the test material. In order to prevent the plastic zone being disturbed by edge effects and to ensure complete yielding of the ligament region before the crack starts to propagate, the maximum ligament length L used should be less than one third of the specimen width W or less than the plastic zone size, whichever is the lower [128]. On the other hand, the length H includes the gauge length h and the amount of material used in gripping the specimen. However, the choice of h is normally not critical. Moreover the ligament length L must be greater than three to five times the specimen thickness B to generate a state of pure plane-stress [127]. Furthermore, for each specimen, two sharp edge notches, directly opposite one another, should be made. Several commonly used techniques are razor pushing, razor

sliding and razor tapping. The fracture tests are conducted in tensile mode on DENT specimens that have the ligament lengths spanning the range of all allowable ligament lengths (as explained above). In particular a minimum of 25 specimens is typically suggested [120].

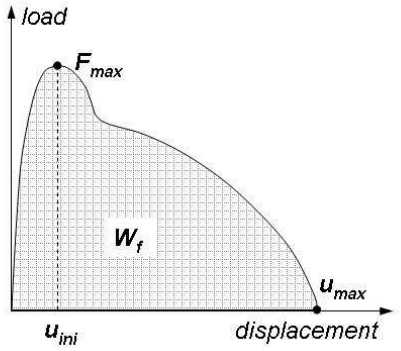

Figure 2.43. A typical load-displacement curve for DENT specimens.

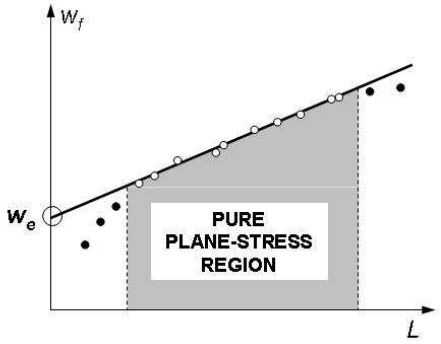

Figure 2.44. Schematic diagram of specific total work of fracture against ligament length.

In addition, by plotting the maximal net-section stress σ_{max}, defined as the ratio between the maximum load and the net-section LB, versus the ligament length for each group of specimens, the data obtained can be checked with Hill's criterion to verify that the tests were performed under plane-stress conditions [125]. If the stress criterion is satisfied, the net-section stress is about $1.15\sigma_y$. A useful check on the validity of the data is provided by the maximum stress on the ligament which can be compared to the tensile yield stress σ_y, as reported in a paper of Williams and Rink about the standardization of the EWF test [129]. The results are assumed to be valid if the maximum stress is within the range of 0.9–1.1 σ_{max} (mean), as reported in Figure 2.45.

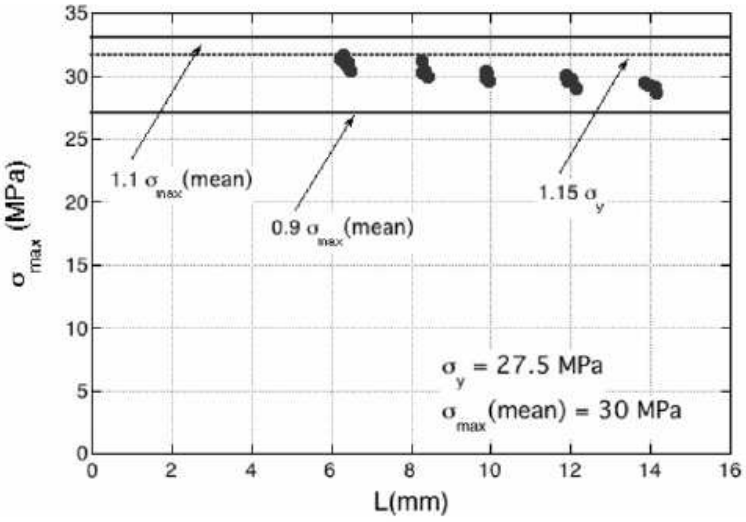

Figure 2.45 Application of the stress criterion in a EWF test

The w_f versus L data are then subjected to a linear regression analysis, and the quality of the data is usually assessed in terms of the standard deviation (S) of the linear fit. In general a value of S < $0.1w_e$ is expected. Any data point which lies outside the range of ± 2S is excluded and the line recalculated. Again this can pick up measurement errors. At this point the correlation coefficient R^2 is computed to assess the quality of the linear fit and values of $R^2 > 0.98$ are expected. These exclusion criteria are useful in detecting random errors such as a misreading of a data point. A systematic error which occurs in all points is more difficult to detect since consistent, but erroneous results are obtained. In order to investigate the energy contribution to different fracture stages, a partition between the specific work of fracture for yielding and for necking and subsequent fracture can be introduced by considering the peak of the load–displacement curves as the cut-off point [121, 122, 126]. As the composed terms are under plane stress, it can be concluded that :

Equation 2.58

$$w_f = w_y + w_n$$

Equation 2.59

$$w_n = w_{n,e} + \beta'' w_{n,p} L$$

where w_y and $w_{n,e}$ are the yielding and the necking and subsequent fracture related components of the specific essential work of fracture, respectively, $\beta'' w_{n,e}$ is the fracture component of the specific non-essential work of fracture.

3 Experimental

3.1 Materials

3.1.1 LLDPE

Polyethylene (PE) is the most widely used commercially available thermoplastic, because of its combination of low cost, high chemical resistance and relatively good mechanical properties. For example in 1992 in the United States 11 million tonnes (one third of the whole USA plastic materials production) of PE were produced.

As reported in Figure 3.1, polyethylene macromolecules are formed by a long chain of carbon atoms linked together by covalent bonds. Every C atom is also linked to a couple of hydrogen atoms [130]. From a chemical point of view polyethylene can be identified with the formula $C_{2n}H_{4n+2}$, where n is the polymerization degree [131]. Typically n is higher than 100 and can reach values as high as 250000, consequently the molecular weight stays between 1400 and 3500000 [132].

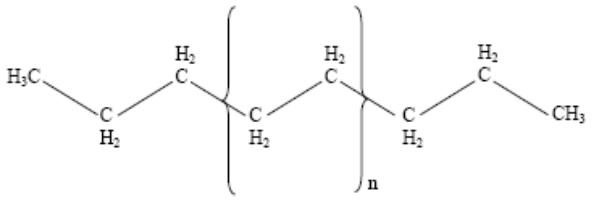

Figure 3.1 Chemical formula of Polyethylene (PE)

There are several types of polyethylene, depending of the molecular weight and the ramification degree. High density polyethylene (HDPE) is a low ramificated PE, and is synthesized through coordination polymerization with a Ziegler-Natta catalysis. In this way an high polymerization degree and a relatively elevated density (0.94-0.97 g/cm^3) can be easily reached.

Low density polyethylene (LDPE), synthesized through a radical process, has an higher ramification degree, consequently a lower crystallization degree and a relatively low density (0.9-0.94 g/cm^3) can be obtained. For these reasons LDPE is more ductile than HDPE.

Linear low density polyethylene (LLDPE), the polymeric matrix used in this work, combines the properties of HDPE and LDPE. It can be obtained through a copolymerization of a mixture of ethylene and α-olefins (buthene, exene, octene) with a Ziegler-Natta or metallocene catalysis. The ramifications are generally ethylic and buthylic groups. The presence of ramificated structure does not allow LLDPE to reach high crystallization degree and high densities (0.9-0.94 g/cm^3). Figure 3.2 reports the chemical structure of the different PE typologies.

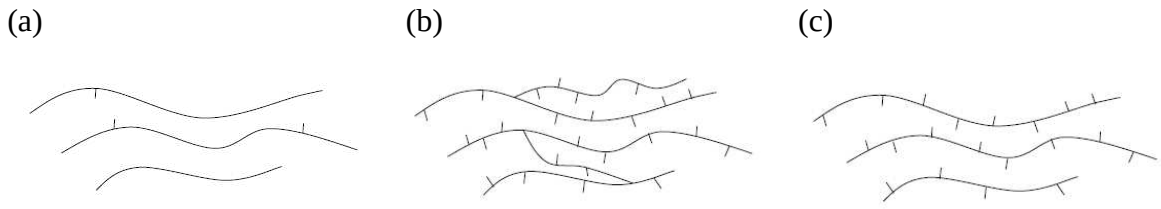

Figure 3.2 Chemical structures of different typologies of PE

One of the main features of LLDPE is its high ductility and wear resistance, if extruded in thin films. For this reason it is extensively used for high quality packages. LLDPE is also used for the production of insulating rods, flexible pipes and several medical devices, by using traditional transformation technologies (extrusion, injection moulding). The organic matrix used in this work was Flexirene® CL10, a linear low density polyethylene, kindly supplied by Polimeri Europa (Mantova, Italy). From a chemical point of view Flexirene® CL10 is a butene copolymer linear low density polyethylene (C_4-LLDPE), additivated with antioxidants, suitable for cast extrusion of thin film with high optical properties. It is recommended for the production of stretch film to be used both in manual and in automatic wrapping machines. In a multilayer film, Flexirene® CL10 enhances the optical properties of the global formulation; moreover, for its high processability, the resin is recommended whenever high productivity has to be reached. Table 3.1 summarizes the main features of this matrix [133].

Properties	Test Method	Typical value
MFI (190 °C, 2.16 kg) (g/10')	ISO 1133	2.6
Mean numeric molecular weight (M_n)	-	27000
Mean ponderal molecular weight (M_w)	-	95000
Density (g/cm^3)	ISO 1183	0.918
Melting Point (°C)	PE method	121
Vicat Softening Point (1 kg) (°C)	ISO 306/A	97
Tensile stress at yield (MPa)	ISO 527-3	9
Tensile stress at break (MPa)	ISO 527-3	35
Secant Modulus 1% (MPa)	ISO 527-3	90
Tear Resistance (N/mm)	ISO 6383-2	38
Coefficient of Friction	ISO 8295	> 0.5
Haze (%)	ISO 14782	2

Table 3.1 Technical datasheet of Polimeri Europa Flexirene® CL10

3.1.2 Fumed Silica Nanoparticles

Fumed silica nanoparticles were used in this work for the preparation of nanocomposites. The description of the chemical nature and of the microstructure of fumed silica nanoparticles is reported in Chapter 2.1.3. A series of Aerosil® commercial fumed silica were kindly supplied by Degussa. These nanoparticles are different for the surface area, i.e. 90 m^2/g for Aerosil 90, 200 m^2/g for Aerosil 200, 300 m^2/g for Aerosil 300, 380 m^2/g for Aerosil 380, and for the surface treatment. In fact Aerosil r816 is obtained by functionalizing Aerosil 200 with hexadecylsilane. The main features of the fumed silica used in this work are reported in Table 3.2.

Property	Aerosil 90	Aerosil 200	Aerosil 300	Aerosil 380	Aerosil r816
BET surface area (m^2/g)	90 ± 15	200 ± 25	300 ± 15	380 ± 30	190 ± 20
Primary particle diameter (nm)	20	12	7	7	12
Tapped density (g/l) DIN EN ISO 787	80	50	50	50	60
Moisture content (wt%) (2h 105 °C)	≤ 1	≤ 1	≤ 1.5	≤ 2.5	-
SiO_2 content (wt%)	≥ 99.8	≥ 99.8	≥ 99.8	≥ 99.8	≥ 99.8

Table 3.2 Technical datasheet of Degussa Aerosil® fumed silica nanoparticles

Aerosil® hydrophilic fumed silica nanopaticles are specifically used in paints and coatings and as filler in liquid silicone rubber (LSR). They are also added in cable resin compounds and unsaturated polyester resins, in adhesives, sealants and printing inks. They are used for rheology and thixotropy control of liquids, binders, polymers, providing an excellent transparency in unsaturated polyester resins. Aerosil® hydrophobic fumed silica nanoparticles (as Aerosil r816) are used in silicone rubber adhesives and sealants, defoamers, and toners. They provide a low thickening effect and excellent processability, enabling high loading levels of polymer systems. By the addition of these nanoparticles an excellent reinforcing properties in silicone rubber applications at high filler loading levels can be obtained [134]. They are also well suited for transparent systems. Figure 3.3 reports a representative TEM image of fumed silica filler having a surface area of 380 m^2/g, in which it is easy to distinguish primary nanoparticles, aggregates and agglomerates.

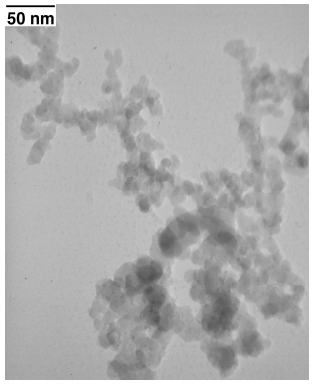

Figure 3.3 TEM image of Aerosil 380 fumed silica nanoparticles

3.1.3 Precipitated Silica Microparticles

In order to analyze the role of the surface area and of the dimensions of the nanofiller on the mechanical properties of LLDPE composites, precipitated silica microparticles were considered. Precipitated silica consists of a three-dimensional network of coagulated primary silica particles. The latter grow to sizes higher than 10 nm before they coagulate to form the aggregated clusters in the micrometric range of size [135, 136]. By simple milling operations aggregates can then be reduced to dimensions of few microns, as represented in Figure 3.4.

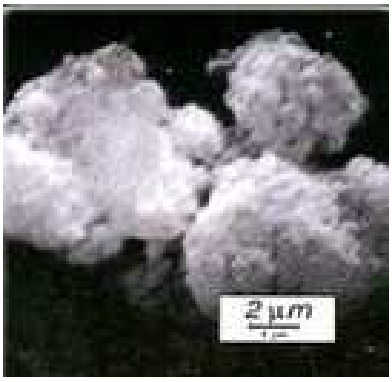

Figure 3.4 Typical morphology of precipitated silica microparticles

From a chemical point of view, precipitated silicas are synthesized by acidifying sodium silicate. In nearly all commercial processes, sulfuric acid is used as the acid source. Under standard conditions, the sodium silicate solution and the acid are fed simultaneously in a stirred vessel containing water. Precipitation is carried out under alkaline conditions. The choice of agitation, duration of precipitation, addition rate of reactants, temperature and concentration, and pH can influence the properties of the silica. The formation of a gel stage is avoided by stirring at elevated temperatures. In the next stage, the precipitated silica slurry is washed to remove soluble salts. The washing conditions, although important, have a negligible effect on the properties of the final product. Different filter types such as filter presses, rotary, or belt filters can be used. The resultant filter cake with typical solid content between 15-25% is then dried. The most common drying techniques are spray drying and rotary drying, which give rise to different particle shapes, degrees of agglomeration and porosity. The dried silica may be subjected to milling and classifying steps to obtain a specific particle size distribution. The precipitated silicas differ from silica gels on the basis of pore structure. Precipitates typically have a broad meso/macroporous structure reflected in the

pore size distribution, whereas gels generally have a more narrow microporous or mesoporous structure. Precipitated silicas are synthetic amorphous silica products. In contrast to naturally occurring silicas, the synthetic origin of these materials eliminates the risk of contamination with crystalline quartz particles as it may occur in mined products. Amorphous silica, in contrast to crystalline silica such as cristobalite or quartz, does not present a potential health hazard to workers with respect to irreversible lung injuries such as lung tumors or silicosis.

In this work Sipernat® 160 precipitated silica microparticles, supplied by Degussa, were used as filler. Despite their micrometric dimensions, these microparticles possess elevated surface area values, because of their high surface porosity. This filler finds applications in tire and rubber goods, in order to improve mechanical performance of some polymers (for example in organic rubbers for footwear and for elastomeric membranes). It is also used in industrial specialties, in nutritions and in dentifrices [134]. The datasheet of these microparticles is reported in Table 3.3.

Property	**Value**
Specific surface area (N_2) ISO 5794-1	165 m^2/g
Mean particle size ASTM C690	7 µm
Tapped density ISO 787-1	65 g/l
SiO_2 content (wt%) ISO 3262-19	99.4

Table 3.3 Technical datasheet of Degussa Sipernat 160 precipitated silica microparticles

3.1.4 Glass Microspheres

Glass microspheres are commonly used as filler for organic compound [137]. In this work glass microparticles were used as comparison, in order to put in evidence the difference in the tensile mechanical response between nanocomposites and traditional microcomposites. In general glass microspheres present high wear and impact resistance, and no health hazards, because of their amorphous structure. The absence of any surface porosity results in a very low surface area. The typical morphology of silica glass microspheres is reported in Figure 3.5.

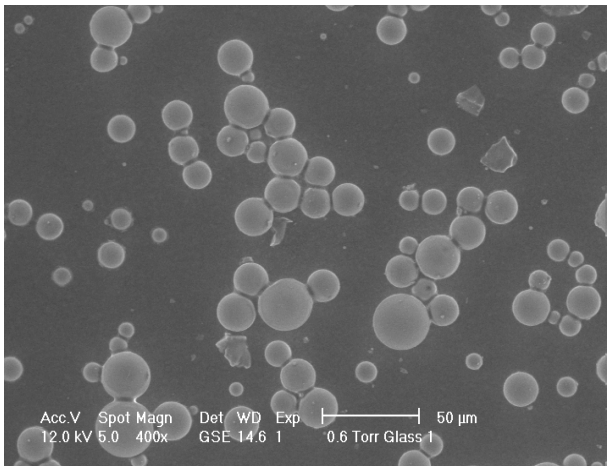

Figure 3.5 A representative ESEM image of silica glass microspheres

In this research, Cores® silica glass microspheres were used. These microparticles have a mean particle size of 50 µm, with a resulting surface area of less than $1 m^2/g$. The microparticles were then sieved in a 32 µm sieve, in order to obtain glass microparticles with a mean diameter of 18 ± 3 µm. This type of glass microspheres are generally used in surface finishing operations of metallic manufacts. Glass microspheres can also reduce the post moulding shrinkage of polymeric composites, improving their final tensile properties. Table 3.4 reports the chemical composition of Cores® glass microspheres.

Oxides	Chemical composition (wt%)
SiO_2	72.0-73.0
Na_2O	13.3-14.3
K_2O	0.2-0.6
CaO	7.2-9.2
MgO	3.5-4
Fe_2O_3	0.08-0.11
Al_2O_3	0.8-2
SO_3	0.2-0.3

Table 3.4 Chemical composition of Cores® silica glass microparticles

Table 3.5 summarizes the principal properties of the silica fillers used in this work.

	Aerosil 90	Aerosil 200	Aerosil r816	Aerosil 300	Aerosil 380	Sipernat 160	Glass microspheres
BET surface area (m^2/g)	90 ± 15	200 ± 25	190 ± 20	300 ± 15	380 ± 30	≈ 165	≈ 0.5
Mean particles diameter	20 nm	12 nm	12 nm	7 nm	7 nm	9 μm	18 μm
SiO_2 content (wt%)	≥ 99.8	≥ 99.8	≥ 99.8	≥ 99.8	≥ 99.8	99.4	72.0 - 73.0

Table 3.5 Summary of the properties of silica fillers used in this work

3.2 Composite preparation

For all the samples a melt compounding process followed by an hot pressing was adopted in order to prepare the sample. Polyethylene chips and all the filler typologies were utilized as received. The filler was melt compounded with LLDPE in a Thermo Haake® internal mixer, at 170 °C for 15 min and 90 rpm. In the case of fumed silica nanocomposites, the nanoparticles were added slowly in the hot chamber of the mixer, immediately after the complete melting of the LLDPE, in order to prevent nanoparticles agglomeration. The materials were then hot pressed in a Carver® press at 170 °C for 15 minutes at low pressure (0.2 kPa), in order to produce square sheets of about 0.8 mm of thickness. The internal mixer and the hot plate press are represented in Figure 3.6.

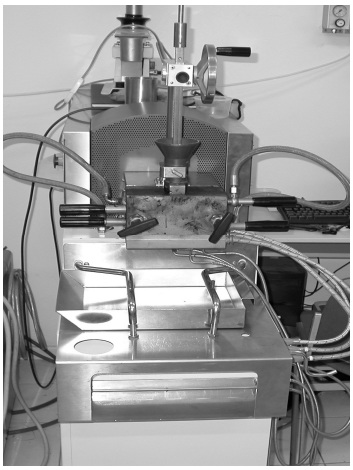

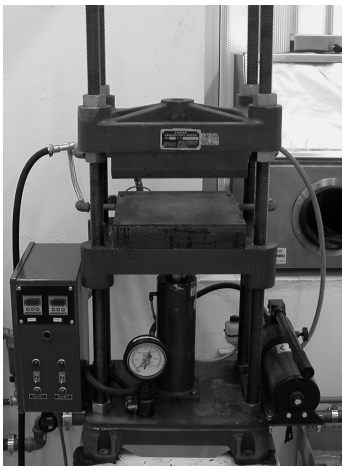

(a) (b)

Figure 3.6 Photographs of (a) Haake® internal mixer and (b) Carver® hot press

In this way LLDPE composites with Aerosil® fumed silica nanoparticles, Sipernat® precipitated silica microparticles and Cores® glass microspheres were prepared. The filler volume loading was varied between 1% and 4%. The filler volume percentage was determined by the weight fraction through Equation 3.1, considering the absence of voids in the composite :

Equation 3.1

$$V_p = \frac{W_p \frac{\rho_m}{\rho_p}}{W_m + W_p \frac{\rho_m}{\rho_p}}$$

where V_p is the filler volume fraction, W_m and W_p are respectively the matrix an the filler weight fraction, ρ_m and ρ_p represent the densities of the matrix and of the filler.

In all the figures and the discussion session, the fumed silica nanopowders were designated with the letter A followed by the indication of the surface area (for example A90 indicates Aerosil 90 nanoparticles). Precipitated silica microparticles were denoted as S160, while glass microspheres were simply designated as Glass. LLDPE indicates the unfilled material, while the composites were denoted with the name of the matrix (LLDPE), followed by the name of the filler and the filler volume content (vol%). For example LLDPE-A200-2 indicates 2 vol% Aerosil 200 fumed silica nanocomposite sample, while LLDPE-S160-4 is referred to 4 vol% Sipernat 160 microcomposite.

During the melt compounding process it was possible to monitoring the process parameters, i.e. melt temperature, rotor speed, torque. As represented in Figure 3.7, after the introduction of the chips in the mixer chamber, the torque increased till the beginning of the melting. Only when the material was completely molten the torque reached a plateau.

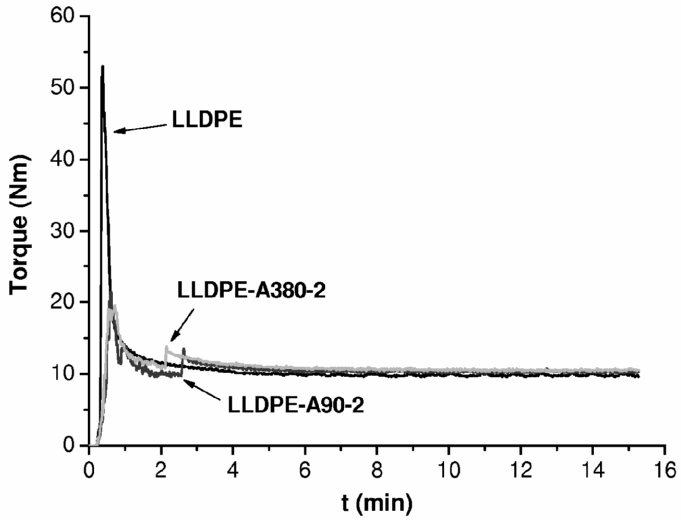

Figure 3.7 Torque values during the melt compounding process for pure LLDPE and relative composites

No thermo-oxidative degradation phenomena could be evidenced by the analysis of the torque. In the case of filled sample, the maximum torque value was lower with respect to the unfilled sample, because a lower LLPDE quantity was introduced. The introduction of the filler caused a little instantaneous increase of the torque, but the plateau value of the torque for the filled sample was practically the same of that of the pure LLDPE.

3.3 Experimental activities

3.3.1 Microstructural characterization

3.3.1.1 Density measurements

Density measurements were performed by using a Micromeritics® Accupyc 1330 helium picnometer, at a temperature of 23 °C, both on the nanofillers and to the microparticles. A testing

chamber of 3.5 cm^3 was utilized for all the samples. In the case of fumed silica nanoparticles, in order to obtain a reproducible evaluation of powders densities, 300 measurements were conducted on every sample, and the mean of the last 80 measures was considered as the plateau density of the silicas. In this way possible overestimations of the real density due to the helium absorption on the surface of the nanofiller during the first 200 measures were avoided. In the case of precipitated silica microparticles and glass beads 100 measurements were sufficient to obtain a plateau value of the density.

In the case of pure LLDPE and 2 vol% filled fumed silica nanocomposites, density measurements were conducted in order to detect the presence of any microvoid in the material. In this case 100 measures were sufficient in order to obtain a constant value of the density of the material, taking the mean of the last 30 measures as the real value of the density. The results were then compared with the theoretical prediction of the density of composites, based on the rule of mixture, as reported in Equation 3.2:

Equation 3.2

$$\rho_c = \rho_m V_m + \rho_p V_p$$

where ρ_c, ρ_m, ρ_p are the densities of the composites, of the pure matrix and of the nanoparticles respectively, while V_m and V_p are the volume fraction of the matrix and of the nanofiller.

3.3.1.2 Evaluation of fillers surface properties

In order to evaluate the influence of the surface morphology of the filler on the mechanical tensile response of LLDPE composites, BET surface area and porosity measurements were conducted both on fumed silica nanoparticles and microparticles. An ASAP® 2010 Accelerated Surface Area and Porosimetry machine, located by the Ceramurgy laboratory of the University of Trento, was utilized. Surface properties were evaluated referring to the nitrogen gas physisorption process, setting a saturation pressure of 738.57 mmHg and a bath temperature of 77.35 K. Adsorption/desorption curves reported the adsorbed nitrogen volume vs the relative pressure, and from the interpolation of the linear part of the adsorption curve the BET (Brunauer, Emmett, Teller) surface area was calculated [138], as reported in Equation 3.3 and in Equation 3.4.

Equation 3.3

$$\frac{P}{V_a(P_0 - P)} = \frac{1}{V_m C} + \frac{C.-1}{V_m C}\left(\frac{P}{P_0}\right)$$

Equation 3.4

$$s = \frac{V_m \sigma N_A}{m V_0}$$

Where P and P_0 are the applied and the saturation pressure respectively, V_a is the volume of the adsorbed gas at the pressure P, V_m is the adsorbed gas when the whole surface is covered with a mono-molecular layer, and C is a constant depending on the probing gas (98.0 for nitrogen). σ is the area of a single gas molecule, N_A is the Avogadro constant, m is the mass of the adsorbing sample and V_0 is the molar volume of the gas. Figure 3.8 reports BET transform plots with the regression lines.

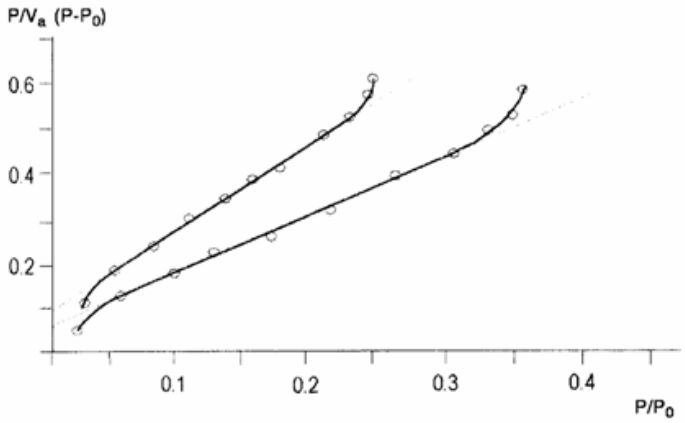

Figure 3.8 BET transform plots, each with a regression curve through the linear region

From the comparison of the absorption and desorption curves is was also possible to analyse the possibility oh having an internal porosity in the sample, while following BJH (Barrett-Joiner-Holenda) [139] method it was possible to determine the pore size distribution and the surface area contribution associated to pores of different dimensions. According to this theory the pores dimension is related to the relative pressure, and in the case of N_2 at 77 K Equation 3.5 and Equation 3.6 are valid during the absorption and desorption process respectively.

Equation 3.5

$$t = \left(\frac{13.99}{(0.034 - \log\left(\frac{P}{P_0}\right)} \right) 0.05$$

Equation 3.6

$$t = 3.54 \left(\frac{-0.5}{\ln\left(\frac{P}{P_0}\right)} \right) 0.333$$

where t is the pore thickness, expressed in nm.

3.3.1.3 Microscopy techniques

Enviromental Scanning Electron Microscopy (ESEM) and Transmission Electron Microscopy (TEM) technique were adopted in order to evaluate the dimensions and the morphology of the fillers and their dispersion degree in the composites.

TEM images were made in order to evaluate the morphological features of fumed silica nanoparticles. In particular they were observed through a Philips® EM 400 T transmission electron microscope. The sample for the observation were prepared dispersing fumed silica powders in acetone, then the solution was ultrasonicated for 3 minutes, in order to break the agglomerates. A little drop of solution was posed on a supporting grid, and the observation was conducted after the complete evaporation of the solvent.

TEM images were also made on fumed silica and precipitated silica composites, in order to evaluate the dispersion state of the aggregates in the matrix and their orientation when a strain was applied. In particular LLDPE-A380-2 and LLDPE-S160-2 samples at different deformation levels (0, 30, 60, 100 %) were observed. A Philips®/FEI CM120 transmission electronic microscope, was utilized, at an acceleration voltage of 80 kV. Thin section of LLDPE and LLDPE-A380-2 samples were ultramicrotomed at a temperature of -70 °C by using a Reichert-Jung® Ultracut FC4E crio-ultramicrotome.

Fumed silica, precipitated silica and silica glass powders were observed at different magnifications by using a Philips® XL30 Enviromental Scanning Electron Microscope, at an acceleration voltage between 15 and 30 kV. In this case the powders were dispersed in ethanol and a little drop of the solution was posed on metallic support. The solvent was removed through a constant air flow.
Fracture surfaces of LLDPE-A380-2, LLDPE-S160-2 and LLDPE-Glass-2 composites at different magnification were also observed with the same instrument. The samples for the observation were prepared immerging notched samples in liquid nitrogen for 30 minutes and breaking them with a impact tensile testing machine. In this case an acceleration voltage of 15 kV was set.

3.3.1.4 Differential Scanning Calorimetry (DSC)

Differential Scanning Calorimetry (DSC) was utilized in order to detect the influence of the fillers on the melting and crystallization behaviour of the resulting material. It was also used to assess the presence of crystallization phenomena in the yielded zone of fumed silica nanocomposites, when an uniaxial stress was applied to the material.
These tests were carried out on pure LLDPE and relative micro and nanocomposites at all the investigated compositions by using a Mettler® DSC30 differential scanning calorimeter. All measurements were performed under nitrogen flow of 100 ml/min. The samples were first heated at a rate of 10°C/min from 0 °C to 200 °C, and then cooled to room temperature at 10 °C/min. A second heating was performed at the same rate until 200 °C. The melting hentalpy (ΔH_m) was determined from the corresponding peak areas in the heating and cooling thermograms. The crystallinity content (X_c) of LLDPE in the composites was calculated as reported in Equation 3.7 :

Equation 3.7

$$X_c = \frac{\Delta H}{(\Delta H_0)(W(LLDPE))}$$

where ΔH is the apparent enthalpy of fusion per gram of composite, ΔH_0 is the heat of fusion of 100% crystallinity polyethylene, taken as 290 J/g [130], and W(LLDPE) is the weight fraction of LLDPE in the composites. In order to verify the possibility of strain induced crystallization phaenomena in nanocomposites, the same tests were then performed on the yielded zone of the dogbone samples of 2 vol% fumed silica filled samples that were previously utilized in quasi-static

uniaxial tensile tests, applying a strain rate of 50 mm/min until a deformation of the 100 % was reached. Even in this case the crystallinity, the melting and crystallization temperatures were evaluated.

3.3.1.5 X-Ray Diffraction (XRD) analysis

In order to evaluate the influence of the different typologies of filler on the crystalline structure of the material, X-Ray diffraction analysis was conducted on LLDPE composites filled with 2 vol% of A200, A380, S160 and Glass particles. A Rigaku® 3D Max X-Ray diffractometer was used, scanning the samples in a 2θ range between 1° and 67°, at a 2θ step of 0.1°. The wavelength of the X-Ray source was 0.154056 nm. In this way the diffractograms reporting the intensity of the diffracted radiation versus 2θ angular position was plotted.

From these diffractograms it was possible to determine the dimensional distribution of the crystalline domains, starting from the Fourier transform of the scattered intensity. Leaving the complete description of this method to more specific works in the field of the microstructural analysis, these operations were performed on the basis of a recent algorithm for Whole Powder Pattern Modelling (WPPM) [140-142]. This approach could be used for any crystal shape, but in this work we considered the case of polydisperse crystalline spherical grains, whose volume could be described by a single length parameter (e.g. sphere diameter or edge for cube, tetrahedron or octahedron). The dimensional distribution of the crystalline domains was analyzed through a lognormal size distribution, that frequently proved to be appropriate in practical cases, like highly dispersed ceramic powders produced by chemical methods (e.g. sol-gel), or in catalysts. Such a distribution was also observed in highly deformed metal grains [140]. A lognormal is described by two parameters, μ and σ, the lognormal mean and variance, respectively, as reported in Equation 3.8:

Equation 3.8

$$g(D) = \frac{1}{D\sigma(2\pi)^{1/2}} e^{\frac{-(\ln D-\mu)^2}{2\sigma^2}}$$

Consequently, mean size of the crystalline domains M(D) and variance V(D) were evaluated, according to the expressions reported in Equation 3.9 and in Equation 3.10 :

Equation 3.9

$$M(D) = \exp\left(\mu + \frac{1}{2}\sigma^2\right)$$

Equation 3.10

$$V(D) = \exp(2\mu + \sigma^2)[\exp(\sigma^2) - 1]$$

It is important to underline that the approach proposed in this work could be developed for any other distribution function (for example the Poisson distribution could be alternatively considered).

3.3.1.6 Infrared (IR) spectroscopy

Infrared spectroscopies (IR) were conducted in order to assess the presence of the different functional groups in the materials. These tests were conducted by using a Perkin Elmer® Spectrum One FT-IR-ATR analyser in a scanning interval between 650 and 4000 cm^{-1}. Pure LLDPE and A380 filled nanocomposite samples were tested, by using small square samples 0.7 mm thick, previously washed in acetone and accurately dried with a nitrogen flow.

3.3.2 Viscoelastic behaviour in the molten state

Dynamic rheological tests were conducted in order to evaluate the influence of the filler morphology and content on the final properties of the material in the molten state. For this reason a TA® Ares Rheometer was used in dynamic mode and in parallel plate configuration, at a melt temperature of 190 °C. A plates diameter of 25 mm at a distance of 0.8 mm was chosen for these tests. A maximum strain (γ_0) of 1% was imposed to the material, while the frequency range adopted was between 0.05 and 200 rad/s. Pure LLDPE and all the prepared composites at the different compositions were testes in this configuration.
For pure LLDPE and relative micro and nanocomposites filled with 2 vol% A380, S160 and Glass rheological tests in the same configuration and at different temperatures were conducted, in order to

obtain G' and G'' master curves at the reference temperature (T_0) of 170 °C, according to the time-frequency superposition principle (see Chapter 2.2.3). The temperature range was set between 125 °C and 210 °C. In this way the rheological behaviour of the tested material over a wider range of frequencies was evaluated.

3.3.3 Viscoelastic behaviour in the solid state

3.3.3.1 Elastic modulus evaluation

Uniaxial tensile tests were performed with an Instron® 4502 tensile machine. ISO 527 type 1BA samples were tested, at a crosshead speed of 0.25 mm/min. The strain was recorded by using a resistance extensometer Instron® model 2620-601 (gage length = 12.5 mm). The test were performed imposing a maximum axial deformation level of 1%. According to ISO 527 standard, the elastic modulus was evaluated as secant modulus between deformation levels of 0.05 % and 0.25 %.

3.3.3.2 Creep tests

Creep tests were performed in order to evaluate the deformational behaviour of the material under a constant load. For these tests an Instron® 4502 tensile testing machine was utilized. Pure LLDPE and 2 vol% micro and nanocomposites were tested at a temperature of 30 °C, imposing a constant stress (σ_0) of 1 MPa, corresponding to about 10% of the stress at yield. In order to avoid problems related to non-uniform gage length, rectangular samples 100 mm long, 5 mm wide and 0.8 mm thick were adopted, setting a gage length of 60 mm. The total duration of the test was 3600 s. In this way the creep compliance D(t), determined as the ratio between the deformation and the applied constant stress, was determined. In order to evaluate the effect of the filler content on the creep behaviour of the material, creep tests with the same configuration were also conducted on A200, A380, S160 and Glass filled composites by varying the filler loading.

Considering that fumed silica nanocomposites showed the best creep stability, isothermal creep tests at 30 °C were conducted on LLDPE, LLDPE-A200-2 and LLDPE-A380-2 nanocomposites, by varying the applied constant stress, ranging from 1 MPa to 5 MPa. In this case the total duration of the test was 1200 s. Isochronous curves were then constructed, considering the deformation of the

samples at different creep stresses at a time of 200 s and 1000 s. Starting from the same tests, the analysis of the non linear tensile behaviour of the samples considering the free volume evaluation approach was performed (see Chapter 2.3.1.4).

In order to evaluate the effect of the temperature on the deformational behaviour of the material, creep tests at different temperatures, ranging from 30 °C to 70 °C, were then conducted on LLDPE, LLDPE-A200-2 and LLDPE-A380-2 samples, at a constant stress of 1 MPa, in order to remain in the linear viscoelastic region of the material. The total duration of these tests was 1200 s. The creep behaviour of the samples was then interpreted by applying the Burgers model (see Chapter 2.3.1.2). By applying time-temperature superposition principle, master curves were then constructed setting a reference temperature (T_0) of 30 °C. In this way it was possible to evaluate the creep behaviour of the material at 30 °C over a wider time scale.

3.3.3.3 Dynamical mechanical thermal analysis

Dynamic mechanical thermal analyses were performed in order to evaluate the tensile behaviour of the prepared samples at different temperatures. For all the test a Polymer Laboratories® MKII testing machine was utilized. Rectangular specimens 15 mm long, 5 mm wide and 0.8 mm thick were tested.

Firstly LLDPE and 2 vol% fumed silica nanocomposites were analyzed, in a temperature range between -130 °C and 80 °C, at an heating rate of 3 °C/min and a frequency of 1 Hz. Imposing a preload of 0.2 MPa, a maximum strain corresponding to a peak to peak displacement of 32 µm was set to the material. In this way the most important viscoelastic functions (E', E'', tanδ) were registered at different temperatures.

In order to evaluate the viscoelastic behaviour of the material as a function of the frequency, multi-frequency DMTA test were conducted on LLDPE, LLDPE-A200-2 and LLDPE-A380-2 nanocomposite samples. Samples were tested from -60 °C to 50 °C at an heating rate of 0.5 °C/min and at the following frequencies : 0.3, 1, 3, 5, 10 and 30 Hz. Setting 30 °C as a reference temperature, E' and E'' master curves were constructed, according to frequency-temperature superposition principle. In this way the dynamic behaviour of the materials over a wide frequency range was determined.

Then LLDPE, precipitated silica and glass filled composites at different filler loading were also tested, in order to evaluate the effect of the filler morphology and content on the dynamic behaviour

of the material. Samples were analyzed in a temperature range between -130 °C and 80 °C at an heating rate of 3 °C/min and a frequency of 1 Hz. In this case a preload of 0.4 MPa and a peak to peak displacement of 32 µm were applied to the material.

3.3.4 Fracture behaviour

3.3.4.1 Quasi-static tensile tests

Quasi-static uniaxial tensile tests at break were performed with an Instron® 4502 tensile machine, setting a crosshead speed of 50 mm/min and without using the extensometer. ISO527 1BA dogbone specimens (gage length 30 mm, width 5 mm, distance between the grips 55 mm, thickness 0.8 mm) were tested. All the prepared composites at all the filler compositions were tested, in order to evaluate the role of the different micro and nanofillers on the most important tensile properties at yield and at break : stress at yield (σ_y), stress at break (σ_b) and strain at break (ε_b). In the case of fumed silica nanocomposites the adsorbed specific Tensile Energy to Break (TEB) was also evaluated, by simply integrating the stress-strain curves.

Considering that fumed silica filled samples showed a better tensile behaviour at break with respect to the unfilled material, the mechanism of the toughening effect associated to the presence of fumed silica nanoparticles was analyzed. In order to detect the presence of a possible filler-matrix debonding mechanism during the application of the load, dilatometric tests were carried out, by using rectangular specimens of LLDPE and LLDPE-A380-2, with a length of 100 mm, width of 10 mm, thickness of about 4 mm and gage length of 60 mm. The tests were carried out with an Instron® 4502 tensile testing machine, at a crosshead speed of 5 mm/min. At least three samples for each material were tested at room temperature. Elongation and specimen width were measured during deformation by using an Instron® 2620-613 bi-axial extensometer [143]. Considering that the two transversal strain components (ε_2) were equal, the volume strain was calculated as reported in Equation 3.11:

Equation 3.11

$$\frac{\Delta V}{V_0} = (1+\varepsilon_1)(1+\varepsilon_2)^2 - 1$$

where ΔV is the change in volume, V_0 the original volume, ε_1 the axial strain, and ε_2 the transversal strain. Volume strain was measured assuming that the changes in the thickness and width were the same, the specimen's cross section remained rectangular and the deformation was affine (non-necking in the measured zone). In our samples the deformation started to be not homogeneous throughout the specimen for the presence of a necked zone at about 30% elongation, but the tests were stopped at a strain level of 10%. No evidence of differential changes in width and thickness were noticed and the cross section remained rectangular shape during straining. In this way Poisson's ratio (ν) was calculated as the negative ratio between the longitudinal and the axial strain, as reported Equation 3.12 :

Equation 3.12

$$\nu = -\frac{\varepsilon_2}{\varepsilon_1}$$

3.3.4.2 Tensile impact tests

Because fumed silica nancocomposites showed a better fracture toughness with respect to the unfilled material, the impact behaviour of these samples was also evaluated. Tensile impact tests were carried out with a CEAST® tensile impact instrumented pendulum. The striker, with a mass of 3.65 kg and an initial angular position of 63°, had an impact speed of 2 m/s and a total impact energy of 7.3 J. In this way the specific tensile energy to break (TEB), obtained by simply integrating load-displacement curves, was obtained.

3.3.4.3 Essential Work of Fracture (EWF) analysis

In order to investigate the toughening mechanism associated to the presence of fumed silica nanoparticles in LLDPE, an elasto-plastic mechanics approach was adopted in order to evaluate the fracture toughness of the nanocomposites. There are different approaches suitable to study the non-linear fracture toughness of polymeric matrices. It can be determined by the J-integral method, which is an energy-based parameter to characterize the stress–strain field near a crack tip surrounded by small-scale yielding. The fracture toughness, J_IC represents the energy required to

initiate crack growth [144-147]. Being the J_IC determination of polymers quite difficult, especially for polymers having high plastic resources, the Essential Work of Fracture (EWF) concept was considered to evaluate the fracture toughness of polymers, under tensile conditions [129]. The complete explanation of this approach is reported in Chapter 2.4.3. In the present work DENT specimens (width 30 mm, height 30 mm, thickness 0.8 mm, distance between the grips 50 mm) were tested (see Figure 3.9).

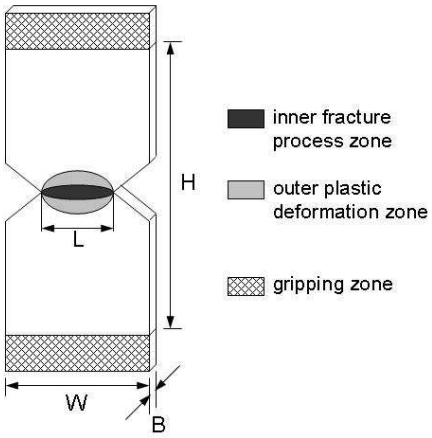

Figure 3.9 Typical configuration of DENT specimens for EWF tests

Four specimens for every ligament length (L) were considered, and five ligament length between 5 and 13 mm were tested at a crosshead speed of 10 mm/min. The notches were prepared by using a razor blade, in order to obtain a very sharp crack tip. The experimental apparatus for the preparation of the DENT specimens is represented in Figure 3.10. From SEM images it was possible to estimate an average crack tip radius of less than 2 µm (see Chapter 4.4.3).

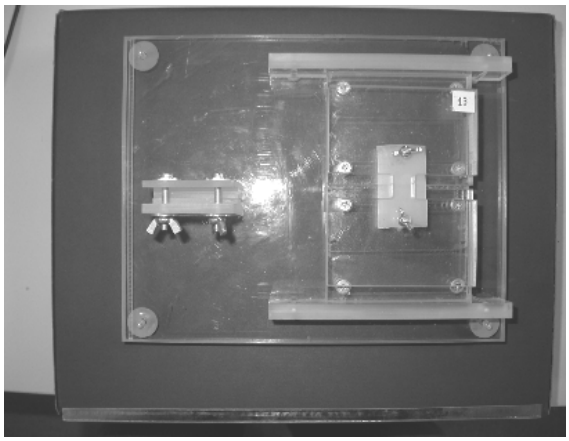

Figure 3.10 Experimental apparatus for the preparation of DENT specimens for EWF tests

The statistical analysis of the collected data was then conducted in accordance to the indications reported in the paper of Williams about the standardization of the EWF test, and is reported in Chapter 2.4.3. In this way the essential work of fracture (w_e) and the specific plastic work of dissipation (βw_p) for LLDPE and 2 vol% fumed silica nanocomposites was evaluated. The necking component of the essential work of fracture (we_{ini}) was also determined.

4 Results and discussion

4.1 Microstructural characterization

A microstructural characterization was conducted both on micro and nanofillers and respective micro-nanocomposites, in order to explore possible correlation between microstructure and properties of the prepared composites.

4.1.1 Microparticles and nanoparticles

4.1.1.1 TEM/ESEM observations

In Figure 4.1 TEM images of fumed silica nanoparticles at different surface area are reported, while in Figure 4.2 and in Figure 4.3 ESEM images of precipitated silica microparticles and glass spheres are respectively represented. It the case of fumed silica nanoparticles, it is evident the structure of the primary nanoparticles, with a diameter between 20 nm and 7-8 nm, according to the producer's data. It is also evident the correlation between primary nanoparticles size and surface area values. These nanoparticles are fused together to form aggregates, and some agglomerates can be easily detected.

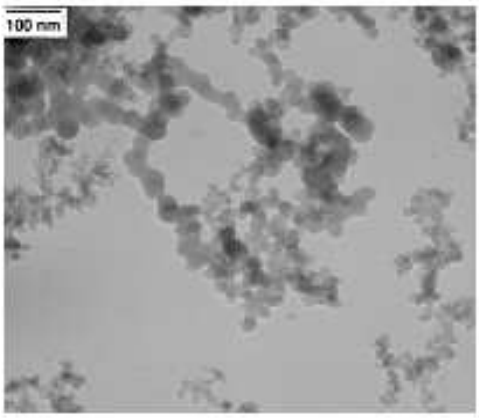

(a)

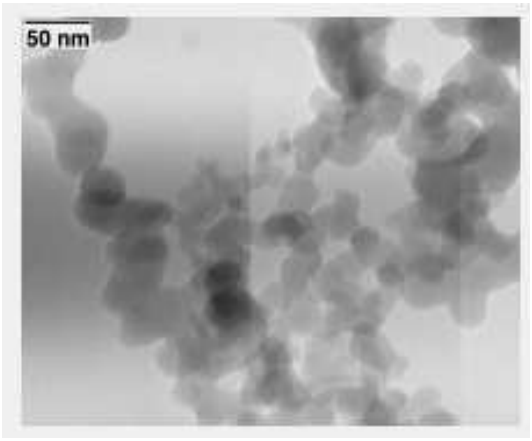

(b)

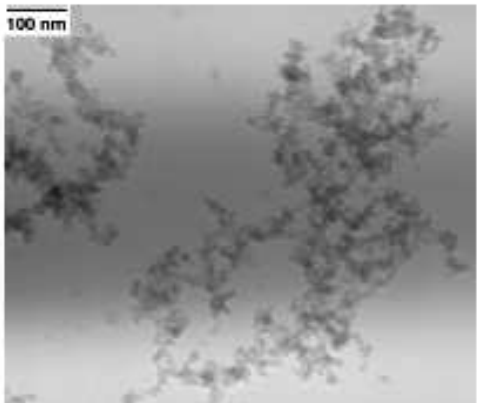

(c)

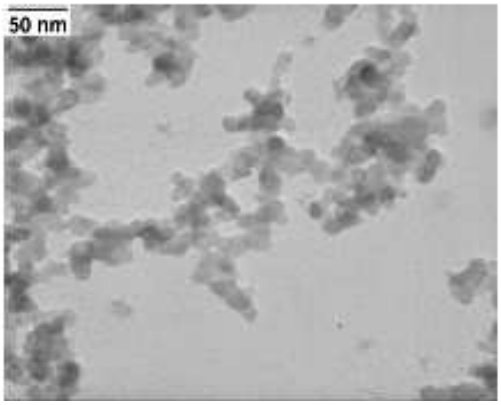

(d)

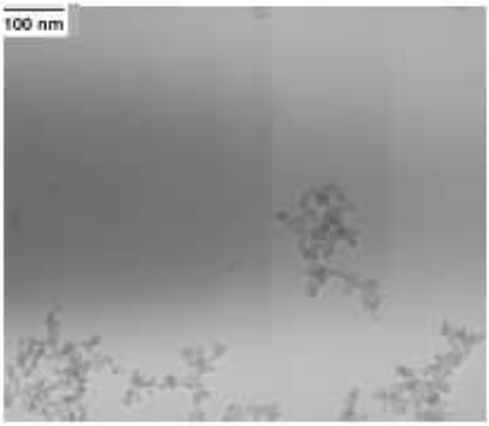

(e)

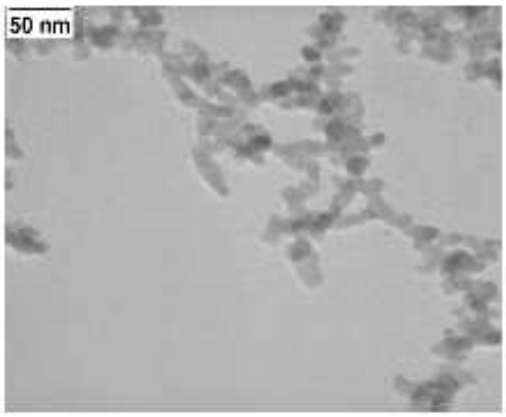

(f)

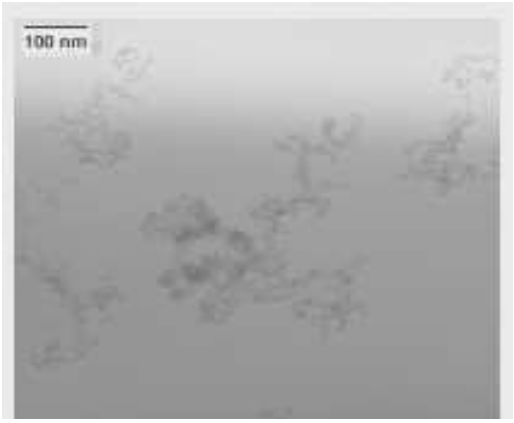

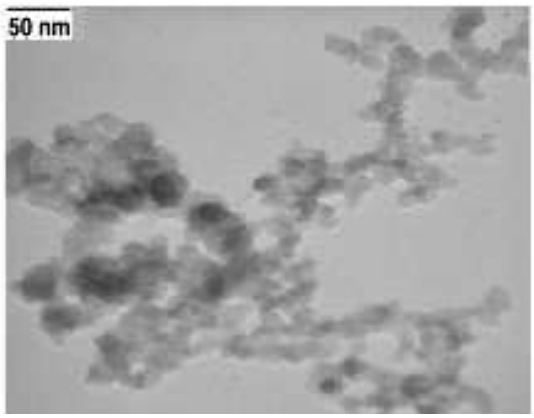

(g) (h)

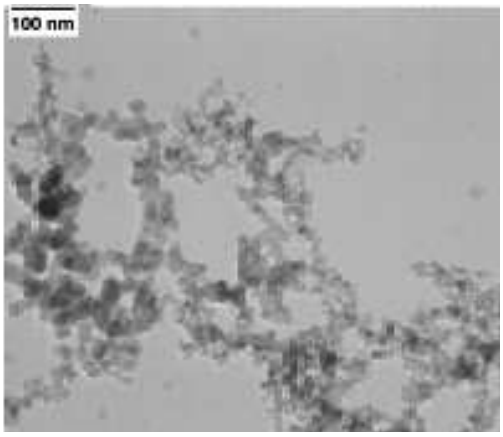

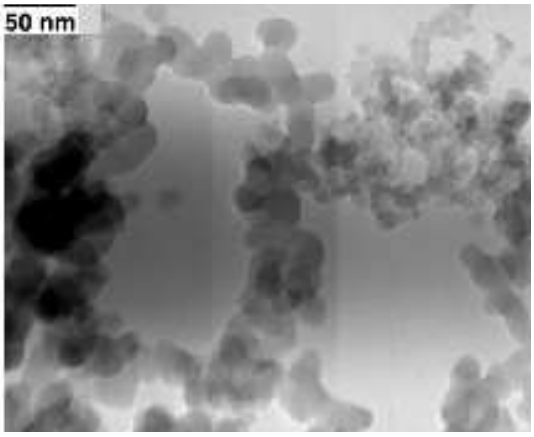

(i) (l)

Figure 4.1 TEM images of fumed silica nanoparticles at different magnifications. (a-b) A90, (c-d) A200, (e-f) A300, (g-h) A380, (i-l) Ar816

For as concern Sipernat® 160 microparticles, ESEM observations reported in Figure 4.2 evidence a structure characterized by spherical irregular nanoparticles, with a mean diameter of 9 ± 2 μm, according to the producer's datasheet. From high magnification photos it is also evident the presence of an elevated surface porosity, responsible of the high surface area value of this microfiller.

As reported in Figure 4.3, Glass microbeads are characterized by an almost spherical shape with mean diameter of 18 ± 3 μm. The surface is very smooth, thus justifying the low surface area value reported in the datasheet. Moreover some beads are physically fused together, forming microparticle agglomerates of 50-60 μm.

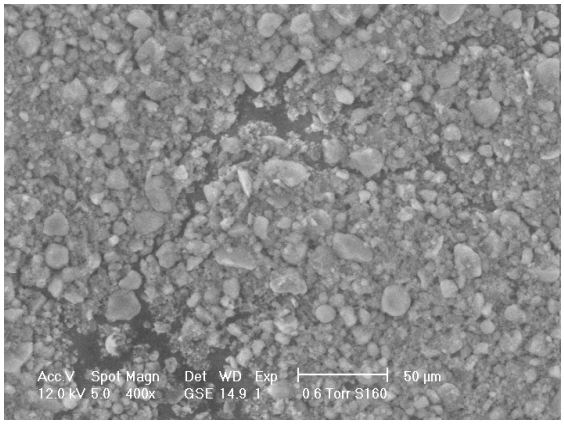

(a)

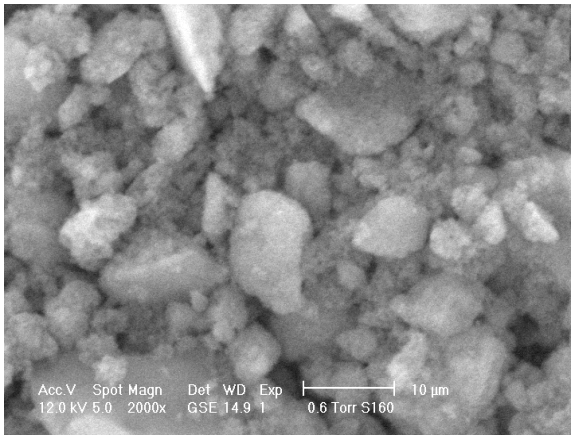

(b)

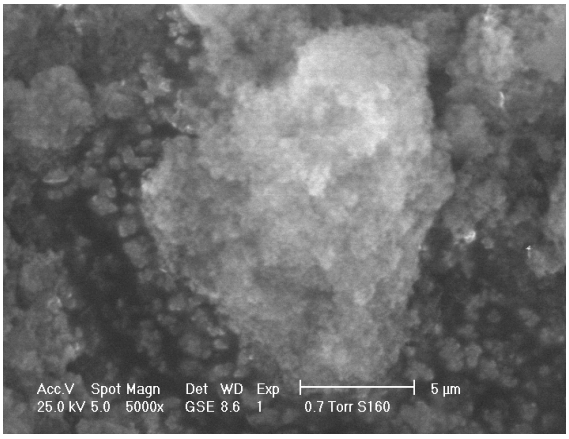

(c)

Figure 4.2 ESEM images of Sipernat® 160 microparticles at different magnifications

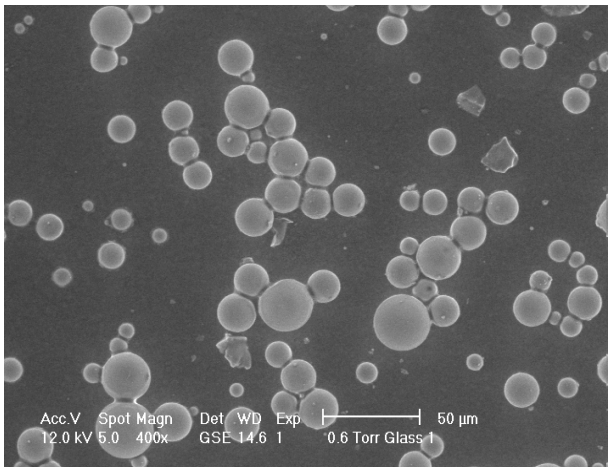

(a)

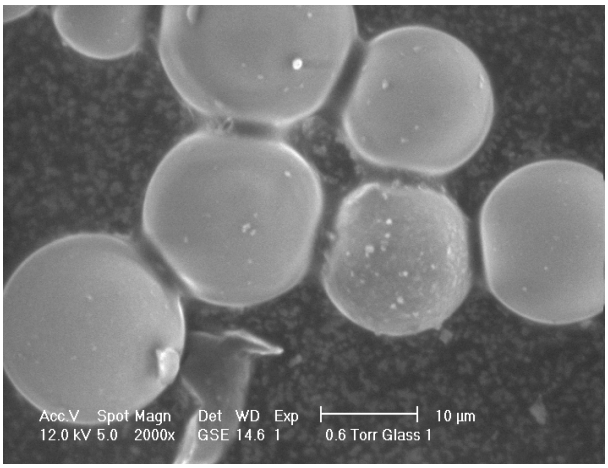

(b)

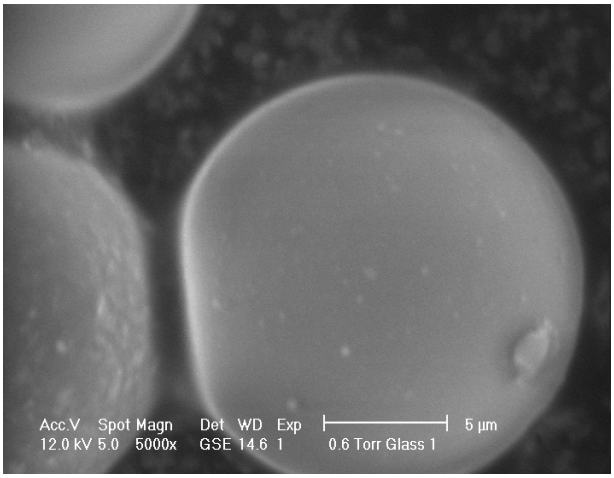

(c)

Figure 4.3 ESEM images of Cores® glass microparticles at different magnifications

4.1.1.2 Density measurements

In Figure 4.4 the helyum pycnometer data obtained on silica micro and nanoparticles are reported, while in Table 4.1 density results are summarized. Regarding fumed silica nanoparticles, it is evident that at least 200 measures are necessary to reach a constant density value. This probably indicates that the surface of fumed silica aggregates has a very diffused open porosity, among which helium molecules can hardly penetrate and diffuse. As evidenced in Figure 4.1, these pores are constituted by the interstitial spaces formed by the random aggregation of fumed silica primary nanoparticles. In the case of untreated fumed silica nanoparticles, density values are around 2.3-2.5 g/cm^3, near the density of a typical non porous silica glass (2.5 g/cm^3). When surface treated nanoparticles are considered (Ar816), the density is considerably lower (2.04 g/cm^3), because of the presence of hydrocarbon chains, with relatively low density, on the surface of primary nanoparticles.

For precipitated silica microparticles (S160) the density is lower (1.85 g/cm^3) and at least 400 density measures are necessary to reach an almost constant value. It is probable that these microparticles have a small amount of internal close porosity and a considerable amount of surface open porosity with little dimensions (a few nanometers), hardly reachable by helium molecules and responsible of the high surface area reported in the datasheet. The presence of an high surface porosity is confirmed by high magnification ESEM images (Figure 4.2).

For glass microspheres, a plateau value of 2.43 g/cm^3 can be easily reached after only 100 measures, because of the absence of pores on the surface of the beads, as evidenced in Figure 4.3.

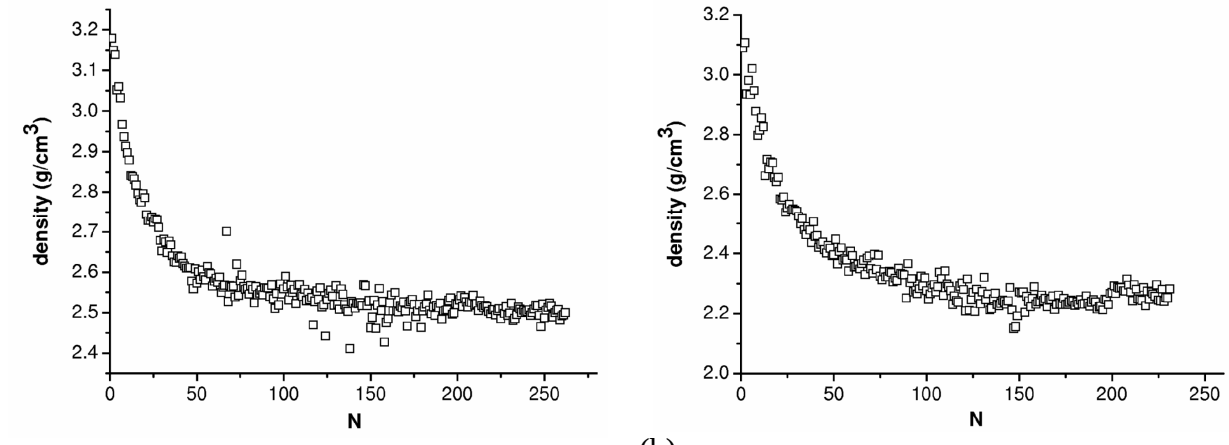

(a) (b)

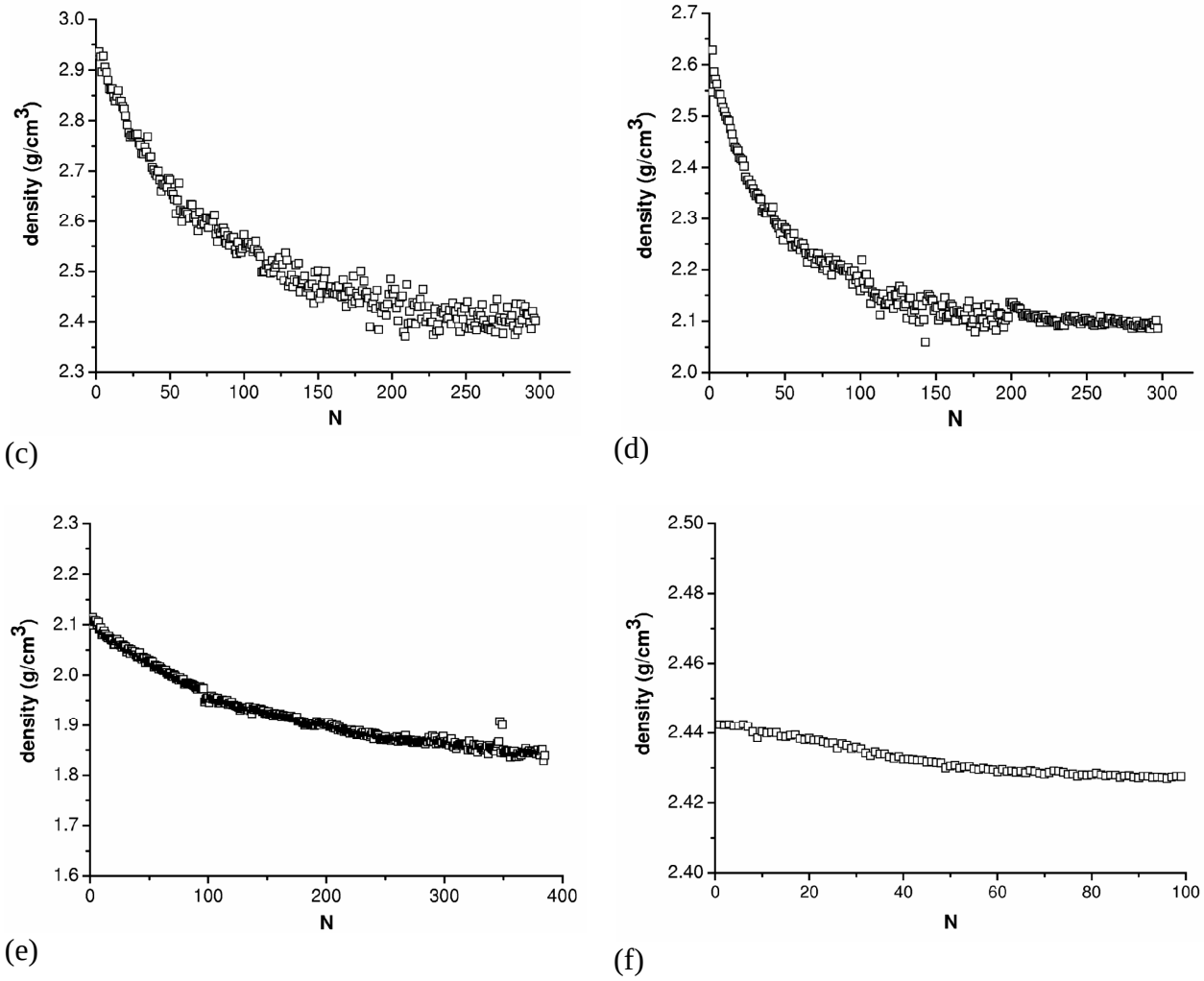

Figure 4.4 Density measurements on the different typologies of silica powders used in this work. (a) A90, (b) A200, (c) A380, (d) Ar816, (e) S160, (f) Glass microparticles

Sample	Density (g/cm^3)
A90	2.502 ± 0.013
A200	2.272 ± 0.021
Ar816	2.042 ± 0.008
A300	2.230 ± 0.019
A380	2.406 ± 0.018
S160	1.850 ± 0.010
Glass	2.430 ± 0.010

Table 4.1 Density measurements on silica micro and nanopowders

4.1.1.3 Evaluation of the surface properties

In Figure 4.5 representative curves of the surface properties of fumed silica nanoparticles, in particular of A90 and A380 sample, are reported. From the absorption/desorption curves it is evident the complete absence of hysteresis phenomena. Referring to the general theories regarding the gas physical absorption by powders and porous solids [148], it is possible to conclude that fumed silica nanoparticles are not internally porous, and the greatest part of the pores is constituted by open pores on the surface of the aggregates. These pores are mainly constituted by interstitial spaces between primary nanoparticles physically fused together. From the extrapolation of the adsorbed gas volume at low relative pressure it is possible to obtain BET surface area of fumed silica nanoparticles, which values are summarized in Table 4.2. The so obtained surface area values are very near to that reported in the datasheets (see Table 3.2). Furthermore through the application of the BJH method it is possible to determine the cumulative pore area distribution, as represented in Figure 4.5c and in Figure 4.5f. In Table 4.2 the surface area contribution due to pores between 1.7 and 300 nm is summarized. Regardless to the total surface area values, it is possible to conclude that the major contribution is due to the presence of pores with diameters between 2 and 10 nm, while the surface area due to micropores (with diameter lower than 2 nm) is relatively low. The arithmetic mean pore diameter reported in Table 4.2 has only a mathematical meaning, because the maximum of the cumulative distribution is around 2-3 nm.

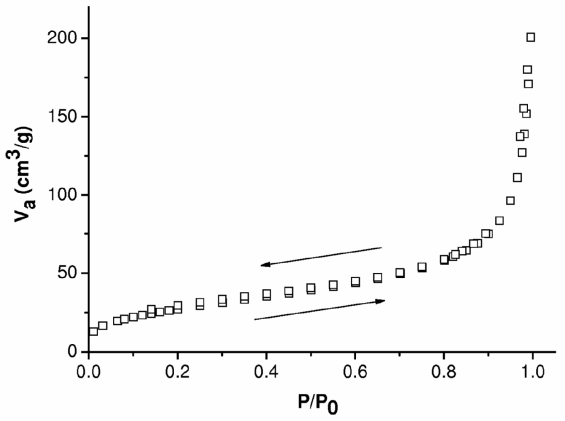

(a)

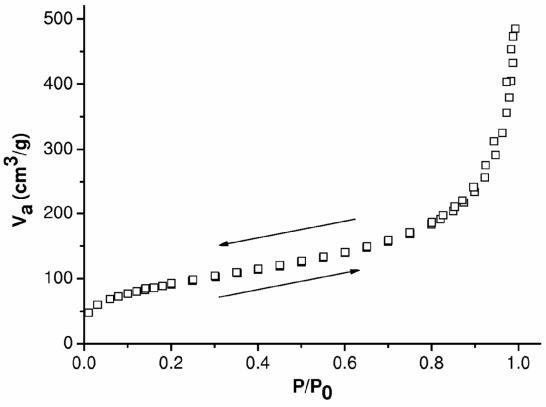

(d)

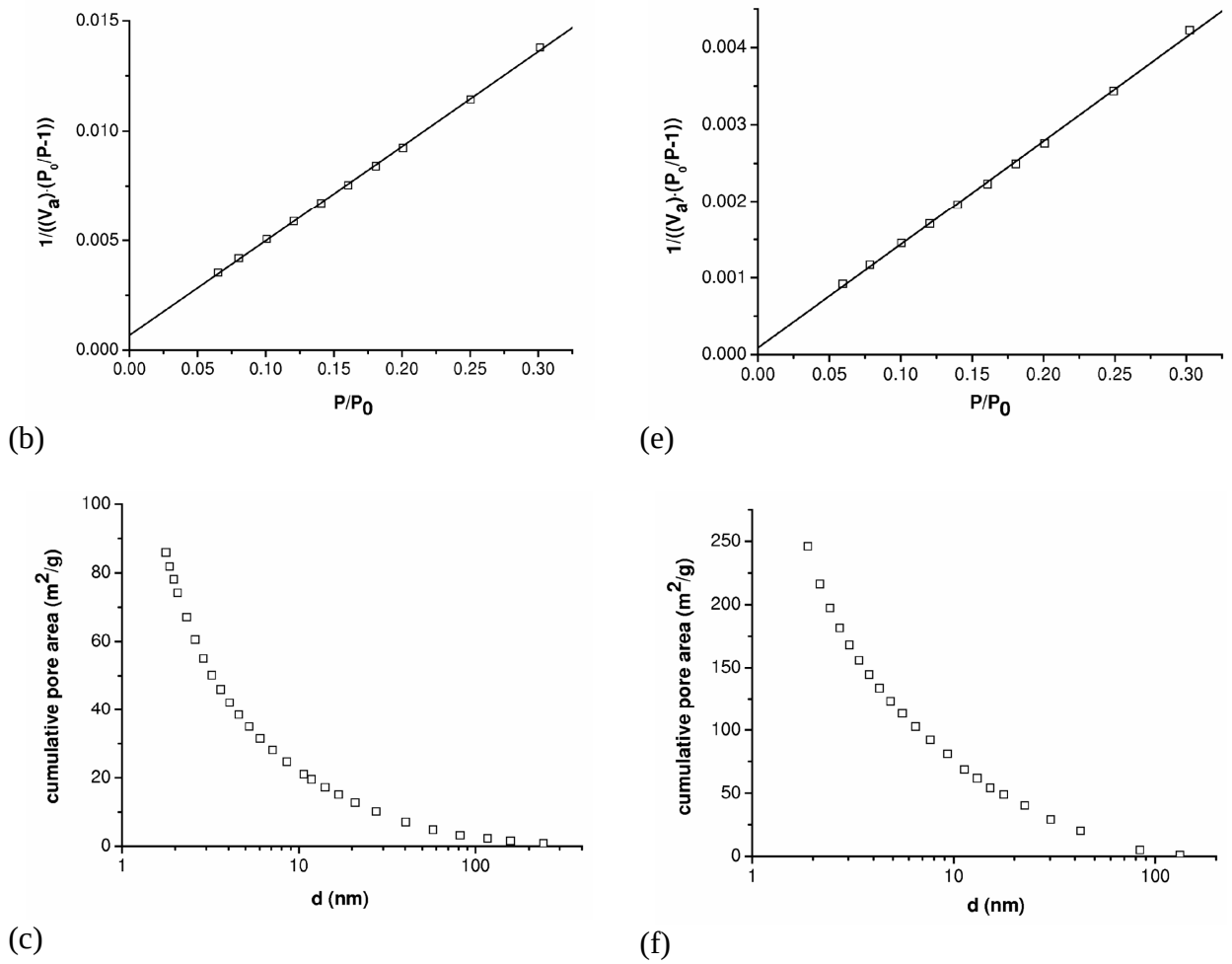

Figure 4.5 Representative curves of the surface properties of fumed silica nanoparticles. (a,b,c) A90, (d,e,f) A380. (a-d) specific gas volume adsorbed vs relative pressure, (b-e) linear plot for the evaluation of the BET surface area, (c-f) cumulative pore area vs pore size

The same analysis was conducted on precipitated silica microparticles and glass microbeads, as represented in Figure 4.6. In the case of S160 microparticles, little hysteresis at high relative pressures can be easily detected. This probably means that these materials are probably internally porous, and that non-rigid slit-shaped pores can be probably found in correspondence of the aggregates of plate-like particles, formed during the synthesis of the microparticles. It can be also hypothesized the presence of open pores that start from the surface with tubular and tortuous structure, responsible of the high surface area of these microparticles. These considerations are supported by ESEM images at high magnification, by the relatively low density and by the difficulty to reach a plateau density value for these microparticles. Even in this case the greatest contribution to the total surface area is due to the presence of pores higher than 2 nm, even if the mean dimension of pores is probably slightly higher than that encountered for fumed silica nanoparticles. In the case of glass microbeads the measured surface area value is very low, this

means that the total amount of adsorbed gas is very low. Consequently the instrumental error is comparable to the measured value, and for this reason the adsorption curve stays above the desorption curve.

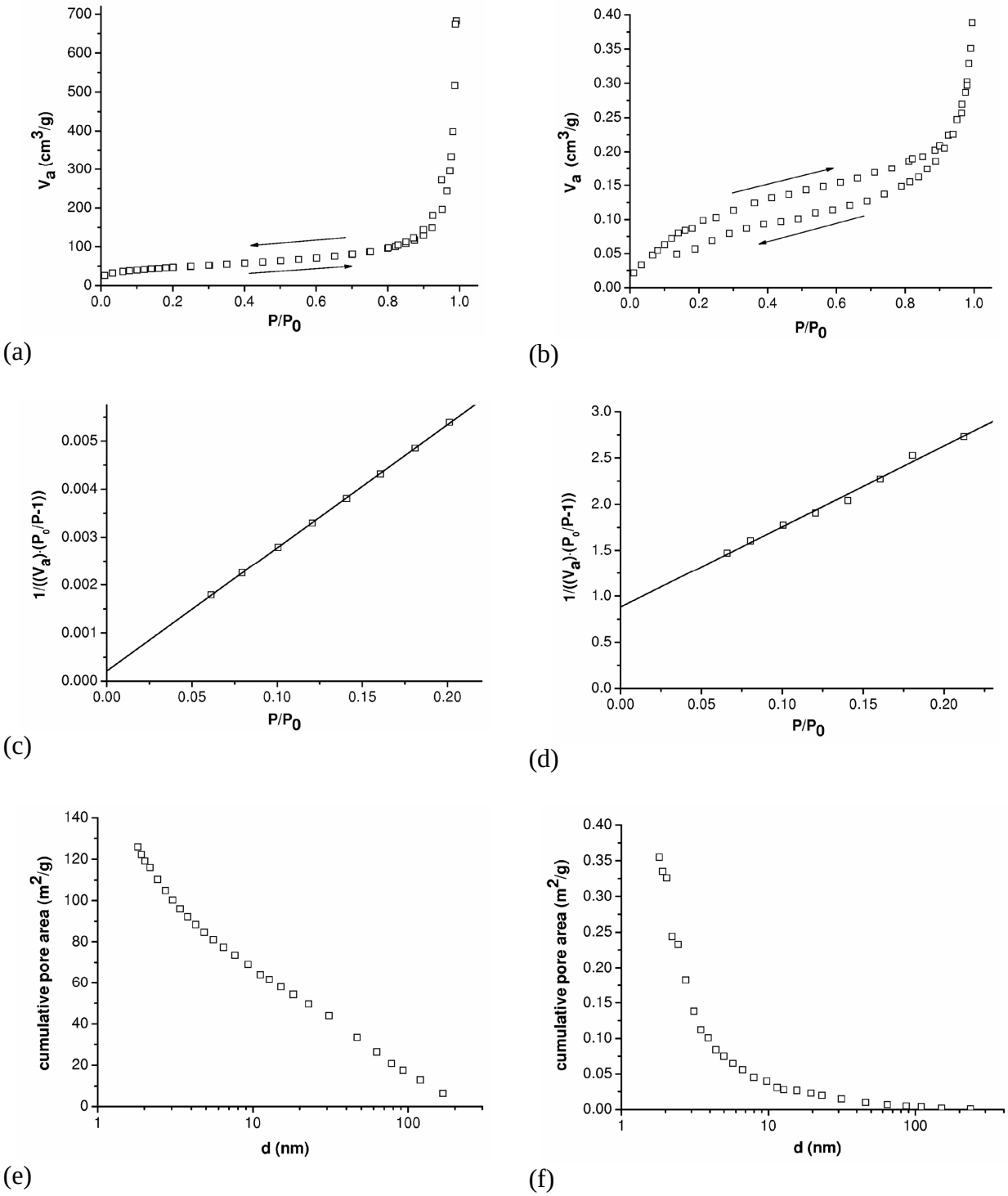

Figure 4.6 Representative curves of the surface properties of (a,c,e) S160 microparticles and (b,d,f) Glass microspheres. (a-b) specific gas volume adsorbed vs relative pressure, (c-d) linear plot for the evaluation of the BET surface area, (e-f) cumulative pore area vs pore size

Sample	BET Surface Area (m^2/g)	BJH Adsorption Cumulative Surface Area of pores (1.7-300 nm) (m^2/g)	BJH Adsorption Average Pore Diameter (nm)
A90	99.5 ± 0.7	85.9	14.1
A200	196.6 ± 1.7	165.2	14.4
Ar816	159.2 ± 1.3	140.0	15.6
A300	274.0 ± 2.6	220.9	11.6
A380	320.8 ± 3.4	247.0	11.5
S160	168.3 ± 0.6	125.9	32.9
Glass	0.5 ± 0.1	0.4	6.7

Table 4.2 Surface properties of fumed silica nanoparticles and silica microparticles used in this work

4.1.2 Composites

4.1.2.1 ESEM/TEM fracture surface images

In Figure 4.7 ESEM images of the fracture surfaces of LLDPE-Glass-2 composite are represented. It is evident the presence of spherical smooth microparticles homogeneously distributed through the sample, with mean dimension of about 15-20 μm.

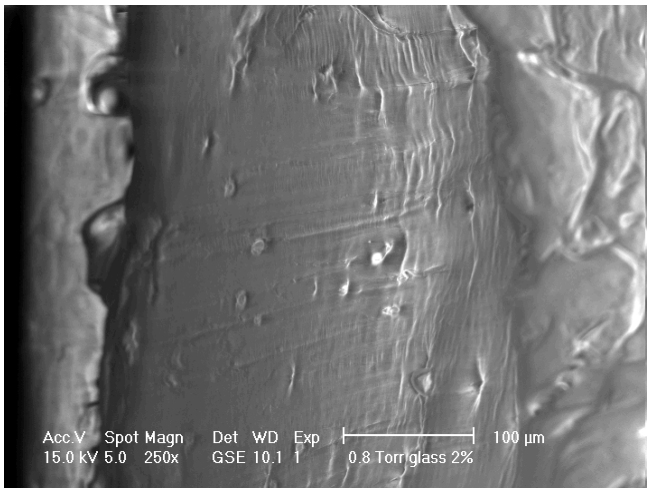

(a)

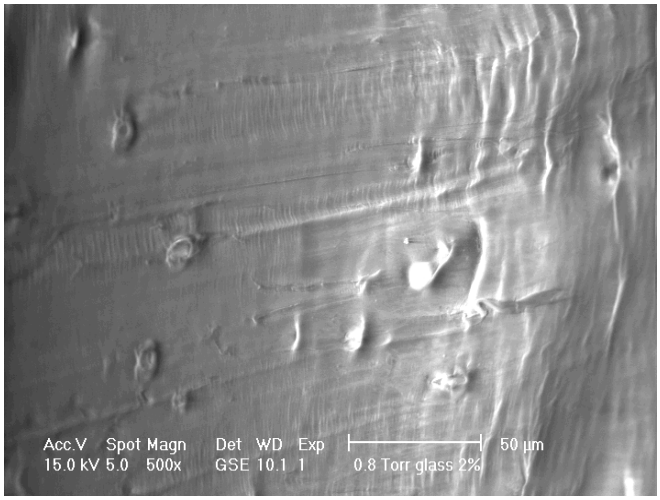

(b)

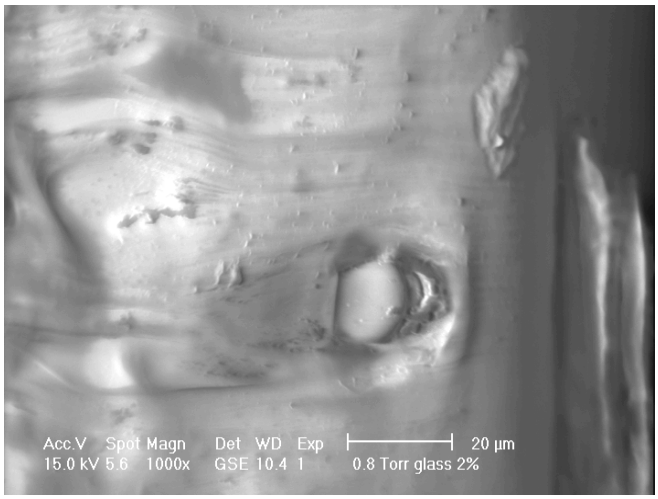

(c)

Figure 4.7 ESEM images of the fracture surfaces of LLDPE-Glass-2 composite at different magnifications

In Figure 4.8 ESEM images of the fracture surfaces of LLDPE-S160-2 composite at different magnifications are represented. The microparticles appear irregular even if substantially spherical, but the most important information is that the mean microparticles dimension is about 1.5-2 μm, much lower than the mean dimensions of the microparticles before melt compounding. It is probable that the high shear forces applied to the very porous precipitated silica microparticles during compounding leads to their partial fracture, as confirmed by SEM observations of precipitated silica composites in the papers of Shim and Isayev on polydimethylsiloxane systems [135] and Uotila et al. on PP/elastomer/microsilica composites [136].

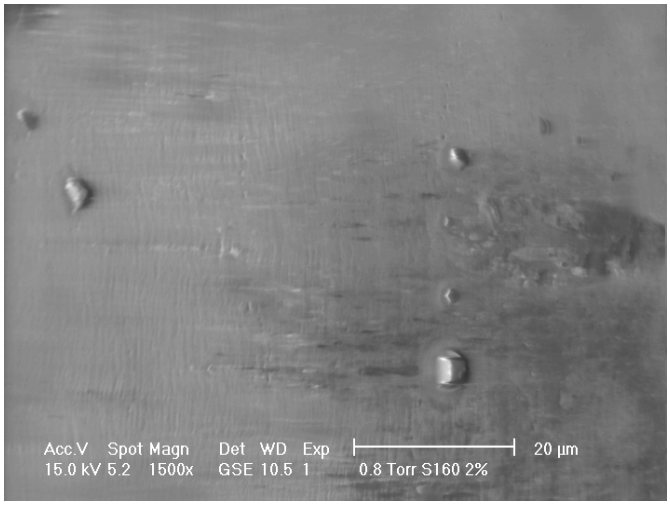

(a)

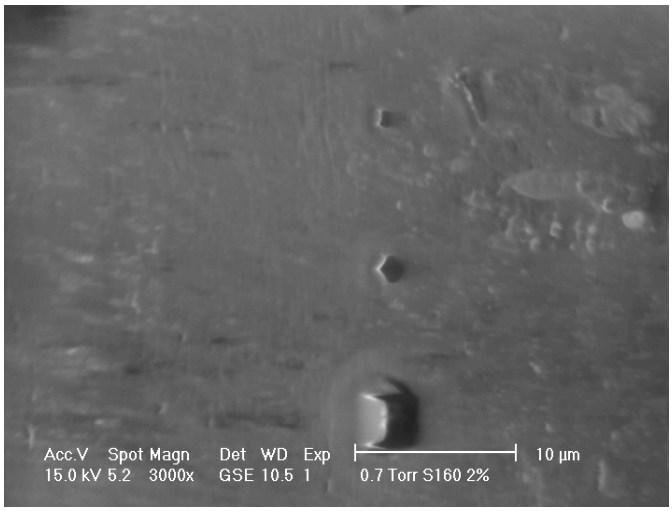

(b)

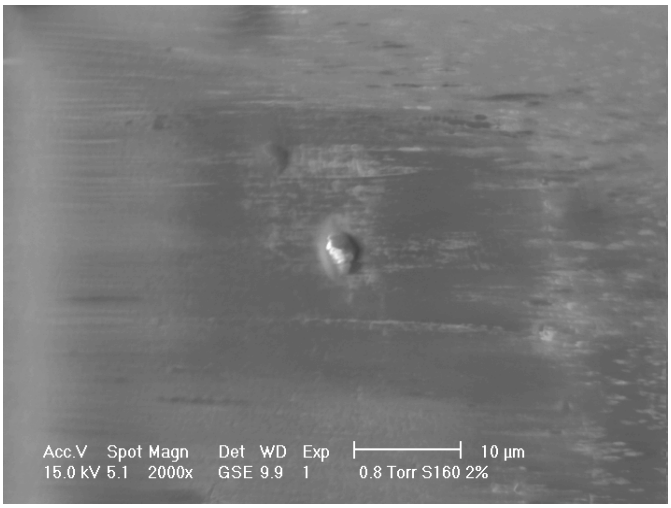

(c)

Figure 4.8 ESEM images of the fracture surfaces of LLDPE-S160-2 composite at different magnifications

A more detailed microstructural analysis can be conducted considering TEM images reported in Figure 4.9 and in Figure 4.10. Isodimensional aggregates of about 400 nm homogeneously dispersed in the matrix can be easily detected. This means that the fracture of the aggregates during melt compounding is more effective than that evidenced by ESEM images. It is important to note that the deformation leads to the orientation of the aggregates along the stress direction, especially when a deformation level higher than 60% is applied to the sample.

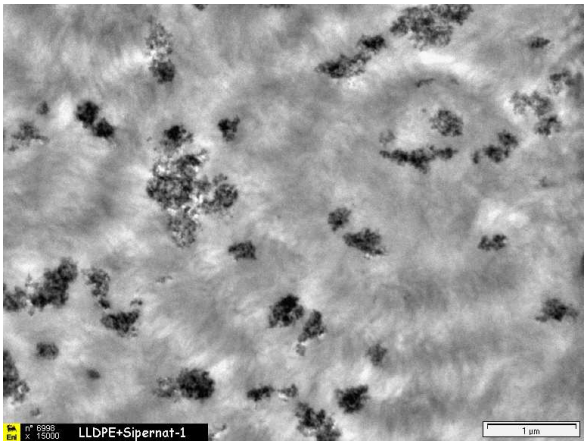

(a)

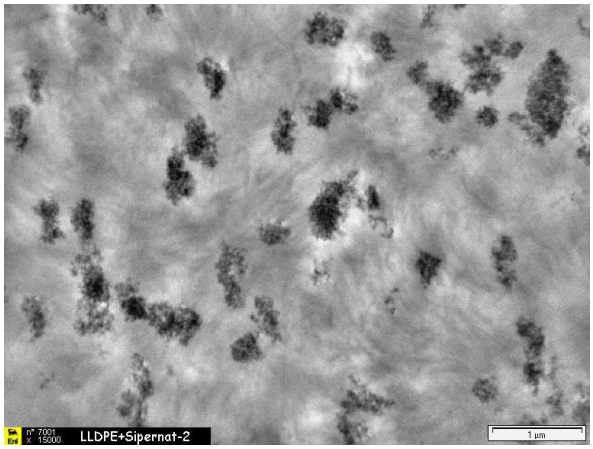

(b)

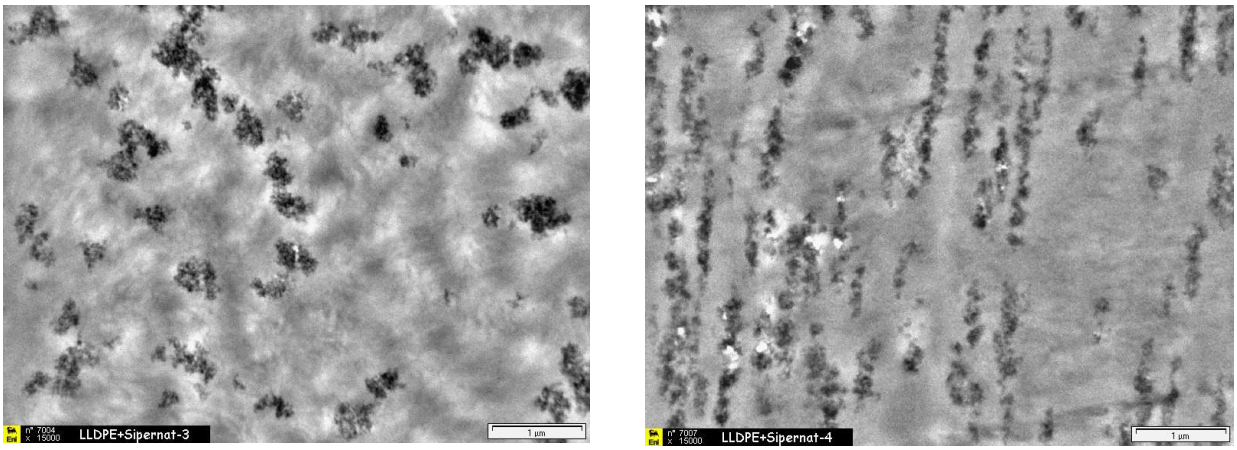

(c) (d)

Figure 4.9 TEM images of the fracture surfaces of LLDPE-S160-2 nanocomposite at different deformation levels (marker 1 µm). (a) 0%, (b) 30%, (c) 60 %, (d) 100%

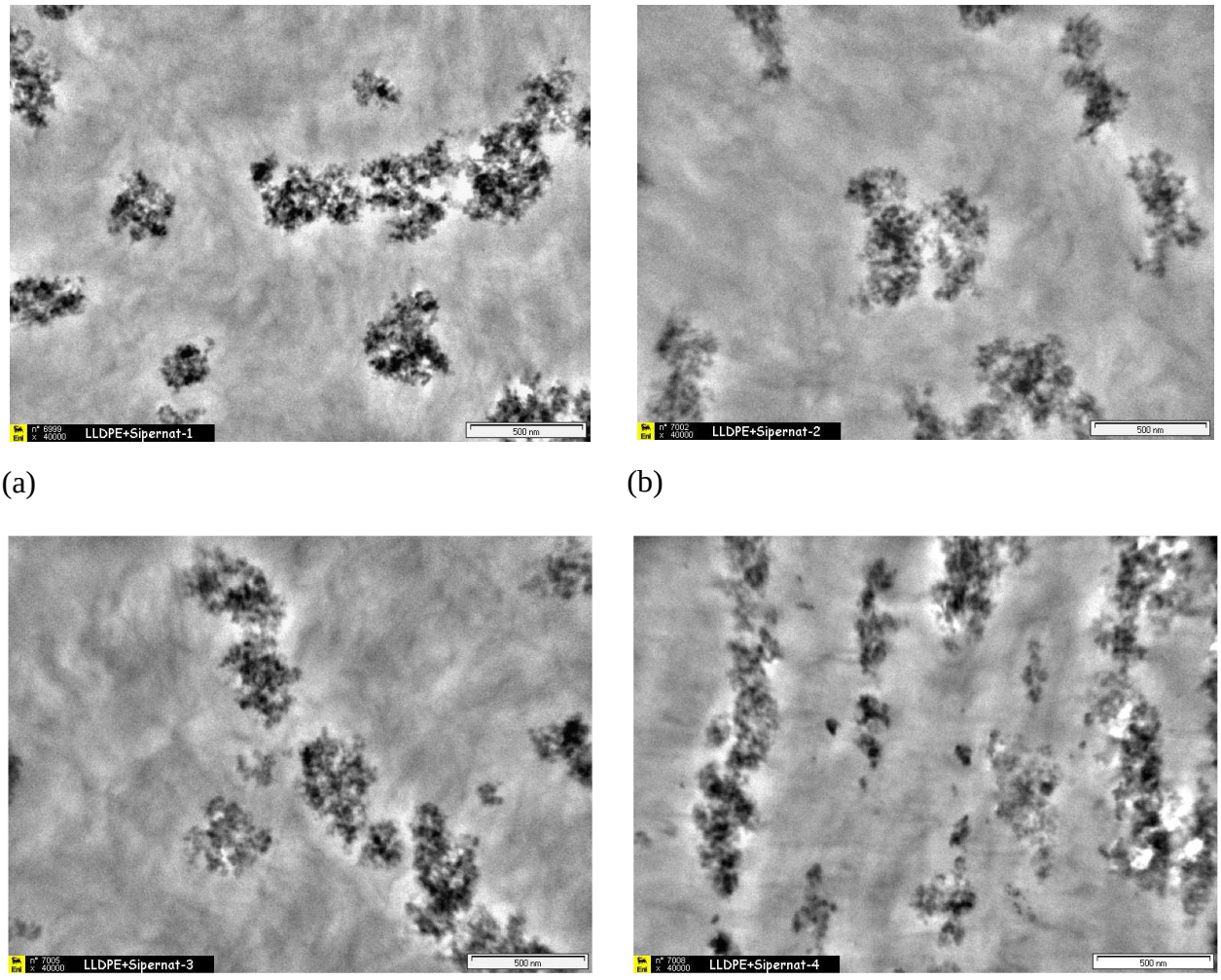

(a) (b)

(c) (d)

Figure 4.10 TEM images of the fracture surfaces of LLDPE-S160-2 nanocomposite at different deformation levels (marker 0.5 µm). (a) 0%, (b) 30%, (c) 60 %, (d) 100%

In Figure 4.11 ESEM images of the fracture surfaces of LLDPE-A380-2 at different magnifications are represented. From high magnification images it is possible to detect the presence of fumed silica agglomerates with submicron size and irregular shape localized in a particular zone of the sample. In any case the relatively low magnification degree and the low resolution of the image do not provide detailed information about the microstructural arrangement of fumed silica nanoparticles in the composite.

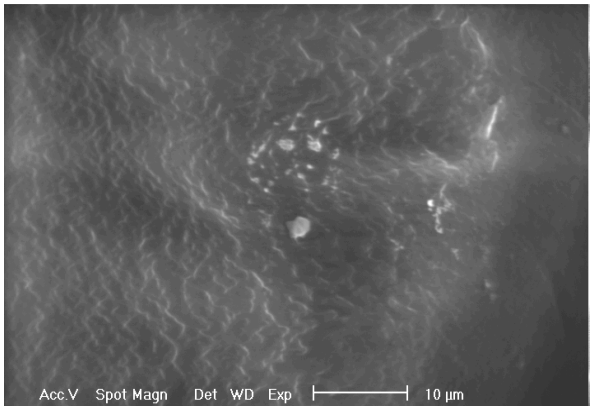

(a)

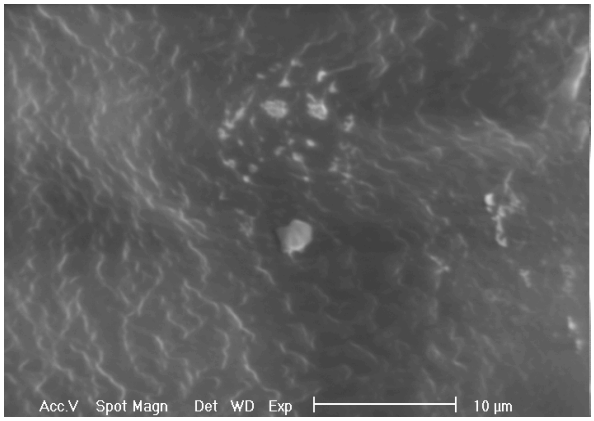

(b)

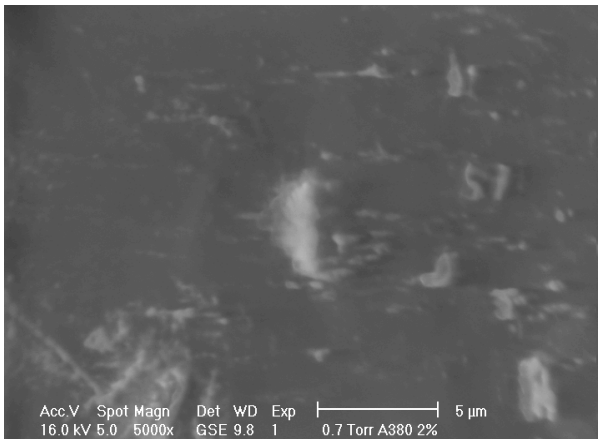

(c)

Figure 4.11 ESEM images of the fracture surfaces of LLDPE-A380-2 nanocomposite at different magnifications

In Figure 4.12 and in Figure 4.13 TEM images of the fracture surfaces of LLDPE-A380-2 nanocomposite at different deformation levels are reported. Considering the un-deformed sample, it is very easy to detect the presence of spherical silica aggregates homogeneously dispersed in the matrix, with mean diameter of about 200 nm. Fumed silica aggregates remain dimensionally unaltered even when deformation levels of 30 % are applied to the samples. For higher applied strains, silica aggregates begin to align themselves along the strain direction, increasing the length/thickness ratio. As it will be clarified in the section on the fracture behaviour, the tensile strain at yield of these nanocomposites is about 25 %. This means that the orientation of fumed silica aggregates begins at strains higher than the yield point, while in the elastic region silica aggregates remain randomly distributed.

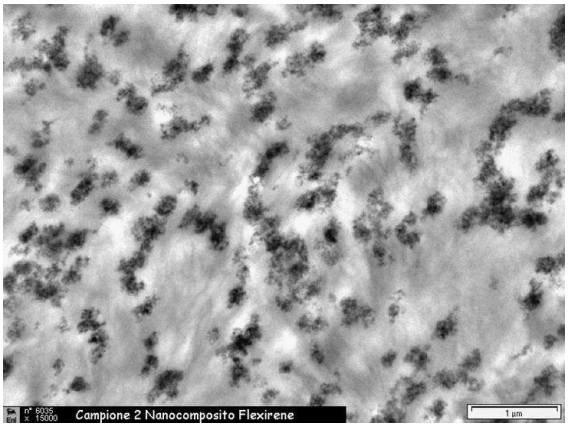

(a)

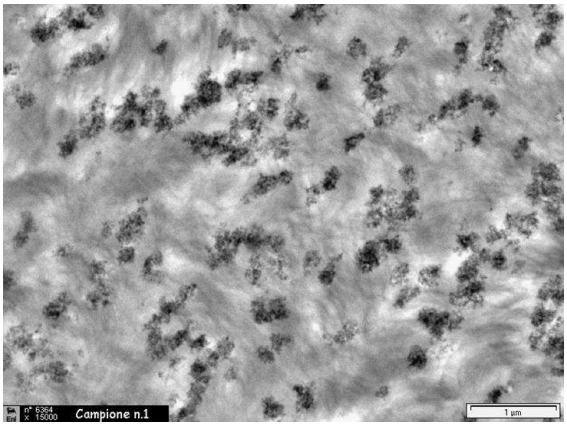

(b)

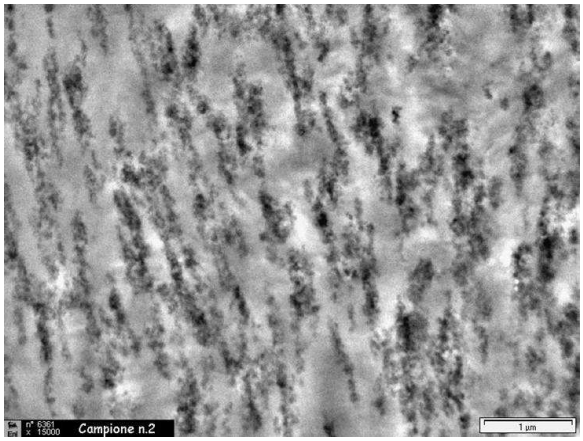

(c)

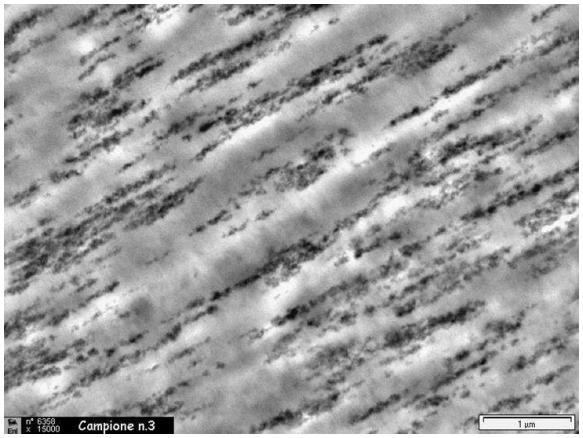

(d)

Figure 4.12 TEM images of the fracture surfaces of LLDPE-A380-2 nanocomposite at different deformation levels (marker 1 µm). (a) 0%, (b) 30%, (c) 60 %, (d) 100%

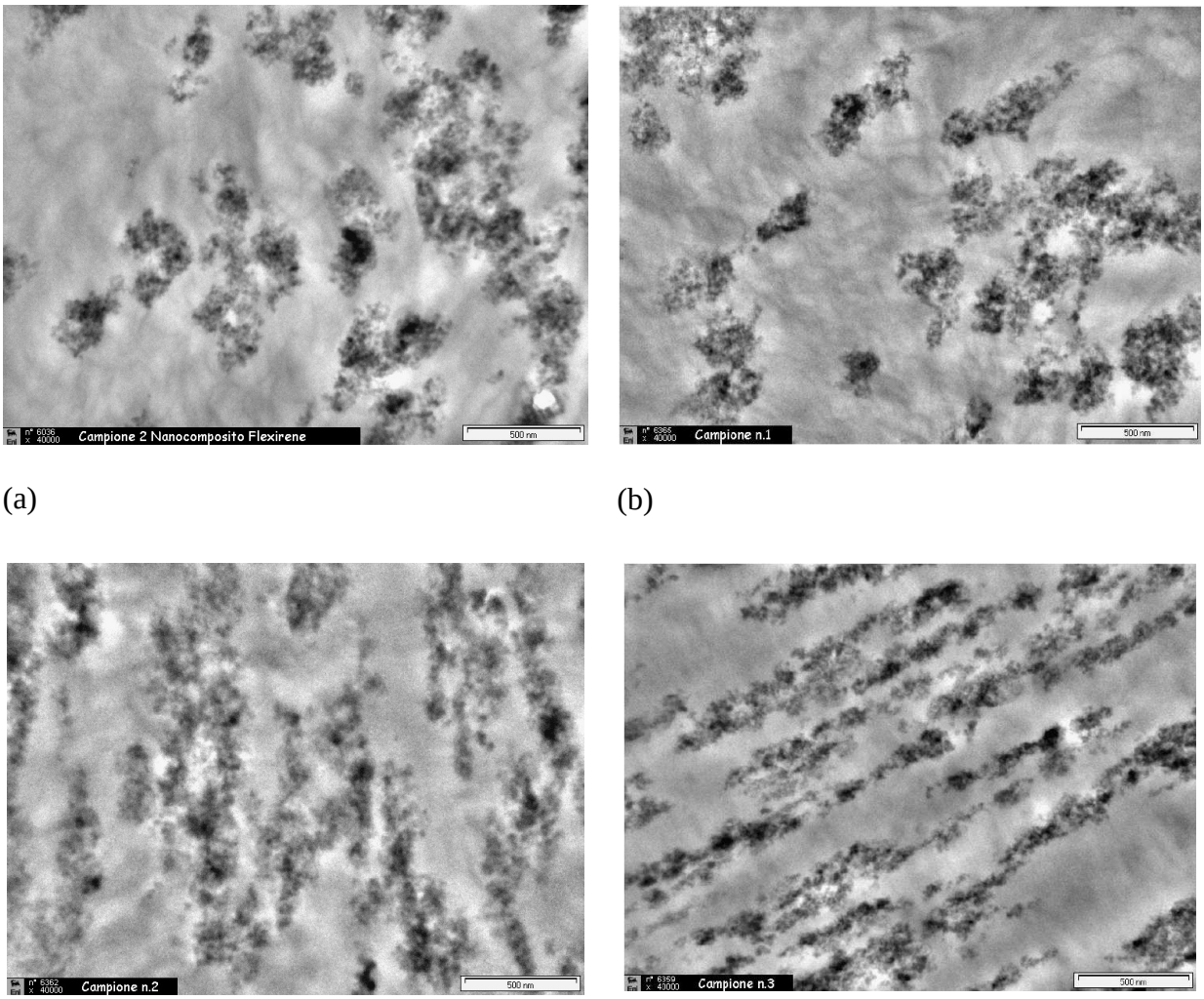

(a) (b)

(c) (d)

Figure 4.13 TEM images of the fracture surfaces of LLDPE-A380-2 nanocomposite at different deformation levels (marker 0.5 µm). (a) 0%, (b) 30%, (c) 60 %, (d) 100%

As a comparison, the mean size of silica aggregates of LLDPE-A380-2 and LLDPE-S160 samples and their length/thickness (L/t) ratio are summarized in Table 4.3. It is evident that the mean diameter of S160 aggregates is slightly higher than that of A380 filled sample. Moreover the orientation of nanoparticles in LLDPE-S160-2 sample is less intense, with lower L/t values with respect to LLDPE-A380-2 sample at the same strain level. This aspect will be considered in the section dedicated to the analysis of the fracture behaviour of the composites (Chapter 4.4.1).

ε (%)	LLDPE-S160-2			LLDPE-A380-2		
	L (nm)	t (nm)	L/t	L (nm)	t (nm)	L/t
0	411 ± 36	405 ± 14	1.0 ± 0.1	198 ± 12	199 ± 21	1.0 ± 0.1
30	546 ± 52	206 ± 40	2.6 ± 0.7	684 ± 79	151 ± 23	4.5 ± 0.7
60	731 ± 88	210 ± 43	3.5 ± 0.7	1011 ± 61	113 ± 9	8.9 ± 0.7
100	999 ± 140	193 ± 25	5.2 ± 0.7	1603 ± 100	76 ± 19	21.1 ± 2.3

Table 4.3 Dimensional analysis of the silica aggregates of the LLDPE-S160-2 and LLDPE-A380-2 samples at different deformation levels

4.1.2.2 Density measurements

In Figure 4.14 density measurements of LLDPE and 2 vol% silica filled composites are reported, while in Table 4.4 plateau density values, compared with theoretical values, are summarized. As can be easily predicted, the density of the composites is only slightly higher than that of the pure LLDPE. Moreover measured density values are in accordance with theoretical density predictions based on traditional rule of mixture. This means that the presence of the filler does not lead to void formation during melt compounding.

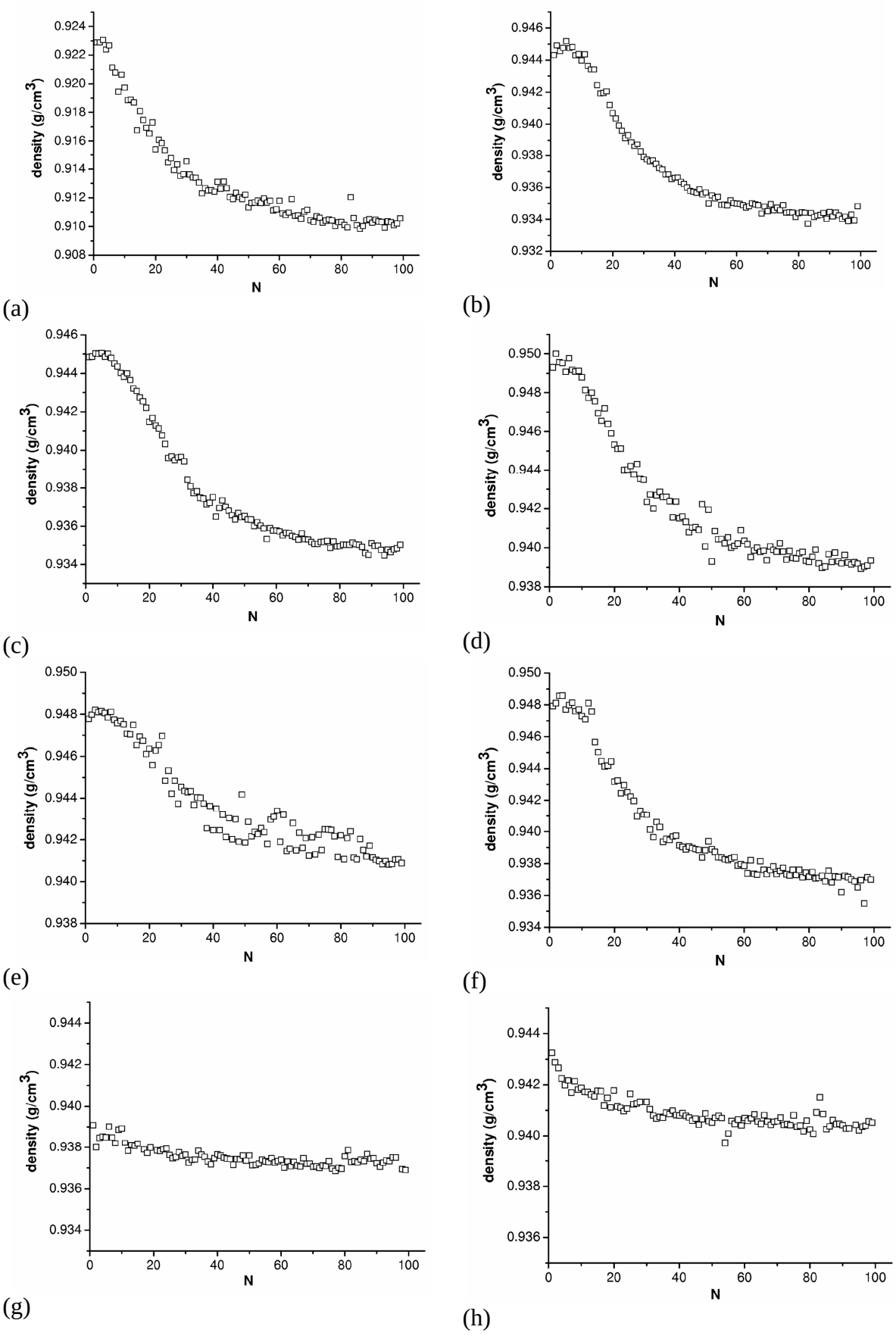

Figure 4.14 Density measurements of LLDPE- 2 vol% filled composites. (a) LLDPE, (b) LLDPE-A90-2, (c) LLDPE-A200-2, (d) LLDPE-A300-2, (e) LLDPE-A380-2, (f) LLDPE-Ar816-2, (g) LLDPE-S160-2, (h) LLDPE-Glass-2

Sample	ρ filler (g/cm^3)	ρ experimental (g/cm^3)	ρ theoretical (g/cm^3)
LLDPE	-	0.911 ± 0.002	0.911
LLDPE-A90-2	2.502 ± 0.013	0.934 ± 0.002	0.940
LLDPE-A200-2	2.272 ± 0.021	0.935 ± 0.002	0.938
LLDPE-Ar816-2	2.042 ± 0.008	0.937 ± 0.001	0.936
LLDPE-A300-2	2.230 ± 0.019	0.939 ± 0.001	0.938
LLDPE-A380-2	2.406 ± 0.018	0.941 ± 0.002	0.940
LLDPE-S160-2	1.850 ± 0.010	0.937 ± 0.001	0.934
LLDPE-Glass-2	2.430 ± 0.010	0.940 ± 0.001	0.940

Table 4.4 Density of LLDPE- 2 vol% composites, compared with theoretical density values

In order to study the deformational mechanisms of fumed silica nanocomposites, density measurements after yielding were conducted. In Figure 4.15 density values of LLDPE and LLDPE-A380-2 nanocomposite are compared, before and after yielding process, while in Table 4.5 plateau density values are summarized. Density of the yielded sample is slightly lower than that of undeformed samples, probably because of the presence of voiding phenomena in the yielded zone. Furthermore, density reduction of LLDPE-A380-2 sample is practically the same of that obtained for the unfilled sample. It is therefore possible to conclude that the presence of nanoparticles does not lead to void formation or microcavitation during the yielding process, in contrast with the conclusion reported by Lazzeri et al. In fact, they associated the observed increase in volume strain with deformation to matrix-particle debonding phenomenon [149].

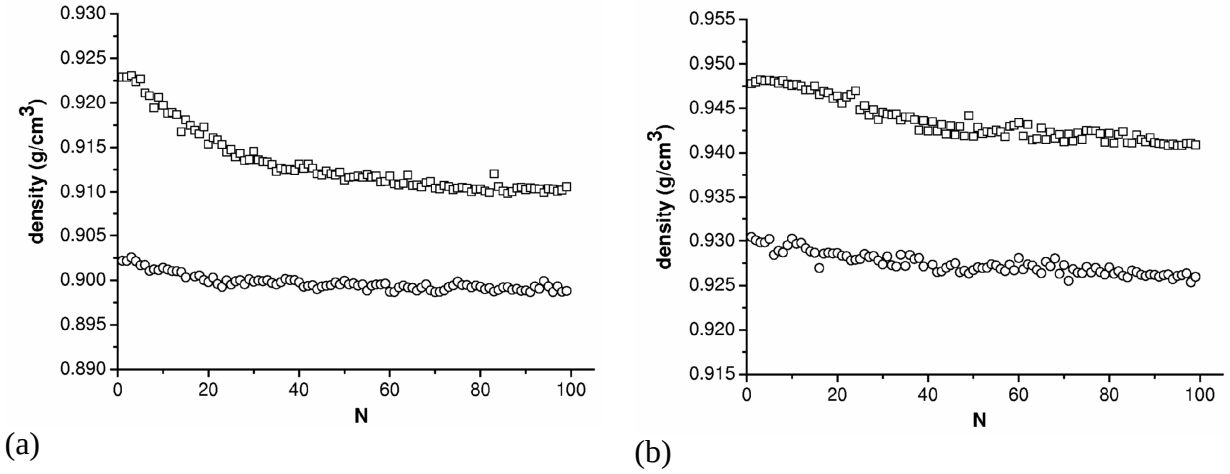

Figure 4.15 Density measurements of (a) LLDPE and (b) LLDPE-A380-2 nanocomposite. (□) Not-yielded sample, (○) yielded sample (v=50 mm/min, deformation level 100%)

Sample	Density (g/cm^3)		Density reduction (%)
	Undeformed	Deformed at ε = 100 %	
LLDPE	0.911 ± 0.001	0.899 ± 0.001	1.31 ± 0.15
LLDPE-A380-2	0.941 ± 0.002	0.927 ± 0.002	1.49 ± 0.29

Table 4.5 Effect of the yielding on the density of LLDPE and LLDPE-A380-2 nanocomposite (yielded samples at v=50 mm/min and at a deformation level of 100%)

4.1.2.3 Differential scanning calorimetry (DSC)

In order to analyze the influence of silica fillers on the melting behaviour and on the crystallinity of the LLDPE matrix, DSC tests were conducted. In Figure 4.16, DSC thermograms of LLDPE and relative 2 vol% fumed silica nanocomposites are reported, while in Figure 4.17 thermograms of 2 vol% precipitated microparticles and glass microbeads filled samples are represented. The most important results are then summarized in Table 4.6. It is evident that the melting behaviour of the material is not affected by the presence of the fillers. In fact melting temperatures and crystallinity content of the composites are practically the same of that of pure LLDPE, both during first and second scans. The presence of crystalline nanoparticles may lead to an increase of the total crystalline amount and of an enhancement of the melting temperatures [149]. In some cases the

presence of nanoparticles is responsible of a substantial increase of the crystallization rate and of significant modifications of the crystalline morphology of the material [150]. It is possible that in our case the amorphous structure of the filler does not induce heterogeneous nucleation phenomena, while more extended crystallization kinetics tests should be necessary to assess the influence of the considered silica filler on the crystallization behaviour of the matrix.

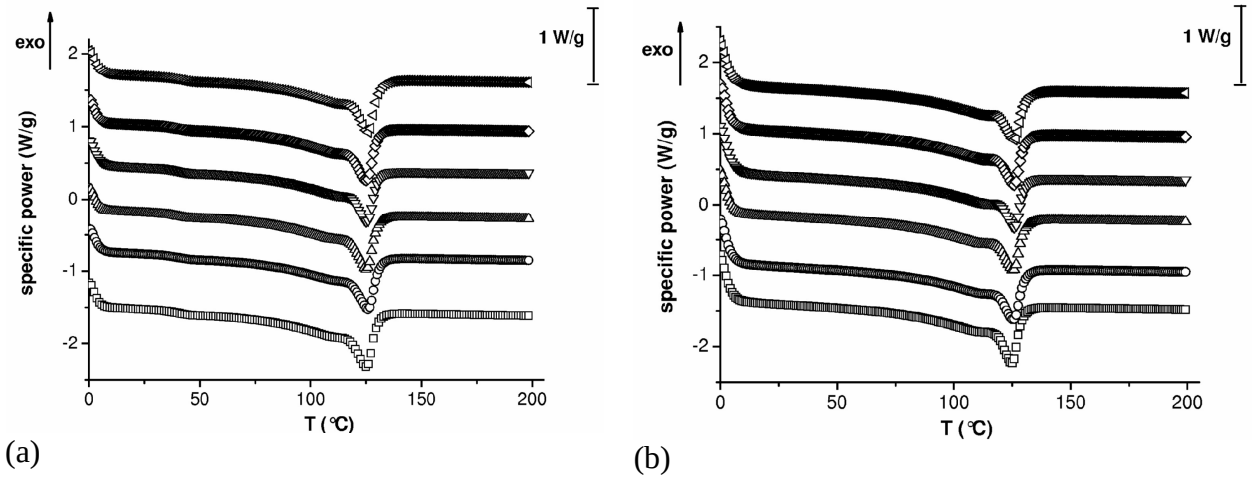

Figure 4.16 DSC on LLDPE - 2 vol% fumed silica nanocomposites, (a) first scan, (b) second scan. (□) LLDPE, (○) LLDPE-A90-2, (△) LLDPE-A200-2, (▽) LLDPE-A300-2, (◊) LLDPE-A380-2, (◁) LLDPE-Ar816-2

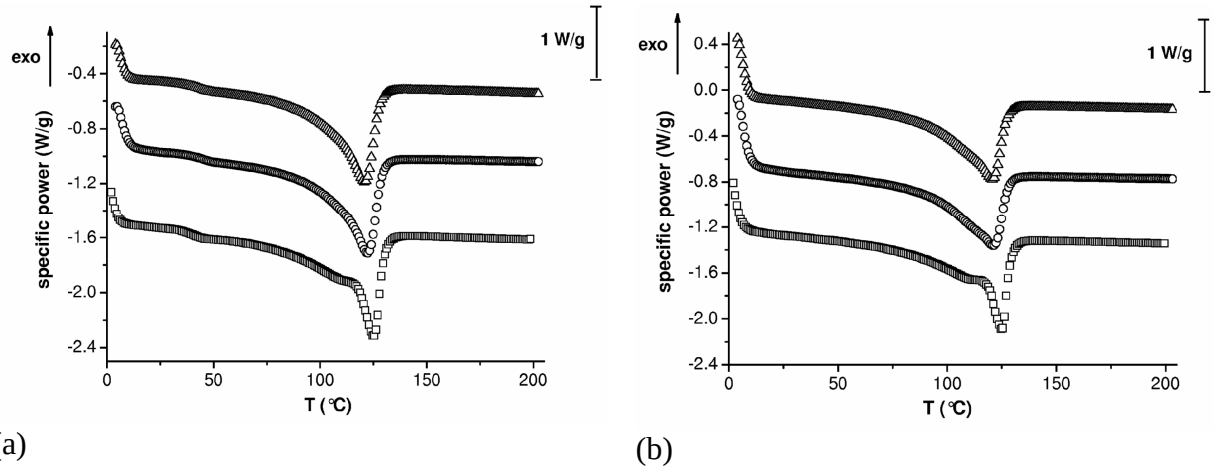

Figure 4.17 DSC on LLDPE - 2 vol% microcomposites, (a) first scan, (b) second scan. (□) LLDPE, (○) LLDPE-S160-2, (△) LLDPE-Glass-2

Sample	T_{m1} (°C)	x_{c1} (%)	T_{m2} (°C)	x_{c2} (%)
LLDPE	123.0	41.7	122.9	38.4
LLDPE-A90-2	123.6	42.1	123.2	39.2
LLDPE-A200-2	123.0	42.5	123.6	40.0
LLDPE-Ar816-2	123.7	41.2	123.8	39.9
LLDPE-A300-2	123.1	43.0	123.7	40.0
LLDPE-A380-2	123.0	42.4	124.1	39.0
LLDPE-S160-2	123.3	41.0	122.5	39.0
LLDPE-Glass-2	123.0	41.0	122.7	39.1

Table 4.6 DSC on LLDPE and relative 2 vol% composites

DSC tests were also conducted on post-yield deformed samples, in order to understand the influence of silica nanoparticles on the deformational behaviour of the prepared nanocomposites. In Figure 4.18 thermograms of LLDPE - 2 vol% fumed silica nanocomposites after yielding are reported, while the most important results are summarized in Table 4.7. Even in this case the melting temperatures and the total crystallinity amount are not substantially affected by the presence of the nanoparticles. This means that the influence of the nanoparticles is not directed on the crystalline part of the material, and that the deformational behaviour of the prepared nanocomposites can not be explained considering modifications of the crystallization behaviour of the material in the yielded zone. Furthermore, it can be easily noticed that yielded samples show slightly lower cristallinity values than the undeformed ones. This is probably due to the fact that the crystalline order of the matrix is partially destroyed when the macromolecules are forced to align themselves along the loading direction during the deformational process.

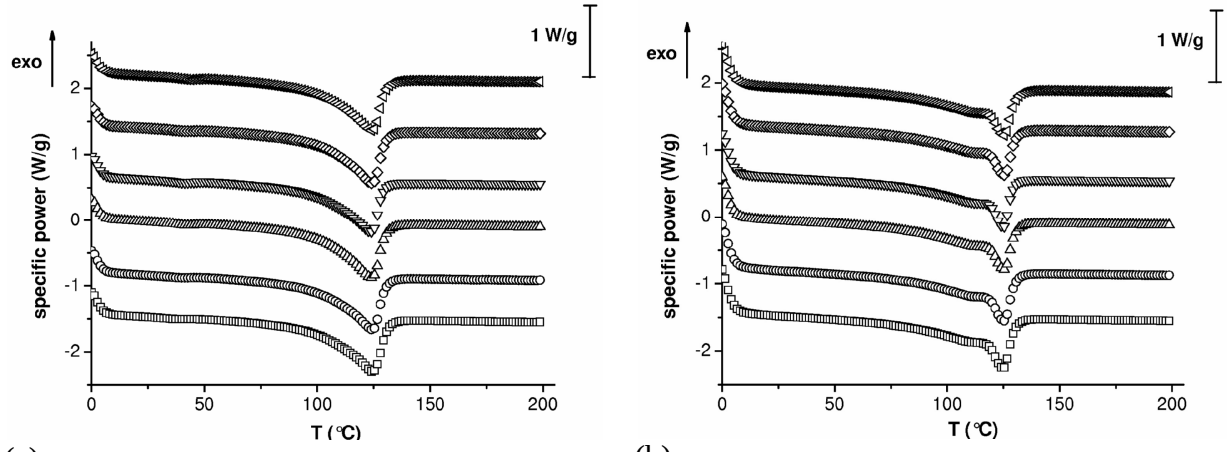

Figure 4.18 DSC on LLDPE - 2 vol% fumed silica nanocomposites after yielding (v=50 mm/min, deformation level 100%) , (a) first scan, (b) second scan. (□) LLDPE, (○) LLDPE-A90-2, (△) LLDPE-A200-2, (▽) LLDPE-A300-2, (◊) LLDPE-A380-2, (◁) LLDPE-Ar816-2

Sample	T_{m1} (°C)	x_{c1} (%)	T_{m2} (°C)	x_{c2} (%)
LLDPE	122.0	39.1	122.4	38.2
LLDPE-A90-2	121.7	39.5	122.5	38.8
LLDPE-A200-2	121.4	39.8	122.8	38.4
LLDPE-Ar816-2	121.6	39.9	122.8	38.2
LLDPE-A300-2	121.6	37.8	123.0	37.8
LLDPE-A380-2	121.4	39.1	122.8	37.7

Table 4.7 DSC on LLDPE and relative 2 vol% fumed silica nanocomposites after yielding (v=50 mm/min, deformation level 100%)

4.1.2.4 X-Ray diffraction analysis

In order to investigate the influence of the different typologies of silica fillers on the crystalline structure of LLDPE, X-Ray diffraction analysis was conducted both on nano and microcomposites. In Figure 4.19 X-Ray diffractograms of LLDPE and relative 2 vol% filled composites are reported, while in Figure 4.20 lognormal distributions of the crystallite size, elaborated through the Whole

Powder Pattern Model (WPPM) algorithm, are represented. The main features of the distributions and the mean crystallite size are summarized in Table 4.8. Even in this case the crystalline structure and the mean crystallites size (about 20 nm) are practically not affected by the presence of silica fillers, neither by using microparticles nor nanoparticles. These considerations are in agreement with the indications emerged from DSC tests, confirming that the crystalline phase of the matrix is not affected by the presence of SiO_2 nanoparticles.

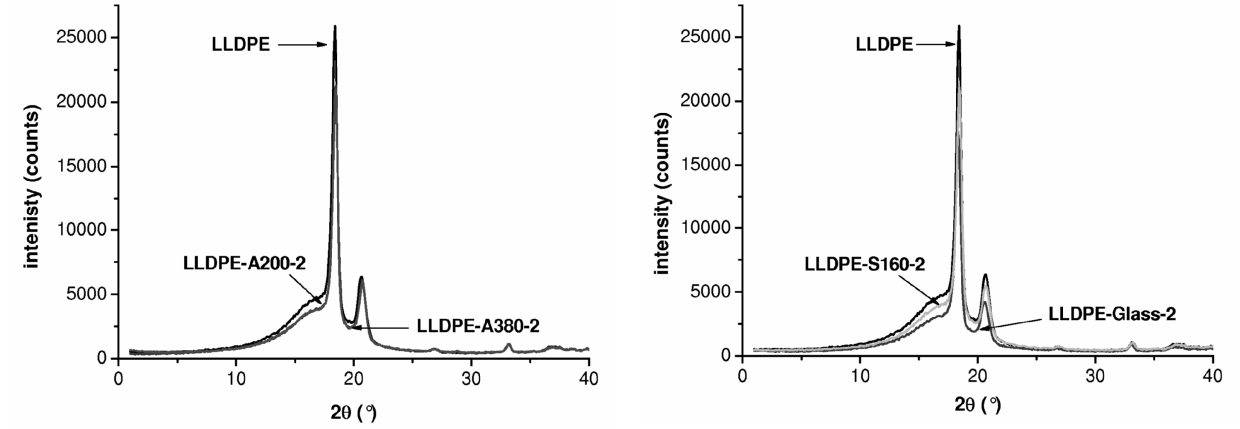

(a) (b)

Figure 4.19 X-Ray diffractograms of LLDPE - 2 vol% filled composites. (a) Nanocomposites, (b) microcomposites

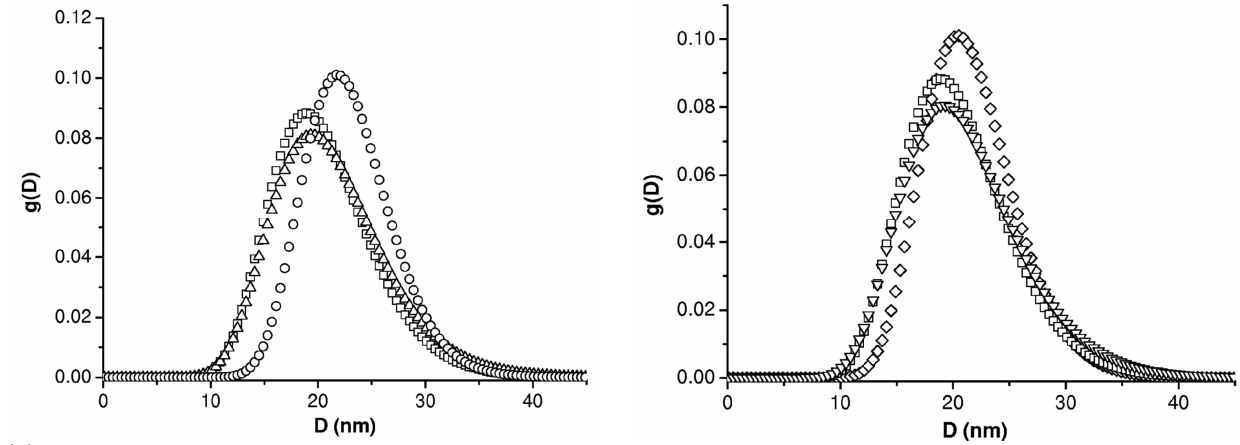

(a) (b)

Figure 4.20 Lognormal distributions of LLDPE crystallites in LLDPE - 2 vol% composites. (a) Nanocomposites, (b) microcomposites. (□) LLDPE, (○) LLDPE-A200-2, (△) LLDPE-A380-2, (▽) LLDPE-S160-2, (◊) LLDPE-Glass-2

Sample	μ	σ	D (nm)
LLDPE	2.995	0.232	20.5 ± 4.8
LLDPE-A200-2	3.114	0.178	22.9 ± 4.1
LLDPE-A380-2	3.026	0.246	21.2 ± 5.3
LLDPE-S160-2	3.053	0.190	21.6 ± 4.1
LLDPE-Glass-2	3.017	0.250	21.1 ± 5.4

Table 4.8 Mean and variance of the lognormal distribution of the crystallites diameter of LLDPE - 2 vol% composites

4.1.2.5 Infrared (IR) spectroscopy

In Figure 4.21 infrared spectroscopy plots of pure A380 powder, LLDPE and A380 filled nanocomposites are reported. All the samples present two distinct peaks around 2900 cm^{-1}, typically associated to the presence of CH_2 groups of polyolefinic materials [151]. Morevover, fumed silica powder and filled samples show an absorption peak at about 1100 cm^{-1}, whose intensity is proportional to the filler content. This absorbance peak can be attributed to Si-O-Si stretching vibrations, indicating the presence of silica on the surface, as largerly confirmed by many observations present in literature on silica and POSS based composites [93, 151-154].

It is important to underline the presence of a very small signal at about 1700 cm^{-1} for the filled samples, whose intensity is proportional to the filler content (see Figure 4.21b). Furthermore this absorption peak is practically absent for pure LLDPE and fumed silica powder. According to infrared spectroscopy handbooks [151], this peak can be attributed to the stretching of carbonylic groups (C=O). The presence of carbonilic groups in polyolefinic material was studied by Della Volpe et al. on PE and PP samples through X-Ray Photoelectron Spectroscopy (XPS) and Electron Spectroscopy for Chemical Analysis (ESCA) [155], leading to the conclusion that, even when ultra-pure polymeric matrices are used, a small percentage of oxygen is present in the product, due to the oxidation induced during the production process [156, 157]. In this case an industrial product was

utilized, and a relatively low temperature was chosen for the melt compounding process (170 °C), consequently a negligible oxidation process can be obtained in the case of pure LLDPE sample.
As reported by Pandey et al. in a review on the degradability of polymer nanocomposites, the presence of this functionalities in the material can be explained considering that the degradation of hydrocarbon chains leads to the formation of hydroxyl (O-H) and carbonylic (C=O) groups [158]. The presence of these functionalities only for the nanofilled samples can be justified in different ways. According to the observation of Pandey and Singh, once oxygen reaches the matrix, it remains for longer time in the case of nanofilled polymers, because the nanoparticles may interfere in the path, thus O_2 is available to initiate the degradation process for more time than for the neat polymer [159]. Moreover, Huaili et al. studied the photo-oxidative degradation of PE/OMMT nanocomposites compared with neat polyethylene. By FT-IR analysis they found a considerable increase in the intensity of the carbonyl signal increasing the irradiation time in the PE/OMMT, while in the pure PE the intensity in the carbonyl region was significantly less [160]. It is also possible that oxygen atoms physically adsorbed on the surface of fumed silica nanoparticles favour the local oxidation process of the polyethylenic matrix, leading to the formation of C=O bonds in correspondence to the interface. Increasing the filler content the availability of oxygen atoms for the oxidation process is enhanced, leading to the formation of an higher number of C=O groups at the interface.

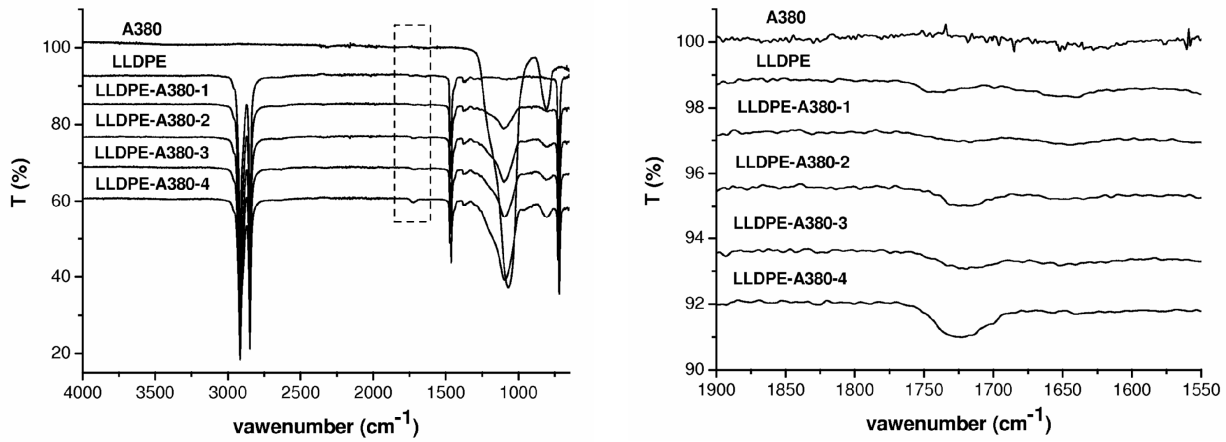

Figure 4.21 Infrared spectroscopy of A380 powder, LLDPE and A380 filled nanocomposites (the curves were shifted along the y-axis). (a) full scale, (b) zoom around 1700 cm^{-1}

The intensity of C=O peak could be compared with that of the other reflections in the spectrum. For example it is possible to normalize the adsorbed intensity of this peak (A_{1720}) with that of the reflection associated to CH_2 stretching at around 2920 cm^{-1} (A_{2920}), taking into account the reduced

amount of the organic phase due to the presence of the filler. In Table 4.9 relative intensity values of the carbonylic group peak of A380 powder, LLDPE and A380 filled nanocomposites (A_{1720}/A_{2920}) are reported. It is evident that C=O peak intensity is gradually increasing with the filler content.

Sample	**A_{1720}/A_{2920} (x 10^{-3})**
A380	-
LLDPE	-
LLDPE-A380-1	5.2
LLDPE-A380-2	7.1
LLDPE-A380-3	14.9
LLDPE-A380-4	24.4

Table 4.9 Relative intensity of the carbonylic group peak of A380 powder, LLDPE and A380 filled nanocomposites

Taking into account the literature references and the observed FT-IR spectra, it can be hypothesizes that when the nanofiller is added to the matrix, the high shear forces during melt compounding and the availability of oxygen atoms at the filler surface can be responsible to a considerable oxidation of polymeric chain around fumed silica nanoparticles, leading to the formation of carbonylic groups at the interface. Even if the intensity of the signal associated to C=O group from IR analysis is relatively low, it has to be considered that all the carbonylic groups were formed around the filler surface.

As can be clearly seen in Figure 4.21, FT-IR analysis does not evidence the presence of OH groups, that generally are associated to reflection peaks at about 3400 cm^{-1}. It has to be considered that, if compared with CH_2 or SiO reflections, the intensity of hydroxyl group peak is relatively low, and more sophisticated analyses should be conducted to detect the presence of OH functionalities in the samples. In any case the presence of silanol groups on the surface of silica powders is well documented in literature, and several attempts were made to estimate the number of hydroxyl groups on the silica surface [161-166].

Consequently it is possible to hypothesize the presence of physical polymer-filler interaction based on hydrogen bonding between C=O groups (and probably OH groups) of the matrix and Si-OH functionalities present on the surface of the nanofiller.

4.2 Viscoelastic behaviour in the molten state

In Figure 4.22 dynamic rheological properties of LLDPE- 2 vol% fumed silica nanocomposites are represented. Regardless to the surface area, it is evident that the introduction of the nanofiller in LLDPE leads to a very strong enhancement both of the storage (G') and shear moduli (G''), and of the viscosity (η), especially at low frequencies, while loss tangent values are strongly lowered, with a shift of the tanδ peak towards higher frequencies. These observations are in agreement with the scientific literature on the rheological properties of nanoparticles filled systems [22, 167-172]. It is important to underline that in the low frequency region G' of nanocomposites becomes frequency independent, which is the characteristic behaviour of solid-like materials (solid-like behaviour).

If in the case of clay filled polymeric nanocomposites the observed G' behaviour in the low frequency region indicates strong interactions between clay layers and polymeric matrix, in fumed silica nanocomposites the solids like behaviour is generally due to particle-particle interactions and the consequent formation of a network structure [22]. As reported in Chapter 2.1.3, these interactions may arise from hydrogen bonds of silanolic groups present on the surface of primary nanoparticles. At high test frequencies these bonds are broken by shear forces, consequently G' begins to be near to that of the unfilled matrix, while the viscosity begins to drop at values comparable to that of pure LLDPE.

The effect of the surface area can be detected only at low frequencies, with arising shear viscosity as the surface area of the nanofiller increases. It is probable that the reduction of the primary nanoparticle diameter for high surface area silicas results in an higher number of sylanol groups on the surface of the aggregates, leading to an higher number of hydrogen bonds and to stronger interactions between nanoparticles.

For the same reason the presence of physical interactions between the nanoparticles leads to a considerable lowering of tanδ values, more consistent than that predictable on the basis of the traditional rule of mixtures. The tanδ peak indicates the beginning of the breakdown of the silica network, and the little shift of the peak towards higher frequencies induced by high surface area silicas is due to stronger interparticle interactions, favoured by the presence of silanol groups at the surface.

Moreover, fumed silica nanocomposites seem to be insensitive to the surface functionalization of the nanoparticles, being the rheological properties of LLDPE-Ar816-2 sample similar to that of

LLDPE-A200-2 sample. Even if in the work of Cassagnau [22] the presence of hydrocarbon functionalities on the surface of fumed silica nanoparticles results in a breakdown in the particle interactions, with a decrease of G' values, it is possible that in this case the grafting density of Ar816 powder is too low to achieve this effect, or the grafted hydrocarbon chains are too short to create a steric repulsion between silica particles.

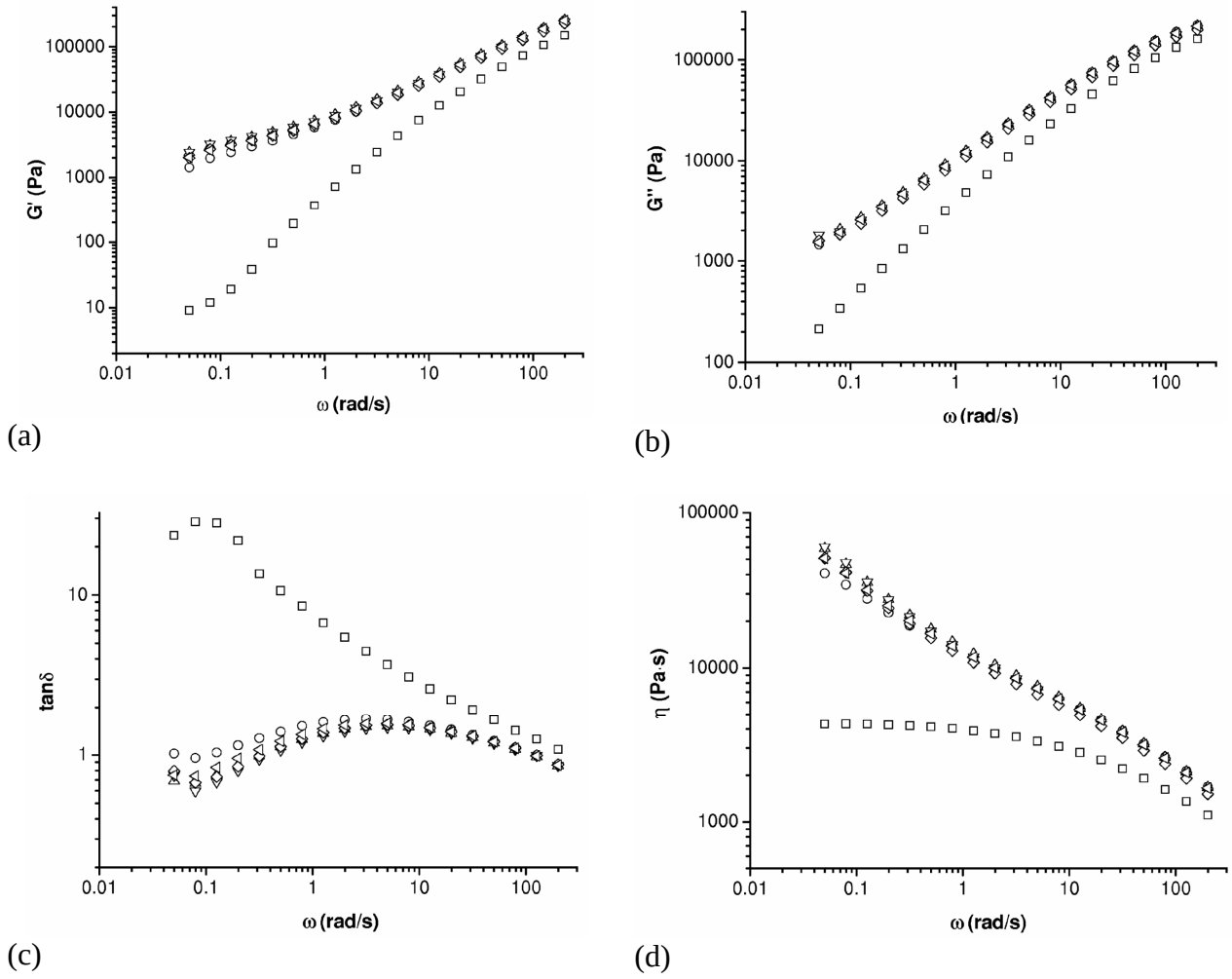

Figure 4.22 Dynamic rheological properties of LLDPE- 2 vol% fumed silica nanocomposites (T=190 °C). (a) G', (b) G'', (c) tanδ, (d) η. (□) LLDPE, (○) LLDPE-A90-2, (△) LLDPE-A200-2, (▽) LLDPE-A300-2, (◇) LLDPE-A380-2, (◁) LLDPE-Ar816-2

The results obtained by using fumed silica nanoparticles can be compared with rheological properties of precipitated silica and glass beads microcomposites, and in Figure 4.23 a comparison of dynamic rheological properties of LLDPE- 2 vol% micro and nanocomposites is reported. It is evident that the behaviour of LLDPE-S160-2 sample is similar to that of fumed silica nanocomposites, with a strong increase of G' and G'' and the presence of the solid-like behaviour

in the low frequency regime, associated to a decrease of tanδ with a shift of the peak towards higher frequencies. Even in this case dynamic shear viscosity curves do not show a Newtonian plateau at low frequencies, probably because of the previously discussed network formation mechanism. When glass microbeads are used as filler, the traditional trend of the rheological behaviour of microparticles filled polymeric systems can be detected [99-102]. Only marginal improvements of G', G'' and η can be measured, especially at low frequencies, while tanδ is only slightly reduced. The great difference between rheological properties of traditional glass microbeads filled systems and precipitated silica microparticles composites is mainly due to the different surface area values (168 m^2/g against 0.45 m^2/g) of the particles.

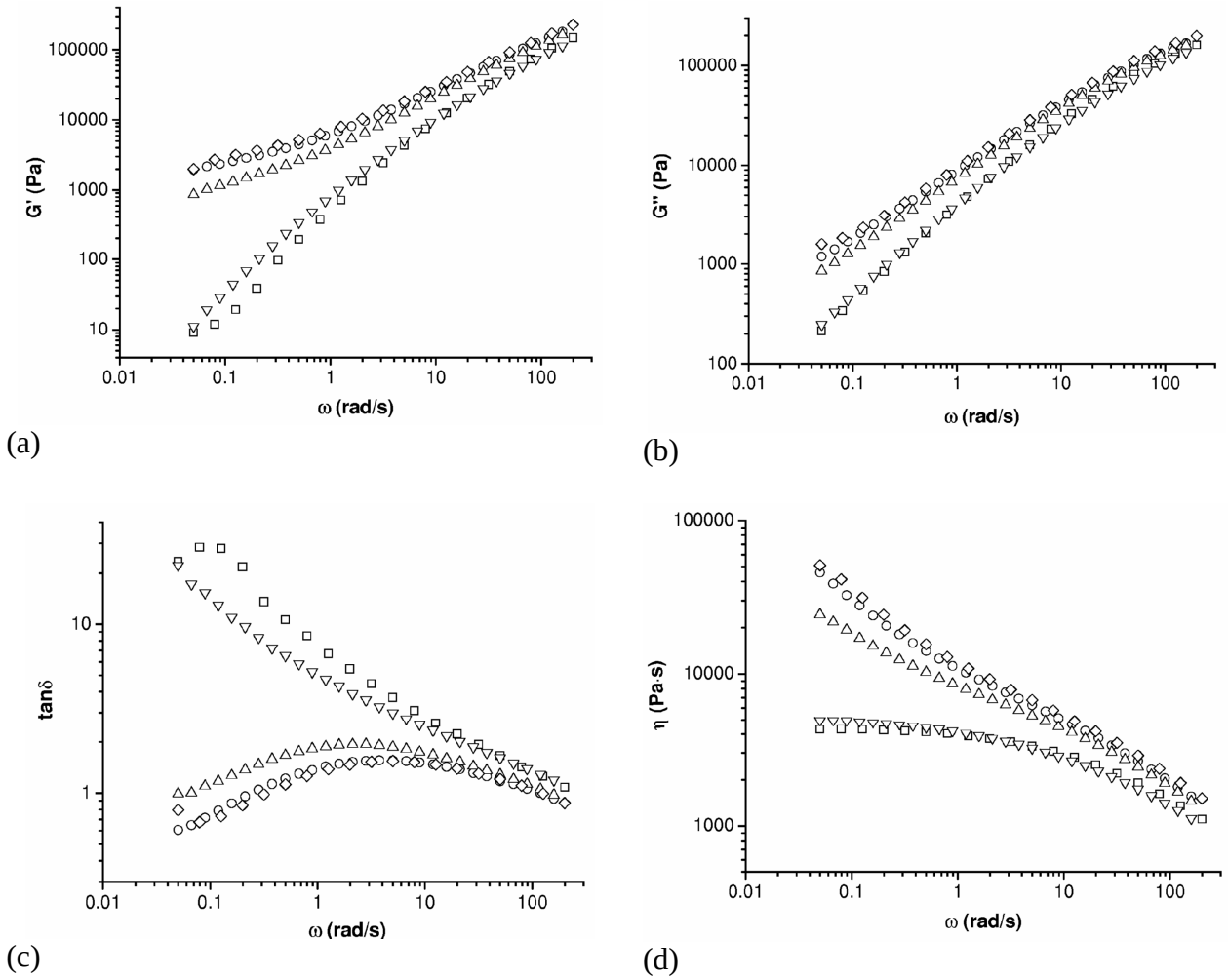

Figure 4.23 Comparison of dynamic rheological properties of LLDPE- 2 vol% composites. (a) G', (b) G'', (c) tanδ, (d) η. (□) LLDPE, (▽) LLDPE-Glass-2, (△) LLDPE-S160-2, (○) LLDPE-A200-2, (◇) LLDPE-A380-2

In order to obtain a deeper comprehension of the influence of the filler typology on the rheological properties of the resulting material, dynamic tests at different temperatures, ranging from 125 °C to

210 °C, were conducted. Dynamic storage modulus (G') and loss modulus (G'') of LLDPE– 2 vol% composites at different temperatures are respectively reported in Figure 4.24 and in Figure 4.25. Through the frequency-temperature superposition principle it was possible to construct G' and G'' master curves (Figure 4.26), in order to evaluate the dynamic behaviour of the materials over a wider frequency range.

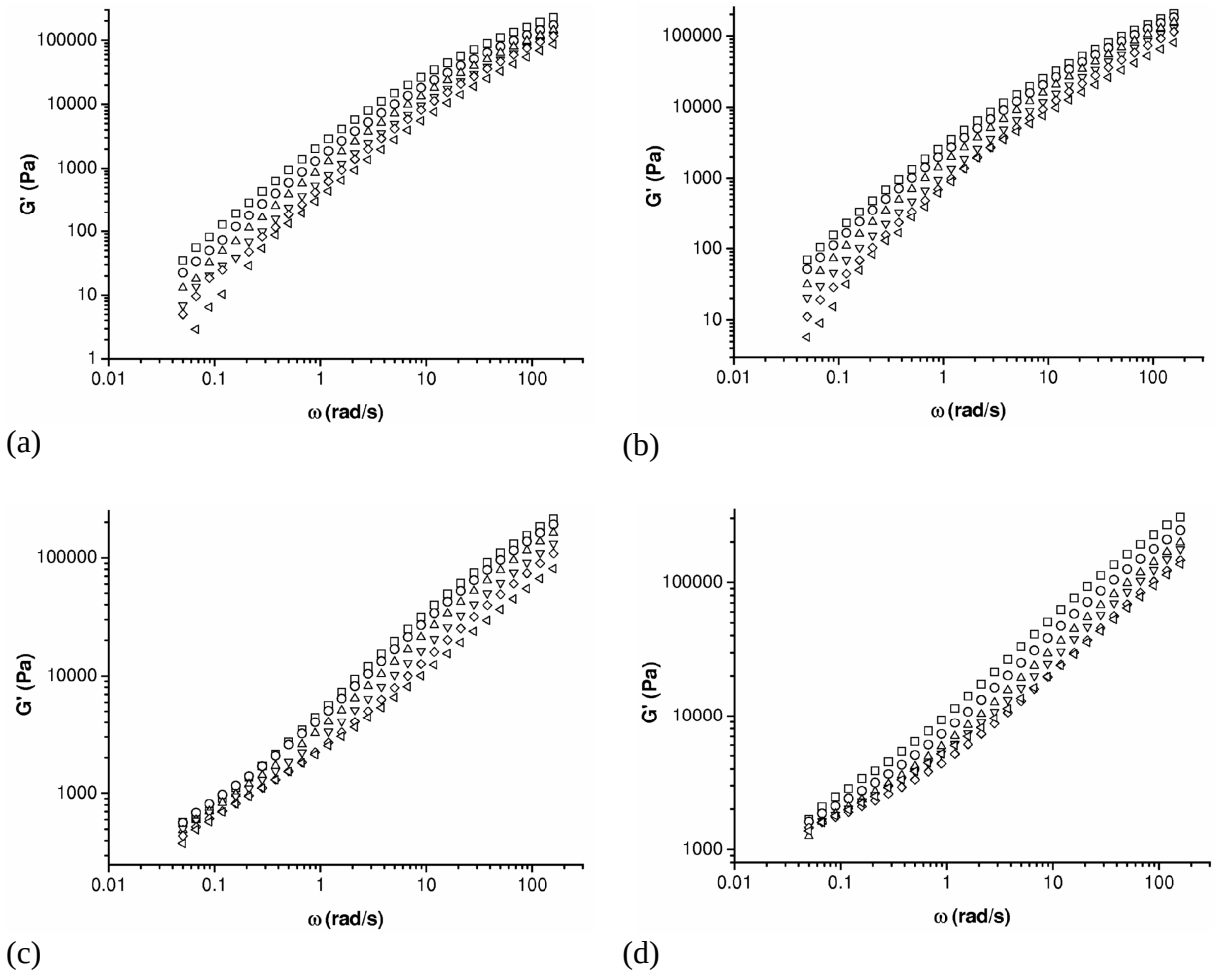

Figure 4.24 Storage modulus (G') of LLDPE– 2vol% composites at different temperatures. (a) LLDPE, (b) LLDPE-Glass-2, (c) LLDPE-S160-2, (d) LLDPE-A380-2. (□) 125 °C, (○) 135 °C, (△) 150 °C, (▽) 170 °C, (◇) 190 °C, (◁) 210 °C

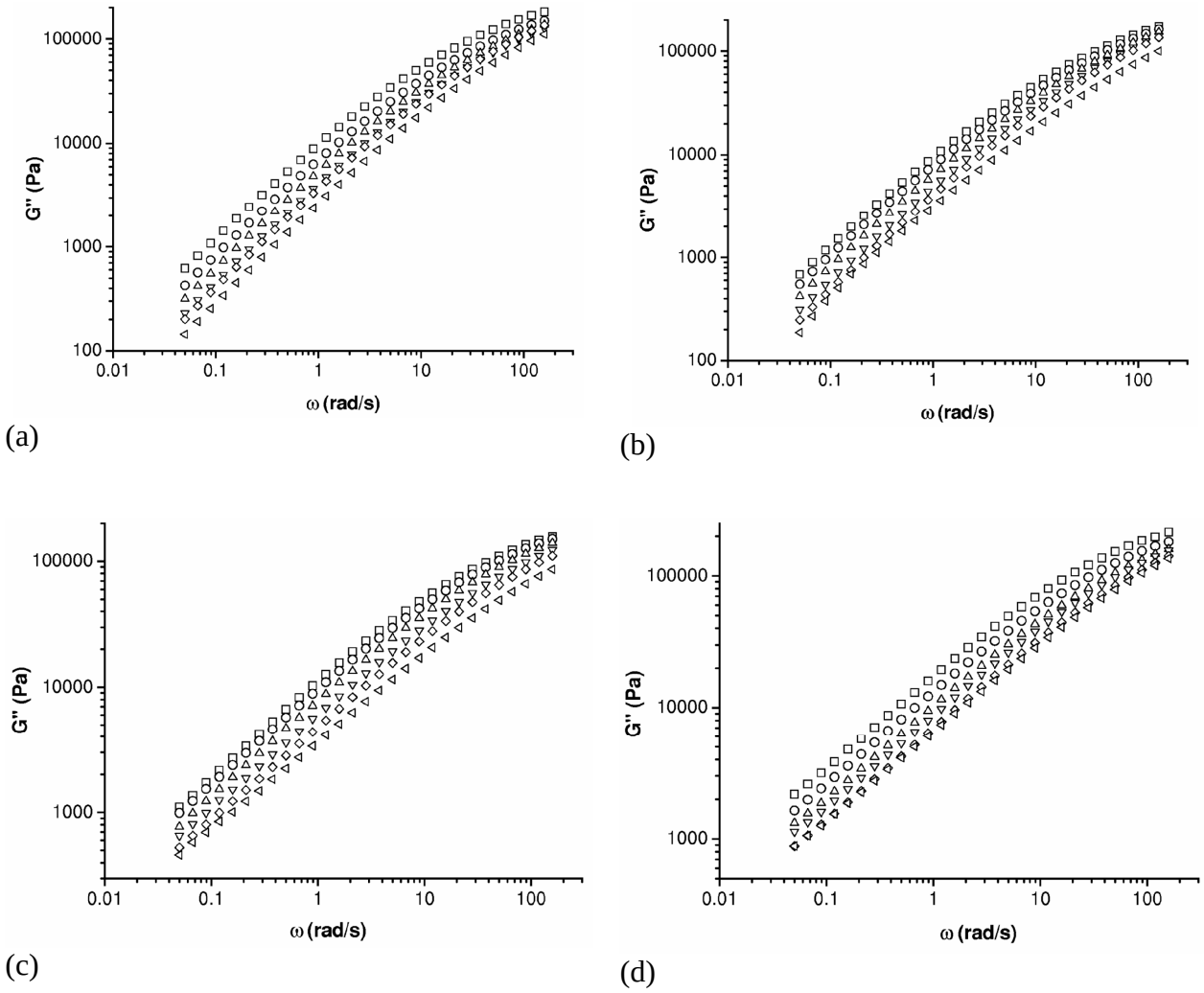

Figure 4.25 Loss modulus (G'') of LLDPE– 2vol% composites at different temperatures. (a) LLDPE, (b) LLDPE-Glass-2, (c) LLDPE-S160-2, (d) LLDPE-A380-2. (□) 125 °C, (○) 135 °C, (△) 150 °C, (▽) 170 °C, (◇) 190 °C, (◁) 210 °C

The analyzed frequency range is only slightly extended by the application of the superposition principle, and the observations previously reported are confirmed. G' and G'' are strongly increased by the presence of fumed silica nanoparticles and precipitated silica microparticles, with the appearance of G' plateau at low frequencies (solid-like behaviour). For glass filled composites only marginal improvements of G'' and G'' can be detected.

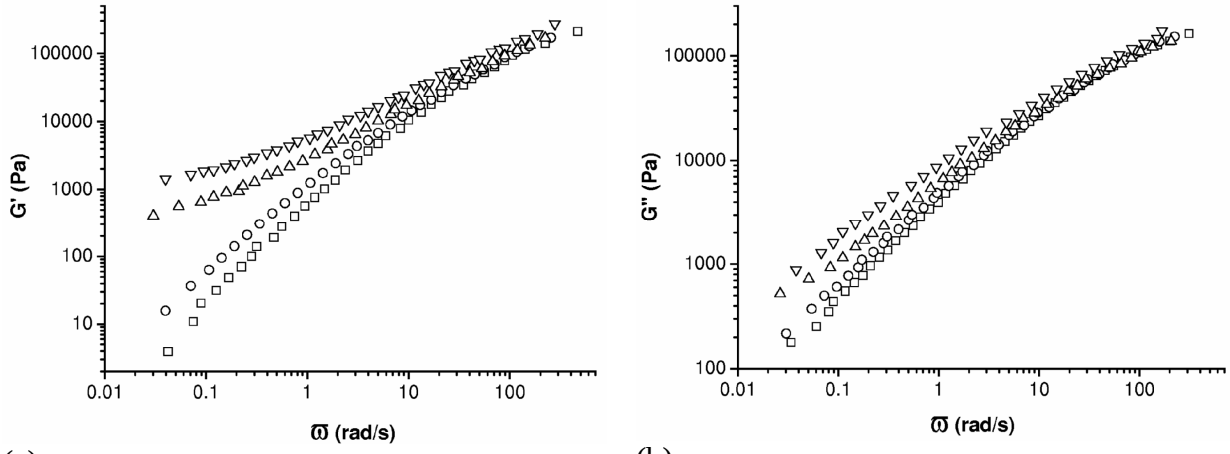

(a) (b)

Figure 4.26 Master curves of LLDPE– 2vol% composites according to the time-frequency superposition principle (T_0=170 °C). (a) G', (b) G''. (□) LLDPE, (○) LLDPE-Glass-2, (△) LLDPE-S160-2, (▽) LLDPE-A380-2

It is also possible to analyze the trends of the shift-factor at the different temperatures, considering G' curves and keeping a reference temperature T_0=170 °C (the same analysis can be done considering G'' curves). As reported in Chapter 2.2.3, at temperatures far above the glass transition of the material, Arrhenius equation can be adopted in order to fit shift factor data (Equation 4.1). In Table 4.10 shift factor values of LLDPE -2 vol% composites at different temperatures are reported, while in Table 4.11 activation energy (E_a) values of LLDPE – 2 vol% composites according to Arrhenius equation are summarized.

Equation 4.1

$$\ln a(T)_{T_0} = \frac{E_a}{R}\left(\frac{1}{T} - \frac{1}{T_0}\right)$$

E_a value obtained for unfilled LLDPE is in accordance with literature data [101], while all the composites show lower energy of activation values. Moreover E_a of LLDPE-A380-2 sample is even lower than that of LLDPE-S160-2 and LLDPE-Glass-2 filled sample. Even if the differences in E_a values are not so much pronounced and further investigations would be necessary to have a complete comprehension of the molecular dynamics of the investigated materials in the molten state, it is possible to explain the lowering of activation energy referring to the polymer-filler interaction. As reported by Ajayan et al. [4], when the interparticle distance is lower than the radius of gyration (R_g) of the macromolecules, a drop of the T_g of the material, due to a decrease of the density of the polymeric chains, can be usually detected. According to the data reported in polymer

handbooks [132], a typical value for the radius of gyration for our LLDPE matrix is about 13 nm. According to TEM observations on LLDPE-A380-2 nanocomposite it is evident that many zones of the samples present interparticles spaces of about 30 nm. Consequently it is possible to hypothesize a local chain depletion in these zone, with a consequent local T_g drop and lower energy of activation values for the viscous flow.

T	1/T	ln(a(T))			
°C	K^{-1}	LLDPE	LLDPE-Glass-2	LLDPE-S160-2	LLDPE-A380-2
125	0.002513	1.082	0.760	0.668	0.852
135	0.002451	0.691	0.553	0.576	0.461
150	0.002364	0.345	0.276	0.345	0.184
170	0.002257	0	0	0	0
190	0.00216	-0.115	-0.231	-0.276	-0.230
210	0.00207	-0.461	-0.484	-0.507	-0.276

Table 4.10 Shift factor values of LLDPE -2 vol% composites from rheological tests at different temperatures (T_0=170 °C)

Sample	E_a (kJ/mol)
LLDPE	27.0 ± 2.6
LLDPE-Glass-2	23.0 ± 0.7
LLDPE-S160-2	23.0 ± 0.8
LLDPE-A380-2	20.2 ± 3.0

Table 4.11 Energy of activation (E_a) values of LLDPE- 2vol% composites according to Arrhenius equation

The effect of the filler content on the composite rheology can be evaluated from G' and G'' curves of LLDPE and relative composites at 190 °C. These curves are reported in Figure 4.27 and in Figure 4.28, while in Figure 4.29 and in Figure 4.30 loss tangent (tanδ) and viscosity (η) values are represented. It can be observed that G' increases proportionally to the filler content. In the case of glass microbeads filled samples the increase of G' is very limited in all the frequency range. For precipitated silica microcomposites the observed behaviour is completely different. A strong G' enhancement can be easily detected even at relatively low silica loading, and the presence of the

solid-like behaviour begins to be evident from filler contents of 2 vol%. The same considerations are valid also for fumed silica nanocomposites, but in this case G' increase is even more evident, especially when high surface area nanoparticles are used.

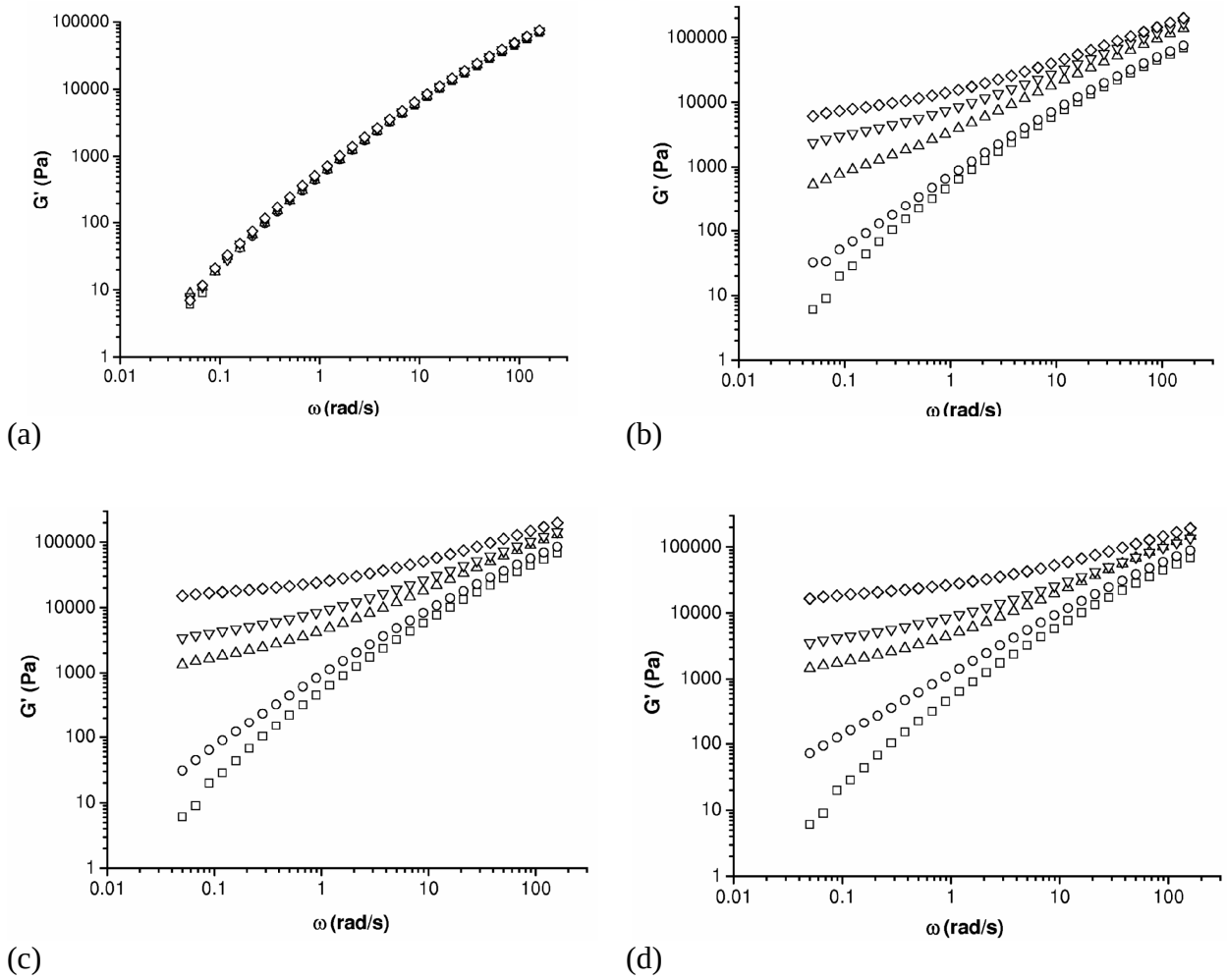

Figure 4.27 Storage modulus (G') curves of LLDPE and relative composites (T=190 °C). (a) LLDPE-Glass-x, (b) LLDPE-S160-x, (c) LLDPE-A200-x, (d) LLDPE-A380-x. (□) LLDPE, (○) x=1 vol%, (△) x=2 vol%, (▽) x=3 vol%, (◇) x=4 vol%

Similar observations arise from the analysis of G'' trends of LLDPE and relative composites. G'' increase for glass microbeads filled composites is marginal, while for S160 microcomposites and fumed silica composites the enhancement of loss modulus is very evident and proportional to the filler content, especially at low frequencies.

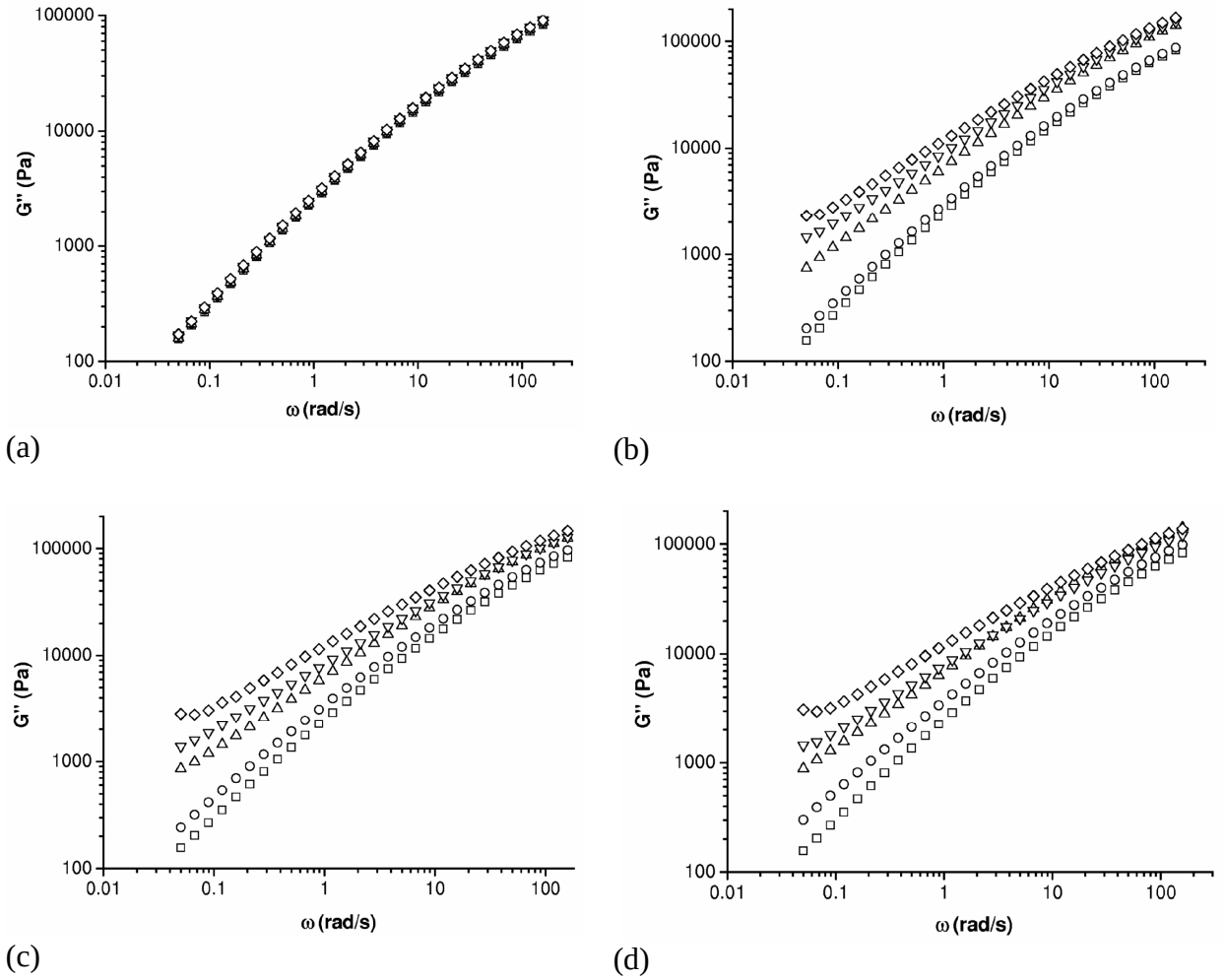

Figure 4.28 Loss modulus (G'') curves of LLDPE and relative composites (T=190 °C). (a) LLDPE-Glass-x, (b) LLDPE-S160-x, (c) LLDPE-A200-x, (d) LLDPE-A380-x. (□) LLDPE, (○) x=1 vol%, (△) x=2 vol%, (▽) x=3 vol%, (◇) x=4 vol%

From the analysis of tanδ curves the difference in the rheological behaviour between glass microbeads and the other fillers is confirmed. If glass filled microcomposites are considered, the decrease of the loss tangent is very limited even at high filler contents. In the case of S160 filled composites it is evident a strong decrease of tanδ values with the filler content. Moreover there is a shift of the peak of tanδ towards higher frequencies. Even in this case this evidence can be justified considering the formation of a stronger silica network for the highly filled samples, because of the higher availability of silanol groups on the filler surface.

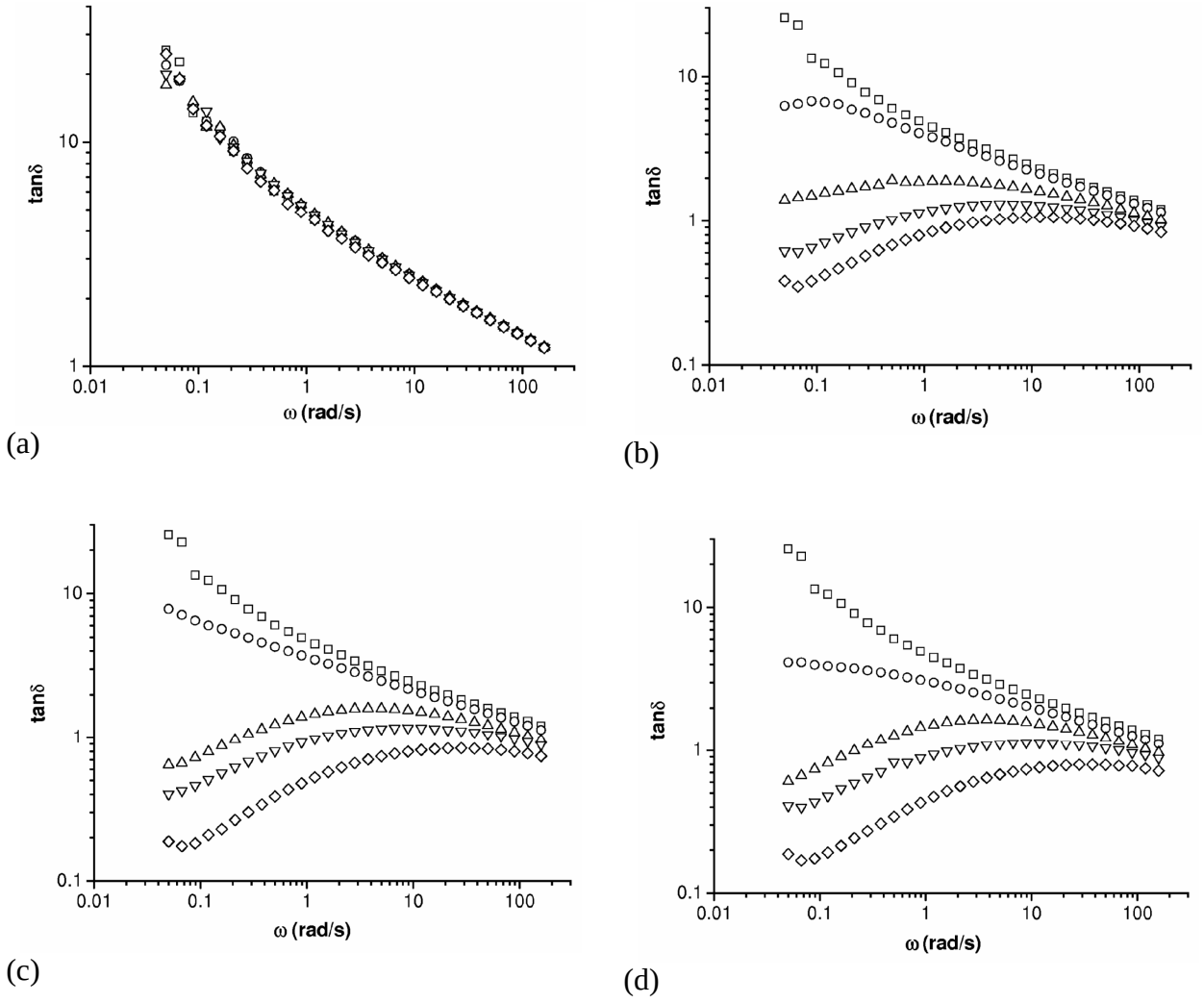

Figure 4.29 Loss tangent (tanδ) curves of LLDPE and relative composites (T=190 °C). (a) LLDPE-Glass-x, (b) LLDPE-S160-x, (c) LLDPE-A200-x, (d) LLDPE-A380-x. (□) LLDPE, (○) x=1 vol%, (△) x=2 vol%, (▽) x=3 vol%, (◇) x=4 vol%

A similar behaviour can be observed for shear viscosity (η) trends. Even in this case glass microcomposites showed only marginal improvements of the viscosity, with the presence of a Newtonian plateau at low frequencies. For precipitated silica microcomposites and fumed silica nanocomposites viscosity enhancement is very pronounced, especially at low frequencies and for high silica loadings. The pseudoplastic plateau disappears for filler contents higher than 2 vol%, probably for the presence of the network formed by silica aggregates through hydrogen bonds.

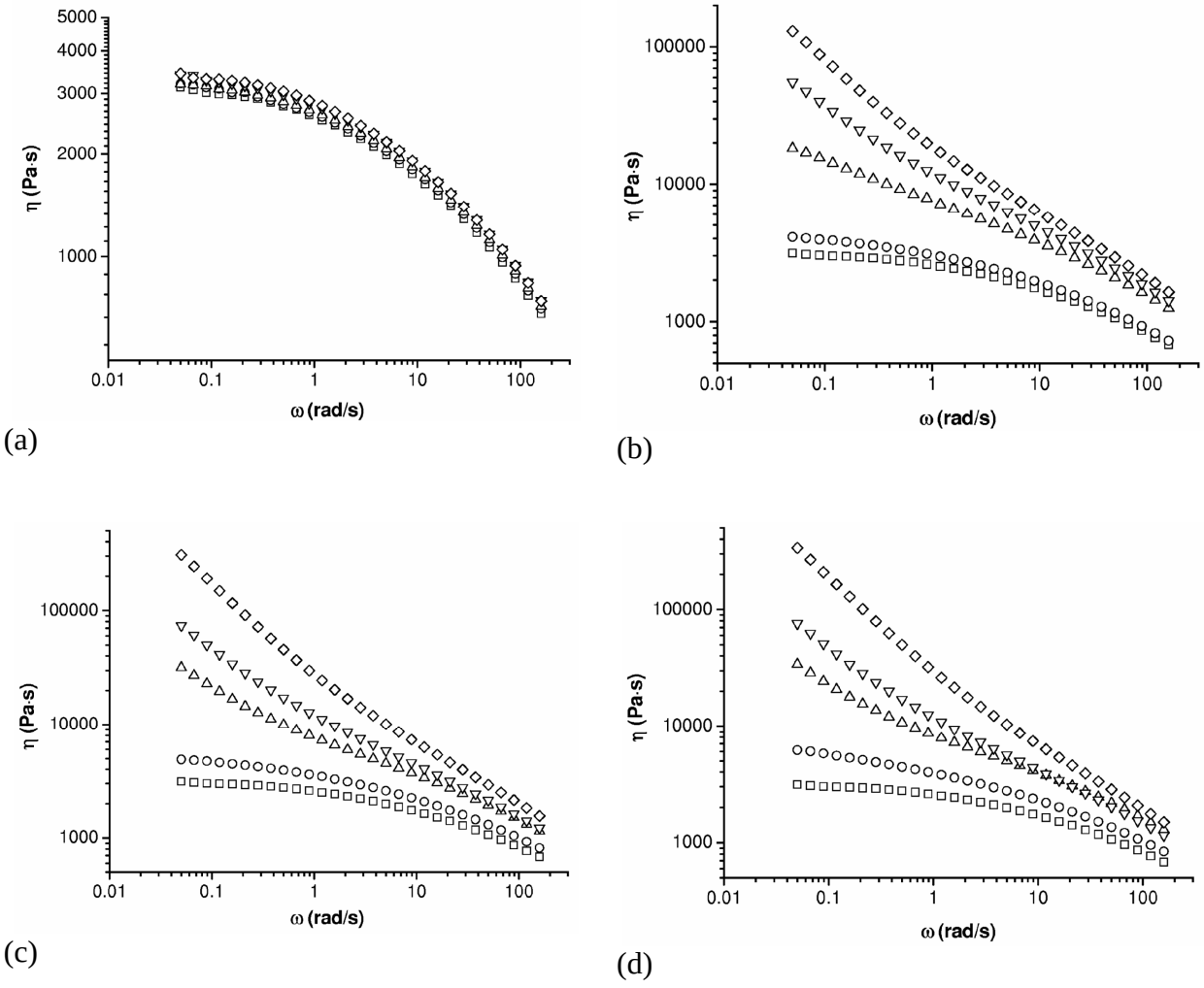

Figure 4.30 Viscosity (η) curves of LLDPE and relative composites (T=190 °C). (a) LLDPE-Glass-x, (b) LLDPE-S160-x, (c) LLDPE-A200-x, (d) LLDPE-A380-x. (□) LLDPE, (○) x=1 vol%, (△) x=2 vol%, (▽) x=3 vol%, (◇) x=4 vol%

In Figure 4.31 relative viscosity of LLDPE and relative composites, both in the low and in the high frequency region, are reported. It is evident that the enhancement of the viscosity is much more pronounced at low frequencies, when the interparticles forces due to hydrogen bonding are more effective. While at 0.05 rad/s the viscosity of the LLDPE-A380-4 sample is about 100 times higher than that of the pure LLDPE, at 158 rad/s the viscosity of the same sample is only 2.4 times higher than that of the unfilled sample, confirming that in the high frequency region the shear forces lead to the breakage of the silica network, with a considerable reduction of viscosity values.

In order to compare the rheological properties of the prepared composites with traditional models, Batchelor relation was adopted [173]. This model was elaborated to calculate the relative viscosity

of polymer composites containing colloidal hard spheres in the limit of low shear rate, and it is based on the following equation :

Equation 4.2

$$\frac{\eta}{\eta_0} = 1 + 2.5\phi + 6.2\phi^2$$

where η and η_0 are the viscosity of the composite and of the matrix, respectively. It can be easily noted that the proposed model is an extension of the Einstein equation [174], originally proposed to predict the effect of a rigid filler on the viscosity of a Newtonian liquid in the case of diluite suspension. It is evident that Batchelor model is well followed by glass filled microcomposites, both in the low and in the high frequency regions, while in the case of precipitated silica microcomposites and fumed silica nanocomposites the relative viscosity increase is largerly underestimated. This means that traditional models are unsuitable to catch the rheological behaviour of polymeric composites containing high surface area fillers.

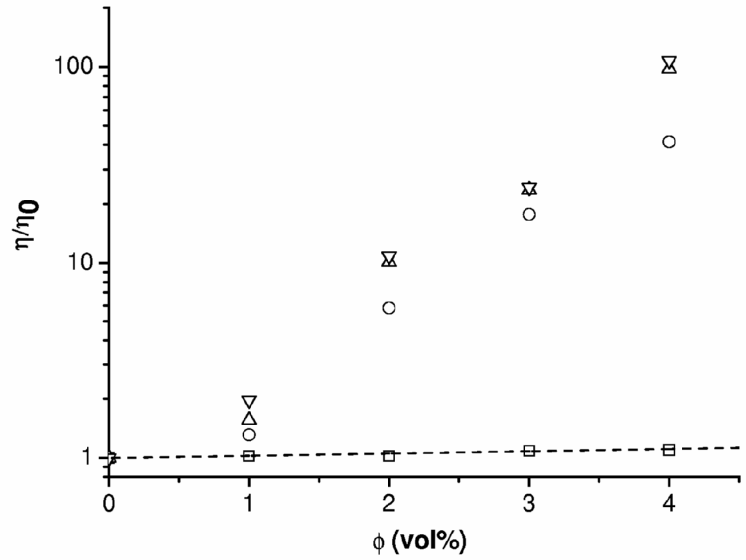

(a)

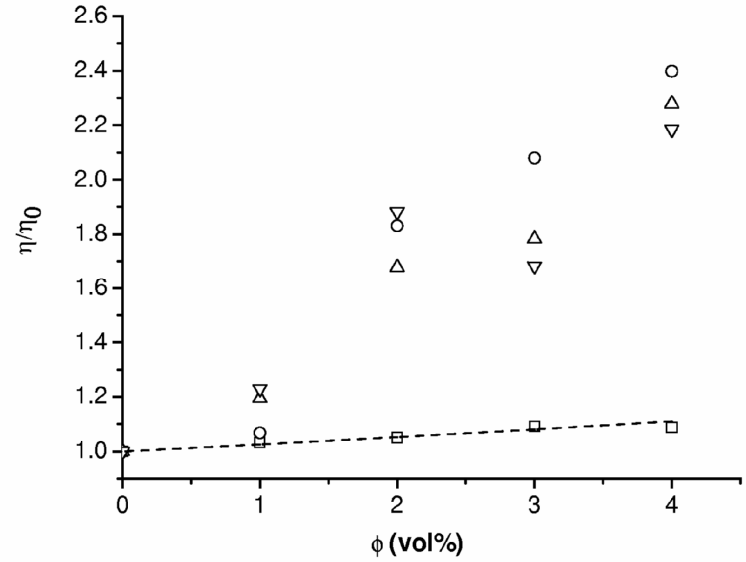

(b)

Figure 4.31 Relative viscosity values of LLDPE and relative composites (T=190 °C) at (a) 0.05 rad/s and (b) 158 rad/s. (□) LLDPE-Glass-x, (○) LLDPE-S160-x, (△) LLDPE-A200-x, (▽) LLDPE-A380-x. The dashed line represent the theoretical prediction of the relative viscosity according to the Batchelor model

As reported in Chapter 2.2.1, quite a variety of non-Newtonian viscosity models, constituted by 2, 3, 4 or 5 elements, have been proposed in the literature [102]. In this case the difficulty of finding a suitable model arises from the difference of viscosity trends between unfilled LLDPE and fumed silica nanocomposites. Among different models, De Kee and Turcotte in 1980 proposed a three-parameter model [175], as reported in Equation 4.3.

Equation 4.3

$$\eta = \frac{\tau_0}{\omega} + \eta_1 e^{-t_1 \omega}$$

The first term on the right side of the equation involves a constant yield stress (τ_0). This parameter is more closely related to the breakage of the solid network formed by silica aggregates. The limiting viscosity (η_1) represent the zero-shear viscosity values when the solid network is absent, while t_1 is a characteristic time, related to the velocity of the viscosity drop at high frequencies. In this work a modification of the original De Kee-Turcotte model was proposed, in order to obtain a better fit of the data even in the high-frequency regime, as reported in Equation 4.4 :

Equation 4.4

$$\eta = \frac{\tau_0}{\omega} + \eta_1 e^{-t_1 \omega^{\alpha}}$$

A comparison between the traditional De Kee-Turcotte model and the modified one was then conducted on pure LLDPE and A380 filled samples, as reported in Figure 4.32. It is evident that the modified De Kee-Turcotte model can more satisfactorily fit experimental data, especially in the high frequency region. For this reason the proposed modified model was used to fit all the viscosity curves of LLDPE and of all the prepared composites. In Figure 4.33 experimental viscosity curves of LLDPE and relative composites at 190 °C, fitted according to the modified De Kee- Turcotte model, are reported. It is evident that this model is able to satisfactorily fit all the rheological curves of the considered samples, even when an high filler content is adopted.

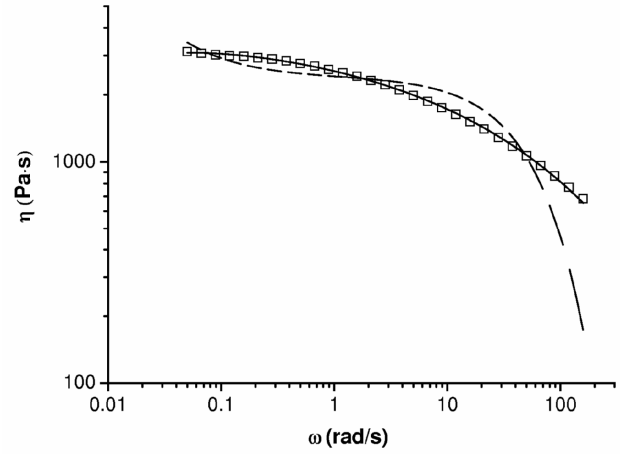

(a)

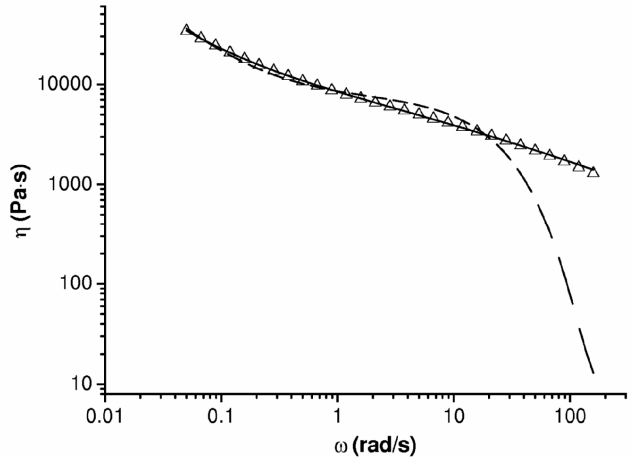

(b)

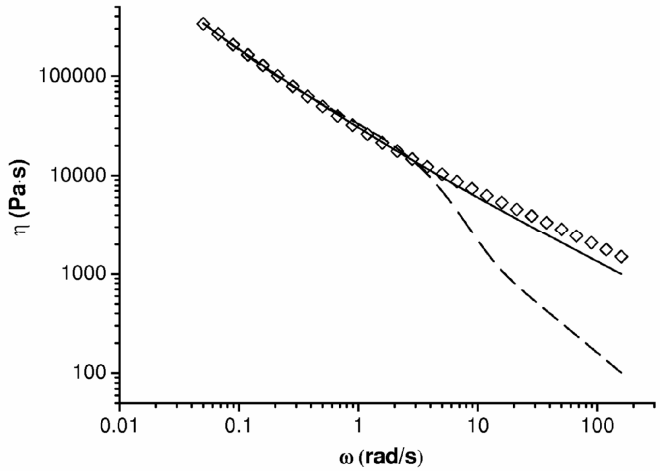

(c)

Figure 4.32 Experimental viscosity (η) curves of (a) LLDPE and (b-c) LLDPE-A380-x nanocomposites (T=190 °C). (□) LLDPE, (△) LLDPE-A380-2, (◊) LLDPE-A380-4. The dashed lines represent the fitted data according to the traditional De Kee-Turcotte model, while the continuous ones the fitted data according to the modified De Kee-Turcotte model

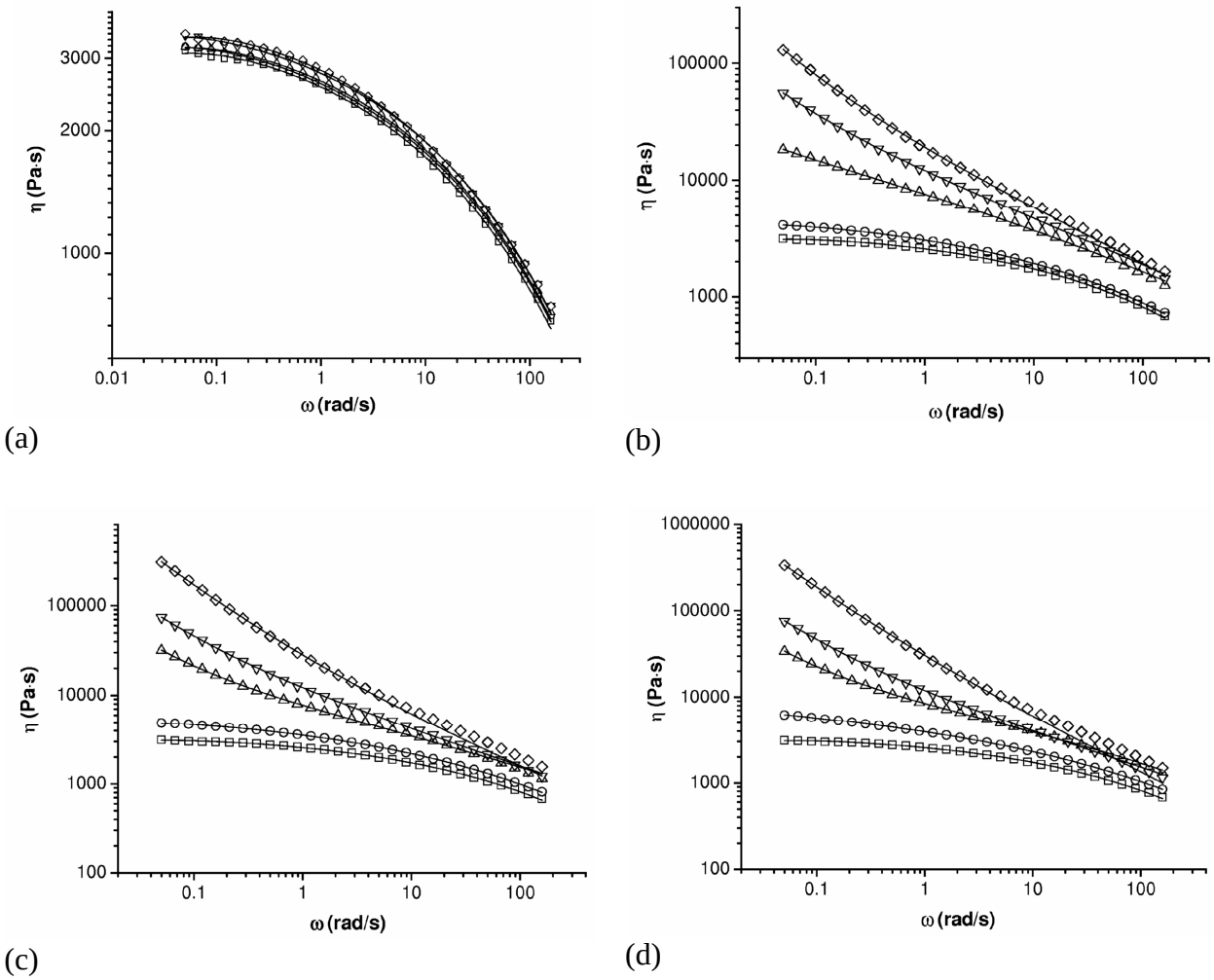

Figure 4.33 Experimental viscosity (η) curves of LLDPE and relative composites (T=190 °C). (a) LLDPE-Glass-x, (b) LLDPE-S160-x, (c) LLDPE-A200-x, (d) LLDPE-A380-x. (□) LLDPE, (○) x=1 vol%, (△) x=2 vol%, (▽) x=3 vol%, (◇) x=4 vol%. The continuous lines represent the fitted data according to the Modified De Kee-Turcotte model

It is now important to evaluate the influence of the filler content and typology on the fitting parameters, as reported in Figure 4.34. It is evident that yield stress (τ_0) is practically zero for pure LLDPE and glass filled composites. For S160 filled composites yield stress begins to increase after a filler content of 2 vol%, while for fumed silica nanocomposites τ_0 increases for a lower filler content. The concentration at which yield stress begins to increase can be interpreted as a percolation threshold, a critical concentration at which the interaction between the particles leads to a formation of a solid network, and the viscosity greatly increases. After the percolation threshold traditional pseudoplastic behaviour of LLDPE, with a Newtonian plateau in the low frequency regime, disappears. The same consideration holds for limiting viscosity (η_1). For pure LLDPE and glass filled composites this parameter is around 3000-4000 Pa·s and can be considered as the zero

shear viscosity. For the other composites η_1 begins to increase for filler contents higher than 2 vol%. It is important to underline that by using elevated silica volume fractions (3-4 vol%) η_1 is around 10^{30} Pa·s, that is the typical viscosity values of a solid material, in accordance of the solid-like behaviour observed for G' curves in the case of S160 filled microcomposites and fumed silica nanocomposites. Even t_1 give us the same picture on the microstructure of the prepared composites. In fact, this parameter rules the viscosity drop at high frequencies. For glass filled composites t_1 is practically the same of that of pure LLDPE, while for S160 and fumed silica composites the characteristic time begins to increase for silica contents higher than 2 vol%, that can be considered the percolation threshold for the rheological properties of the prepared composites. For the same reason α parameter is practically insensitive to the filer content for glass filled composites, while for S160 and fumed silica filled samples α considerably drops with the filler content.

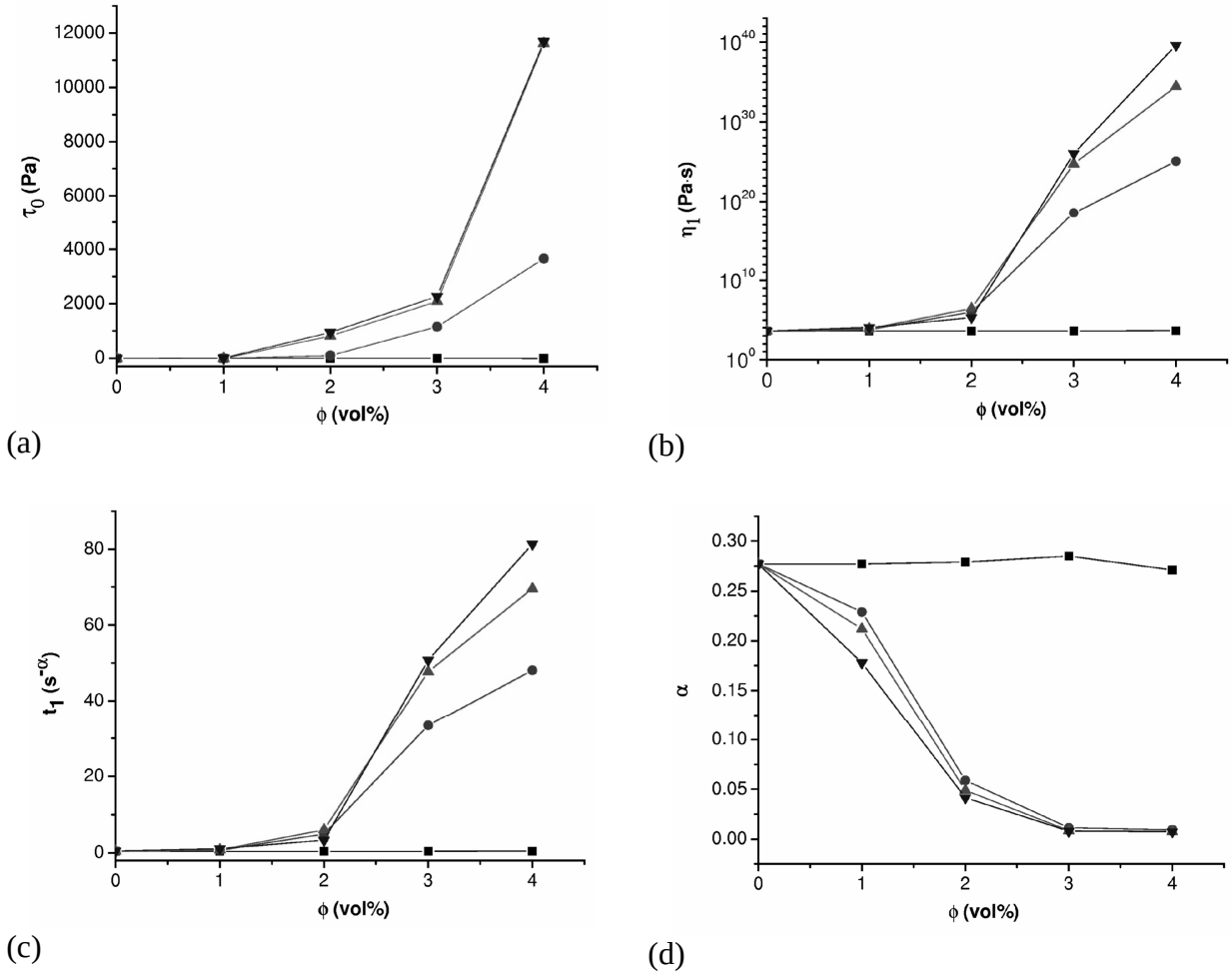

Figure 4.34 Evaluation of the Modified De Kee- Turcotte parameters derived from the fitting of the viscosity curves of LLDPE and relative composites.). (a) τ_0, (b) η_1, (c) t_1, (d) α. (■) LLDPE-Glass-x, (●) LLDPE-S160-x, (▲) LLDPE-A200-x, (▼) LLDPE-A380-x

4.3 Viscoelastic behaviour in the solid state

4.3.1 Elastic modulus evaluation

In Figure 4.35 representative curves of quasi-static tensile tests for the evaluation of the elastic modulus of LLDPE - 2 vol% fumed silica nanocomposites are represented, while all the results are summarized in Table 4.12. It is evident the strong increase of the stiffness of the material with the surface area of the nanofiller. For example LLDPE-A380-2 sample shows an improvement of the elastic modulus of about 43 %. It is important to underline that the elastic modulus of functionalized nanoparticles (Ar816) filled sample is equal to that of the composite filled with untreated nanofillers with the same surface area (A200). The stiffening effect due to the presence of nanoparticles in polymeric systems is a well known phenomenon, and many papers dealing with this topic can be found in literature [21, 23, 176-185]. Consequently it is possible to conclude that the enhancement of the elastic modulus obtained by using fumed silica nanoparticles is comparable and in many cases superior to the improvements reported in literature on polyolefin based nanocomposite systems.

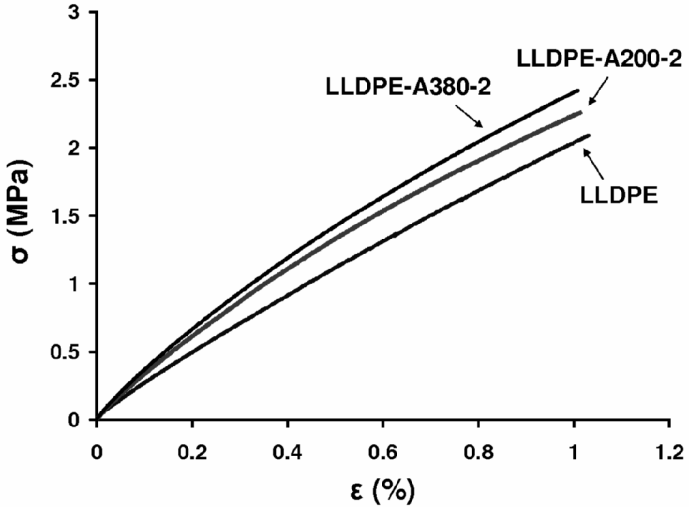

Figure 4.35 Representative curves of quasi-static tensile tests for the evaluation of the elastic modulus of LLDPE - 2 vol% fumed silica nanocomposites

Sample	E (MPa)
LLDPE	199 ± 27
LLDPE-A90-2	262 ± 25
LLDPE-A200-2	274 ± 6
LLDPE-Ar816-2	275 ± 10
LLDPE-A300-2	311 ± 41
LLDPE-A380-2	285 ± 46

Table 4.12 Elastic modulus (E) results of LLDPE - 2 vol% fumed silica nanocomposites

It is now important to compare the results found for fumed silica nanocomposite with that of precipitated silica nanoparticles and glass beads filled microcomposites, assessing also the influence of the filler content on the elastic properties of the prepared samples. In Figure 4.36 elastic moduli of LLDPE and relative composites at different filler contents are represented. It is immediately evident that in all cases the elastic modulus increases with the silica loading. In the case of glass microcomposites the stiffening effect is very limited, while for S160 filled composites a very interesting improvement of the elastic modulus can be detected. The stiffening effect obtained for S160 microcomposites is close to that found for A200 filled nanocomposites, while using fumed silica nanoparticles with the highest surface area (A380) the elastic modulus enhancement is even more pronounced. It can be concluded that quasi-static elastic properties of the composites are only marginally affected by the presence of glass beads at very low silica loadings, while they markedly depend on the surface area of the filler rather than on its dimensions.

An attempt has been made to model the elastic modulus by considering the theoretical approaches developed for traditional microcomposites. The elastic modulus E_c (shear, Young's, or bulk) of a stiff polymer filled with hard, almost spherical, microparticles can be well represented by the modified Kerner equation proposed by Lewis and Nielsen [186] in the following form:

Equation 4.5

$$\frac{E_c}{E_m} = \frac{1 + AB\phi_p}{1 - B\psi}$$

where :

$$A = \frac{7 - 5\nu_m}{8 - 10\nu_m} \qquad B = \frac{E_p/E_m - 1}{E_p/E_m + A} \qquad \psi = 1 - \exp\left(\frac{-\phi_p}{1 - (\phi_p/\phi_m)}\right)$$

In Equation 4.5 E_m and E_p are the elastic modulus of the matrix and of the particles respectively, Φ_p is the particle volume fraction, ν_m is the matrix Poisson ratio, while Φ_m represents the maximum packing fraction of the filler (0.632 for randomly close packed non-agglomerated spherical particles [12]). For as concern the choice of the matrix Poisson's ratio, different experimental values, ranging from 0.4 to 0.5, can be found in literature. In this work a value of 0.44 was chosen for ν_m [187]. It should be noted that, in this model, the Young's modulus does not explicitly depend on the particle size and particle size distribution, while the effect of surface treatment enters only indirectly into the model through the maximum packing fraction Φ_m. The modulus value of the silica particles is not known since its evaluation is of considerable experimental difficulty. In literature it can be easily found that a value of the Young's modulus of about 70 GPa is generally reported for amorphous silicon dioxide [188]. While in the case of glass filled composites Lewis-Nielsen model can be successfully used to fit experimental data, the stiffening effect of the precipitated silica microparticles and fumed silica nanoparticles is in any case much higher than that theoretically predicted on the basis of the modified Kerner equation.

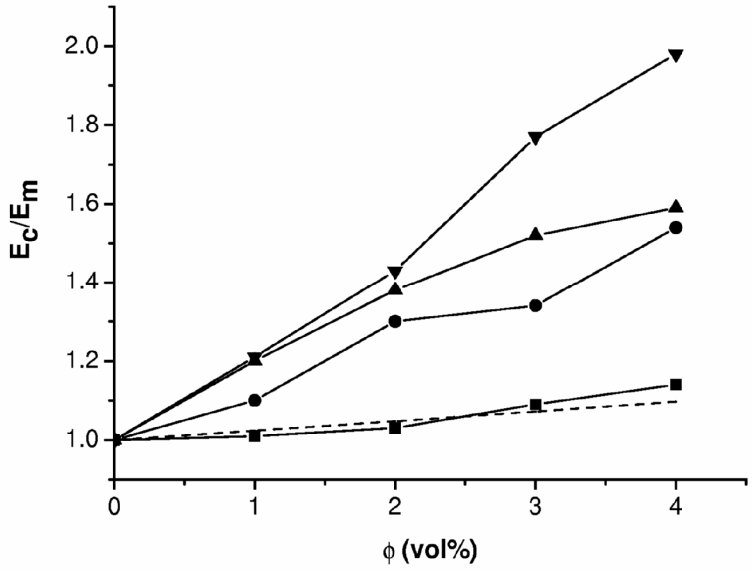

Figure 4.36 Relative elastic modulus of LLDPE-SiO_2 composites. (■) LLDPE-Glass-x, (●) LLDPE-S160-x, (▲) LLDPE-A200-x, (▼) LLDPE-A380-x. The dashed line is the theoretical prediction according to the Lewis-Nielsen model

Therefore, we can conclude that the classical models adopted for microcomposites are not considering that in polymers filled with submicron particles in the interfacial area is much extended, and new models, taking into account the possibility of matrix-particle and particle-particle physical interactions, have to be elaborated. Two possible mechanisms are generally invoked in order to

explain the marked elastic modulus improvement obtained by using nanoparticles [4]. According to the first mechanism, if a high modulus filler is added to a lower modulus polymer, then load transfers from matrix to the filler, leading to an increase in modulus. In some nanocomposites polymeric chains and filler are almost the same size. Stress is transferred via shear stress at the filler/matrix interface, and the rate of load transfer depends on the shear stress. This highlights the role of the interface in controlling the modulus of filled polymers. For example, the higher the interfacial shear stress and the shorter the load transfer length, the more efficient the filler is in carrying load and the higher the composite modulus. The second mechanism takes into account the fact that the filler can constrain the mobility of the polymer chains as well as their relaxation spectra [189], thus modifying the glass transition temperature and the modulus of the matrix.

In order to find suitable models for the interpretation of the elastic properties of nanocomposites, many attempts can be found in literature. For example Hirsch elaborated an empirical model, by using a combination of equal strain and equal stress conditions in the reinforcement and matrix phases [190]. Even if this model was successfully applied in many cases to predict the elastic response of nanofilled polymeric systems, it does not provide a complete explanation of the stiffening mechanism of the nanocomposites. Moreover the effects of the filler size and the possibility of interfacial interactions are not taken into account [191]. Recently, new models which incorporate the effect of the interface were proposed [192, 193]. Basing on Takayanagi's two-phase model [194], a three phase model including the matrix, interfacial region and fillers was proposed by Ji et al. to estimate the tensile modulus of polymer nanocomposites, assuming that the composites can be represented by three independent segments connected to one another, in a series or a parallel fashion and considering a linear gradient of the properties in the interphase [193]. The expression proposed by these authors is rather complicated, taking into account the shape of the dispersed particle size, the thickness of the interfacial region and parameters related to the linear gradient change in modulus between the matrix and the surface of particles. The analysis of the rheological properties indicated that the solid like behaviour showed by nanofilled samples at low frequencies is probably due to hydrogen bonding between silica nanoparticles. In the solid state the extent of the reinforcing effect provided by the nanoparticles is considerably lower, moreover interparticle interactions are not effective anymore, because hydrodynamic forces are predominant. Considering that in our work the viscoelastic behaviour of the composites is mainly ruled by the filler surface area both in the molten and in the solid state, we propose a model that takes into account the physical interfacial interaction between the matrix and particles. Due to their relative high hydrophobicity, it is generally believed that polyolefins cannot have a good interaction with

inorganic fillers, moreover the lack of chemical affinity often does not allow to obtain a good dispersion degree [21, 178-180, 182, 195-197]. On the other hand the physico-chemical interaction and the filler dispersion degree is favoured in relatively polar matrices (polyamides, polyurethanes, epoxy resins, etc…) [2, 16, 52, 53, 198].

The model proposed in this work starts from the consideration that physical polymer-matrix interactions are possible even in polyethylene filled systems, because of the presence of carbonylic and hydroxyl groups on the backbone of the matrix macromolecules. In fact, from FT-IR analysis, an absorption peak at about 1720 cm^{-1}, associated to the stretching of carbonylic groups, was detected for LLDPE-A380-x nanocomposites at high filler loadings. Even if this aspect is completely neglected in many works, it is reasonable to think that the presence of these polar groups can be important for the possibility of surface interaction between matrix and filler.

The situation can be visualized as in Figure 4.37 and in Figure 4.38. It is reasonable to hypothesize that only amorphous segments of LLDPE chains interact with silica nanoparticles. In fact, in the present case any change of the crystalline phase due to the presence of nanoparticles can be excluded, as explained in Chapters 4.1.2.3 and in Chapter 4.1.2.4. The hydrogen bonding between hydroxyl groups of fumed silica aggregates and carbonyl/hydroxyl groups in thermally oxydized parts of LLDPE chains may create physical entanglements, with relevant consequences on the mechanical response of the material.

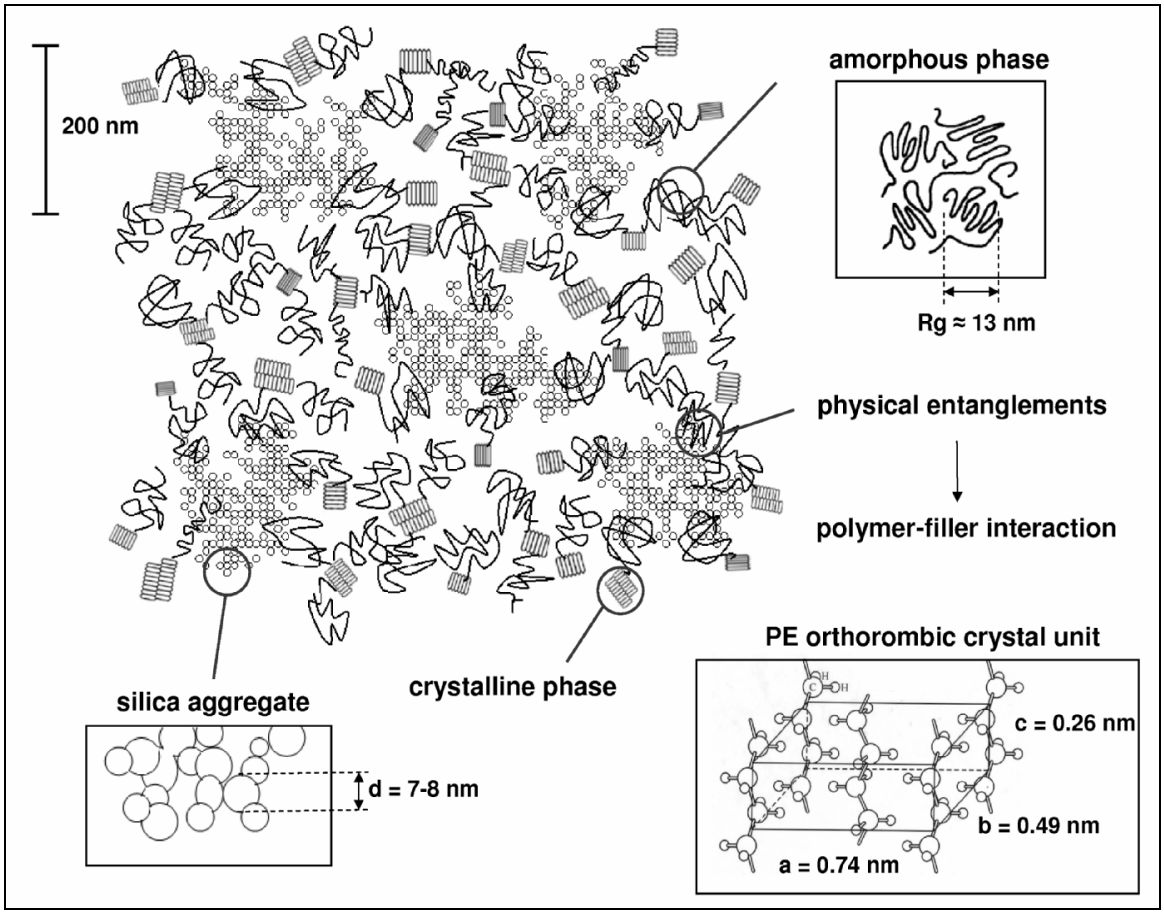

Figure 4.37 Proposed schematic of the state of structural organization and polymer-filler interaction in the LLDPE-fumed silica nanocomposites

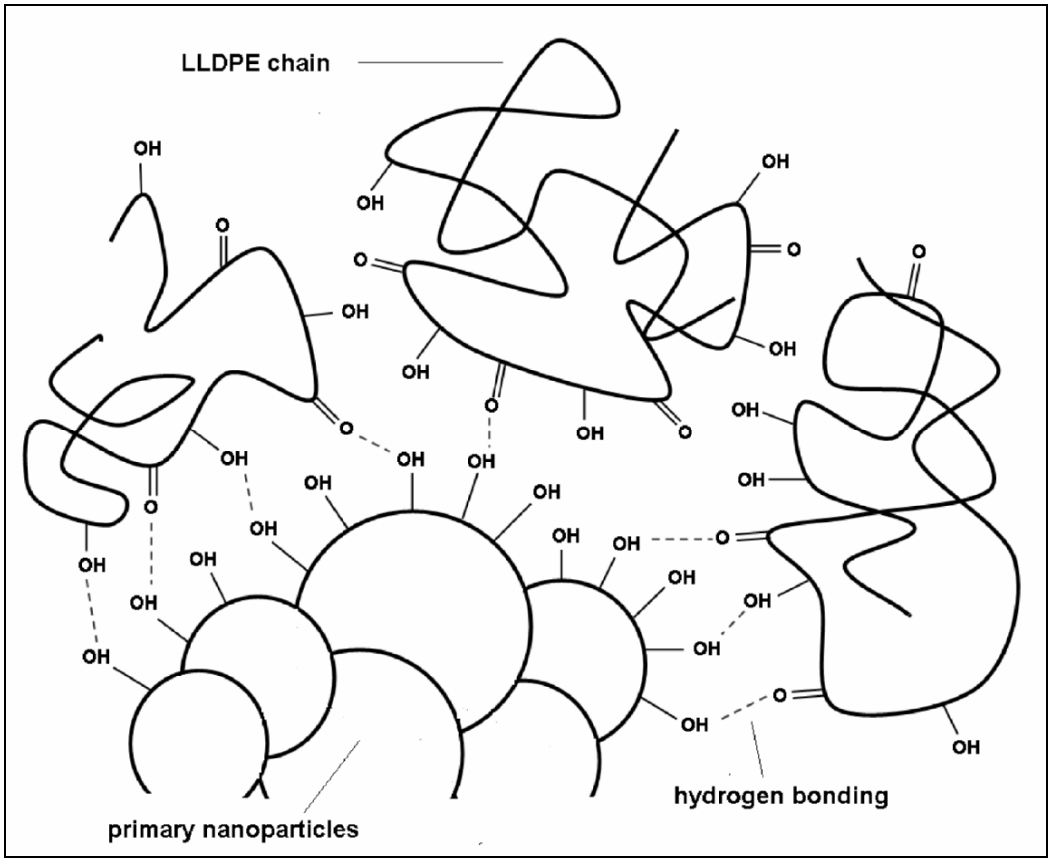

Figure 4.38 Schematic representation of the polymer-filler interaction in LLDPE-fumed silica nanocomposites

Beside the traditional reinforcing effect provided by particulate microfiller, the effect of the polymer-filler physical interaction, based on hydrogen bonding, should be taken into account. Being the hydroxyl groups (-OH) present on the surface of the filler responsible of the interaction with the matrix, it can be hypothesized that the stiffening effect provided by the introduction of the particles is proportional to the total number of -OH groups at the matrix-filler interface. The number of hydroxyl groups is proportional to the total surface area per unit volume of the composite. It can be also supposed that only a fraction of the surface -OH groups is involved in hydrogen bonding with hydroxyl and carbonyl groups of the polymeric matrix, depending on the surface morphology of the filler. A tentative model can be therefore based on the expression reported in Equation 4.6 :

Equation 4.6

$$\frac{E_c}{E_m} = \frac{1 + AB\phi}{1 - B\psi} + k\rho(SSA)\phi$$

where ρ is the density of the filler (g/m^3), Φ is the filler volume fraction, SSA is the surface area (m^2/g) effectively available for the interaction with polymeric chains, while k is a parameter depending on the surface density of hydroxyl groups and the surface morphology of the filler (number, shape and dimensions of pores). Furthermore, being k related to the probability of physical polymer-filler interactions, this parameter will also depend on the factors characterizing macromolecules mobility, such as the typology of matrix utilized (LLDPE in this case), the average molecular weight and the temperature.

The determination of the effective SSA can be quite complex. According to the BET observations previously reported, the major part of the total surface area derives from pores with size higher than 1.7 nm. Moreover, the lateral dimensions of a PE chain is around 0.2 nm [199]. So it can be reasonably assumed that major part of the measured BET surface area is available for the physical interaction with polymeric chains. This means that all the open pores on the surface of the filler could be reached by PE macromolecules, consequently k parameter should depend only on the surface density of -OH groups.

For a quantitative assessment of k it is necessary to have reliable quantitative data on the concentration of -OH groups for different kinds of SiO_2 fillers in the fully hydroxylated state (no thermal treatments were conducted on the fillers). In 1957 De Boer and Vleeskens compared silanol numbers for completely hydroxylated surfaces of amorphous silica and crystalline modifications of silica (β-cristobalite, β-tridymite) whose density is close to that of amorphous SiO_2 [162]. They found that the surface concentration of -OH groups of amorphous silica is practically the same of that of the crystalline ones (4.6-4.9 -OH/nm^2). Since, Zhuravlev and co-workers determined the -OH surface density values of about 150 hydroxylated SiO_2 samples which were prepared by different methods and had different structural characteristics, through BET measures by using low temperature adsorption of krypton [164-166]. The average silanol number (arithmetical mean) was found to be 4.9 OH/nm^2. Calculations by the least squares method yielded a value of 4.6 OH/nm^2. These values are in agreement with those reported by De Boer and Vleeskens as well as with results reported by other researchers. It was concluded that the magnitude of the silanol number, which is independent of the origin and structural characteristics of amorphous silicas is considered to be a physicochemical constant. The results fully confirmed the idea predicted earlier by Kiselev and co-workers on the constancy of the silanol number for a completely hydroxylated silica surface [161, 163], and this constant (4.6 ± 0.5 OH/nm^2) now is known in literature as the Kiselev-Zhuravlev constant. More recently, the total number of surface hydroxyl groups of different kind of silica samples was estimated from the amount of methane evolved by the reaction of the Grignard reagent

with the active hydrogen of the hydroxyls [200]. In that case a slightly lower OH surface density value for fumed silica nanoparticles was found (2.3 OH/nm^2), similar to that reported in the same paper for a silica gel prepared by a sol-gel method and for a porous silica glass.

Therefore it can be concluded that k parameter of the proposed model should be a constant for all typologies of investigated fillers. In Figure 4.39 relative elastic moduli of LLDPE and relative composites are compared with theoretical predictions according to the proposed model. The choice of the right value of k is fundamental for a correct prediction of the elastic modulus of the prepared composites. The k parameter was determined minimizing the sum of the squares of the differences between the theoretical and experimental values for all the samples. It can be concluded that, if a k value of $3 \cdot 10^{-8}$ m is chosen, the accordance of the model with the experimental data is good for all the typologies of the adopted fillers.

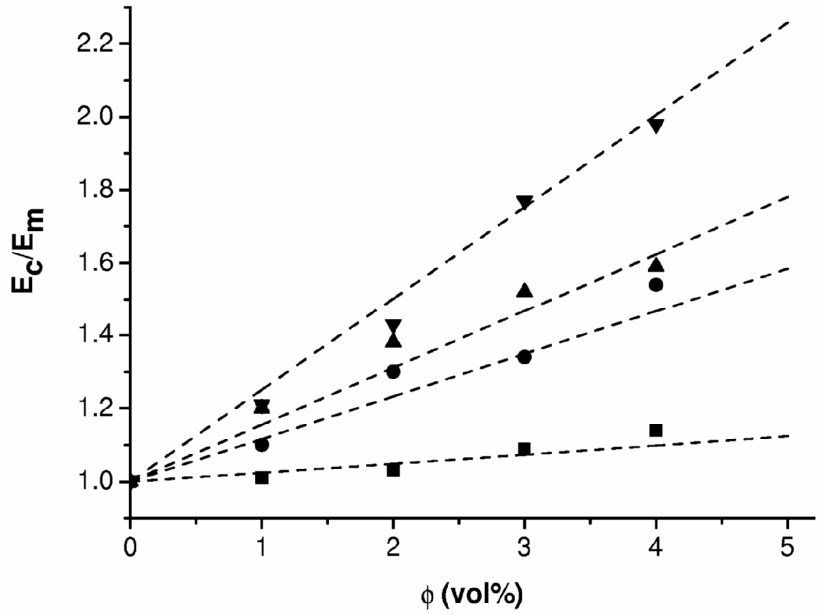

Figure 4.39 Relative elastic modulus of LLDPE-SiO_2 composites. (■) LLDPE-Glass-x, (●) LLDPE-S160-x, (▲) LLDPE-A200-x, (▼) LLDPE-A380-x. The dashed line is the theoretical prediction according to the modified Lewis-Nielsen model

It is important to underline that this model can be successfully applied both for the nanocomposites, in which the contribution of the surface interaction is predominant, and for traditional microcomposites, in which the effect of the surface area is very low and the classical contribution predicted by Lewis-Nielsen equation is more important.

4.3.2 Creep tests

In Figure 4.40 isothermal creep compliance of LLDPE - 2 vol% fumed silica nanocomposites, under a constant load of 1 MPa and at 30 °C, is reported, while in Table 4.13 elastic (D_e) and total components of the creep compliance after a time of 2000 s (D_{t2000}) are summarized. It is evident that the introduction of fumed silica nanoparticles leads to a relevant improvement of the creep stability of the material. In fact, both the elastic and the viscoelastic components of the creep compliance of the composites are sensibly lower than that of the pure LLDPE. Moreover, the creep resistance increases with the surface area of the nanofiller. It is important to underline that the effect on the creep compliance of functionalized nanoparticles (Ar816) is the same of that obtained by using untreated nanoparticles with the same surface area (A200), similarly to what observed in quasi-static tests for the evaluation of the elastic modulus. The improvement in the creep stability due to the introduction of nanoparticles was already reported in some literature papers. For example, titania nanoparticles have been proven to markedly reduce the creep compliance of nylon-66 [185, 201, 202], while alumina nanoparticles resulted to effectively reduce the creep compliance of polystyrene [203]. Also this research group documented a marked reduction of the creep compliance of high density polyethylene (HDPE) filled with submicron titania particles [21] and organoclays [180]. Moreover, Ranade et al. [181] reported that the creep compliance of HDPE blown films can be significantly reduced by the introduction of a layered silicate (Cloisite® 15A) and maleated polyethylene. Even in this case, it is generally believed that nanoparticles may effectively restrict the motion of polymer chains, influencing the stress transfer at a nanoscale, with positive effects on the final creep stability of the material.

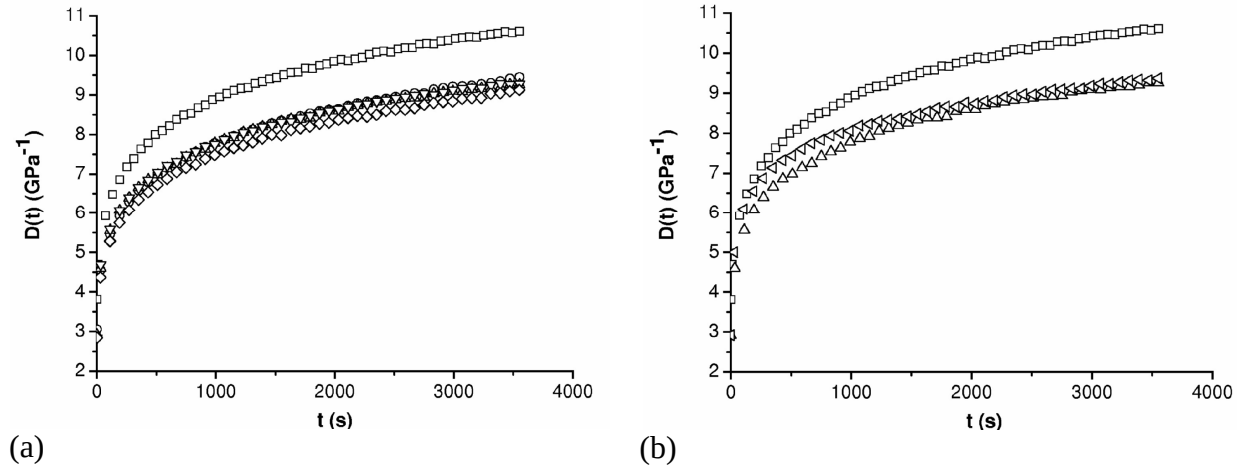

Figure 4.40 Creep compliance (D(t)) of LLDPE - 2 vol% fumed silica nanocomposites (T=30 °C, σ_0=1 MPa). (a) Effect of the silica surface area, (b) effect of the surface functionalization. (□) LLDPE, (○) LLDPE-A90-2, (△) LLDPE-A200-2, (▽) LLDPE-A300-2, (◊) LLDPE-A380-2, (◁) LLDPE-Ar816-2

sample	D_e (GPa^{-1})	D_{ve2000} (GPa^{-1})	D_{t2000} (GPa^{-1})
LLDPE	3.81	6.05	9.86
LLDPE-A90-2	3.05	5.61	8.66
LLDPE-A200-2	2.92	5.63	8.55
LLDPE-Ar816-2	2.92	5.86	8.78
LLDPE-A300-2	2.83	5.74	8.57
LLDPE-A380-2	2.84	5.46	8.30

Table 4.13 Elastic (D_e), viscoelastic (D_{ve2000}) and total creep compliance at 2000 s (D_{t2000}) of LLDPE - 2 vol% fumed silica nanocomposites

It is interesting to evaluate the effect of the filler content on the creep behaviour of the prepared composites. In Figure 4.41 the total creep compliance of LLDPE and relative silica composites at various volume fractions (from 1 to 4 vol%), under a constant load of 1 MPa and at 30 °C, are represented, while in Figure 4.42 relative creep compliance values at 2000 s are summarized. It is evident that the creep compliance of the composites decreases with the filler content. In the case of glass filled composites the enhancement of the creep stability is much lower in comparison to that of fumed silica and precipitated silica sample. The reinforcing effect obtained by using precipitated silica nanoparticles is comparable to that observed by using fumed silica nanoparticles, confirming the observation, already reported commenting elastic modulus tests, that the deformational

behaviour of the material in the solid state is mainly governed by the filler surface area, while particles dimension seems to be less important.

As already reported in quasi-static tensile tests, the reinforcing effect due to the presence of the nanoparticles can be explained considering the polymer-filler surface physical interaction due to the presence of hydrogen bonds at the interface. This means that even in this case the enhancement of the creep resistance experienced for fumed silica filled sample can be explained on the basis of the large availability of -OH groups on the filler surface.

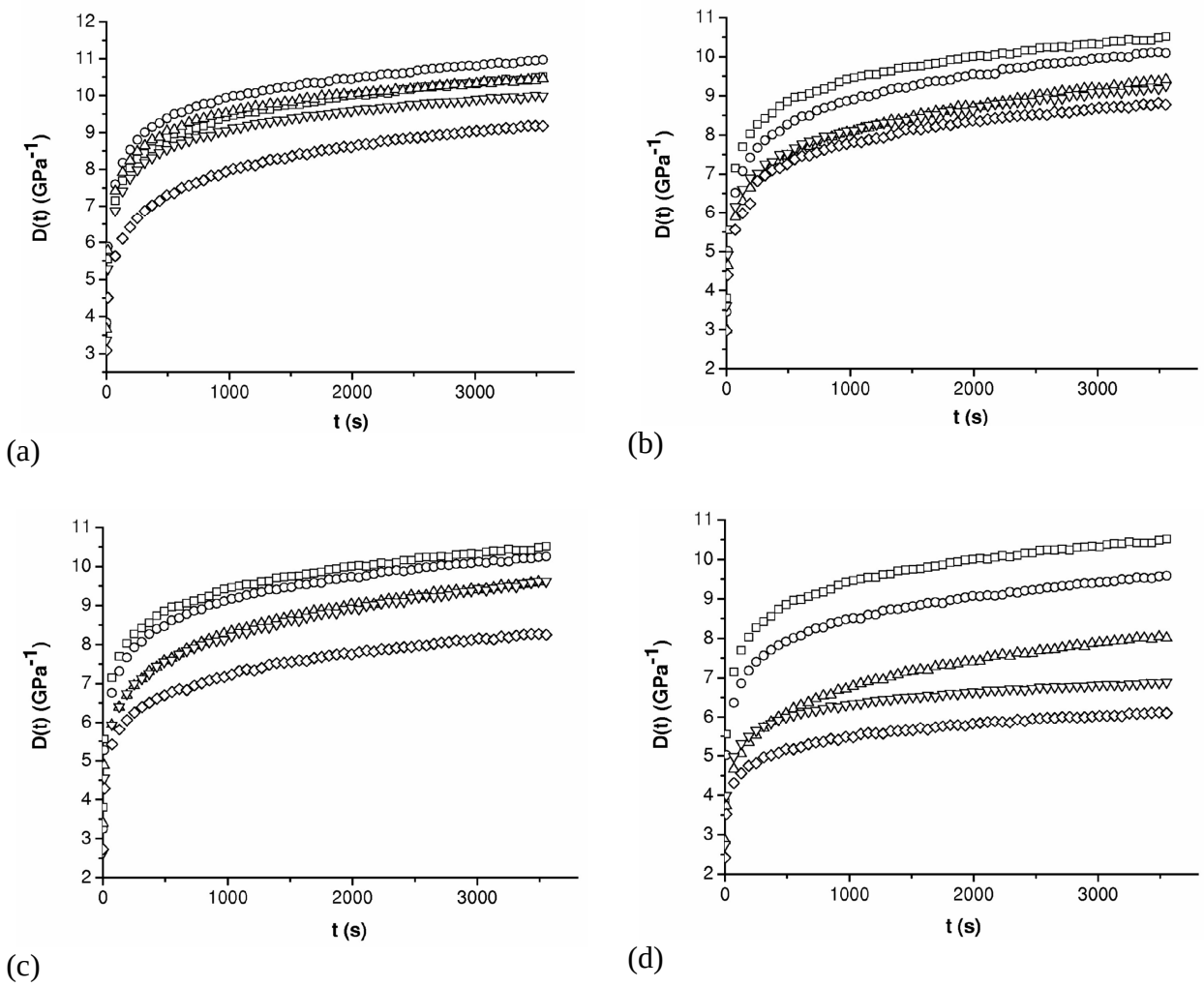

Figure 4.41 Creep compliance (D(t)) of LLDPE – silica composites (T=30 °C, σ_0=1 MPa). (a) LLDPE-Glass-x, (b) LLDPE-S160-x, (c) LLDPE-A200-x, (d) LLDPE-A380-x. (□) LLDPE, (○) x=1 vol%, (△) x=2 vol% ,(▽) x=3 vol%, (◇) x=4 vol%

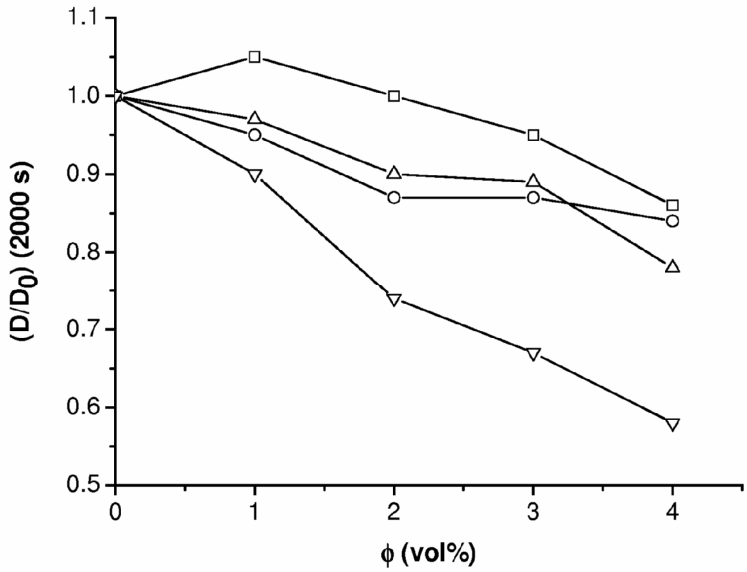

Figure 4.42 Relative creep compliance at 2000 s of LLDPE and relative composites (σ_0=1MPa, T=30 °C). (□) LLDPE-Glass-x, (○) LLDPE-S160-x, (△) LLDPE-A200-x, (▽) LLDPE-A380-x

Considering that fumed silica nanocomposites showed the highest creep stability among the investigated materials, a more detailed analysis on these samples, focused on the effect of the stress and the temperature on the creep behaviour of the material, is required. In Figure 4.43 isothermal creep compliance at 30°C of LLDPE, LLDPE-A200-2 and LLDPE-A380-2 nanocomposites, are represented. Considering that the stress at yield of LLDPE is about 10 MPa, constant stress levels (σ_0) between 1 MPa and 5 MPa were applied. As it can be easily predicted, the creep compliance increases with the applied strain, and it is also evident that the creep compliance of LLPDE is sensibly higher than that of LLDPE-A200-2 and LLDPE-A380-2 samples, if D(t) values under the same load are compared.

Also Zhang, Yang and Friedrich studied the effect of the stress on the creep behaviour of PA66-TiO_2 nancomposites [185], finding that the creep resistance of the matrix could be significantly improved with a very low filler fraction (2 vol%). The same conclusions were reported by Wang and Zhao in a paper on the viscoelastic properties of polyimide-silica nanocomposites [204].

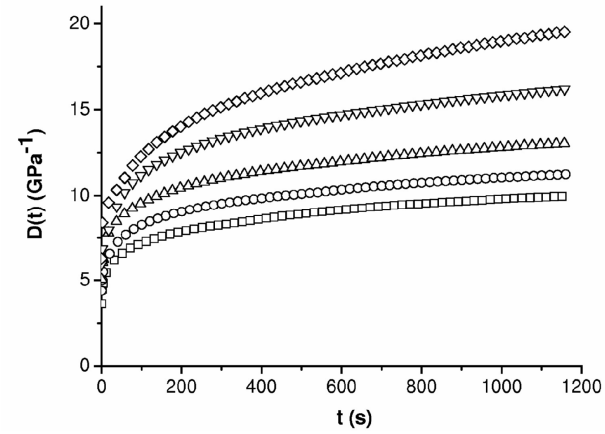

(a)

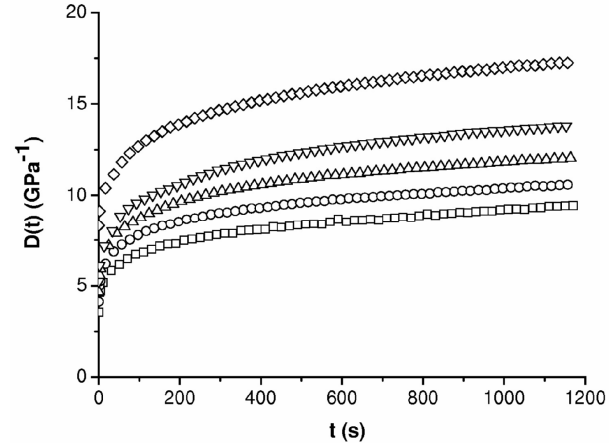

(b)

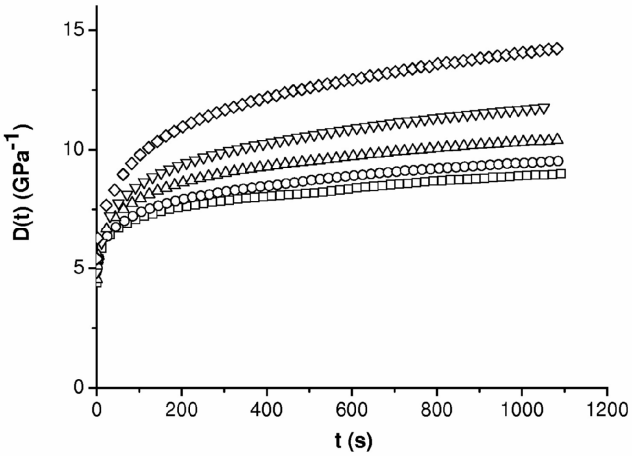

(c)

Figure 4.43 Creep compliance (D(t)) of LLDPE – 2 vol% fumed silica nanocomposites (T=30 °C). (a) LLDPE, (b) LLDPE-A200-2, (c) LLDPE-A380-2. (□) σ_0= 1 MPa, (○) σ_0= 2 MPa, (△) σ_0= 3 MPa, (▽) σ_0= 4 MPa, (◇) σ_0= 5 MPa

In Figure 4.44 isochronous curves of LLDPE, LLDPE-A200-2 and LLDPE-A380-2 samples, at times between 200 s and 1000 s, while a direct comparison between isochronous curves at times of 200 s and 1000 s are reported in Figure 4.45. Considering that isochronous creep curves of the filled samples lay above that of pure LLDPE, it is evident that even in this case a better creep stability can be evidenced by using fumed silica nanoparticles with the highest surface area (A380). As an example, the strong lowering of the creep compliance due to the presence of nanoparticles can be evidenced considering that isochronous curve of LLDPE-A380-2 sample at 1000 s superimposes to that of pure LLDPE at 200 s. Moreover analyzing creep curves at 200 s it can be concluded that the linearity limit, corresponding to the linear viscoelastic behaviour of the material, can be extended by the presence of nanoparticles in the matrix. This means that while the creep compliance of LLDPE is independent from the applied stress if σ_0 is lower than 2 MPa (20% of σ_y), the linearity limit is extended to 3 MPa in the case of LLDPE-A200-2 sample and to 4 MPa for LLDPE-A380-2 filled nanocomposite. This aspect can be very important for structural applications of plastic engineering, when the deformational behaviour under constant loads is considered.

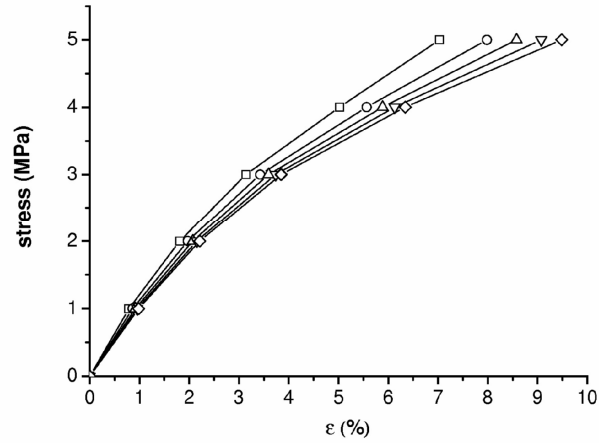

(a)

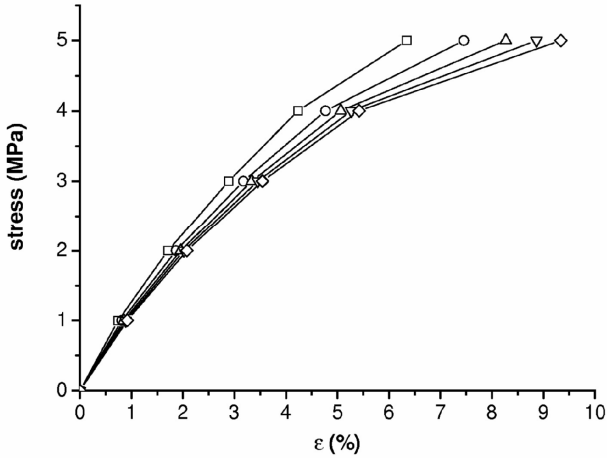

(b)

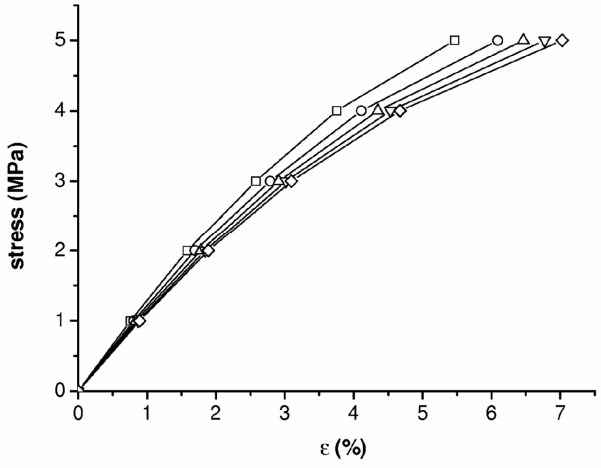

(c)

Figure 4.44 Isochronous curves of LLDPE- 2 vol% fumed silica nanocomposites (T=30 °C). (a) LLDPE, (b) LLDPE-A200-2, (c) LLDPE-A380-2. (□) t=200 s, (○) t=400 s, (△) t=600 s, (▽) t=800 s, (◊) t=1000 s

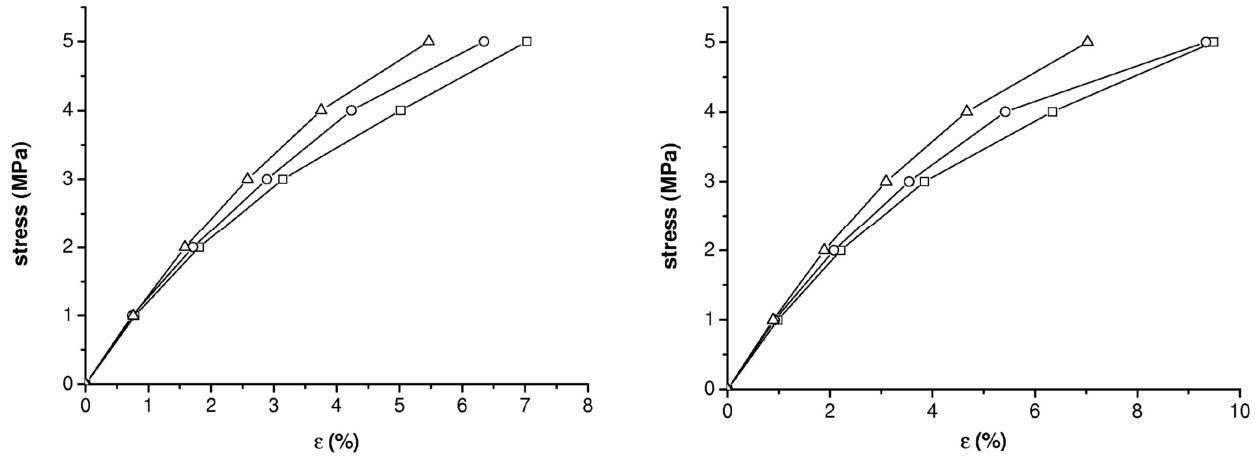

(a) (b)

Figure 4.45 Comparison between isochronous curves of LLDPE- 2 vol% fumed silica nanocomposites (T=30 °C). (a) t=200 s, (b) t=1000 s. (□) LLDPE, (○) LLDPE-A200-2, (△) LLDPE-A380-2

A time-strain superposition principle can be adopted to construct an isothermal creep compliance master curve at the reference stress, simply superimposing creep curves at different stresses [201, 205]. Even if in many papers this procedure was satisfactorily adopted in order to predict the creep behaviour of the material over long time-scales, in this case we tried to consider the possibility to construct creep compliance master curves taking into account the non-linear viscoelastic behaviour of the material when relatively high stresses are applied. As reported in Chapter 2.3.1.4, this approach was originally developed by Kolarik et al. [108, 109, 114], and it is based to the consideration that the free volume of the matrix depends on the applied strain. In order to correctly develop this approach, a suitable choice of model's parameter must be done.

In Table 4.14 the parameters chosen for the evaluation of the non linear tensile behaviour of LLDPE, LLDPE-A200-2 and LLDPE-A380-2 composites are summarized. The glass transition temperature (T_g) of polyethylene can be easily found in many handbooks and it will be reported both for LLDPE and for fumed silica nanocomposites in the section dedicated for dynamical mechanical measurements (Chapter 4.3.3). As it will be explained in that section, T_g values of nanocomposites are little lower than that of pure LLDPE, but an approximate value of -100 °C can be reasonably adopted for all the samples, because strain dependent shift factors $\log(a_\varepsilon)$ are not very sensitive to variation of T_g. The free volume at the glassy state (f_g) is generally taken as 0.025, but in the case of polyethylene a lower values of f_g can be considered (0.0125). In fact polyethylene is a semicrystalline material with an high degree of crystallinity, for this reason it is possible that the amorphous part of LLDPE is more compact and well ordered with respect to that of other fully amorphous polymers. On the other hand a direct measure of the free volume at the glass transition temperature is rather complicate in practice. For the same reason it is possible that the difference between the expansion coefficients of the material above and below T_g (α_{fv}) is lower than that reported by Kolarik for PP [109], and a value of 0.0002 K^{-1} can be reasonably adopted. The crystalline fraction was taken from DSC tests in Chapter 4.1.2.3, while Poisson's ratio was chosen as 0.44, the same value utilized in Chapter 4.3.1. The parameter B is related to the ratio of the volume of a jumping segment to the volume of critical vacancy necessary for the implementation of a segment jump, and it is generally expected to be close to 1. The other values reported in Table 4.14 are determined by using the equations reported in Chapter 2.3.1.4.

Parameter	Value
f_g	0.0125
T_g (°C)	-100
T (°C)	30
α_{fv} (K^{-1})	0.0002
Δf_{Tc}	0.026
x_c	0.42
v_2	0.42
v_{2cr}	0.156
q	1.8
M	1.51
v	0.44
B	1

Table 4.14 Parameter's choice for the evaluation of the non linear tensile behaviour of LLDPE- 2 vol% fumed silica nanocomposites

In Figure 4.46 creep compliance curves of LLDPE, LLDPE-A200-2 and LLDPE-A380-2 at 30 °C, and relative superimposed curves according to strain dependent shift factors log(a_ε) (see Equation 2.44), are reported. It is evident that, if creep data are represented considering an internal time (t*), the superposition of the creep curves is very good for all the considered sample. This means that this approach for the analysis of the non-linear tensile creep behaviour of LLDPE and relative nanocomposites can be successfully applied, if appropriate parameters are selected. In Figure 4.47 master curves of LLDPE and relative nanocomposites are compared. Even in this case it possible to conclude that the creep compliance of LLDPE is considerably higher than that of nanocomposites with fumed silica nanoparticles. Moreover, the creep stability of the material increases with the surface area of the nanoparticles.

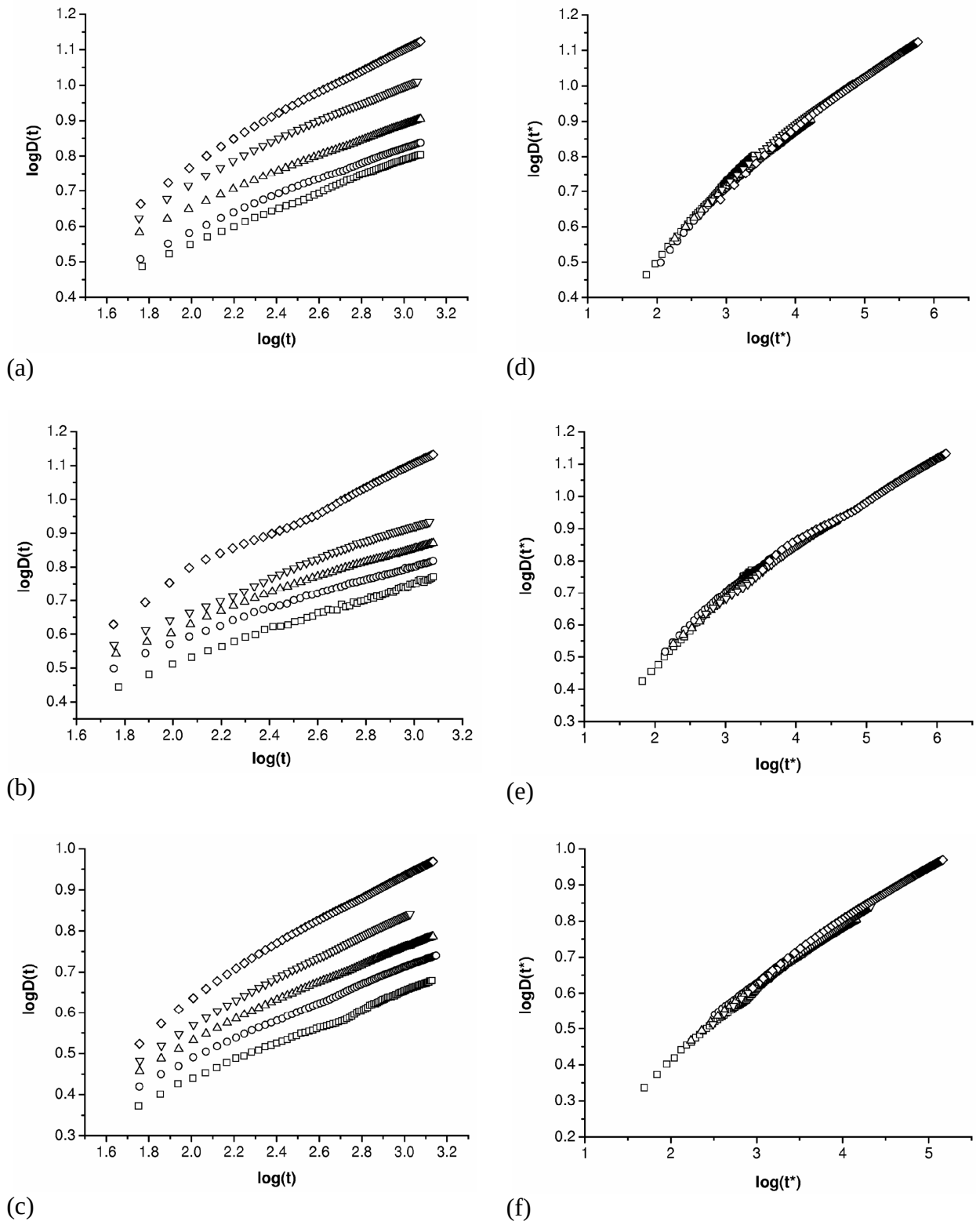

Figure 4.46 Creep compliance (D(t)) of LLDPE – 2 vol% fumed silica nanocomposites (T=30 °C). (a) LLDPE, (b) LLDPE-A200-2, (c) LLDPE-A380-2. Superimposed creep curves according to the no linear tensile creep approach, (d) LLDPE, (e) LLDPE-A200-2 , (f) LLDPE-A380-2. (□) σ_0= 1 MPa, (○) σ_0= 2 MPa, (△) σ_0= 3 MPa, (▽) σ_0= 4 MPa, (◇) σ_0= 5 MPa

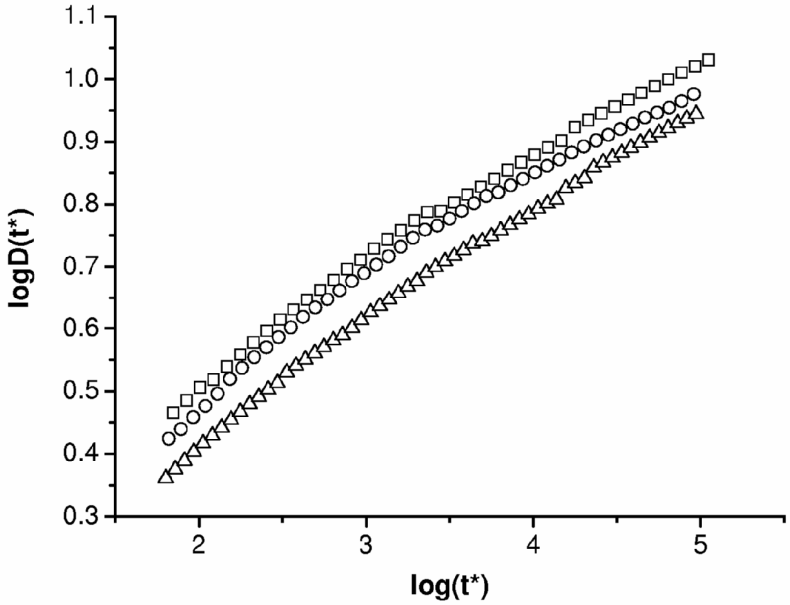

Figure 4.47 Master curves of the creep compliance (D(t)) of LLDPE – 2 vol% fumed silica nanocomposites according to the non linear tensile creep superposition principle (T=30 °C). (□) LLDPE, (○) LLDPE-A200-2, (△) LLDPE-A380-2

This approach can be followed to fit creep data over the real time scale, in order to predict the creep behaviour of the samples over extended periods. As described in Chapter 2.3.1.4, it is possible to express the trend of the creep compliance in the real time by using Equation 2.43 and Equation 2.44. In Figure 4.48 creep compliance curves are compared with the theoretical ones, derived from the fitting according to the non linear tensile creep approach (solid lines). It is evident that the superposition is good for all the samples, even when the applied strain is relatively high.

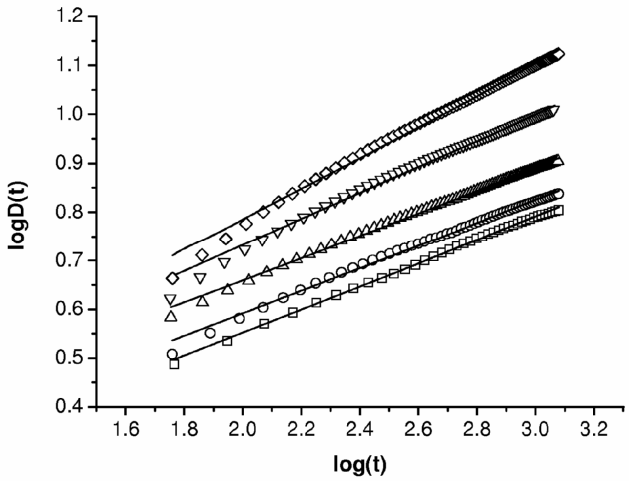

(a)

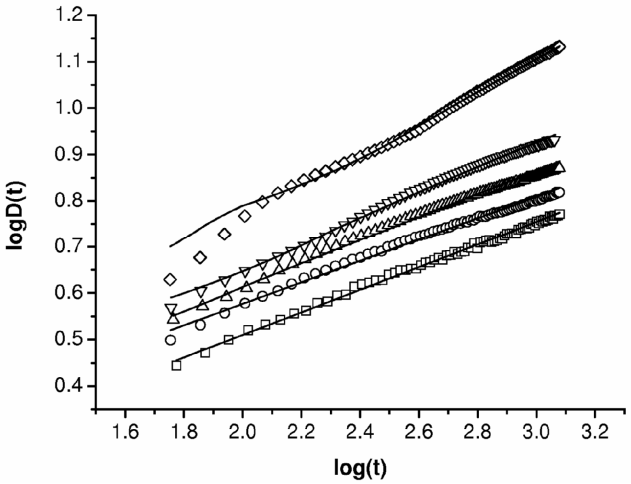

(b)

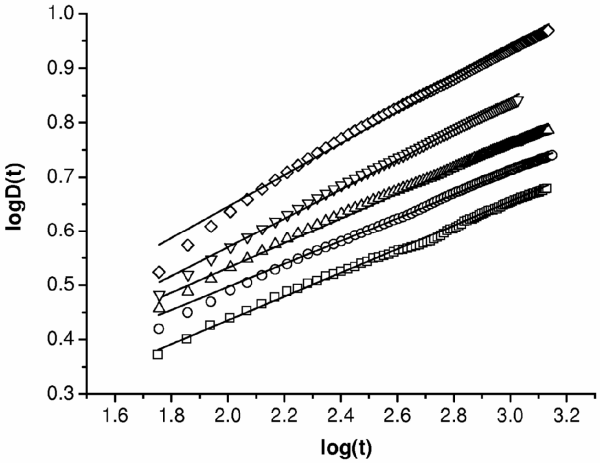

(c)

Figure 4.48 Creep compliance (D(t)) of LLDPE – 2 vol% fumed silica nanocomposites (T=30 °C), with the theoretical curves derived from the fitting according to the non linear tensile creep approach (solid lines). (a) LLDPE, (b) LLDPE-A200-2, (c) LLDPE-A380-2. (□) σ_0= 1 MPa, (○) σ_0= 2 MPa, (△) σ_0= 3 MPa, (▽) σ_0= 4 MPa, (◇) σ_0= 5 MPa

Furthermore, in Table 4.15 fitting parameters based on Equation 2.43 and on Equation 2.44 are summarized. R^2 values are in general higher than 0.995, confirming the good accordance with experimental data. As it can be easily predicted, logC* increases with the applied stress. According to Equation 2.43 n* should be independent from σ_0, in fact from Table 4.15 it is evident that the dependence of n* on the applied stress is very weak. It can be concluded that the proposed approach can be successfully applied also to LLDPE and relative fumed silica nanocomposites, providing a convenient way to analyze the stress dependency of the deformational behaviour of the prepared composites.

	LLDPE			**LLDPE-A200-2**			**LLDPE-A380-2**		
σ_0 (MPa)	**logC***	**n***	**R^2**	**logC***	**n***	**R^2**	**logC***	**n***	**R^2**
1	0.0894	0.2117	0.9983	0.0375	0.2183	0.9962	0.0006	0.2050	0.9974
2	0.1509	0.1841	0.9951	0.1337	0.1864	0.9933	0.0935	0.1784	0.9994
3	0.2268	0.1617	0.9963	0.1507	0.1766	0.9950	0.0956	0.1734	0.9952
4	0.2732	0.1523	0.9931	0.2002	0.1604	0.9980	0.0873	0.1765	0.9960
5	0.2954	0.1450	0.9944	0.3310	0.1310	0.9970	0.1676	0.1575	0.9951

Table 4.15 Parameters of the fitting from the creep data of LLDPE- 2 vol% fumed silica nanocomposites according to Equation 2.43

The temperature dependence of the tensile creep response of LLDPE based nanocomposites is now considered. In Figure 4.49 creep compliance of LLDPE, LLDPE-A200-2 and LLDPE-A380-2 samples at temperatures ranging from 30 °C to 70 °C, under an applied stress of 1 MPa, are reported. As it could be noted, the deformational behaviour of the materials is strongly dependent on the temperature. Moreover, at every investigated temperature the introduction of fumed silica nanoparticles leads to an evident lowering of the creep compliance, especially at high temperatures. At an applied stress of 1 MPa both LLDPE and relative nanocomposites behave in a linear viscoelastic manner (see Figure 4.45), and a time-temperature superposition principle can be applied, as explained in Chapter 2.3.1.3. In Figure 4.50 superimposed curves, taking the creep curve at 30 °C as reference, are represented. It is evident that for every temperature the superposition of the curves is very good both for the pure matrix and the fumed silica filled samples.

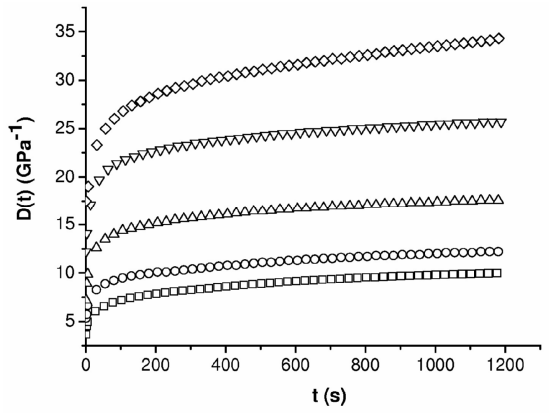

(a)

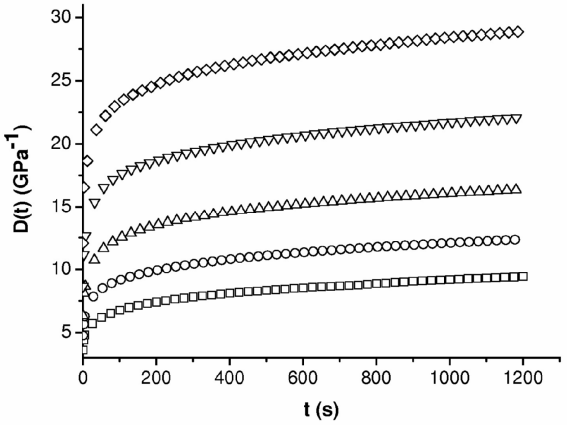

(b)

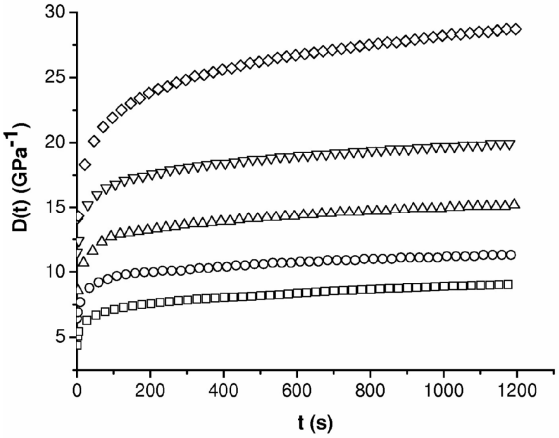

(c)

Figure 4.49 Creep compliance (D(t)) of LLDPE – 2 vol% fumed silica nanocomposites (σ0=1 MPa), at different temperatures. (a) LLDPE, (b) LLDPE-A200-2, (c) LLDPE-A380-2. (□) T=30 °C, (○) T=40 °C, (△) T=50 °C, (▽) T=60 °C, (◇) T=70°C

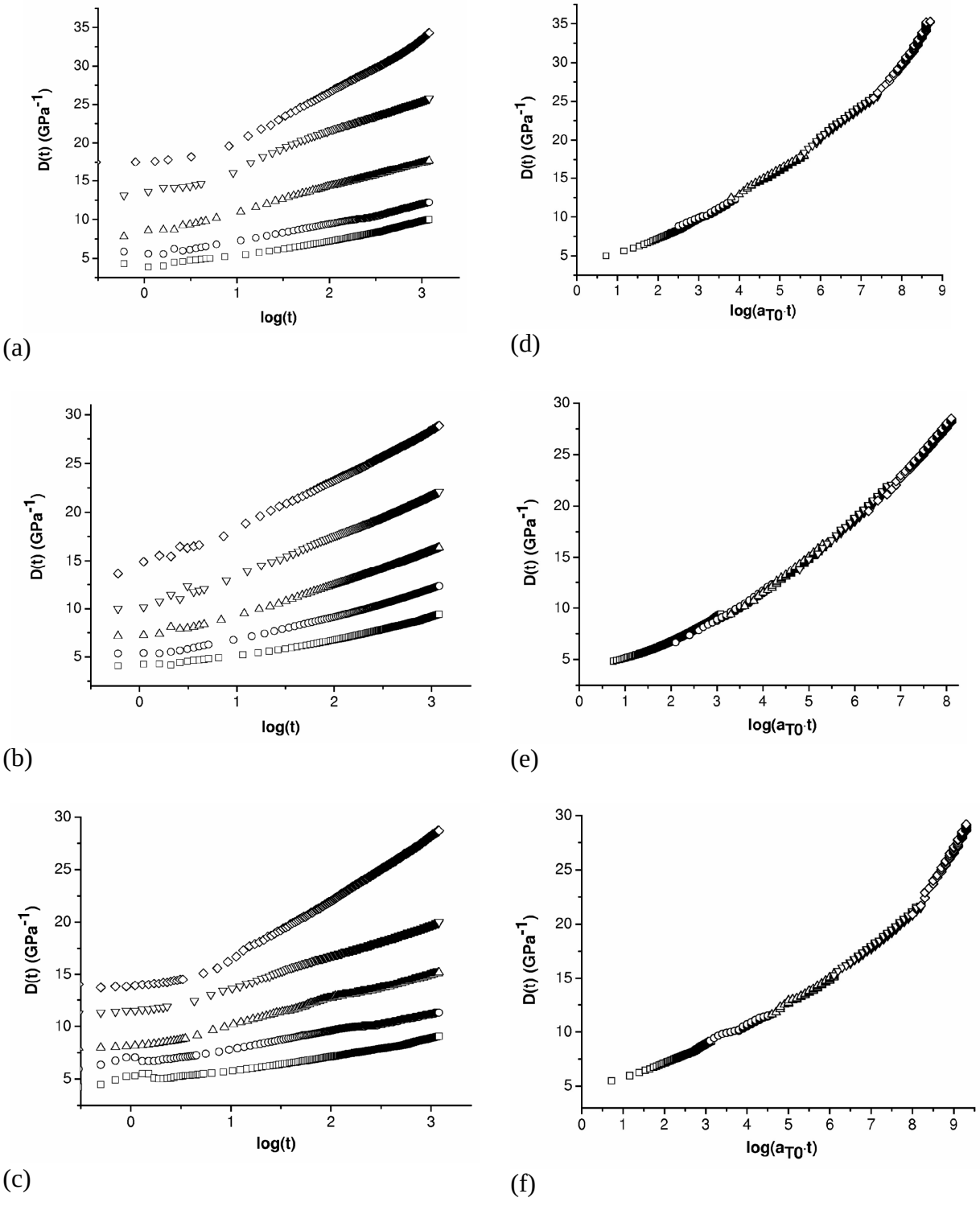

Figure 4.50 Creep compliance (D(t)) of LLDPE – 2 vol% fumed silica nanocomposites (σ_0=1 MPa), at different temperatures. (a) LLDPE, (b) LLDPE-A200-2, (c) LLDPE-A380-2. Superimposed curves according to the time-temperature superposition principle. (□) T=30 °C, (○) T=40 °C, (△) T=50 °C, (▽) T=60 °C, (◊) T=70°C

In Figure 4.51 master curves of LLDPE and of fumed silica nanocomposites are directly compared. It can be concluded that even in this case the creep stability increases with the surface area of the

nanofiller. Moreover, being the reinforcing effect due to the introduction of the nanofiller more evident at high temperatures, it can be concluded that the lowering of the creep compliance of the nanocomposites is more efficient when long creep times are considered. A similar observation was already reported when stress dependence of the creep behaviour was analyzed. The temperature dependence of the creep behaviour of nanocomposites was already studied by other researchers. For example Yang et al. characterized polypropylene and polyamide 66 based nanocomposites filled with short and long aspect-ratio multiwalled carbon nanotubes at different temperatures, finding that creep stability could be significantly improved with reduced creep deformation and creep rate at long-term loading periods [202, 206].

Through the superposition principle it is possible to determine the creep behaviour of the material for extended times. As an example, the time necessary to reach a creep compliance of 20 GPa^{-1} can be obtained. For LLDPE, this target value is reached in about 10 days, while for LLDPE-A200-2 and LLDPE-A380-2 samples times of respectively 24 days and 554 days are necessary to reach such that target compliance.

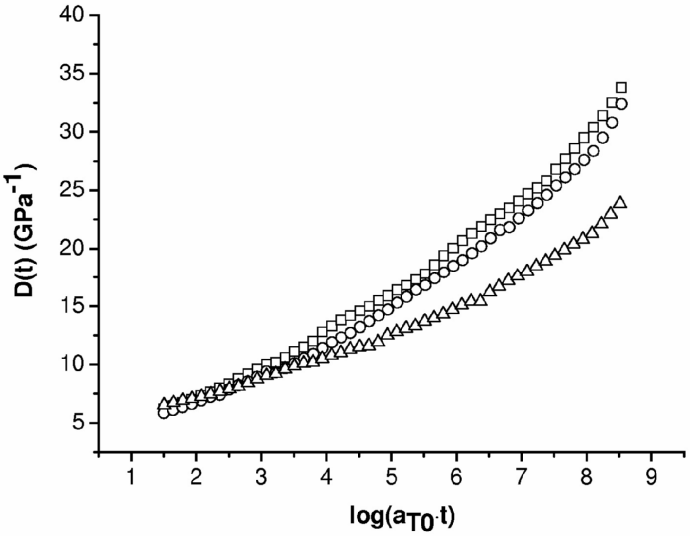

Figure 4.51 Master curves of the creep compliance (D(t)) of LLDPE-fumed silica nanocomposites according to the time-temperature superposition principle (T_0= 30 °C, σ_0=1MPa). (□) LLDPE, (○) LLDPE-A200-2, (△) LLDPE-A380-2

In order to study the correlation between creep properties and polymeric chain dynamics, an analysis of the shift factors derived from the time-temperature superposition principle has been conducted. In Figure 4.52 shift factors of LLDPE and LLDPE-A200-2 and LLDPE-A380-2 nanocomposites at different temperatures are reported. If shift factors are plotted versus the reciprocal of the absolute temperature, a linear trend can be easily detected. This means that

Arrhenius equation (see Equation 2.29) can be successfully applied to determine the shift factor dependency on the temperature. From the slope of the obtained regression lines it is possible to determine the activation energy values (E_a), that provides an indication of the energy required for the flow process. In Table 4.16 E_a values for pure LLDPE and for relative nanocomposites are summarized. The activation energy found for unfilled matrix is consistent with the data reported in literature, but from the E_a values of fumed silica nanocomposites is hard to detect a clear trend. In other words from the analysis of the shift factors it is impossible to assess if the flow dynamics of LLDPE macromolecules are really influenced by the presence of nanoparticles. Considering the relatively high standard deviation of E_a values, it is probable that viscous flow of the macromolecules is substantially not dependent by the presence of the nanofiller. Anyway further investigations would be necessary to have a better comprehension of the temperature dependent molecular dynamics of the prepared samples in the solid state.

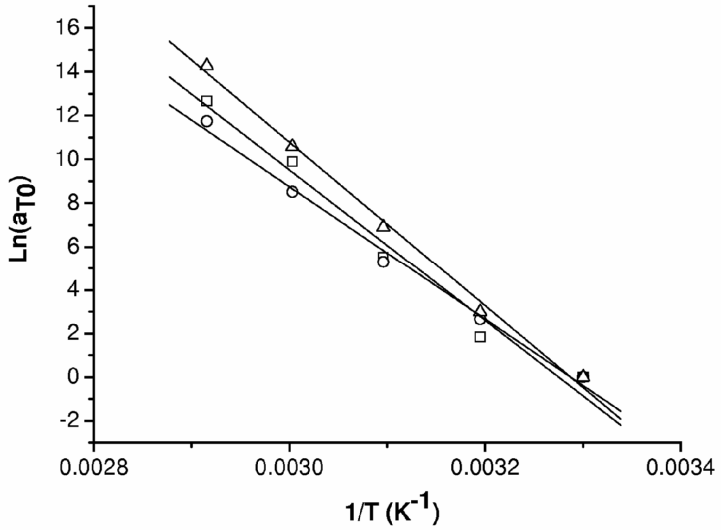

Figure 4.52 Shift factors for (□) LLDPE, (○) LLDPE-A200-2, (△) LLDPE-A380-2 samples, with fitting lines according to Arrhenius equation

Sample	E_a (kJ/mol)
LLDPE	287.6 ± 24.3
LLDPE-A200-2	252.3 ± 12.8
LLDPE-A380-2	311.9 ± 12.7

Table 4.16 Activation energy values from the fitting of the shift factor data according to the Arrhenius equation

Creep behaviour at different temperatures of LLDPE and fumed silica nanocomposites can be also analyzed considering viscoelastic mechanical models available for thermoplastics materials. Among various models available, Burgers model resulted to be the best for our samples. As reported in Chapter 2.3.1.1, this model derives from the combination in series of the Maxwell and Kelvin models, as described by the constitutive law reported in Equation 2.23. In Figure 4.53 creep compliance curves of LLDPE and relative fumed silica nanocomposites at different temperatures are compared with the fitted data according to the Burgers model (represented by straight lines), and in Table 4.17 parameters derived from the fitting procedure are summarized. It is evident that the accordance of the model with experimental data is quite good for all the samples and at all the investigated temperatures, especially for long creep times. In fact R^2 values higher than 0.97 can be obtained for all the considered samples. The effectiveness of this viscoelastic model in interpreting creep data of nanofilled samples was recently reported in some papers. For example non-linearity in the creep response of polyethylene-montmorillonite nanocomposites was successfully modeled by using the Burgers model by Ranade et al. [181]. The time-dependent deformation under constant and fatigue loading of polyimide-silica nanocomposites was simulated based on Burgers model and Findley power law by Wang and Zhao [204], adopting the parameters analysis to interpret the structure–property relationship and deformation mechanisms of this kind of composites.

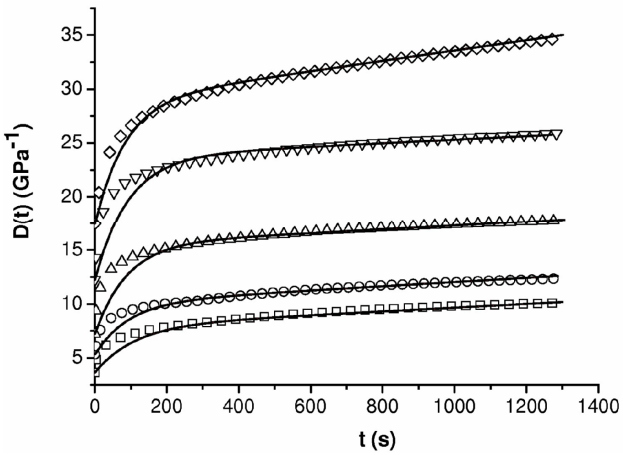

(a)

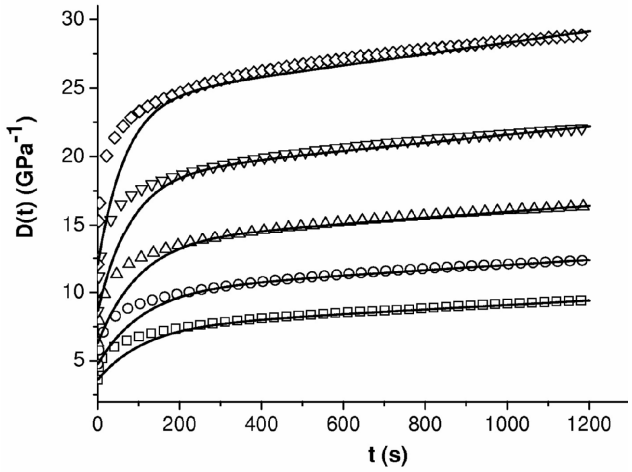

(b)

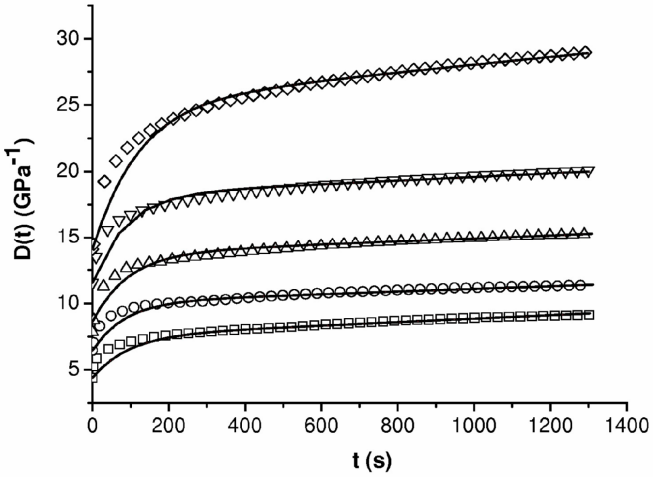

(c)

Figure 4.53 Creep compliance (D(t)) of LLDPE – 2 vol% fumed silica nanocomposites (σ_0=1 MPa), at different temperatures. (a) LLDPE, (b) LLDPE-A200-2, (c) LLDPE-A380-2, with the fitted data according to the Burgers model (straight lines). (□) T=30 °C, (○) T=40 °C, (△) T=50 °C, (▽) T=60 °C, (◇) T=70°C

As reported in Table 4.17, viscous (η_K, η_M) and elastic (E_K, E_M) parameters of the Burgers model decrease with the temperature, but the most important conclusion is that the enhancement of the creep resistance of the material can be related to a substantial increase of the elastic (especially E_K) and viscous components (both η_K and η_M) of the model, with a clear dependency on the surface area of the nanofiller.

Sample	T (°C)	E_K (MPa)	η_K (GPa·s)	E_M (MPa)	η_M (GPa·s)	R^2
LLDPE	30	240	25.1	274	518.1	0.9945
	40	211	19.7	188	510.2	0.9839
	50	121	10.6	138	555.6	0.9898
	60	89	7.5	82	537.6	0.9810
	70	88	7.4	57	207.9	0.9884
LLDPE-A200-2	30	262	29.1	277	606.1	0.9975
	40	186	20.3	211	531.9	0.9938
	50	133	13.5	158	460.8	0.9939
	60	100	8.0	116	334.4	0.9934
	70	83	5.5	83	241.5	0.9914
LLDPE-A380-2	30	316	30.1	228	781.3	0.9938
	40	268	22.5	155	934.6	0.9800
	50	196	18.0	116	826.4	0.9852
	60	150	12.8	87	724.6	0.9710
	70	91	10.8	71	341.3	0.9830

Table 4.17 Parameters of the fitting of the creep data of LLDPE-2 vol% fumed silica nanocomposites at different temperatures (σ_0=1MPa), according to the Burgers model

4.3.3 Dynamic mechanical thermal analysis

In Figure 4.54 storage moduli and loss tangent values derived from dynamic mechanical analysis of LLDPE-2 vol% fumed silica nanocomposites are reported, while some relevant values are summarized in Table 4.18. It is evident that the introduction of the nanofiller leads to an increase of E' both in the glassy region and in the rubbery regions, especially when high surface area nanoparticles are utilized. Storage modulus values obtained by using functionalized nanoparticles are similar to that obtained with untreated nanoparticles with the same surface area, confirming the observations based on quasi-static and creep tests. In fact, the presence of organosilanes does not substantially affect the deformational behaviour of the material, when the applied strain is relatively low. An enhancement of the storage modulus of polymeric materials due to the presence of

nanoparticles was already detected by Joshi and Viswanathan in a work on polypropylene/clay nanocomposites [207], while Kontou and Niaounakis reported the same conclusion studying an LLDPE-fumed silica systems [23]. In this latter work, the increase of E' values was explained considering that the matrix of the composite can be assumed as consisting of two parts: a bulk region, where the state of the macromolecular chains is the same as that in the pure LLDPE, and an interphase, formed by the physical or chemical adsorption of the polyethylene molecules and/or trans-crystallization on the filler's surface. The larger the interfacial area and the stronger the interaction between the matrix and the filler, the greater the volume of the interphase. Because the macromolecular chains of the interphase are restricted to the surface of the fillers, the molecular motion is greatly limited. This means that the storage modulus of the interphase is higher than that of the bulk region, and an increase in the silica content enlarges the interfacial area and results in an increased volume of interphase.

The experienced increase of E' values for fumed silica nanocomposites in the present work is accordance with the observations derived from quasi-static tensile tests and creep tests. The physical polymer-filler interaction due to the presence of hydrogen bonds at the composite interface hinders the molecular chain mobility around the nanoparticles, and the larger availability of hydroxyl groups for high surface area nanoparticles leads to a more effective block of the segmental motion of the macromolecules.

Considering the trends of the loss tangent values, it is evident that tanδ values of filled samples are lower than that of pure LLDPE, while considering the position of tanδ peak it can be concluded that the glass transition temperature (T_g) is slightly lowered by the presence of the nanofiller. In fact it passes from -95.6 °C for the pure LLDPE to -103.4 °C for LLDPE-A200-2 sample. For the LLDPE-Ar816-2 sample T_g is practically the same of the unfilled sample. The lowering of the glass transition temperature due to the presence of nanoparticles on LLDPE-SiO_2 systems was already detected by Kontou and Niaounakis [23], who did not provide a satisfactory explanation of this result. As already mentioned in the section on creep tests, the T_g drop observed in our nanocomposites can be explained referring to the molecular dynamics analysis of the nanofilled systems reported in the book of Ajayan et al. [4]. Referring to TEM images of our nanocomposites, several zones of the samples show an interparticle distance comparable to the double of the radius of gyration of PE macromoleclues (in this case about 30 nm). As reported by several authors in literature [208-211], when the thickness of polymeric films is lowered down to 20-30 nm, a sensible glass transition decrease can be detected. From molecular dynamics simulations [212] it was

demonstrated that this T_g drop is caused by a decrease in the chain density, which in turn increases the mobility of the macromolecules. It is also possible that the polymer-filler interaction leads to a partial physical adsorption of the macromolecules at the surface, with a consequent chain depletion in the interparticle region and a little increase of the chain mobility in this region. In any case the drop of the chain density in the interparticle region is largerly overcompensated by the reinforcing effect provided by the polymer-filler interaction at the interface.

Furthermore when organosilane nanoparticles filled samples (Ar816) are considered, the T_g decrease is practically absent. It is possible that the presence of a long chain organosilane (C16) at the filler surface limits the possibility of the hydrogen bonding between polymer and nanoparticles, hindering the consequent physical chain adsorption at the surface and the macromolecules depletion in the interparticle spaces.

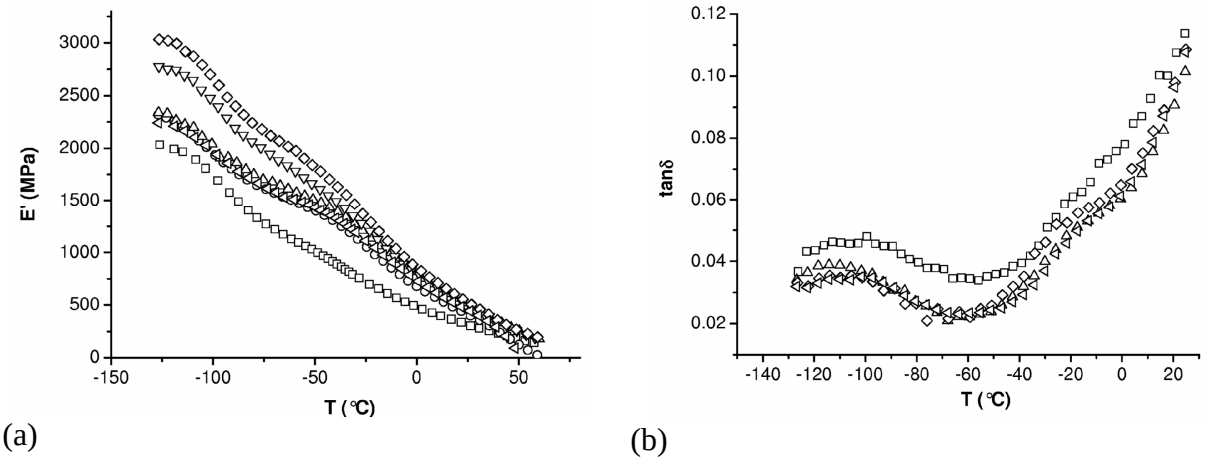

Figure 4.54 Dynamic mechanical properties of LLDPE-2 vol% fumed silica nanocomposites (f=1 Hz). (a) Storage modulus (E'), (b) Loss tangent (tanδ). (□) LLDPE, (○) LLDPE-A90-2, (△) LLDPE-A200-2, (▽) LLDPE-A300-2, (◇) LLDPE-A380-2, (◁) LLDPE-Ar816-2

Sample	E' (-130 °C) (GPa)	T_g (°C)	E' (20 °C) (GPa)
LLDPE	1.99	-95.6	0.34
LLDPE-A90-2	2.30	-103.6	0.46
LLDPE-A200-2	2.32	-103.4	0.55
LLDPE-Ar816-2	2.22	-97.5	0.50
LLDPE-A300-2	2.76	-100.5	0.56
LLDPE-A380-2	3.01	-99.7	0.59

Table 4.18 Dynamic mechanical properties of LLDPE - 2 vol% fumed silica nanocomposites (f=1 Hz)

In order to reach a better comprehension on the viscoelastic phenomena affecting the dynamic mechanical behaviour of the prepared composites, multi-frequency dynamic mechanical tests were conducted. In Figure 4.55 storage modulus of LLDPE-2 vol% fumed silica nanocomposites at frequencies between 0.3 Hz and 30 Hz are reported. In Figure 4.56 isothermal curves at temperatures between -60 °C and +45 °C are represented. Even in this case an increase of E' with the surface area of the nanofiller can be easily detected, confirming the conclusions reported in mono-frequency dynamic tests. Moreover in Figure 4.56 superimposed curves of the storage modulus according to time-frequency superposition principle, taking as reference temperature T_0=30 °C, are represented. It is evident that the superposition of E' curves is good for all the samples and over the whole frequency range.

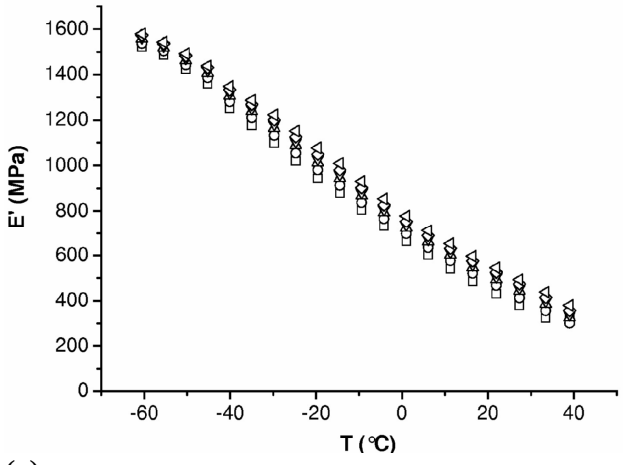

(a)

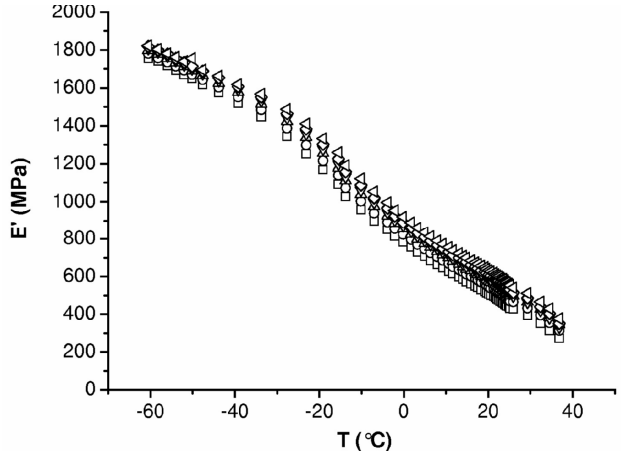

(b)

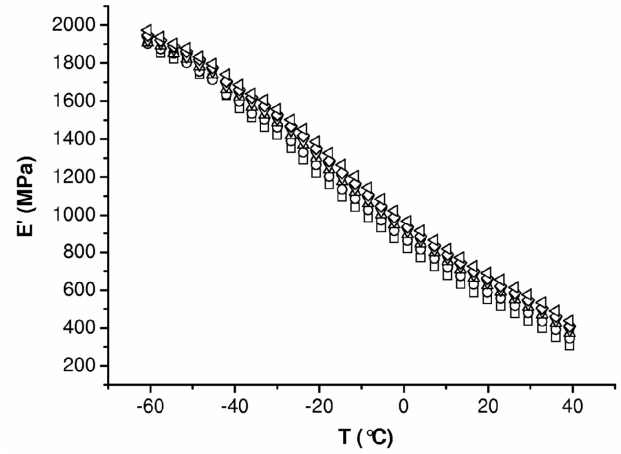

(c)

Figure 4.55 Storage modulus (E') of LLDPE-2 vol% fumed silica nanocomposites from dynamic multi-frequency tests. (a) LLDPE, (b) LLDPE-A200-2, (c) LLDPE-A380-2. (□) f=0.3 Hz, (○) f=1 Hz, (△) f=3 Hz, (▽) f=5 Hz, (◇) f=10 Hz, (◁) f=30 Hz

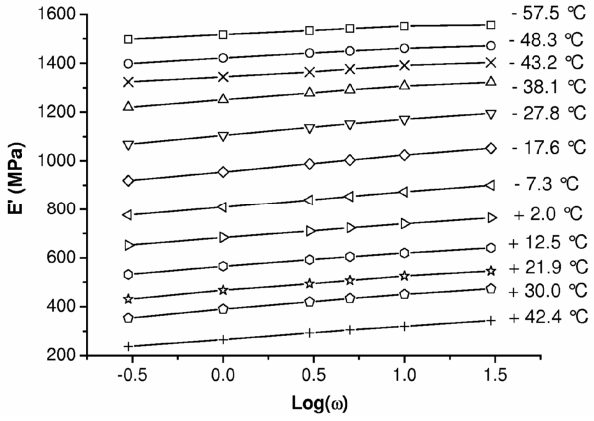

(a)

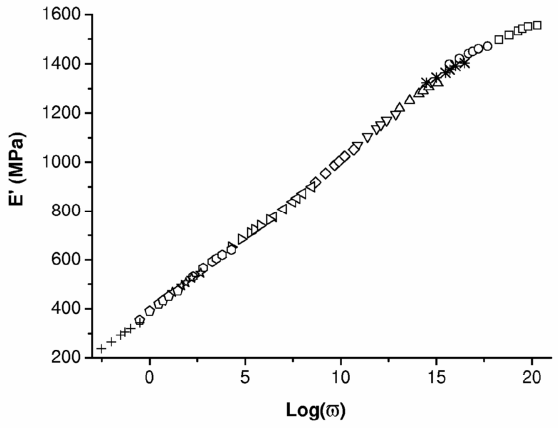

(d)

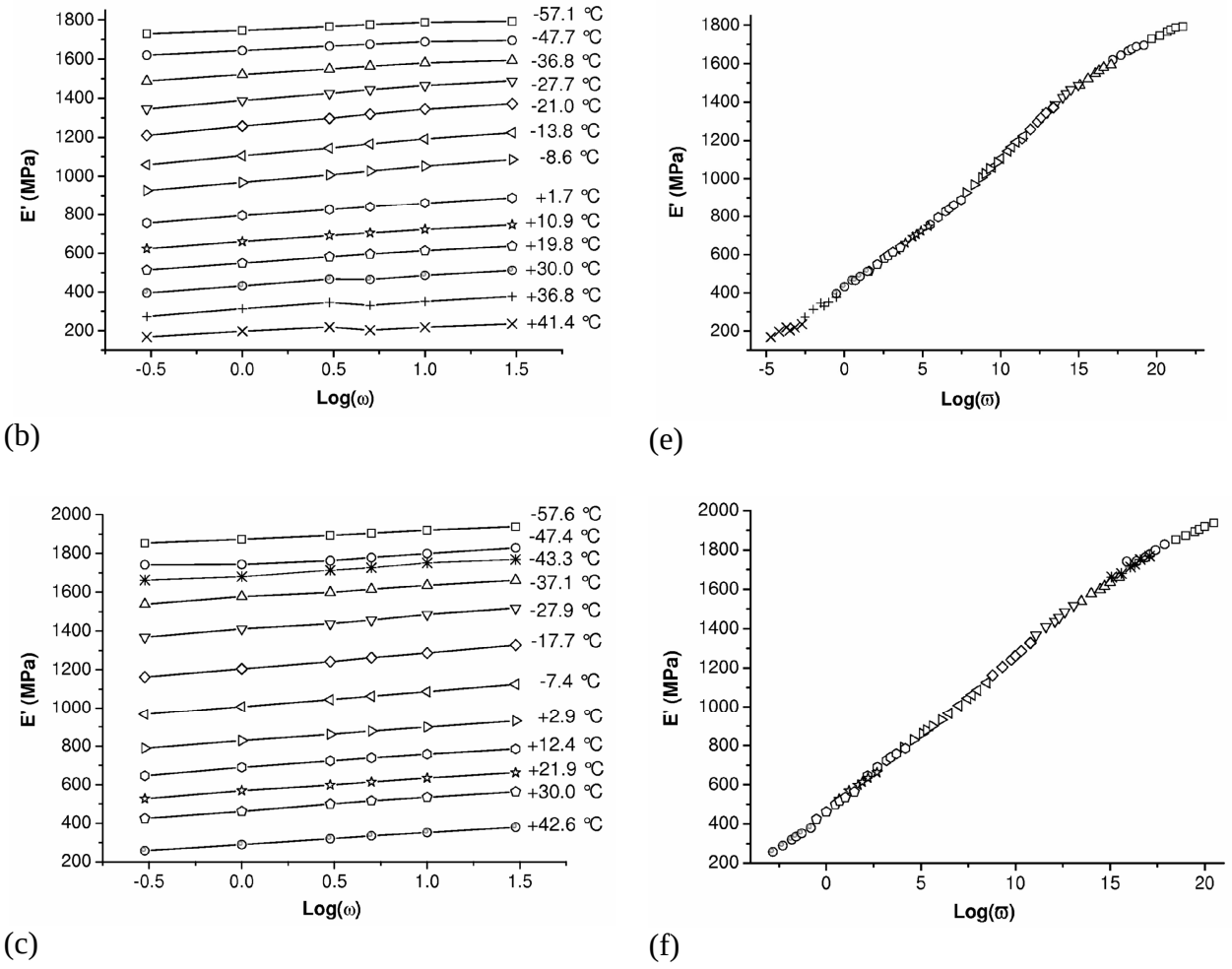

Figure 4.56 Isothermal sections of the storage modulus (E') of LLDPE- 2 vol% fumed silica nanocomposites from dynamic multi-frequency tests. (a) LLDPE, (b) LLDPE-A200-2, (c) LLDPE-A380-2. Superimposed curves according to the time-frequency equivalence principle (T_0=30 °C)

A direct comparison between E' master curves is represented in Figure 4.57. It is evident that the enhancement of the storage modulus is dependent on the surface area of the nanofiller.

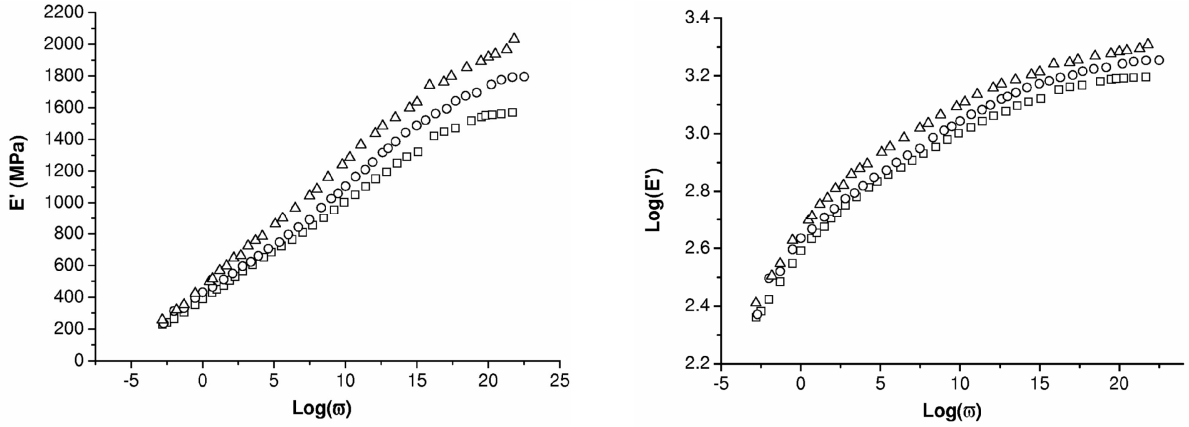

Figure 4.57 Comparison between E' master curves from multi-frequency dynamic tests on LLDPE-2 vol% fumed silica nanocomposites (T_0=30 °C). (a) Linear plot, (b) Logarithmic plot. (□) LLDPE, (○) LLDPE-A200-2, (△) LLDPE-A380-2

As already done for creep tests at various temperatures, an analysis of the shift factor trends was conducted, and in Figure 4.58 shift factors derived from the construction of the master curves are reported. Even in this case, Arrhenius equation can be utilized (see Equation 2.29) in order to obtain activation energy (E_a) values, summarized in Table 4.19. E_a values determined with dynamic multi-frequency tests are similar to that obtained with creep tests at different temperatures. Neither in this case a monotonic trend of E_a with the surface area of the nanofiller was detected, and considering the relative errors it is possible to conclude that energy of activation values of fumed silica nanocomposites are very near to that obtained for pure LLDPE.

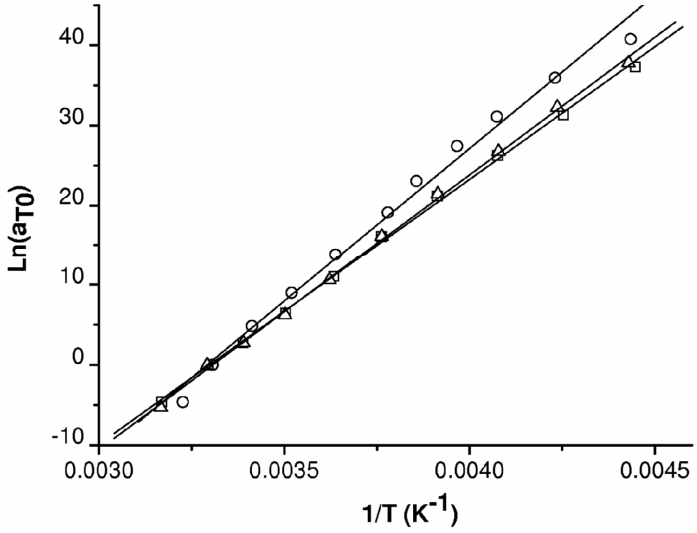

Figure 4.58 Shift factor for the construction of the E' master curves from multi-frequency dynamic tests on LLDPE-2 vol% fumed silica nanocomposites (T_0=30 °C), with fitting lines according to Arrhenius equation. (□) LLDPE, (○) LLDPE-A200-2, (△) LLDPE-A380-2

Sample	E_a (kJ/mol)
LLDPE	275.4 ± 3.6
LLDPE-A200-2	318.2 ± 10.1
LLDPE-A380-2	285.7 ± 3.3

Table 4.19 Energy of activation values (Ea) of LLDPE-2 vol% fumed silica nanocomposites according to Arrhenius equation

The dynamic behaviour of fumed silica nanocomposites can be compared to that of precipitated silica and glass filled samples at various filler loadings. In Figure 4.59 representative curves of the storage modulus of LLDPE and relative composites from dynamic mechanical tests conducted at 1 Hz are reported, while in Figure 4.60 E' and tanδ at 25 °C are summarized. It can be generally concluded that E' increases with the filler content for all the typologies of filler in the whole temperature range. As already reported in tensile quasi-static and creep tests, the improvement obtained by using glass microspheres is limited, if compared with that determined by using fumed silica nanoparticles at high surface area (A380). The storage modulus at ambient temperature of S160 filled samples is near to that of A200 composites. Considering tanδ trends with the filler content, it can be easily concluded that in the case of glass microcomposites loss tangent values are practically unaffected by the presence of the filler, while for precipitated silica and fumed silica nanoparticles tanδ decreases with the filler content. Even in this case the behaviour of S160 samples is similar to that of A200 filled nanocomposites, being the dynamic behaviour of the material mainly ruled by the surface area of the filler.

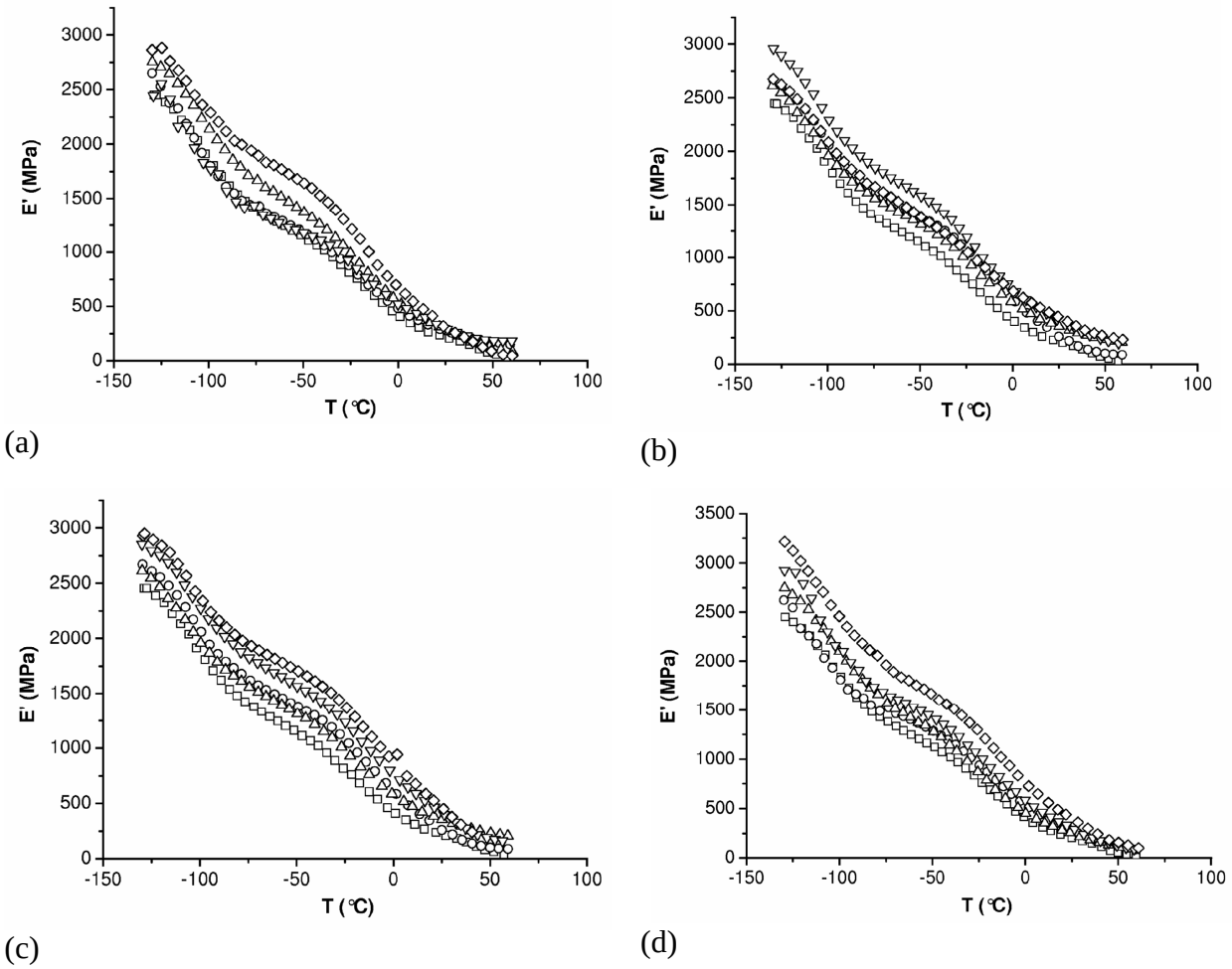

Figure 4.59 Storage modulus (E') of LLDPE and relative composites from dymanic mechanical tests (f=1 Hz). (a) LLDPE-Glass-x, (b) LLDPE-S160-x, (c) LLDPE-A200-x, (d) LLDPE-A380-x. (□) LLDPE, (○) x = 1 vol%, (△) x = 2 vol%, (▽) x = 3 vol%, (◇) x = 4 vol%

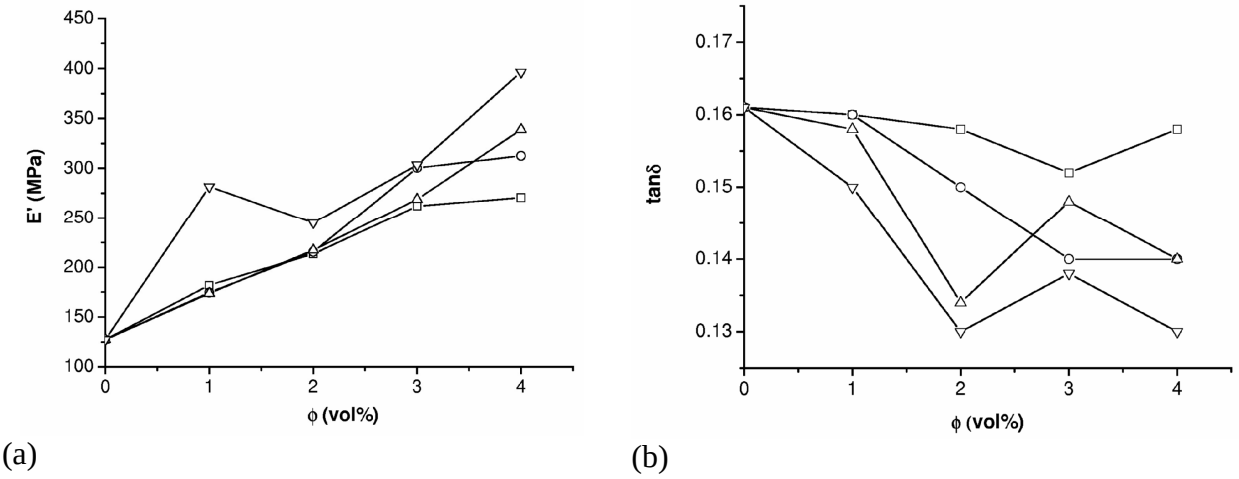

Figure 4.60 Dynamic properties of LLDPE and relative composites from DMTA tests (f=1 Hz) at T=25 °C. (a) Storage modulus (E'), (b) loss tangent (tanδ). (□) LLDPE-Glass-x, (○) LLDPE-S160-x, (△) LLDPE-A200-x, (▽) LLDPE-A380-x

Furthermore in Figure 4.61 loss tangent values of LLDPE and relative composites at low temperatures are reported, while glass transition temperatures, obtained from the peak of loss tangent curves, are summarized in Figure 4.62. If T_g is practically not influenced by the introduction of glass beads in the material, glass transition temperatures for fumed silica nanocomposites are considerably lower than that of pure LLDPE, especially for LLDPE-A380-x sample at high filler loadings. Even in this case the decrease of the glass transition temperature could be explained by a drop of the chain density in the interparticle region, more intense when high nanofilled samples are considered, because of the reduction of the interparticle distances. It is also possible that the higher number of polymer-filler surface interaction for the highly filled samples causes a more intense chain depletion in the interparticle region. The effect displayed by fumed silica nanoparticles in this work was completely different from that reported by Bugnicourt et al. in a paper about the mechanical performances of epoxy-fumed silica nanocomposites [213]. In that case the strong enhancement of the glass transition temperature due to the presence of silica nanoparticles was related to a reduction in the molecular mobility of the macromolecules around the filler due to strong physical polymer-filler interactions, comprising dispersion and dipolar interaction and hydrogen bonds to silica silanols. This discrepancy can be temptatively explained considering the different chemical nature and molecular mobility conditions of an LLDPE matrix with respect to an epoxy resin.

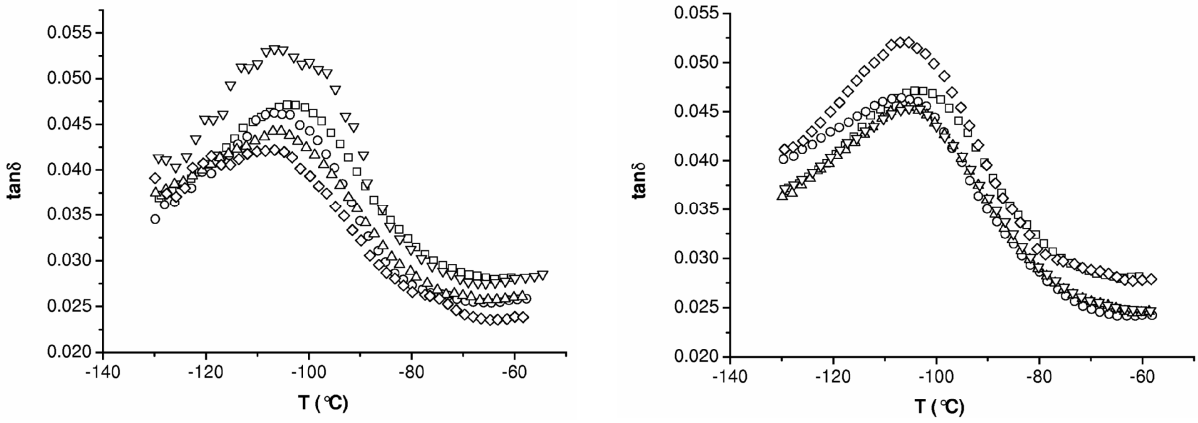

(a) (b)

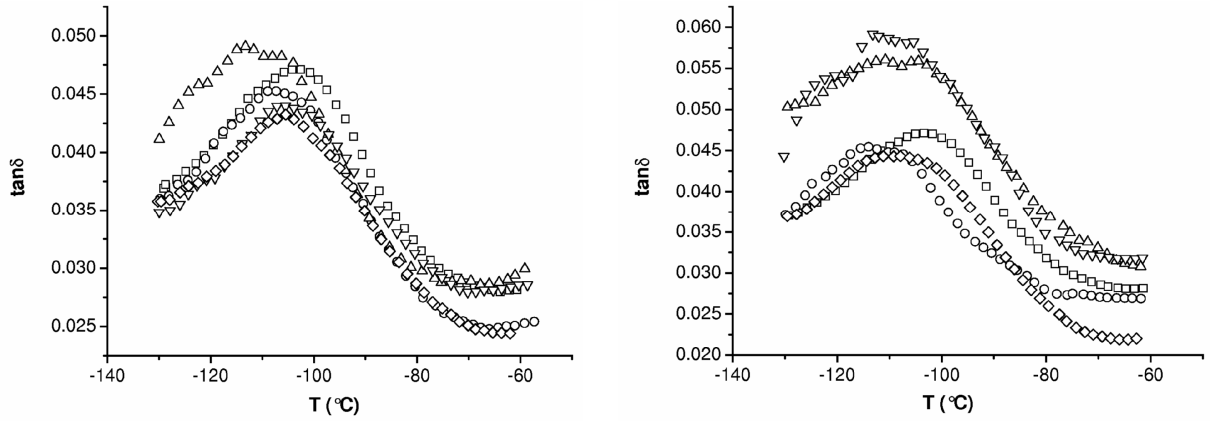

Figure 4.61 Loss tangent of LLDPE and relative composites from DMTA tests (f=1 Hz). (a) LLDPE-Glass-x, (b) LLDPE-S160-x, (c) LLDPE-A200-x, (d) LLDPE-A380-x. (□) LLDPE, (○) x=1 vol%, (△) x=2 vol%, (▽) x=3 vol%, (◇) x=4 vol%

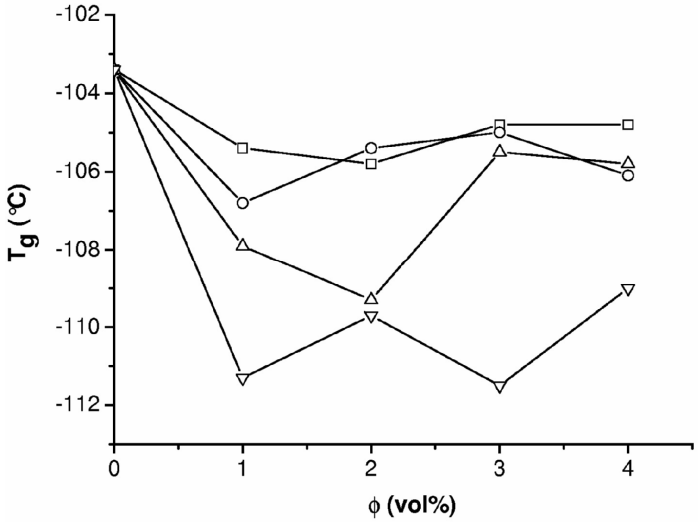

Figure 4.62 Glass transition temperatures (T_g) of LLDPE and relative composites from DMTA tests (f=1 Hz). (□) LLDPE-Glass-x, (○) LLDPE-S160-x, (△) LLDPE-A200-x, (▽) LLDPE-A380-x

4.4 Fracture behaviour

4.4.1 Quasi-static tensile tests

In Figure 4.63 representative stress-strain curves of LLDPE- 2 vol% fumed silica nanocomposites derived from quasi-static tensile tests are reported, while in Table 4.20 tensile properties at yield and at break are summarized.

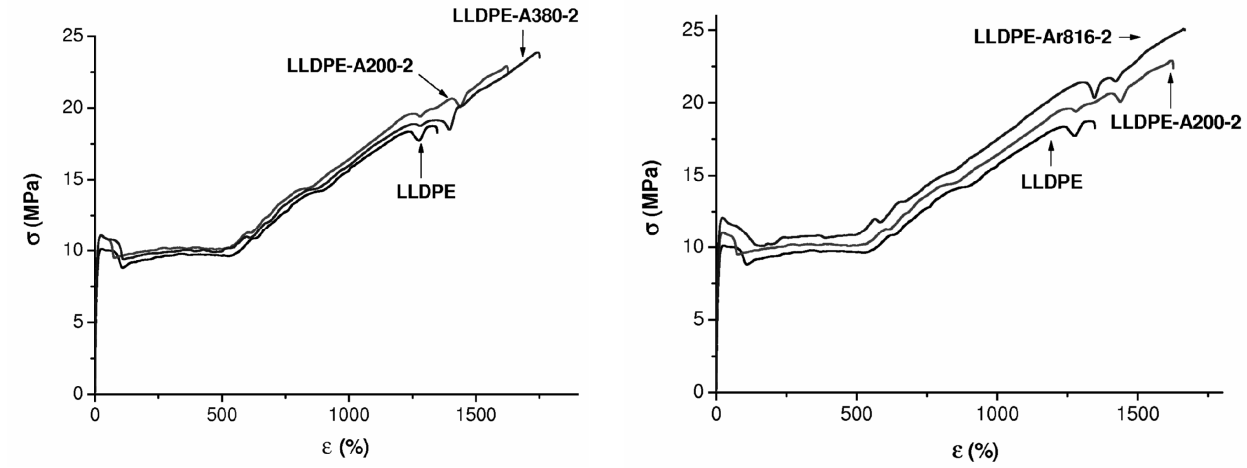

(a) (b)

Figure 4.63 Representative stress-strain curves of LLDPE- 2 vol% fumed silica nanocomposites from quasi-static tensile tests. (a) Effect of the surface area, (b) effect of the surface functionalization

Sample	σ_y (MPa)	ε_y (%)	σ_b (MPa)	ε_b (%)	TEB (J/mm^2)
LLDPE	10.11 ± 0.07	26.6 ± 1.1	19.8 ± 2.0	1439 ± 141	5.1 ± 0.5
LLDPE-A90-2	10.77 ± 0.07	24.8 ± 0.2	22.6 ± 0.3	1625 ± 49	7.1 ± 0.2
LLDPE-A200-2	10.99 ± 0.07	24.1 ± 1.3	22.3 ± 0.9	1613 ± 78	7.2 ± 0.5
LLDPE-Ar816-2	11.96 ± 0.10	22.8 ± 0.5	25.7 ± 0.7	1738 ± 65	8.6 ± 0.5
LLDPE-A300-2	11.07 ± 0.02	22.9 ± 0.6	22.9 ± 1.1	1637 ± 76	7.6 ± 0.5
LLDPE-A380-2	11.09 ± 0.04	23.9 ± 0.5	23.3 ± 0.3	1722 ± 40	7.9 ± 0.3

Table 4.20 Quasi-static tensile properties at yield and at break of LLDPE-2 vol% fumed silica nanocomposites

First of all, tensile stress at yield (σ_y) slightly increases with the surface area of the nanofiller, and this improvement is more evident when functionalized silica nanoparticles are used. The slight improvement of the yield strength is a signal of a quite good interfacial adhesion between LLDPE and nanoparticles, otherwise σ_y would decrease with the introduction of the filler [12, 192, 214, 215]. In fact, as suggested by Galeski et al. [216-218], in polyolefins filled with traditional microfiller (chalk, calcium carbonate) the strong increase in the elastic modulus of the material is

associated to an heavy decrease of the yield stress. This follows from the fact that traditional fillers do not bear the load in the direction of deformation. The same conclusions for the yield properties can be made for as concern the stress at break (σ_b) and the strain at break values (ε_b), that increase with the surface area and are positively affected by the presence of the organosilane on the surface of the nanoparticles. For example LLDPE-Ar816-2 sample shows an enhancement of the stress at break of about 30%, associated to an increase of the 21% of the strain at break. Furthermore specific tensile energy to break (TEB) values were obtained by integrating stress-strain curves in quasi-static tensile tests. The influence of the nanofiller dimension and of the surface modifications can be easily observed. In particular, it is worthwhile to note the marked TEB increase induced by the functionalized silica nanoparticles. Pure LLDPE sample shows TEB value of 5.74 J/mm^2, while for Ar816 filled material a TEB value of 8.50 J/mm^2 is reported.

The toughening effect encountered for fumed silica nanocomposites in this work is a very particular and interesting result, that is confirmed by the conclusions of the paper of Kontou and Niaounakis on LLDPE-fumed silica nanocomposite systems [23]. In fact in the major part of the works on polyolefin nanocomposites, the stiffening effect was accompanied by an heavy embrittlement, with a reduction of the tensile strain at break [180, 195]. Galeski confrmed that the most undesirable effect due to the introduction of traditional microfiller in polymeric systems is the loss of toughness [216], indicating the softening of a polymer-filler interface as the best way to recover toughness in traditional microcomposites.

It is now interesting to evaluate the effect of the filler content on the tensile properties at yield and at break, considering also precipitated silica and glass beads filled microcomposites. The effect of the various fillers on the tensile stress at yield (σ_y) is summarized in Figure 4.64 as relative values with respect to the unfilled materials. It is immediately evident that σ_y increases with the filler content. While glass filled samples show negligible σ_y enhancements with respect to the unfilled matrix, the effect is more evident if precipitated microsilica and fumed silica nanoparticles are used. As reported by Ganss et al. [168], several equation are availale to predict the yield strength of particulate filled polymers. The Nicolais-Narkis equation is a two-third power law function with K as a parameter for filler-matrix adhesion [219] :

Equation 4.7

$$\frac{\sigma_{yc}}{\sigma_{ym}} = 1 - K(\phi)^{2/3}$$

This model predicts a decrease of the yield strength of the composite with respect of the pure matrix as the filler amount increases. According to this model, traditionally adopted for particulate filled microcomposites, the stress at yield would gradually decrease with the filler content. As an example, in the case of poor filler-matrix adhesion 2 vol% filled nanocomposites would have a relative σ_y of 0.91. More recently the following equation was proposed by Pukanszky et al. [220] :

Equation 4.8

$$\frac{\sigma_{yc}}{\sigma_{ym}} = \left(\frac{1-\phi}{1+2.5\phi} \right) \exp(B\phi)$$

where B is an empirical parameter characterizing the degree of filler-matrix interaction. The value of parameter B depends on all factors influencing the load-bearing capacity, i.e. strength and size of the interface [221]. In Figure 4.64 relative tensile stress at yield data of LLDPE and relative composites with the fitting lines according to Pukanszky and Nicolais-Narkis equation are reported. B values of the Pukanszky model were choosen minimizing chi-square values during the fitting procedure, while for Nicolais-Narkis equation a theoretical K value of 1.21, commonly used in the case of poor filler-matrix adhesion, was utilized.

It is evident that Nicolais-Narkis equation is completely unsuitable to describe the yield behaviour of the prepared samples, because negative K values would be necessary to fit yield strength data. The inappreciable significance of the parameters based on these models is attributed to the fact that dynamics of polymer-filler interaction are fundamentally different from the same as in the case of nanocomposites, where the presence of a wide interface alters the physical significance of polymer-filler interaction at the molecular level since structural organization of the matrix at the interface is largerly different from that in the bulk

Pukanszky model seems to better interprete yield stress data. For glass filled sample B has a relatively low value (3.95), if compared with that of precipitated silica microcomposites (6.71). B values for nanocomposites is even more elevated, around 8. The values found for B parameter are reasonable, considering that generally B parameter for different nanocomposites remains between 2 and 15 [222]. This evidence confirms that the filler-matrix interaction, mainly related to nanofiller dimensions, can not be neglected for the prepared nanocomposites.

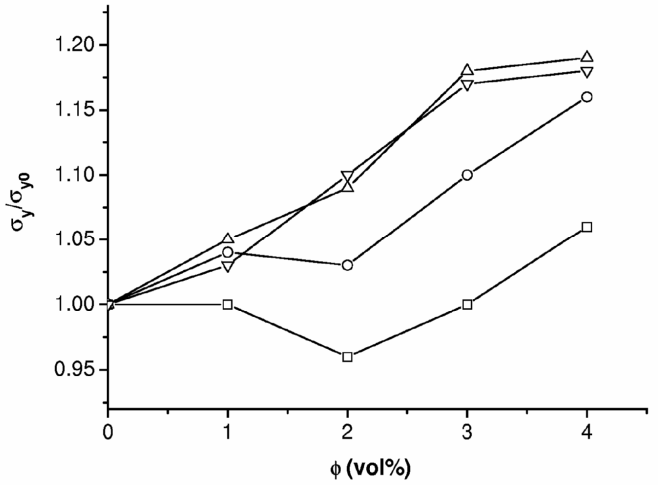

(a)

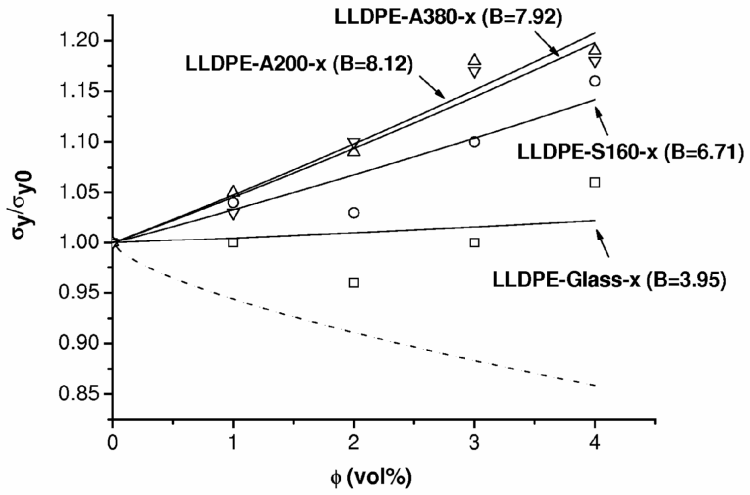

(b)

Figure 4.64 Relative tensile stress at yield of LLDPE and relative composites (a), with fitting curves (b) according to Pukanszky model (continuous lines) and Nicolais-Narkis equation (dashed line) in the case of poor filler-matrix adhesion (K=1.21). (□) LLDPE-Glass-x, (○) LLDPE-S160-x, (△) LLDPE-A200-x, (▽) LLDPE-A380-x.

In Figure 4.65 relative stress at break and strain at break data are reported. It is evident that the introduction of fumed silica nanoparticles leads to a remarkable improvement of the stress and strain at break with maximum increments close to about 20% with respect to the pure matrix for A380 filled samples. It is also evident that an optimal filler loading of 2-3 vol% maximizes the stress and strain at break values that can be achieved. After this critical concentration the failure behaviour is most probably negatively affected by nanoparticles agglomeration. On the contrary, when micrometric silica particles are used, such as S160 or glass microbeads, a slight reduction of

the tensile properties at break is detected. The negative trend is more evident when glass microbeads are used. The fracture behaviour seems therefore to strictly depend on the dimensions of the filler. As comparison, the prediction of Nielsen model [223], originally proposed to predict the strain at break of spherical microparticles filled composites with good adhesion between filler and matrix is also reported in Figure 4.65. The model is based on the following equation :

Equation 4.9

$$\varepsilon_{bc} = \varepsilon_{bm}\left(1-\phi^{1/3}\right)$$

where ε_{bc} and ε_{bm} are respectively the stress at break of the composite and of the pure matrix, while Φ is the filler volume fraction. It is evident that the model is not able to capture the behaviour of the investigated materials, and the negative trend observed for microbeads filled composites is overestimated. It has to be considered that this model was elaborated for traditional composites with good filler-matrix adhesion. It can be concluded that the trends of the tensile properties at break observed for fumed silica nanocomposites are not explicable on the basis of the models proposed for traditionally microcomposites.

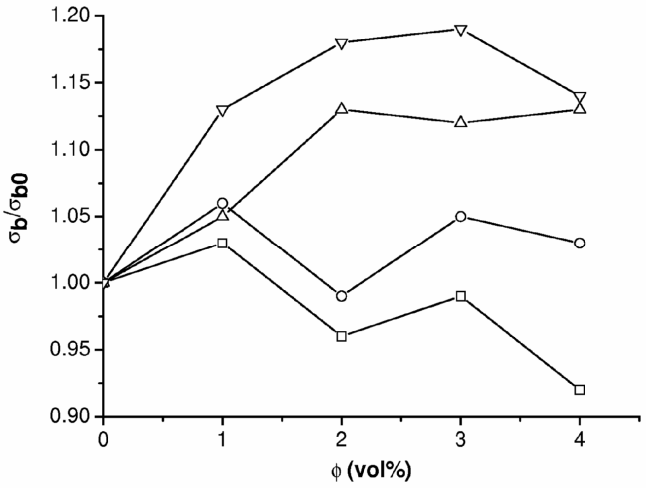

(a)

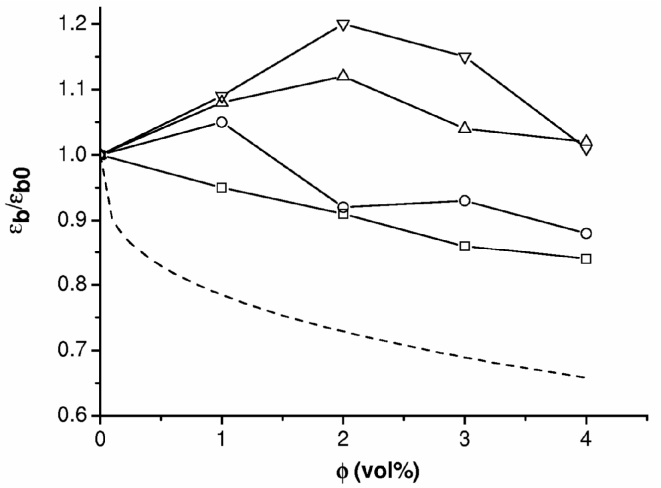

(b)

Figure 4.65 Quasi-static tensile properties at break of LLDPE and relative composites. (a) Relative stress at break, (b) relative strain at break. (□) LLDPE-Glass-x, (○) LLDPE-S160-x, (△) LLDPE-A200-x, (▽) LLDPE-A380-x. The dashed line is the theoretical prediction of the strain at break according to the Nielsen model (Equation 4.9)

A microstructural explanation for the toughnening effect due to the introduction of fumed silica nanoparticles in these systems is then required. Lazzeri et al. studied the debonding mechanism during tensile tests in 10 wt% $CaCO_3$-HDPE nanocomposites [149]. In this paper the stress whitening zones appearing along the gauge length during tensile tests were attributed to the matrix-particle debonding and to the consequent void growth. Volume measurements confirmed this hypothesis, since the volume increased with deformation for $CaCO_3$ filled samples, while for pure HDPE a decrease in volume with elongation was observed. Moreover TEM observations showed cavities and voids due to debonding and deformation bands in the stress whitened areas. In order to analyze the debonding process and the various stages of void formation during tensile tests, Sudar et al. conducted volume strain measurements on PE/$CaCO_3$ composites, by using different matrices and various amounts of filler [224]. Starting from the consideration that in thermoplastic composites filler-matrix debonding and plastic deformation of the matrix are competitive processes, they found that the number of voids formed was inversely proportional to the stiffness of the matrix. In stiff matrices (i.e. elastic modulus higher than 1 GPa) almost the entire amount of filler separated from the matrix under the effect of external load, while for soft matrices (with an elastic modulus lower than 0.4 GPa) the debonding was completely absent and the composite could deform exclusively by shear yielding. In Figure 4.66 the trends of the volume strain and of the Poisson's ratio versus the longitudinal strain of LLDPE and LLDPE-A380-2 samples are reported. A neat decrease of the volume strain with deformation for pure LDPE can be easily detected. Lazzeri et al. [149],

following the considerations of Gaucher-Miri et al. [225], suggested that the decrease can be probably due to the fact that the stretching of amorphous phases led to the orientation of the amorphous chains along the strain direction and the consequent formation of a mesomorphic structure similar to those found in liquid–crystal polymers in the smectic state, with a consequent decrease in volume strain. The strain induced decrease in volume in pure HDPE could not be attributed to further crystallization, being the crystallinity of the yielded samples practically the same of the undeformed ones (see Chapter 4.1.2.3). The volume decreases with the deformation also for LLDPE-A380-2 sample, in accordance with the trend reported by Sudar et al. [224], being the elastic modulus of LLDPE relatively low (about 0.2 GPa). Furthermore from Figure 4.66 it is evident that even Poisson's ratio is not practically affected by the presence of nanoparticles, being ν values around 0.45-0.5 for an applied strain of 10%. This means that in our system the filler-matrix debonding mechanism is practically absent and the composite deformed by shear yielding. This consideration is supported by the density measurements reported in Chapter 4.1.2.2, from which any void formation during melt compounding can be excluded, being the experimental density values of the nanocomposites very close to the theoretical ones. Moreover the little decrease of the density detected for yielded sample with respect to the not deformed samples is practically the same for LLDPE and LLDPE-A380-2 samples.

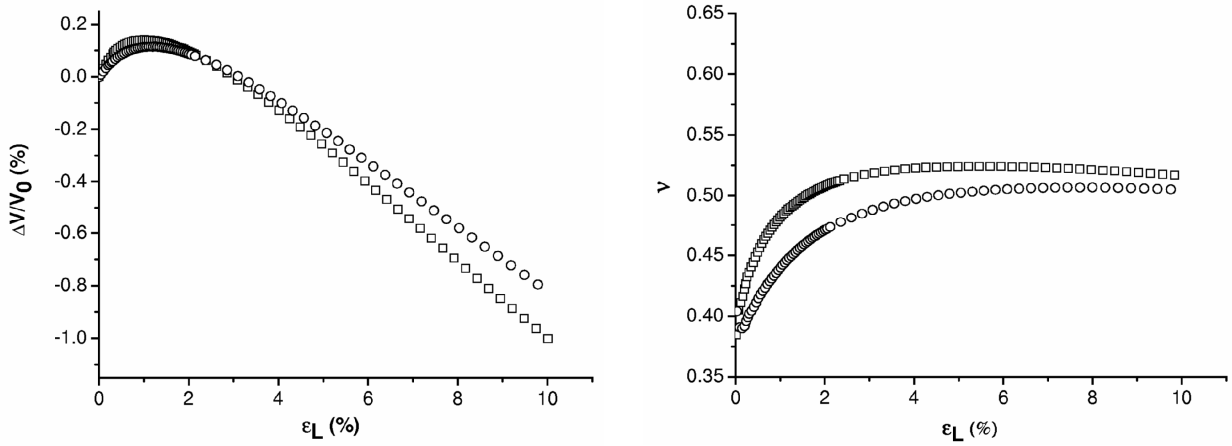

(a) (b)

Figure 4.66 Dilatometric tests on LLDPE and LLDPE-A380-2 nanocomposite. (a) Volume strain vs longitudinal strain, (b) Poisson's ratio vs longitudinal strain. (□) LLDPE, (○) LLDPE-A380-2

A possible explanation of the toughening effect encountered for the silica composites can be found considering TEM images of LLDPE-A380-2 samples at different strain levels, reported in Figure 4.12 and in Figure 4.13. As explained in Chapter 4.1.2.1, the nanofiller is well dispersed in the

LLDPE matrix, being the mean diameter of the aggregates around 200 nm. The aggregates remain isodimensional up to an applied strain of 30 %, for higher deformation levels a strong orientation along the stress direction is evident. This means that for deformations higher than the strain at yield (about 25% for all the samples considered) the shear yielding process becomes very intense and the nanoparticles can align parallel to the strain direction. For a strain of 100 %, silica aggregates are about 1.5 μm long and less than 100 nm large, and are separated of about 100 nm. It is possible that during the viscous flow produced by shear yielding the nanoparticles, segregated in the amorphous regions, orient themselves along the strain direction. This experimental evidence is supported by Jeol et al. [226], which studied the deformation induced modification of the dispersion state of 2.5 wt% silica nanoparticles in PET nanocomposites, after a stretch-blowing process just above the glass transition temperature of the matrix. They found that the fumed silica nanoparticles tended to agglomerate and orient parallelly to the elongation direction, forming long streams of aggregates (more than 2 μm), regularly spaced by a distance of 50-100 nm. They concluded that the nanoparticles were rejected from the highly oriented crystalline domains induced by the strain, on the contrary of that happened using spherical silica nanoparticles, for which the long streams of nanoparticles where oriented perpendicular to the elongation direction. They hypothesized that this unexpected orientation was produced by the extended growth of mesophases and crystallites perpendicular to the orientation and that stacked lamellae were formed rather than microfibrils. In our case it is probable that the very little width of silica aggregates at high deformation (less than 100 nm) is well below the critical defect size for crack nucleation of LLDPE, moreover the long streams of aggregates along the stress direction favoures the matrix-filler load transfer mechanism. In these conditions the load sustained by the polymeric phase is reduced and LLDPE macromolecules can deform at an higher extent before breaking.

As reported in Figure 4.9 and in Figure 4.10, in the case of LLDPE-S160-2 sample silica aggregates have an higher mean size (about 400 nm). Furthermore, the orientation of silica aggregates is less pronounced and begins to be effective at higher deformation levels with respect to LLDPE-A380-2. This considerations can explain why the stress and the strain at break of LLDPE are not improved by the presence of precipitated silica microparticles.

4.4.2 Tensile impact tests

Considering that an optimal fracture behaviour was obtained for 2 vol% fumed silica nanocomposites, a more detailed analysis was conducted for this composition. In particular tensile behaviour under impact conditions was evaluated. In Figure 4.67 representative force-time curves of tensile impact tests of LLDPE and LLDPE-Ar816-2 nanocomposite are reported, while in Table 4.21 specific Tensile Energy to Break (TEB), determined through the integration reported in Equation 4.10, are summarized.

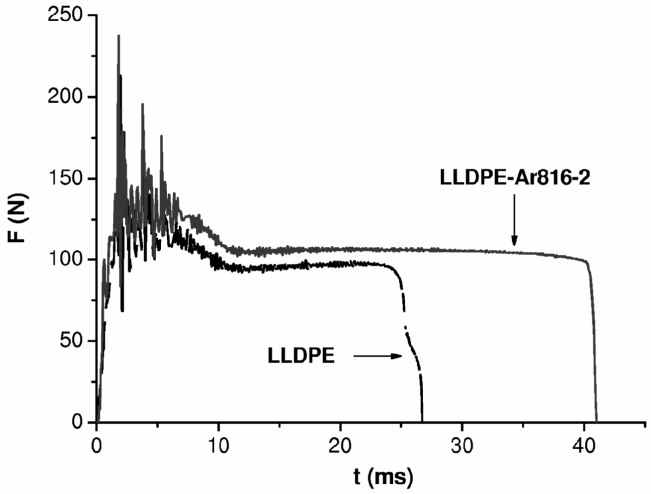

Figure 4.67 Representative curves of tensile impact tests of LLDPE-2 vol% fumed silica nanocomposites (v=2 m/s)

Equation 4.10

$$TEB = \left(\frac{1}{A}\right)\left[V_0 \int_0^{t_r} F dt - \frac{1}{2m}\left[\int_0^{t_r} F dt\right]^2\right]$$

It is evident that even when the load is applied at high speed (2 m/s) the introduction of fumed silica nanoparticles leads to an interesting increase of the energy adsorbed at break. The toughening effect is more intense as the nanoparticles are surface functionalized, in accordance with the conclusions reported in quasi-static tensile tests.

sample	TEB (J/mm^2)
LLDPE	0.62 ± 0.01
LLDPE-A90-2	0.70 ± 0.13
LLDPE-A200-2	0.65 ± 0.12
LLDPE-Ar816-2	0.86 ± 0.12
LLDPE-A300-2	0.74 ± 0.09
LLDPE-A380-2	0.67 ± 0.12

Table 4.21 Specific tensile energy values of LLDPE- 2 vol% fumed silica nanocomposites from tensile impact tests (v=2 m/s).

While the presence of the organic modifier on the surface of the nanoparticles seems to not affect the viscoelastic response of the resulting material, tensile properties at break are interestingly improved in the case of Ar816 filled nanocomposites, both in quasi-static and in impact test. Rong et al. [227, 228] and Wu et al. [229] already found that the addition of small amount of modified nanoparticles (SiO_2 or $CaCO_3$, typically less than 3% by volume) could improve the strength and the fracture toughness of polypropylene more effectively than the untreated ones.

According to the indications of Zhang [230] and Kontou [23], it is possible that the presence of the organosilane on the surface of the nanoparticles increases their hydrophobicity, facilitating filler/matrix miscibility and allowing a more uniform dispersion of the nanoparticles during melt compounding. It is also possible that filler/matrix interaction is enhanced through the entanglements between the surface modifier and the polymer matrix, thus delaying the shear yielding of the matrix and favouring the filler-matrix load transfer mechanism. Further investigations will be necessary to reach a better comprehension of the effect of the surface modification on the tensile response of the prepared nanocomposites.

4.4.3 Essential Work of Fracture (EWF) analysis

In order to complete the analysis of the fracture behaviour of LLDPE-fumed silica nanocomposites, essential work of fracture (EWF) tests were conducted on unfilled matrix and relative 2 vol% filled samples. In Figure 4.68 SEM images of the notch tip of LLDPE DENT samples for the EWF tests

at different magnifications are reported. It is evident that the crack tip is very sharp, with a mean radius of curvature of about 1-2 μm. Williams and Rink summarizing the standardisation efforts of the EWF tests [129], recommended a crack tip with a radius lower than 20 μm. This means that the prepared experimental apparatus (see Figure 3.10) and the cutting technique are suitable to prepare the specimens required for the EWF test.

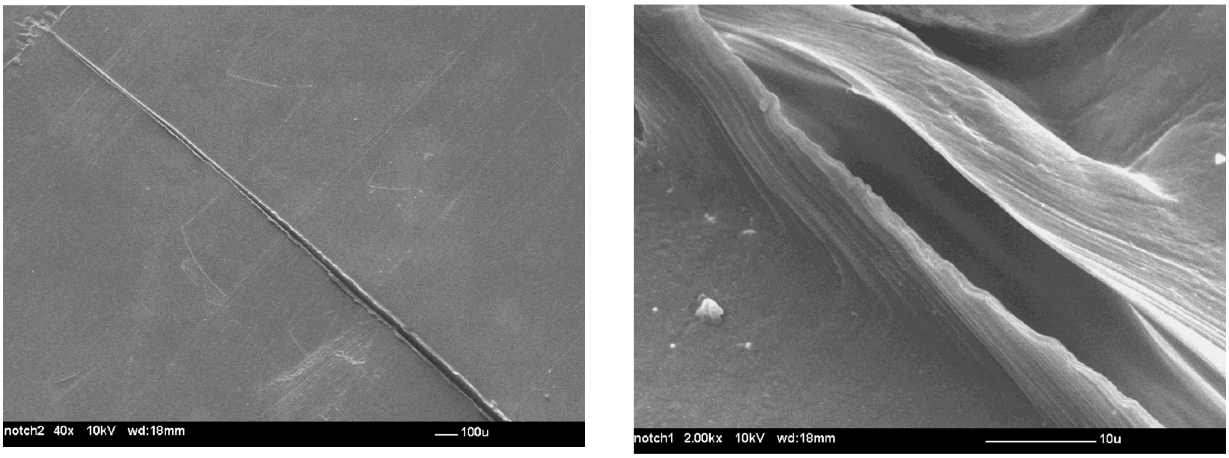

(a) (b)

Figure 4.68 SEM images of the notch tip of LLDPE DENT samples for the EWF tests at different magnifications

In Figure 4.69 representative pictures of the EWF tests at different times of pure LLDPE and LLDPE-A380-2 samples are reported. The unfilled sample does not show stress whitening in the yielded zone, while for all the filled samples the yielding process is associated to an evident stress whitening, which makes easy the determination of the initiation of the propagation of the plastic zone in the material. The yielding starts at the crack tip, where the stress concentration favours the plastic deformation process. When the yielded zone is extended over the whole ligament length, the propagation of the plastic zone is faster and the sample can be deformed with a lower load, until the fracture of the specimen is reached. Referring to TEM images of the yielded samples (see Figure 4.12 and Figure 4.13), the stress withening of the yielded samples experienced by fumed silica nanocomposites can be explained considering the alignment of silica aggregtes along the stress direction, forming streams of nanoparticles 2 μm long, well above the visible light vawelength. The concentration of the crystalline zones with the segregation of the nanoparticles along the stress direction during the yielding process can be hypothesized as another explanation for the stress whitening of the nanocomposites. It is important to underline that the whitening for traditional glass

beads microcomposites is less evident, probably because of the formation of a less oriented microstructure during the straining process.

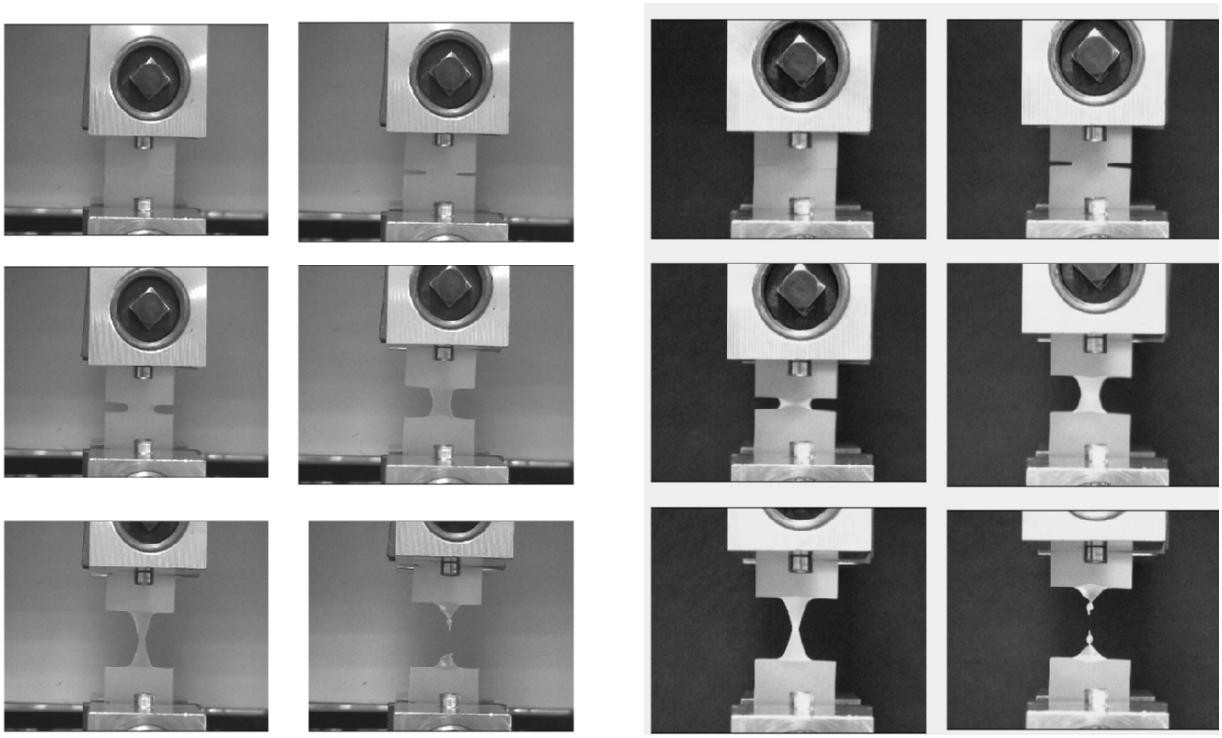

(a) (b)

Figure 4.69 Photograms of the EWF tests at different times. (a) LLDPE, (b) LLDPE-A380-2 samples

Figure 4.70 reports representative curves from EWF tests at different ligament lengths, while in Figure 4.71 representative linear plots of specific total work of fracture (w_f) versus ligament length (L) of LLDPE and relative 2 vol% fumed silica nanocomposites are represented. The most important results are then summarized in Table 4.22. It is evident that the introduction of silica nanoparticles leads to a remarkable improvement of the specific essential work of fracture (w_e), that increases with the surface area of untreated silica nanoparticles, in accordance with the results of tensile quasi-static and impact tests. In particular an enhancement of the w_e value of 43 % is determined for LLDPE-A380-2 sample. Moreover, the increase of specific essential work of fracture values with the surface area is accompanied by a slight reduction of the specific plastic work of dissipation (βw_p), due probably to a parallel reduction of the plastic zone.

w_e value of LLDPE-Ar816-2 sample is practically the same of that obtained for the sample containing the same amount of untreated A200 nanoparticles with the same surface area (around 31 kJ/m^2). In all cases, R^2 values are around 0.99, this means that a good fitting, with little dispersion

of data, was obtained, in accordance with the indication reported in the work of Williamson about the standardisation of the EWF method [129]. The essential work of fracture approach was also adopted by Bureau et al. [231, 232] for studying the fracture behavior of polymer nanocomposites (PNCs) based on a polypropylene with organo-modified clays, finding an interesting improvement of w_e (+20%). In that case toughness improvement was attributed to higher voiding and improved matrix resistance attributed to finer, more oriented clay nanoparticles. Tjong and Bao [196] prepared high density polyethylene (HDPE)-organoclay (MMT) nanocomposites toughened with maleated styrene–ethylene–butylene–styrene (SEBSg-MA) elastomer by melt compounding. SEBS-g-MA additions were found to exhibit beneficial effect on the specific essential work of fracture of HDPE/2% OMMT and HDPE/4% OMMT nanocomposites. Such enhanced tensile fracture toughness was attributed to an improved shear yielding of the matrix. An enhancement of w_e values due to silica nanoparticles was also detected from Musto et al. [233] in a work on polyimides filled by in situ generated SiO_2 nanoparticles.

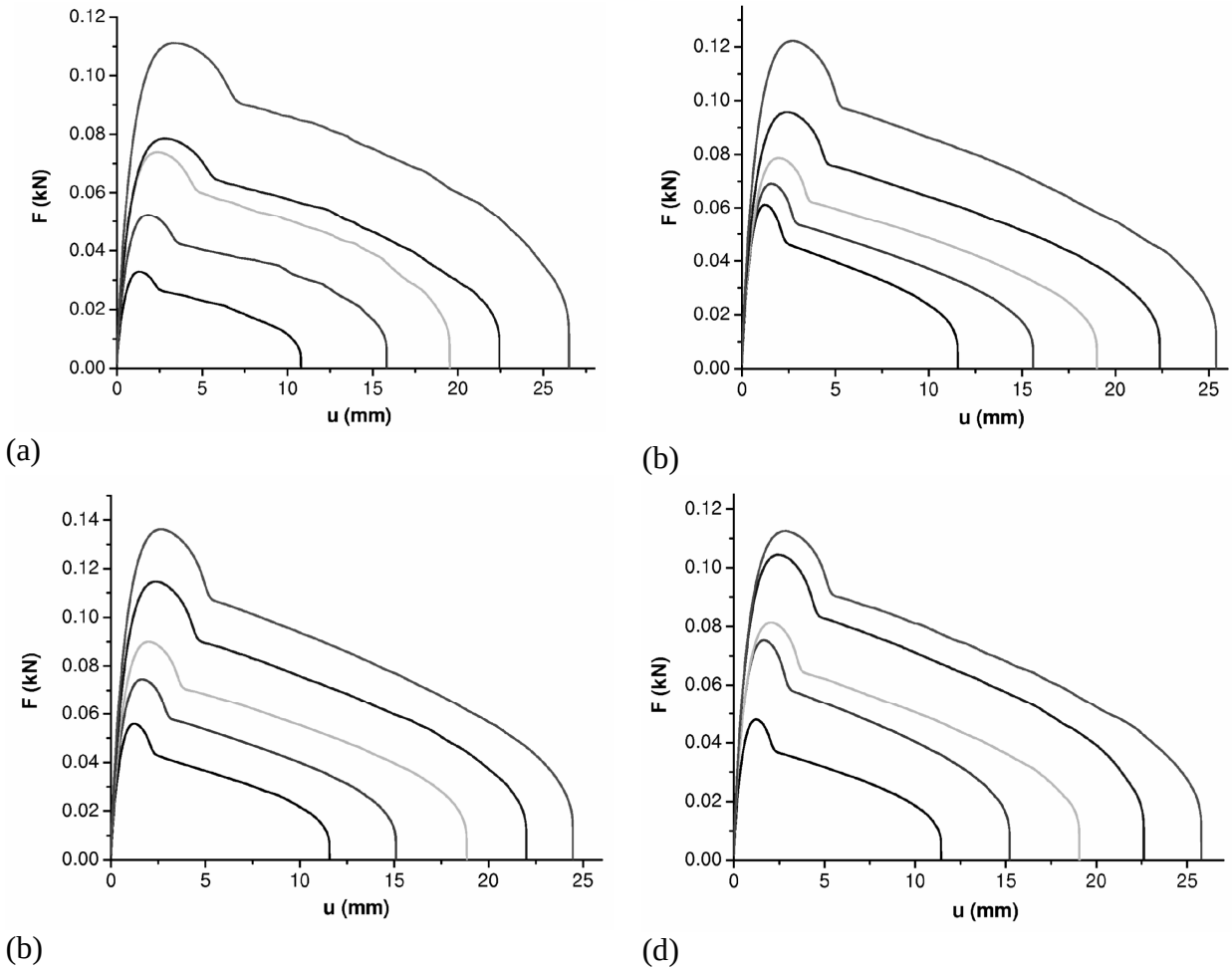

Figure 4.70 Representative curves from EWF tests on LLDPE-2 vol% fumed silica nanocomposites. Every line refers to a different ligament length. (a) LLDPE, (b) LLDPE-A200-2, (c) LLDPE-A380-2, (d) LLDPE-Ar816-2

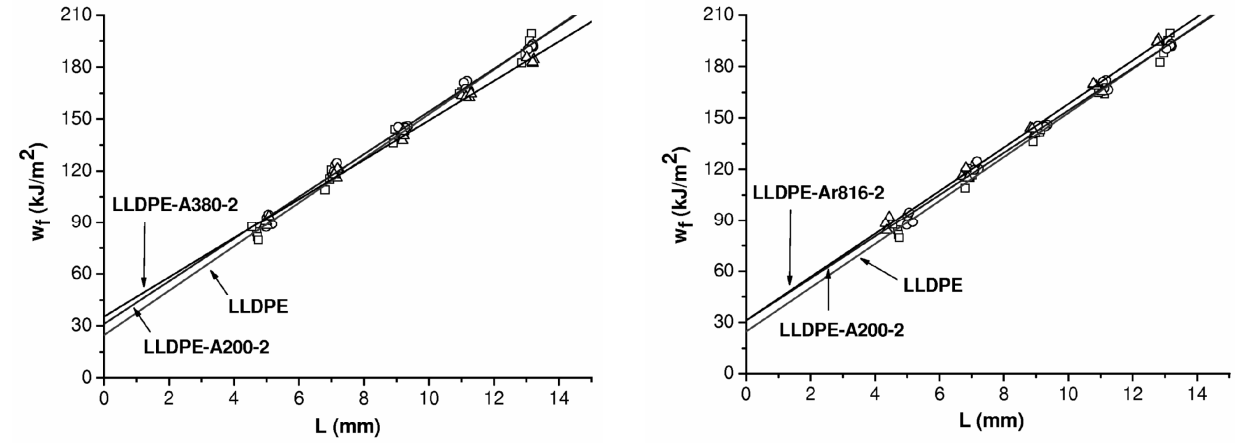

Figure 4.71 Specific work to fracture vs ligament length from EWF tests on LLDPE- 2 vol% fumed silica nanocomposites. (a) Effect of the surface area, (□) LLDPE, (○) LLDPE-A200-2, (△) LLDPE-A380-2. (b) Effect of the surface functionalization, (□) LLDPE, (○) LLDPE-A200-2, (△) LLDPE-Ar816-2

In Figure 4.72 representative linear plots of the specific work to yield of LLDPE and relative 2 vol% fumed silica nanocomposites are reported, while in Table 4.22 the specific work for crack initiation (w_{ini}) values are reported. The essential work of crack initiation is positively affected by the introduction of silica fumed nanoparticles, increasing w_{ini} with the filler surface area, even if the major part of the fracture toughness enhancement is related to the propagation part. Similar conclusions were reported by Zhang et al. [234], who studied the crack initiation fracture toughness of various nanoparticles filled polyamide 66 in a broad temperature range by using the EWF approach. In that case, the addition of nanoparticles led to an enhancement of specific EWF parameters at most test temperatures at the cost of a reduction of the non-essential terms.

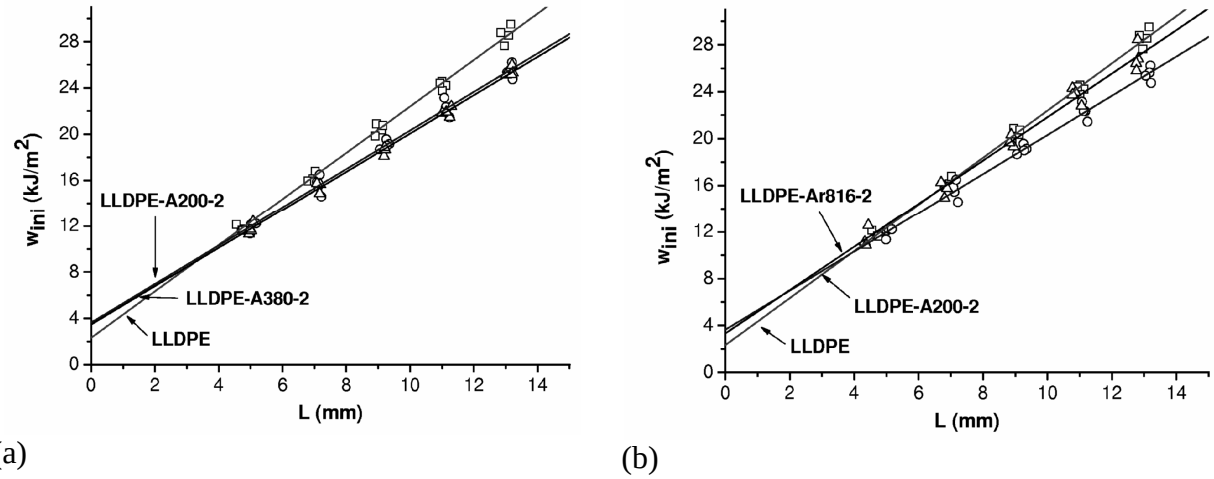

Figure 4.72 Specific work to yielding vs ligament length from EWF tests on LLDPE- 2 vol% fumed silica nanocomposites. (a) Effect of the surface area, (□) LLDPE, (○) LLDPE-A200-2, (△) LLDPE-A380-2. (b) Effect of the surface functionalization, (□) LLDPE, (○) LLDPE-A200-2, (△) LLDPE-Ar816-2

Sample	w_e (kJ/m^2)	βw_p (MJ/m^3)	w_{ini} (kJ/m^2)	W_{prop} (kJ/m^2)
LLDPE	24.7 ± 2.7	12.8 ± 0.3	2.3 ± 0.3	22.4 ± 2.7
LLDPE-A90-2	21.0 ± 2.7	13.1 ± 0.3	2.4 ± 0.5	18.6 ± 2.7
LLDPE-A200-2	31.1 ± 2.2	12.3 ± 0.3	3.6 ± 0.4	27.5 ± 2.2
LLDPE-Ar816-2	31.2 ± 2.1	12.7 ± 0.2	3.3 ± 0.6	27.9 ± 2.1
LLDPE-A300-2	28.4 ± 2.3	12.2 ± 0.2	3.2 ± 0.4	25.2 ± 2.3
LLDPE-A380-2	35.3 ± 1.8	11.4 ± 0.2	3.5 ± 0.3	31.8 ± 1.8

Table 4.22 Results of the EWF tests on LLDPE - 2 vol% fumed silica nanocomposites

5 Conclusions

Linear low density polyethylene (LLDPE) based composites were prepared through a melt compounding process, by using different kinds of amorphous silicon dioxide (SiO_2) micro and nanoparticles, in order to detect the role of the filler size and surface area on the viscoelastic and fracture behaviour of the resulting composites. In particular, various nanocomposites were prepared by using different percentages of hydrophilic and surface treated fumed silica nanoparticles. A comparion was then conducted with micrometric precipitated silica and glass microspheres composites.

- The rheological behaviour of the composites in the molten state manifested a strong dependence on the surface area of the filler. The introduction of fumed silica nanoparticles and precipitated silica microparticles in the composites led to a remarkable enhancement both of the storage (G') and shear moduli (G''), and of the viscosity (η) at low frequencies, especially at high filler loadings, while glass microbeads marginally affected rheological properties of the material. This result was explained considering the formation of a network structure arising from particle-particle interactions due to hydrogen bonding between silanol groups. The presence of the solid like behaviour for the filled samples al low frequencies was confirmed by fitting viscosity data with a modified De-Kee Turcotte model, taking into account the presence of an initial yield stress.

- Also the viscoelastic behaviour in the solid state was mainly ruled by the surface area of the fillers. When precipitated silica microparticles or fumed silica nanoparticles were considered, a very interesting improvement of the elastic modulus with the filler content was observed, while in the case of glass particle filled microcomposites the stiffening effect was rather limited. Considering that FT-IR analysis evidenced the presence of carbonylic groups

in the matrix, probably due to the thermal oxydation induced during the production processes, elastic modulus data were interpreted accordingly to a new model, incorporating the surface interaction between the matrix and silanols present on the surface of the particles. Isothermal creep tests at various stress levels and temperatures confirmed the link between the surface area of the nanofiller and the creep stability of the material. Through the application of a time-temperature superposition approach, creep curves at different temperatures allowed the construction of creep master curves. It was therefore possible to conclude that the stabilizing effect provided by the nanoparticles was more effective at long loading times. Even the dynamic mechanical behaviour of the prepared composites was related to the surface area of the filler. Storage modulus (E') enhancement obtained by using glass microspheres was limited, if compared with that provided by precipitated silica microparticles and fumed silica nanoparticles of high surface area. Interestingly, the glass transition temperature (T_g) of the LLDPE matrix was slightly lowered by the presence of untreated nanofillers, probably because polymer-filler interaction lead to a partial physical adsorption of the macromolecules at the surface, with a consequent chain depletion in the interparticle region.

- Filler dimensions revealed important also when the fracture behaviour of the prepared composites was considered. In the case of fumed silica nanocomposites, tensile properties at yield and at break slightly increased with the surface area of the nanofiller and were positively affected by the presence of an organosilane on the surface of the nanoparticles, especially when an optimal filler loading of 2-3 vol% was used. The original toughness of the material was negatively affected if precipitated silica and glass microcomposites filled samples were considered. The fine dispersion of fumed silica aggregates and their strong orientation along the stress direction could explain the toughening effect provided by these nanoparticles, while cavitation or induced crystallization phenomena during the application of the load were excluded. Tensile impact tests and the essential work of fracture (EWF) approach confirmed the enhancement of the fracture toughness provided by fumed silica nanoparticles, with considerable improvements of the specific essential work of fracture parameter (w_e) with the nanofiller surface area. Concurrently, a slight reduction of the specific plastic work of dissipation (βw_p), probably due to a parallel reduction of the plastic zone, was observed. It was also found that the major part of the fracture toughness enhancement was related to the crack propagation component.

6 References

1. Sawhney, A.P.S., et al., *Modern Applications of Nanotechnology in Textiles.* Textile Research Journal, 2008. **78**(8): p. 731-739.
2. Kojima, Y., et al., *Synhesis of nylon 6-clay hybrid by montmorillonite intercalated with ε-caprolactam.* Journal of Polymer Science Part A : Polymer Chemistry, 1993. **31**: p. 983-986.
3. Paul, D.R. and L.M. Robeson, *Polymer nanotechnology: Nanocomposites.* Polymer, 2008. **49**: p. 3187-3204.
4. Ajayan, P.M., P.V. Braun, and L.S. Schadler, *Nanocomposite science and technology* ed. Wiley-VCH. 2003, Weinheim.
5. Breuer, O., *Big Returns From Small Fibers: A Review of Polymer/Carbon Nanotube Composites.* Polymer Composites, 2004. **25**(6): p. 630-645.
6. Goettler, L.A., K.Y. Lee, and H. Thakkar, *Layered silicate reinforced polymer nanocomposites: Development and applications.* Polymer Reviews, 2007. **47**: p. 291-317.
7. Hashemi, S., *Temperature dependence of work of fracture parameters in polybutylene terephthalate (PBT).* Polymer Engineering and Science, 2000. **40**(6): p. 1435-1446.
8. Thostenson, E.T., Z.F. Ren, and T.W. Chou, *Advances in the science and technology of carbon nanotubes and their composites: a review.* Composites Science and Technology, 2001. **61**: p. 1899-1912.
9. *www.isiwebofknowledge.com.*
10. Findley, W.N., J.S. Lai, and K. Onaran, *Creep and Relaxation of Nonlinear Viscoelastic Materials*. 1989, New York: Dover Pubblications.
11. Mallick, P.K., *Fiber-reinforced composites: materials, manufacturing, and design*, ed. Dekker. 1988, New York.
12. Nielsen, L.E. and R.F. Landel, *Mechanical properties of polymers and composites*, ed. Dekker. 1994, New York.

13. Szleifer, I. and R. Yerushalmi-Rozen, *Polymers and carbon nanotubes—dimensionality, interactions and nanotechnology.* Polymer, 2005. **46**(19): p. 7803-7818.
14. Tjong, S.C., *Structural and mechanical properties of polymer nanocomposites.* Materials Science and Engineering R, 2006. **53**: p. 73-197.
15. Xie, X.L., Y.W. Mai, and X.P. Zhou, *Dispersion and alignment of carbon nanotubes in polymer matrix: A review.* Materials Science & Engineering Reports, 2005. **49**: p. 89-112.
16. Chang, J.H. and Y.U. An, *Nanocomposites of Polyurethanes with various organoclays: thermomechenical properties, morphology,and gas permeability.* Journal of polymer science, 2002. **40**: p. 670-677.
17. Kim, D.S., J.T. Kim, and W.B. Woo, *Reaction Kinetics and Characteristics of PU/clay vnanocomposites.* Journal of applied polymer science, 2004 **96**: p. 1641-1647.
18. Song, M., et al., *High performance nanocomposites of polyurethane elastomer and organically modified layered silicate.* Journal of applied polymer science, 2003. **90**: p. 3239-3243.
19. Song, M. and K.J. Yao, *X-ray diffraction detection of compliance in polyuretahane-organoclay nanocomposites.* Material Science and Tecnology, 2004. **20**.
20. Varghese, S., et al., *Morphology and Mechanical Properties of Layered Silicate Reinforced Natural and Polyurethane Rubber Blends Produced by Latex Compounding.* Journal of applied polymer science, 2004. **92**: p. 543-551.
21. Bondioli, F., et al., *High-density polyethylene reinforced with submicron titania particles* Polymer Engineering and Science, 2008. **48**(3): p. 448-457.
22. Cassagnau, P., *Melt rheology of organoclay and fumed silica nanocomposites.* Polymer, 2008. **49**: p. 2183-2196.
23. Kontou, E. and M. Niaounakis, *Thermo-mechanical properties of LLDPE/SiO2 nanocomposites.* Polymer, 2006. **47**: p. 1267-1280.
24. Jancar, J. *Role of Interphase on micro and nanoscale: micromechanics vs polymer physics*. 2004. Trento (Italy).
25. Pinnavaia, T.J. and G.W. Beall, *Polymer-clay nanocomposites. 2000*, ed. Wiley. 2000.
26. Ou, C.F. and M.C. Hsu, *Preparation and Properties of Cycloolefin Copolymer/Silica Hybrids.* Journal of Applied Polymer Science, 2007. **104**: p. 2542-2548.
27. Ou, C.F. and M.C. Hsu, *Preparation and characterization of cyclo olefin copolymer (COC)/silica nanoparticle composites by solution blending.* J Polym Res, 2007. **14**: p. 373-378.

28. Wichmann, M.H.G., K. Schulte, and H.D. Wagner, *On nanocomposite toughness.* Composites Science and Technology, 2008. **68**(1): p. 329-331.
29. Agag, T., T. Koga, and T. Takeichi, *Study on thermal and mechanical properties of polyimide-clay nanocomposites.* Polymer, 2001. **42**: p. 3399-3408.
30. Ng, C.B., et al., *A study of the mechanical and permeability properties of nano and micro TiO_2 filled epoxy nanocomposites.* Advanced Composites Letters, 2001. **10**: p. 101-111.
31. Krishnamoorti, R., R.A. Vaia, and E.P. Giannelis, *Structure and dynamics of polymer layered silicates nanocomposites.* Chemistry of Materials 1996. **8**: p. 1728-1734.
32. Okamoto, M., et al., *Synthesis and structureof smectic clay/poly(methylmethacrylate) and clay/polystirene nanocomposites via in situ intercalative polymerization.* Polymer 2000. **41**: p. 3887-3890.
33. Xiao, P., M. Xiao, and K. Gong, *Preparation of exfoliated graphite/polystirene composite by polymerization-filling technique.* Polymer, 2001. **42**: p. 4813-4816.
34. Krishnamoorti, R. and E.P. Giannelis, *Rheology of tethered polymer layered silicate nanocomposites.* Macromolecules, 1997. **30**: p. 4097-4102.
35. Sternsten, S.S. and A.J. Zhu, *Reinforcement mechanism of nanofilled polymer melts as elucidated by non linear viscoelastic behaviour.* Macromolecules, 2002. **35**: p. 7262-7263.
36. Avella, M., E. Errico, and E. Martuscelli, *Novel PMMA/$CaCO_3$ Nanocomposites Abrasion Resistant Prepared by an in Situ Polymerization Process.* Nano Letters, 2001. **1**: p. 213-217.
37. Van Zanten, J.H., W.E. Wallace, and W.L. Wu, *Effect of strongly favorable substrate interactions on thermal properties of ultrathin polymer films.* Physical review E, 1996. **53 R2053**.
38. Yano, K., et al., *Synthesis and properties of polyimide clay hybrids.* Journal of Polymer Science: Part A Polymer Chemistry, 1993. **31**: p. 2493-2498.
39. Kraus, G., *Reinforcement of elastomers*. 1965, New York: Interscience.
40. Picard, E., J.F. Gerard, and E. Espuche, *Water transport properties of polyamide based nanocomposites prepared by melt blending : On the importance of the clay dispersion state on the water transport properties at high water activity* Journal of Membrane Science, 2008. **313**: p. 284-295.
41. Picard, E., et al., *Barrier properties of nylon-6 montmorillonite nanocomposite membranes prepared by melt blending : Influence of the clay content and dispersion state. Consequences on modelling* Journal of Membrane Science, 2007. **292**: p. 133-144.

42. Cussler, E.L., et al., *Barrier Membranes.* Journal of Membrane Science, 1988. **38**: p. 161-174.
43. Nielsen, L., *Models for permeability of filled polymer systems.* Journal of Macromolecular Science and Chemistry, 1967. **A1**: p. 929-942.
44. Jacquelot, E., et al., *Morphology and Gas Barrier Properties of Polyethylene-Based Nanocomposites.* Journal of Polymer Science, Part B: Polymer Physics, 2006. **44**: p. 431-440.
45. Picard, E., et al., *Influence of the Compatibilizer Polarity and Molar Mass on the Morphology and the Gas Barrier Properties of Polyethylene/Clay Nanocomposites.* Journal of Polymer Science, Part B: Polymer Physics, 2008. **46**: p. 2593-2604.
46. Vermogen, A., et al., *Assessing Crystalline Lamellae Orientation Impact on the Properties of Semi-Crystalline Polymer-Clay Nanocomposites.* Journal of Polymer Science, Part B: Polymer Physics, 2008. **46**: p. 1966-1975.
47. Blumstein, A., *Polymerization of adsorbed monolayer II. Thermal degradation of the inserted polymer.* Journal of Polymer Science, part A: polymer chemistry 1965. **3**: p. 2665.
48. Burnside, S.D. and E.P. Giannelis, *Synthesis and properties of new poly(dimethylsiloxane) nanocomposites.* Chemistry of Materials, 1995. **7**: p. 1597-1600.
49. Kuchta, F.D., et al., *Materials with improved properties from polymer ceramic nanocomposites* MRS symposia proceedings, 1999. **576**: p. 363-368.
50. Gilman, J., *Flammability and thermal stability of polymer layered silicate (clay) nanocomposites* Applied Clay Science 1999. **15**: p. 31-49.
51. Gilman, J., T. Kashiwagi, and J. Lichtenhan, *Nanocomposites : a revolutionary new flame retardant approach.* SAMPE J., 1997. **33**: p. 40.
52. Chen-Yang, Y.W., et al., *Thermal and anticorrosive properties of polyurethane/clay nanocomposites.* Journal of applied polymer research, 2004. **11**: p. 275-283.
53. Song, et al., *Study on the properties of flame retardant polyurethane/organoclay nanocomposite.* Polymer Degradation and Stability, 2005. **87**: p. 111-116.
54. Kyprianidou-Leodidou, T., W. Caseri, and U. Suter, *Size variation of PbS particlesi high refractive index nanocomposites.* Journal of Physical Chemistry, 1994. **98**: p. 8992-8997.
55. Zimmermann, L., et al., *High refractive index films of polymeric nanocomposites* Journal of Materials Resistance 1993. **8**: p. 1742.
56. Kyprianidou-Leodidou, T., et al., *High refractive index materials of iron sufides and poly(ethylene oxide).* Journal of Materials Resistance, 1997. **12**: p. 2198-2206.

57. Alexandre, M. and P. Dubois, *Polymer-layered silicate nanocomposites: preparation, propertiesand uses of a new class of materials.* Materials Science and Engineering, 2000. **28**: p. 1-63.
58. Giannelis, E.P., R. Krishnamoorti, and E. Manias, *Polymer-silica nanocomposites: model systems for confined polymers and polymer brushes.* Advances in Polymer Science, 1999. **118**: p. 108-147.
59. Theng, B.K.G., *The Chemistry of Clay-Organic Reactions*, ed. Wiley. 1974, New York.
60. Kovarova, L., et al., *Structure Analysis of PVC Nanocomposites* Macromolecular Symposia, 2005. **221**: p. 105-114.
61. Peprnicek, T., et al., *Polyvinylchloride/clay nanocomposites : X-ray diffraction, thermal and rheological behaviour.* Polymer Degradation and Stability, 2006. **91**: p. 1855-1860.
62. Peprnicek, T., et al., *Polyvinylchloride-paste/clay nanocomposites : Investigation of thermal and morphological characteristics.* Polymer Degradation and Stability, 2006. **91**: p. 3322-3329.
63. Song, L., et al., *Study on the properties of flame retardant polyurethane/organoclay nanocomposite.* Polymer Degradation and Stability, 2005. **87**: p. 111-116.
64. Boucard, S., et al., *Processing of Polypropylene-Clay Hybrids.* Macromolecular Symposia, 2003. **194**: p. 241-246.
65. Mailhot, B., et al., *Photodegradation of polypropylene nanocomposites.* Polymer Degradation and Stability, 2003. **82**: p. 163-167.
66. Vaia, R.A. and E.P. Giannelis, *Lattice of polymer melt intercalation in organically-modified layered silicates.* Macromolecules, 1997. **30**: p. 7990-7999.
67. Iijima, S., *Helical microtubules of graphitic carbon. Nature.* Nature, 1991. **354**: p. 56-58.
68. Grobert, N., *Carbon nanotubes - becoming clean. Materials Today.* Materials Today, 2007. **10**(1-2): p. 2835.
69. Haddon, R.C., *Carbon Nanotubes.* Accounts of Chemical Research, 2002. **35**(12): p. 997.
70. Reich, S., Thomsen, and J. Maultzsch, *Carbon nanotubes: basic concepts and physical properties*, ed. Wiley-VCH. 2004, Weinheim.
71. Salvetat, J.P., et al., *Elastic and Shear Moduli of Single-Walled Carbon Nanotube Ropes.* Physical Review Letters, 1999. **82**(5): p. 944-947.
72. Tenne, R. and A.K. Zettl, *Carbon Nanotubes: Synthesis, structure, properties and applications*. 2000, New York: Springer.

73. Stephan, O., et al., *Doping Grphitic and Carbon nanotube structures with boron and nitrogen.* Science, 1994. **266**: p. 1683-1685.
74. Tenne, R., *Dopedand heteroatom continuity fullerene like structures and nanotubes.* Advanced Materials, 1995. **7**: p. 965.
75. Ajayan, P.M., et al., *Carbon nanotubes as removable templates for metal oxide nanocomposites and nanostructures.* Nature, 1995. **375**: p. 564-567.
76. Stober, W., A. Fink, and E. Bohn, *Controlled growth of monodisperse silica spheres in the micro size range* Journal of Colloid Interface Science, 1968. **26**: p. 62-69.
77. Friedlander, S.K., *Smode, Dust and Haze: Fundamental of Aerosol Behavior*. 1977, New York: Wiley Interscience.
78. Friedlander, S.K., *R&D Status and Trends*, ed. R.W. Siegel, E. Hu, and M.C. Roco. 1998, Dordrecht (Netherlands).
79. Donnet, J.B., R.C. Bansal, and M.J. Wang, *Carbon black: science and technology*, ed. Dekker. 1993, New York.
80. Wypych, G., *Handbook of fillers*. 2000, New York.
81. Heidenreich, R.D., W.M. Hess, and L.L. Ban, *A test object and criteria for high resolution electron microscopy.* Journal of Applied Crystallography, 1968. **1**(1): p. 1-19.
82. Granqvist, C.G. and R.A. Buhrman, *Ultrafine metal particles.* Journal of Applied Physics 1976. **47**: p. 2200.
83. Kimoto, K., et al., *Electron Microscope study on fine metal particles prepared by evaporation in Argon gas at low pressure.* Japanese Journal of Applied Physics, 1963. **2**: p. 702-713.
84. Johnston, G.P., et al., *Reactive laser ablation synthesis of nanosize aluminum nitride.* Journal of American Ceramic Society, 1992. **75**: p. 3293-3298.
85. Kato, M., *Preparation of ultrafine partiles of refractory oxides by gas evaporatio method.* Japanese Journal of Applied Physics, 1976. **15**: p. 757-760.
86. Ogawa, K., et al., *Elastic properties of nanparticles chain aggregates of TiO_2, Al_2O_3 and Fe_2O_3 generated by laser ablation* Journal of Applied Physics, 2000. **87**: p. 63-73.
87. Hyeon-Lee, J., G. Beaucage, and E. Pratsinis, *Aerosol-gel synthesis of nanostructured silica powders.* Chemistry of Materials, 1997. **9**: p. 2400-2403.
88. Grohn, F., et al., *Dendrimer templates for the formation of gold nanoclusters.* Macromolecules, 2000. **33**: p. 6042-6050.

89. Guo, L., et al., *Highly monodisperse polymer capped ZnO nanoparticles : preparation and optical properties.* Applied Physics Letters, 2000. **76**: p. 2901.
90. Suslick, K.S., T. Hyeon, and M. Fang, *Nanostructured materials generated by high-intensity ultrasound:sonochemical synthesis and catalytic studies.* Chemistry of Materials, 1996. **8**: p. 2172.
91. Sunstrom IV, J.E., W.R. Moser, and B. Marshik-Guerts, *General route to nanicrystalline oxides by hydrodynamic cavitation.* Chemistry of Materials, 1996. **8**: p. 2061-2067.
92. Scott, D.W., *Thermal Rearrangement of Branched-Chain Methylpolysiloxanes.* Journal of American Chemical Society, 1946. **68**: p. 356-368.
93. Xiao, F., et al., *Preparation, Thermal and Mechanical Properties of POSS Epoxy Hybrid Composites.* Journal of Applied Polymer Science, 2007. **104**: p. 2113-2121.
94. Zhao, Y. and D.A. Schiraldi, *Thermal and mechanical properties of polyhedral oligomeric silsesquioxane (POSS)/polycarbonate composites.* Polymer, 2005. **46**: p. 11640-11647.
95. Phillips, S.H., T.S. Haddad, and S.J. Tomczak, *Developments in nanoscience: polyhedral oligomeric silsesquioxane (POSS)-polymers.* Current Opinion in Solid State and Materials Science, 2004. **8**: p. 21-29.
96. Bourbigot, S., S. Duquesne, and C. Jama, *Polymer Nanocomposites: How to Reach Low Flammability?* Macromolecular Symposia, 2006. **233**: p. 180-190.
97. Morgan, A.B., *Flame retarded polymer layered silicate nanocomposites:a review of commercial and open literature systems{*. Polymers for advanced technologies, 2006. **17**: p. 206-217.
98. Baldi, F., et al., *Mechanical Characterization of Polyhedral Oligomeric Silsesquioxane/Polypropylene Blends.* Journal of Applied Polymer Science, 2007. **105**: p. 935-943.
99. Malkin, A.Y., *Rheology fundamentals*. 1994, Toronto (Canada): ChemTech Publishing.
100. Barnes, H.A., J.E. Hutton, and K. Walters, *An introduction to rheology*. 1989, Amsterdam: Elsevier.
101. Gupta, R.K., *Polymer and Composite Rheology*. 2000, New York-Basel: Dekker.
102. Carreau, P.J., D.C.R. De Kee, and R.P. Chhabra, *Rheology of Polymeric Liquids*. 1997, Munich-Vienna-New York: Hanser.
103. Ferry, J.D., *Viscoelastic properties of polymers*. 1980, New York: Wiley.
104. Lakes, R.S., *Viscoelastic Solids*. 1999, Boca Raton, London, New York, Washington DC: CRC Press.

105. McCrum, N.G., B.E. Read, and G. Williams, *Anelastic and dielectric effects in polymeric solids.* 1984, New York: Dover.
106. Riande, E., et al., *Polymer Viscoelasticity, Stress and Strain in Practice*. 2000, New York, Basel: Dekker.
107. Plazek, D.J., *A myopic review of the viscoelastic behavior of polymers.* Journal of Non-Crystalline Solids, 1991. **131-132**(2): p. 836-851.
108. Kolarik, J., et al., *Prediction of the Creep of Heterogeneous Polymer Blends: Rubber-Toughened Polypropylene/Poly(Styrene-co-Acrylonitrile).* Polymer Engineering and Science, 2002. **42**(1): p. 161-169.
109. Kolarık, J. and A. Pegoretti, *Non-linear tensile creep of polypropylene: Time-strain superposition and creep prediction.* Polymer, 2006. **47**: p. 346-356.
110. Crawford, R.J., *Plastics engineering*. 1988, Oxford: Butterworth-Heinemann.
111. Moore, D.R. and S. Turner, *Mechanical evaluation strategies for plastics*. 2001, Cambridge: Woodhead.
112. Rodriguez, F., *Principles of polymer systems*. 1996, Washington, DC: Taylor & Francis.
113. Ward, I.M. and D.W. Hadley, *An introduction to the mechanical properties of solid polymers*. 1993, Chichester: Wiley.
114. Kolarık, J., et al., *Non linear long term tensile creep of polypropylene/cycloolefn copolymer blends with fibrous structure.* Macromolecular Materials Engineering, 2003. **288**: p. 629-641.
115. Bueche, F., *Physical properties of polymers*. 1962, New York: Interscience.
116. Sax, J. and J.M. Ottino, *Modelling of transport of small molecules in polymer blends, application of effective medium theory.* Polymer Engineering and Science, 1983. **23**: p. 165.
117. Kolarık, J., *Simultaneous prediction of the modulus, tensile strength and gas permeability of binary polymer blends.* European Polymer Journal, 1998. **34**(5-6): p. 585-590.
118. Beckwith, T.G., N.L. Buck, and R.D. Marangoni, *Mechanical measurements*. 1982, Reading: Addison-Wesley.
119. Figliola, R.S. and D.E. Beasley, *Theory and design for mechanical measurments*. 1995, New York: Wiley.
120. *ESIS Test Protocol for Essential Work of Fracture.* 2002.
121. Arkhireyeva, A. and S. Hashemi, *Fracture behaviour of polyethylene naphthalate (PEN).* Polymer, 2002. **43**: p. 289-300.

122. Arkhireyeva, A., S. Hashemi, and M. O'Brien, *Factors affecting work of fracture of uPVC film.* Journal of Materials Science, 1999. **34**: p. 5961-5974.
123. Broberg, K.B., *Critical review of some theories in fracture mechanics.* International Journal of Fracture, 1968. **4**(1): p. 11-19.
124. Cotterell, B. and J.K. Reddel, *The essential work of plane stress ductile fracture.* International Journal of Fracture, 1977. **13**(3): p. 267-277.
125. Hill, R., *On discontinuous plastic states, with special reference to localized necking in thin sheets.* Journal of the Mechanics and Physics of Solids, 1952. **1**(1): p. 19-30.
126. Karger-Kocsis, J., T. Czigány, and E.J. Moskala, *Deformation rate dependence of the essential and non-essential work of fracture parameters in an amorphous copolyester.* Polymer, 1998. **39**: p. 3939-3944.
127. Mai, Y.W. and B. Cotterell, *On the essential work of ductile fracture in polymers.* International Journal of Fracture, 1986. **32**: p. 105-125.
128. Saleemi, A.S. and J.A. Nairn, *The plane-strain essential work of fracture as a measure of the fracture toughness of ductile polymers.* Polymer Engineering and Science, 1990. **30**(4): p. 211-218.
129. Williams, J.G. and M. Rink, *The standardisation of the EWF test.* Engineering Fracture Mechanics, 2007. **74**: p. 1009-1017.
130. Brandrup, J., E.H. Immergut, and E.A. Grulke, *Polymer Handbook.* 1999: Wiley.
131. Sperling, L.H., *Introduction to physical polymer science.* 2006, Hoboken (New Jersey): Wiley.
132. Mark, J.E., *Polymer data handbook.* 1999: Oxford University Press.
133. *www.polimerieuropa.com.*
134. *www.degussa.com.*
135. Shim, S.E. and A.I. Isayev, *Rheology and structure of precipitated silica and poly(dimethyl siloxane) system.* Rheological Acta, 2004. **43**: p. 127-136.
136. Uotila, R., et al., *Compatibilization of PP/elastomer/microsilica composites with functionalized polyolefins: Effect on microstructure and mechanical properties.* Polymer, 2005. **46**: p. 7923-7930.
137. *www.resine-cores.it.*
138. Brunauer, S., P.H. Emmett, and E. Teller, *Adsorption of gases in multimolecular layers.* Journal of American Chemical Society, 1938. **60**: p. 309.

139. Barret, E., L. Joyner, and P. Holenda, *The determination of the pore volume and area distributions in porous substances.* Journal of American Chemical Society, 1951. **73**: p. 373-380.

140. Leoni, M., J. Martinez-Garcia, and P. Paolo Scardi, *Dislocation effects in powder diffraction.* Journal of Applied Crystallography, 2007. **40**: p. 719-724.

141. Scardi, P. and M. Leoni, *Diffraction line profiles frompolydisperse crystalline systems.* Acta Crystallographica, 2001. **A57**: p. 604-613.

142. Scardi, P. and M. Leoni, *Whole powder pattern modelling.* Acta Crystallographica, 2002. **A58**: p. 190-200.

143. Thio, Y.S., A.S. Argon, and R.E. Cohen, *Role of interfacial adhesion strength on toughening polypropylene with rigid particles.* Polymer, 2004. **45**: p. 3139.

144. Bernal, C.R., P.E. Montemartini, and P.M. Frontini, *The Use of Load Separation Criterion and Normalization Method in Ductile Fracture Characterization of Thermoplastic Polymers.* Journal of Polymer Science: Part B Polymer Physics, 1996. **34**: p. 1869-1880.

145. Brosa, V.G., C.R. Bernal, and P. Frontini, *Calibration of fracture mechanics parameters and J-R curve determination in polyethylene side-grooved arc-shaped specimens.* Engineering Fracture Mechanics, 1999. **62**: p. 231-248.

146. Mohrain, C. and J.I. Velasco, *J -R curve determination of magnesium hydroxide filled polypropylene using the normalization method.* Journal of Materials Science, 2002. **37**: p. 1635-1644.

147. Wainstein, J., P.M. Frontini, and A.N. Cassanelli, *J-R curve determination using the load separation parameter $_{Spb}$ method for ductile polymers.* Polymer Testing, 2004. **23**: p. 591-598.

148. Roquerol, F., J. Roquerol, and K. Singh, *Adsorption by powders and porous solids*. 1999, San Diego (USA): Academic Press.

149. Lazzeri, A., et al., *Filler toughening of plastics. Part 1—The effect of surface interactions on physico-mechanical properties and rheological behaviour of ultrafine $CaCO_3$/HDPE nanocomposites.* Polymer, 2005. **46**: p. 827-844.

150. Yuan, Q., S. Awate, and R.D.K. Misra, *Nonisothermal crystallization behavior of polypropylene–clay nanocomposites.* European Polymer Journal, 2006. **42**: p. 1994-2003.

151. Silverstein, R.M., G.C. Bussler, and T.C. Morril, *Spectroscopic Identification of Organic Compounds* 1981, New York: Wiley.

152. Fina, A., et al., *Polypropylene–polyhedral oligomeric silsesquioxanes (POSS) nanocomposites.* Polymer, 2005. **46**: p. 7855-7866.
153. Misra, R., B. Fu, and S.E. Morgan, *Surface Energetics, Dispersion, and Nanotribomechanical Behavior of POSS/PP Hybrid Nanocomposites.* Journal of Polymer Science, Part B: Polymer Physics, 2007. **45**: p. 2441-2455.
154. Ramasundaram, S.P. and K.J. Kim, *In-situ Synthesis and Characterization of Polyamide 6/POSS Nanocomposites.* Macromol. Symp., 2007. **249-250**: p. 295-302.
155. Della Volpe, C., et al., *Recent theoretical and experimental advancements in the application of the van Oss-Chaudhury-Good acid-base theory to the analysis of polymer surfaces II. Some peculiar cases.* Journal of Adhesion Science and Technlogy, 2003. **17**(11): p. 1425-1456.
156. Garbassi, F., E. Occhiello, and F. Polato, *Surface effect of flame treatments on polypropylene.* Journal of Material Science, 1987. **22**: p. 207-212.
157. Garbassi, F., E. Occhiello, and F. Polato, *Surface effect of flame treatments on polypropylene. Part 2 SIMS (FABMS) and FTIR-PAS studies.* Journal of Material Science, 1987. **22**: p. 1450-1456.
158. Pandey, J.K., et al., *An overview on the degradability of polymer nanocomposites.* Polymer Degradation and Stability, 2005. **88**: p. 234-250.
159. Pandey, J.K. and R.P. Singh, *On the durability of low-density polyethylene nanocomposites.* e-polymers, 2004. **051**.
160. Huaili, Q., et al., *Photo-oxidative degradation of of polyethylene-montmorillonite nanocomposite.* Polymer Degradation and Stability, 2003. **81**(3): p. 497.
161. Belyakova, L.D. and A.V. Kiselev, Zhurnal Fizicheskoi Khimii, 1959. **33**: p. 2624.
162. De Boer, J.H. and J.M. Vleeskens, Proceedings of Koninklijke Nederlandse Akademie van Wetenschappen Series B 1957. **60**.
163. Zhdanov, S.P. and A.V. Kiselev, Zhurnal Fizicheskoi Khimii, 1957. **31**: p. 2213.
164. Zhuravlev, L.T., *Concentration of hydroxyl groups on the surface of amorphous silicas.* Langmuir, 1987. **3**: p. 316-318.
165. Zhuravlev, L.T., *Structurally bound water and surface characterization of amorphous silica* Pure and Applied Chemistry, 1989. **61**(11): p. 1969-1976.
166. Zhuravlev, L.T., *Surface characterization of of amorphous silica-a review of work from the former USSR.* Colloids Surfaces A, 1993. **74**: p. 71-90.

167. Abdel-Goad, M. and P. Potschke, *Rheological chracterization of melt processed polycarbonate-multiwalled carbon nanotube composites.* Journal of Non-Newtonian Fluid Mechanics, 2005. **128**: p. 2-6.
168. Ganss, M., et al., *Structural interpretations of deformation and fracture behaviour of polypropylene/multi-walled carbon nanotbe composites.* Acta Materialia, 2008. **56**: p. 2247-2261.
169. Renger, C., et al., *Rheology studies on highly filled nano-zirconia suspensions.* Journal of the European Ceramic Society 2007. **27**: p. 2361-2367.
170. Sarvestani, A.S., *Modelling the solid-like behaviour of entangled polymer nanocomposites at low frequency regimes* European Polymer Journal, 2008. **44**: p. 263-269.
171. Sepehr, M., et al., *Polystyrenes with macro-intercalated organoclay. Part II. Rheology and mechanical performance* Polymer, 2005. **46**: p. 11569-11581.
172. Wu, D., et al., *Rheology and thermal stability of polylactide/clay nanocomposites* Polymer Degradation and Stability, 2006. **91**: p. 3149-3155.
173. Batchelor, G.K., *The effect of the Brownian motion on the bulk stress in a suspension of spherical particles.* Journal of Fluid Mechanics, 1977. **83**: p. 97-117.
174. Einstein, A., *Investigations on the Theory of the Brownian Movement* 1956, Dover, New York.
175. De Kee, D. and G. Turcotte, *Viscosity of biomaterials* Chemical Engineerng Communications, 1980. **6**: p. 273-282.
176. Gopakumar, T.G., et al., *Influence of clay exfoliation on the physical properties of montmorillonite/polyethylene composites.* Polymer, 2002. **43**: p. 5483-5491.
177. Hotta, S. and D.R. Paul, *Nanocomposites formed from linear low density polyethylene and organoclays* Polymer, 2004. **45**: p. 7639-7654.
178. Kato, M., et al., *Preparation and Properties of Polyethylene-Clay Hybrids.* Polymer Engineering and Science, 2003. **43**: p. 1312-1316.
179. Lee, J.H., et al., *Properties of Polyethylene-layered silicate nanocomposites prepared by melt intercalatin with a PP-g-MA compatibilizer.* Composites Science and Technology, 2005. **65**: p. 1996-2002.
180. Pegoretti, A., A. Dorigato, and A. Penati, *Tensile mechanical response of polyethylene – clay nanocomposites.* Express Polymer Letters, 2007. **1**(3): p. 123-131.
181. Ranade, A., et al., *Maleated and non maleated polyethylene-montmorillonite layered silicate blown films: creep, dispersion and cristallinity.* Polymer 2005. **46**: p. 7323-7333.

182. Wang, K.H., et al., *Morphology and Physical Properties of Polyethylene/Silicate Nanocomposite Prepared by Melt Intercalation.* Journal of Polymer Science, Part B: Polymer Physics, 2002. **40**: p. 1454-1463.
183. Wanjale, S.D. and J.P. Jog, *Poly(4-methyl-1-pentene)/clay nanocomposites: effect of organically modified layered silicates.* Polymer International, 2004. **53**: p. 101-105.
184. Zhang, J., D.D. Jiang, and C.A. Wilkie, *Polyethylene and polypropylene nanocomposites based upon an oligomerically modifed clay.* Thermochimica acta, 2005. **430**: p. 107-113.
185. Zhang, Z., J.L. Yang, and K. Friedrich, *Creep resistant polymeric nanocomposites.* Polymer, 2004. **45**: p. 3481-3485.
186. Lewis, T.B. and L.E. Nielsen, *Dynamic mechanical properties of particulate-filled polymers.* Journal of Applied Polymer Science, 1970. **14**: p. 1449-1471.
187. Meyyappan, M., *Carbon Nanotubes : Science and Applications*. 2005: CRC Press.
188. Klocek, P., *Handbook of Infrared Optical Materials*. 1991: CRC Press.
189. Baschnagel, J. and K. Binder, *On the glass transition in polymer films : Recent Monte Carlo results.* MRS symposia proceedings, 1999. **543**: p. 157-162.
190. Hirsch, T.J., *Modulus of elasticity of concrete affected by elastic moduli of cement paste matrix and aggregate* Journal of American Concrete Institute, 1962. **59**: p. 427-451.
191. Fang, L., Y. Leng, and P. Gao, *Processing and mechanical properties of HA/UHMWPE nanocomposites.* Biomaterials, 2006. **27**: p. 3701-3707.
192. Ahmed, S. and F.R. Jones, *A review of particluate reinforcement theories for polymer composites.* Journal of Material Science, 1990. **25**(12): p. 4933-4942.
193. Ji, X.L., et al., *Tensile modulus of polymer nanocomposites.* Polymer Engineering and Science 2002. **42**(5): p. 983-993.
194. Takayanagi, M., S. Vemura, and S. Minami, *Application of equivalent model method to dynamic rheo-optical properties of crystalline polymer* Journal of Polymer Science Part C, 1964. **5**: p. 113-122.
195. Durmus, A., et al., *Intercalated linear low density polyethylene (LLDPE)/clay nanocomposites prepared with oxidized polyethylene as a new type of compatibilizer: Structural, mechanical and barrier properties.* European Polymer Journal, 2007. **43**: p. 3737-3749.
196. Tjong, S.C. and S.P. Bao, *Fracture toughness of high density polyethylene/SEBS-g-MA/montmorillonite nanocomposites.* Composites Science and Technology, 2007. **67**: p. 314-323.

197. Wang, K., et al., *Effect of aspect ratio of clay on melt extensional process of maleated polyethylene/clay nanocomposites.* Polymer Bulletin, 2001. **46**: p. 499-505.

198. Dan, C.H., et al., *Effect of clay modifiers on the morphology and physical properties of thermoplastic polyurethane/clay nanocomposites.* Polymer 2006. **47**: p. 6718-6730.

199. Peacock, A.J., *Handbook of Polyethylene: Structures, Properties, and Applications*. 2000, New York: Dekker.

200. Takei, T. and M. Chikazawa, *Origin of Differences in Heats of Immersion of Silicas in Water.* Journal of Colloid Interface Science, 1998. **208**: p. 570-574.

201. Starkova, O., J. Yang, and Z. Zhang, *Application of time-stress superposition to nonlinear creep of polyamide 66 filled with nanoparticles of various sizes* Composites Science and Technology, 2007. **67**: p. 2691.

202. Yang, J.L., et al., *On the characterization of tensile creep resistance of polyamide 66 nanocomposites. Part I. Experimental results and general discussions.* Polymer, 2006. **47**: p. 2791–2801.

203. Siengchin, S., J. Karger-Kocsis, and R. Thomann, *Creep behaviour of Polystyrene/Fluorohectorite Micro and Nanocomposites* Journal of Applied Polymer Science, 2007. **105**: p. 2963-2972.

204. Wang, Z.D. and X.X. Zhao, *Modeling and characterization of viscoelasticity of PI/SiO_2 nanocomposite films under constant and fatigue loading.* Materials Science and Engineering A, 2008. **486**: p. 517-527.

205. Jazouli, S., et al., *Application of time–stress equivalence to nonlinear creep of polycarbonate.* Polymer Testing, 2005. **24**: p. 463-467.

206. Yang, J., et al., *Creep Resistant Polymer Nanocomposites Reinforced with Multiwalled Carbon Nanotubes.* Macromolecular Rapid Communications, 2007. **28**: p. 955-961.

207. Joshi, M. and V. Viswanathan, *High-Performance Filaments from Compatibilized Polypropylene/Clay Nanocomposites.* Journal of Applied Polymer Science, 2006. **102**: p. 2164-2174.

208. Forrest, K.J.A., et al., *Effect of Free Surfaces on the Glass Transition Temperature of Thin Polymer Films.* Physical Review Letters, 1996. **77**: p. 2002-2005.

209. Keddie, J.L., R.A.L. Jones, and R.A. Covy, Europhysics Letters, 1994. **27**: p. 59.

210. Mattsson, J., J.A. Forrest, and L. Borjesson, *Quantifying the Glass Transition in Ultrathin Freely Standing Polymer Films.* Physical Review E, 2000. **62**: p. 5187-5200.

211. Reiter, G., Europhysics Letters, 1993. **23**: p. 579.

212. Mansfield, K.F. and D.N. Theodorou, *Molecular Dynamics Simulation of a Glassy Polymer Surface.* Macromolecules, 1991. **24**: p. 6283-6294.

213. Bugnicourt, E., et al., *Effect of sub-micron silica fillers on the mechanical performances of epoxy-based composites.* Polymer, 2007. **48**: p. 1596-1605.

214. Bigg, D.M., *Mechanical properties of particulate filled polymers.* Polymer Composites, 1987. **8**(2): p. 115-122.

215. Jancar, J., A. Dianselmo, and A.T. Dibenedetto, *The yield strength of particulate reinforced thermoplastic composites.* Polymer Engineering and Science, 1992. **32**(18): p. 1394-1399.

216. Galeski, A., *Strength and toughness of crystalline polymer systems* Progress in Polymer Science, 2003. **28**: p. 1643-1699.

217. Galeski, A. and R. Kalinski, *Polymer blends : processing, morphology and properties* ed. E. Martuscelli, R. Palumbo, and M. Kryszewski. 1980, London: Plenum Press.

218. Mitsuishi, K., S. Kodama, and H. Kawasaki, *Mechanical properties of polypropylene filled with calcium carbonate.* Polymer Engineering and Science, 1985. **25**: p. 1069-1073.

219. Nicolais, L. and L. Nicodemo, *Strength of particulate composite* Polymer Engineering and Science, 1973. **13**: p. 469.

220. Guzman de Villoria, R. and A. Miravete, Acta Materialia, 2007. **55**: p. 3025-3031.

221. Turcsanyi, B., B. Pukanszky, and F. Tudos, *Composition dependence of tensile yield stress in filled polymers* Journal of Material Science Letters, 1988. **7**: p. 160-162.

222. Szazdi, L., et al., *Quantitative estimation of the reinforcing effect of layered silicates in PP nanocomposites.* Polymer 2006. **47**: p. 4638-48.

223. Nielsen, L.E., *Simple Theory of the Stress-Strain Properties of Filled Polymers.* Journal of Applied Polymer Science, 1966. **10**: p. 97-103.

224. Sudar, A., et al., *The mechanism and kinetics of void formation and growth in particulate filled PE composites.* Express Polymer Letters, 2007. **11**(1): p. 763-772.

225. Gaucher-Miri, V., C. Depecker, and R. Seguela, *Reversible strain induced order in the amorphous phase of a low density ethylene/butene copolymer.* Journal of Polymer Science: Part B:Polymer Physics, 1997. **35**: p. 2151-2159.

226. Jeol, S., et al., *Drastic Modification of the Dispersion State of Submicron Silica during Biaxial Deformation of Poly(ethylene terephthalate).* Macromolecules, 2007. **40**: p. 3229-3237.

227. Rong, M.Z., et al., *Irradiation graft polymerization on nano-inorganic particles : an effective means to design polymer-based nanocomposites.* Composites Science and Technology, 2000. **19**: p. 1159-1161.

228. Rong, M.Z., et al., *Structure-property relationship of irradiation grafted nano-inorganic particles filled polypropylene composites.* Polymer 2001. **42**: p. 167183.

229. Wu, C.L., et al., *Tensile peformance improvement of low nanoparticles filled polypropylene composites.* Composites Science and Technology, 2002. **62**: p. 1327.

230. Zhang, M.Q., et al., *Mechanical Properties of Low Nano-Silica Filled High Density Polyethylene Composites.* Polymer Engineering and Science, 2003. **43**(2): p. 490-500.

231. Bureau, M., F. Perrin-Sarazin, and M.T. Ton-That, *Polyolefin Nanocomposites : Essential Work of Fracture Analysis.* Polymer Engineering and Science, 2004. **44**(6): p. 1142-1151.

232. Bureau, M.N., M.T. Ton-That, and F. Perrin-Sarazin, *Essential work of fracture and failure mechanisms of polypropylene–clay nanocomposites.* Engineering Fracture Mechanics, 2006. **73**: p. 2360-2374.

233. Musto, P., et al., *Toughness enhancement of polyimides by in situ generation of silica particles.* Polymer, 2004. **45**: p. 4265-4274.

234. Zhang, H., et al., *Temperature dependence of crack initiation fracture toughness of various nanoparticles filled polyamide 66.* Polymer, 2006. **47**: p. 679-689.

7 Publications

(Updated to March 29th, 2009)

7.1 Published

- Pegoretti, A. Dorigato, A. Penati ***"Tensile mechanical response of polyethylene – clay nanocomposites".*** Express Polymer Letters (2007), 1(3), pp. 123-131.

- A.Pegoretti, A.Dorigato, A.Penati ***"Contact angle measurements as a tool to investigate the filer-matrix interactions in polyurethane-clay nanocomposites from blocked prepolymer".*** European Polymer Journal (2008), 44, pp. 1662-1672.

- F.Bondioli, A.Dorigato, P.Fabbri, M.Messori, A.Pegoretti ***"High-Density Polyethylene Reinforced With Submicron Titania Particles".*** Polymer Engineerin and Science (2008), 48 (3), pp. 448-457.

- F. Bondioli, A. Dorigato, P. Fabbri, M. Messori ***"Improving the creep stability of high-density polyethylene with acicular titania nanoparticles".*** Journal of Applied Polymer Science (2009), pp.1045-1055.

7.2 In press

- A.Dorigato, A.Pegoretti ***"Tensile creep behaviour of Poly(Methylpentene)-Fumed Silica nanocomposites"***, Polymer International.

- A.Dorigato, A.Pegoretti, C.Migliaresi ***"Physical properties of Cycloolefin Copolymer (COC)-Polihedral Oligomeric Silsesquioxanes (POSS) nanocomposites"***, Journal of Applied Polymer Science.

7.3 In preparation

- A.Pegoretti, A.Dorigato, A.Penati ***"Fracture toughness of polyethylene-silica nanocomposites"***, 12th International Conference on Fracture (ICF12), Ottawa (Canada), July 12th-17th, 2009.

- A.Dorigato, A.Pegoretti, A.Penati ***"Tensile creep behaviour of LLDPE-Fumed Silica Nanocomposites"*** *in* ***"Special Topics on Materials Science and Technology-An Italian Panorama",*** *BRILL.*

- A.Dorigato, A.Pegoretti, A.Penati ***"Effect of organoclay on the thermo-mechanical properties of Polyurethane (PU)-clay nanocomposites from blocked prepolymer".***

- C.Lonardi A.Dorigato, A.Pegoretti ***"Thermo-mechanical response of Cycloolefin Copolymer (COC)-fumed silica nanocomposites".***

- C.Lonardi A.Dorigato, A.Pegoretti, L.Fambri ***"Preparation and properties of Cycloolefin Copolymer (COC)- Linear Low Density Polyethylene (LLDPE) blends".***

- A.Dorigato, A.Pegoretti, A.Penati ***"Effect of fumed silica nanoparticles on the fracture behaviour of Linear Low Density Polyethylene (LLDPE) – fumed silica nanocomposites".***

- A.Dorigato, A.Pegoretti, A.Penati ***"Rheological behaviour of Linear Low Density Polyethylene (LLDPE) – fumed silica nanocomposites".***

- A.Dorigato, A.Pegoretti, A.Penati ***"Non linear tensile creep behaviour of Linear Low Density Polyethylene (LLDPE) – fumed silica nanocomposites".***

- A.Dorigato, A.Pegoretti, A.Penati ***"Viscoelastic Response of Linear Low Density Polyethylene (LLDPE) – fumed silica nanocomposites".***

- A.Dorigato, M.Tomaselli, A.Pegoretti ***"Viscoelastic behaviour of High Density Polyethylene (HDPE)- TiO_2 nanocomposites".***

- W.Bonani, A.Dorigato, C.Migliaresi ***"Preparation and properties of Polycaprolactone (PCL)-Polyhedral Oligomeric Silsesquioxanes (POSS) electrospun fibers for biomedical applications".***

- A.Dorigato, M.Quaresimin, A.Pegoretti ***"Fracture and fatigue behaviour of carbon fiber-epoxy resin-clay ternary systems".***

8 Congress contributions

(Updated to March 29th, 2009)

8.1 Italian Congress contributions

- A.Dorigato, A.Pegoretti, A.Penati **"Mechanical characterization of high density polyethylene (HDPE) – clay nanocomposites",** First National Forum Joung Researchers on Polymeric Materials and Biomaterials, September 18-20th 2006, Modena (Italy).

- A.Dorigato, A.Pegoretti, A.Penati, **"Filler-matrix interactions in polyurethane-clay nanocomposites",** VIII Convegno Nazionale AIMAT, June 27th – July 1st 2006, Palermo (Italy).

- A.Dorigato, A.Pegoretti, A.Penati **"Fracture behaviour of linear low density-silica nanocomposites"**, XVIII Convegno Italiano AIM, September 16-20th 2007, Catania (Italy).

- A.Dorigato, A.Pegoretti, A.Penati **"Comportamento a creep di nanocompositi LLDPE - silice",** IX Convegno Nazionale AIMAT, June 29th – July 2nd 2008, Piano di Sorrento (Italy).

- F.Bondioli, A.Dorigato, P.Fabbri, M.Messori, A.Pegoretti **"Polietilene ad alta densità (HDPE) rinforzato con titania e zirconia",** IX Convegno Nazionale AIMAT, June 29th – July 2nd 2008, Piano di Sorrento (Italy).

- A.Dorigato, A.Pegoretti, A.Penati **"Viscoelastic behaviour of linear low density polyehtylene (LLDPE)-fumed silica nanocomposites",** II National Forum Joung Researchers on Polymeric Materials and Biomaterials, July 4-5th 2008, Genova (Italy).

8.2 International Congress Contributions

- A.Dorigato, A.Pegoretti, A.Penati **"Production and characterization of polyurethane-clay nanocomposites",** Nanofun-Poly 2006, 2nd International Symposium on "Nanostructured and functional polymer-based materials and composites", May 29- 31th 2006, Lyon (France).

- V.Tagliazucca, E.Callone, A.Dorigato, A.Pegoretti, S.Dirè **"Synthesis of organic/inorganic hybryd nanoparticles by sol-gel chemistry",** SAMIC 2006, 3-7th December 2006, Bressanore (Italy).

- Oral presentation : F. Bondioli, A. Dorigato, P. Fabbri, M. Messori, A. Pegoretti, F. Pilati **"High-density polyethylene reinforced with titania nanoparticles"**, Book of abstracts (ISBN 978-961-907317-9), European Polymer Congress (EPF) 2007, July 2-6th 2007, Portoroz (Slovenia).

- A.Dorigato, S.Monteforte, C.Migliaresi **"Polyvinylalcohol (PVOH)-clay nanocomposites for oxygen barrier coatings",** TICME, December 16-19th 2007, Trento (Italy).

- A.Dorigato, A.Pegoretti, A.Penati **"Toughening effect of silica nanoparticles in Linear Low Density Polyethylene (LLDPE)-silica nanocomposites",** TICME, December 16-19th 2007, Trento (Italy).

- F.Bondioli, A.Dorigato, P.Fabbri, A.M. Ferrari, M. Messori, A.Pegoretti **"High-density polyethylene reinforced with titania nanoparticles",** Nanotech, June 1-5th 2008, Boston (U.S.A).

9 Acknowledgements

First of all, I would like to thank my tutors, prof.Alessandro Pegoretti and prof. Amabile Penati (Department of Materials Engineering and Industrial Technologies, University of Trento, Italy) for their constant support throughout my graduate studies.

I would gratefully thank Leonardo Castellani and Polimeri Europa S.p.A (Mantova, Italy) for their kind provision of LLDPE chips and TEM images of the composites. I would like to thank prof. Riccardo Ceccato (Ceramurgy Laboratory, University of Trento, Italy) for the analysis of the surface properties of the fillers, and prof. Stefano Gialanella (Microstructure and Metallurgy Laboratory, University of Trento, Italy) for TEM images of fumed silica nanopowders. Furthermore, I would gratefully thank prof. Paolo Scardi and Dr. Mirco D'Incau (Microstructure and Metallurgy Laboratory, University of Trento, Italy) for their help with X-Ray Diffraction analysis on micro and nanocomposites. Moreover, I would like to thank prof. Jan Kolarik for his precious help in the application of non linear tensile creep approach on fumed silica nanocomposites.

I would gratefully thank all the people which worked with me in the Polymers and Composites Laboratory of the Department of Materials Engineering and Industrial Technologies (University of Trento, Italy). In particular I would like to thank the technicians (Alfredo Casagranda, Claudia Gavazza and Lorenzo Moschini) for their precious help in the experimental activity.

Last but not least, I would gratefully thank my family for their loving support trough all of these years. My parents Anna and Luciano, and my brother Paolo.

Trento, April 2009